

Modeling droplets flowing in microchannels

THÈSE N° 6269 (2014)

PRÉSENTÉE LE 20 AOÛT 2014

À LA FACULTÉ DES SCIENCES ET TECHNIQUES DE L'INGÉNIEUR
LABORATOIRE DE MÉCANIQUE DES FLUIDES ET INSTABILITÉS
PROGRAMME DOCTORAL EN MÉCANIQUE

ÉCOLE POLYTECHNIQUE FÉDÉRALE DE LAUSANNE

POUR L'OBTENTION DU GRADE DE DOCTEUR ÈS SCIENCES

PAR

Mathias NAGEL

acceptée sur proposition du jury:

Prof. C. Ancey, président du jury
Prof. F. Gallaire, directeur de thèse
Prof. J.-C. Baret, rapporteur
Dr Ph. Marmottant, rapporteur
Prof. Ph. Renaud, rapporteur



ÉCOLE POLYTECHNIQUE
FÉDÉRALE DE LAUSANNE

Suisse
2014

Leon Ernest Martin,
seinem geliebten Erstgeborenen widmet
der Autor diese aufschlussreichen Seiten.

Acknowledgements

In the last decade the field of microfluidics has widely expanded with new applications being developed every day. This vast field of research offered a lot of possibilities for a scientific exploration and most of the problems that I engaged in this work have been studied before by other researchers that introduced me to the matter and shared their results and ideas in an open manner.

I am much obliged to express my gratitude to Prof. Charles Baroud of the LadHyX at Ecole Polytechnique Palaiseau in France and his PhD student Rémi Dangla. They do a very inspiring work and provided us often their results and practical advice. Furthermore I am thankful to Prof. Anke Lindner at PMMH of UMPC in Paris. She invited me for experimental works on fibers in microchannels with her PhD student H el ene Berthet, whom I thank as well. For discussions and inspiration I thank Benjamin Dollet and Beno t Scheid, who maintained a long lasting contact and were always good for advice.

For numerical matters I thank Prof. emeritus Michel Deville, Marc-Antoine Habisreutinger and Lailai Zhu, whose advice and comments have contributed to my understanding and improved the quality of the approach.

Prof. Philippe Renaud from the Microsystems Laboratory 4 at EPFL was so generous to provide us with a laboratory space. None of our experimental results in this thesis would have been possible without his support and generosity. For their interest and recommendations I am much obliged as well to Prof. Jean-Christophe Baret and Philippe Marmottant.

It is not for formal reasons that the lions share of my respect and gratitude goes to my thesis director Prof. Fran ois Gallaire who, supported me with the right mixture of liberty and guidance. He created the laboratory of Fluid Mechanics and Instabilities just when I came to EPFL and made it an excellent group. I am grateful that I was part of the LFMI lab and thank especially PostDoc, Pierre-Thomas Brun, with whom I worked together on a few subjects that largely improved due to the cooperation with him, and to my long-time office mate Edouard Boujo, who was always a source of advice and a personal enrichment.

Due acknowledgement goes also to the European Research Commission who has funded the SimCoMiCs (Simulation in complex microchannels) project, in which I have been working the last years.

Finally I wish the best to Giacomo Gallino and Gioele Balestra who recently began a thesis at LFMI and will continue this work.



Neuch atel, July 20th 2014

Abstract

This thesis concentrates on the study of droplets in microfluidics, mostly performed numerically. The work motivation is rooted in the existing discrepancy between the level of complexity achieved in experimental microfluidics or even Lab-on-a-chip applications and our fundamental/theoretical understanding of such experiments. For the sake of completeness, other objects than droplets, such as fibers, are also considered in this work.

The numerical study of such systems and the multiphase flows that they encounter or create is challenging, mostly because of the multiplicity of moving interfaces in a reduced space. Herein is derived a simplified set of governing equations and a numerical method favoring the discretization of free interfaces. Such boundary element scheme has proven to be robust, efficient, and versatile allowing for the investigation of a wealth of theoretical and practical situations: from revisiting the well-known Saffman-Taylor instability to the theoretical prediction of the velocity of droplet in a microchannel, via the capture of droplets using microfluidic traps, the relaxation of a deformed droplet in a microchannel and the study of solid objects as the earlier evoked fibers.

This numerical tool has systematically been confronted to experiments, either from the literature when available or carried out directly in the laboratory when needed. The numerical simulations have in the majority of cases proven successful in reproducing the experiments and have helped gaining a greater physical understanding of the fundamental mechanisms underpinning Lab-on-a-chip applications.

Keywords: multi-phase flow, lab-on-a-chip, boundary element method, microhydrodynamics, droplet microfluidics, depth-averaged model

Zusammenfassung

Das Schwerpunkt dieser Doktorarbeit ist die Untersuchung von Tröpfchen basierter Mikrofluidik, mit einem Schwerpunkt auf numerischer Simulation. Das Interesse an diesen Strömungen wird motiviert durch die bestehende Diskrepanz zwischen der Komplexität die in experimentellen Lab-On-A-Chip (Labor-auf-dem-Chip) Anwendungen erreicht wird und dem bestehenden fundamentalen und theoretischen Verständnis. Vollständigkeitshalber berücksichtigt diese Arbeit abgesehen von Tröpfchen auch den Transport von Festkörpern, wie rigiden Fasern.

Die numerische Analyse solcher Systeme und der darin auftretenden Zweiphasenströmungen ist herausfordernd, vor allem wegen der beweglichen Phasengrenze und der räumliche Eingrenzung. Wir beschreiben hier ein vereinfachtes Gleichungssystem und eine numerische Randelementemethode, die für bewegliche Phasengrenzen optimiert ist. Für die hier benutzte Randelementemethode konnte Robustheit, Effizienz und Vielseitigkeit nachgewiesen werden, wodurch eine Vielzahl an theoretischen und praktischen Situationen untersucht werden konnte: Von der wohlbekannte Saffman-Taylor Instabilität über die theoretische Bestimmung der Tröpfchengeschwindigkeit, das Einfangen von Tröpfchen mit mikrofluidischen Ankern und die Entspannung von verformten Tröpfchen in Mikrokanälen bis zur Betrachtung von Festkörpern, wie den anfangs erwähnten Fasern.

Ergebnisse dieser numerische Berechnung wurden systematisch mit Experimenten konfrontiert, entweder aus der Fachliteratur oder, falls nicht vorhanden, mit selbst durchgeführten Versuchen. In fast allen Fällen konnte die numerische Methode die Experimente erfolgreich nachbilden und erlaubte jeweils einen tieferen Einblick in die fundamentalen Mechanismen, auf welchen Lab-On-A-Chip Anwendungen beruhen.

Schlüsselworte: Mehrphasenströmung, Labor-auf-dem-Chip, Randelementemethode, Mikrohydrodynamik, Tröpfchenmikrofluidik, höhengemitteltes Model

Résumé

Cette thèse de doctorat est consacrée à l'étude, principalement numérique, de la dynamique des gouttes dans le domaine de la microfluidique. Ce travail trouve son origine dans la disparité entre le niveau de complexité atteint dans la microfluidique expérimentale et dans ses applications dans des laboratoires sur puce et notre compréhension fondamentale/théorique de telles expériences. Par soucis d'exhaustivité, d'autres objets tels que les fibres ont également été pris en compte dans ce travail.

L'étude numérique de ces systèmes et les écoulements multiphasiques qui s'y produisent représentent un défi, principalement en raison de la multiplicité des interfaces mobiles confinés dans un espace réduit. Une série d'équations simplifiées à l'ordre dominant et une méthode numérique favorisant la discrétisation des interfaces libres sont dérivées dans le travail qui suit. La méthode des éléments de frontière s'est avérée robuste, efficace et versatile, permettant l'étude d'une multitude de situations théoriques et pratiques : de la relecture de l'instabilité emblématique de Saffman-Taylor, à la prédiction théorique de la vitesse d'une goutte dans un micro-canal, en passant par la capture de gouttes utilisant des pièges microfluidiques, jusqu'à la relaxation d'une goutte déformée dans un micro-canal ou l'étude d'objets solides tels que les fibres évoquées précédemment.

Cet outil numérique a été confronté systématiquement à des expériences, soit issues de la littérature lorsque celles-ci existaient, soit directement réalisées en laboratoire. Dans la majorité des cas, les simulations numériques ont pu reproduire les expériences avec succès et ont apporté un nouvel éclairage des mécanismes fondamentaux se trouvant à la base des applications de microfluidique de gouttes pour les laboratoires sur puce.

Mots clés : Écoulement multi-phasique, laboratoire sur puce, méthode des éléments frontière, hydrodynamique à micro échelle, microfluidique des gouttes, model moyenné en hauteur

Riassunto

L'oggetto di questa tesi è lo studio, principalmente numerico, della dinamica di gocce nel campo della microfluidica. La motivazione di questo lavoro è radicata nell'esistente divario tra il livello di complessità raggiunto nella microfluidica sperimentale, ad esempio nelle applicazioni dei Lab-on-a-chip, e la nostra conoscenza teorica di questi esperimenti. Per ragioni di completezza, altri oggetti, in particolare delle fibre, sono stati considerati in questo lavoro.

Lo studio numerico di questi sistemi e dei fluidi multifasici che vi partecipano o ne sono creati è complesso, principalmente per il gran numero di interfacce in movimento in uno spazio ridotto. Un sistema di equazioni semplificate che governano la fisica del problema e un metodo numerico adatto alla discretizzazione delle interfacce sono derivati in questo lavoro. Tale metodo numerico (Boundary element method) ha dimostrato di essere robusto, efficiente e versatile, permettendo lo studio di un gran numero di fenomeni teorici e pratici: dalla revisione della emblematica instabilità di Saffman-Taylor alla predizione teorica della velocità di gocce in microcanali, passando per la cattura di gocce usando trappole microfluidiche e lo studio di oggetti solidi come le sopra citate fibre.

Questo strumento numerico è stato confrontato sistematicamente con esperimenti, provenienti dalla letteratura quando disponibili o direttamente svolti in laboratorio. Le simulazioni numeriche hanno avuto, nella maggior parte dei casi, esito positivo nel riprodurre gli esperimenti e hanno permesso di comprendere meglio i meccanismi fisici che intervengono nelle applicazioni dei Lab-on-a-chip.

Parole chiave: flusso multifasico, lab-on-a-chip, metodo degli elementi di contorno, microidrodinamica, microfluidica in gocce, modello mediato sull'altezza

Contents

Acknowledgements	v
Abstract (English/Français/Deutsch/Italiano)	vii
1 From Microhydrodynamics to Droplet Microfluidics	1
1.1 Scaling laws in Droplet Microfluidics	2
1.2 Fields of application for microfluidics	4
1.3 From microfluidic experiments to microhydrodynamic simulations	10
I Theory and 2D model description	17
2 A depth-averaged fluid model for confined shallow flows	21
2.1 Dimensional analysis of the Navier-Stokes equation	21
2.2 Depth-averaging the Stokes equation	23
2.3 Solutions for undeformable droplets	31
3 Numerical solution of the deformable interfaces	47
3.1 Transformation to boundary integrals	47
3.2 Numerical solution of the boundary integral equation	52
3.3 Boundary integrals to solve for field variables	62
3.4 Implementation	64
4 Liquid interface evolution in theory and experiment	67
4.1 Saffman-Taylor Instability	67
4.2 The relaxation of an ellipse	79
4.3 Free space droplet migration	90
4.4 Droplet deformation driven by the channel geometry	95
II Modified theory and 3D influences	101
5 Dynamic Film formation	105
5.1 Origin of dynamic film formation	105
5.2 Dynamic meniscus boundary condition	109
5.3 Experimental study on droplet velocity	116

Contents

6	Topographical boundary conditions	121
6.1	A topographical model for microfluidic anchors and rails	121
6.2	A numerical investigation of anchors	126
6.3	Discussion and droplets on rails and anchors	132
6.4	Droplet formation on a tearing slope	136
7	Solution of rigid objects	141
7.1	Problem formulation for rigid objects	142
7.2	Lubrication gap flow profile	144
7.3	Microfluidic transport of discs	146
7.4	Microfluidic transport of fibers	152
8	Conclusion and perspectives	161
A	Appendix	171
A.1	Numerical evaluation of Bessel functions	171
A.2	An undeformable droplet based on Darcy's law	175
A.3	Force integration on the top and bottom faces of a confined droplet	176
A.4	Green's functions for 2D Stokes flow	177
A.5	Integral transformations	177
A.6	Resolving issues with singular integrals	179
A.7	Fabrication of microfluidic chips	183
	Nomenclature	185
	Bibliography	188
	Curriculum Vitae	197

1 From Microhydrodynamics to Droplet Microfluidics

*Il est vraisemblable que vous n'avez aucune notion,
Panmuphle, huissier porteur de pièces,
de la capillarité, de la tension superficielle,
ni des membranes sans pesanteur, hyperboles équilatères,
surfaces de nulle courbure, non plus généralement
que la pellicule élastique qui est épiderme de l'eau.*

— Alfred Jarry, Gestes et opinions du docteur Faustroll

Mechanics is about forces and displacement of objects. In classical fluid mechanics the origin of these forces are capillarity, inertia, gravity and viscosity. Fluid motion creates forces due to these contributions, which balance each other perfectly.

Fluid motion of more than one distinct fluid or one fluid present at different phases, e.g. liquid and gaseous, is termed multi-phase flow or two-phase flow, when two fluids or two phases are considered. A bubble suspended in a surrounding fluid is an example of such a two-phase flow. The two-phases are considered to be immiscible and so the interface between both phases marks a sharp transition and is generally a complicated two-dimensional surface in a

three-dimensional space. Although the equations that describe the motion of a bubble can also be used to describe the motion of the atmosphere and ocean, a very large two-phase.

When at small scale, surface forces like capillary forces will start to dominate over volume forces, like gravitational forces, which explains for instance the minimal size of droplets dripping from a faucet. Volume forces increase with the length scale to the power of three, $V \propto L^3$, and surface forces with the length scale to the power of two, $A \propto L^2$. When the length scale increases the influence of volume forces compared to surface forces increases with L . When both forces are about equal the characteristic length is referred to as the capillary length. Droplets dripping from a leaking faucet will have a size in the order of the capillary length because smaller droplets will resist gravity by surface tension.

In this example size makes a difference. In the following section the differences between micrometer scale and meter scale fluid dynamics is outlined with the help of scaling laws. The physics that dominates the microscale will then be related to recent technological developments and applications for microfluidic flow in section 1.2.

The objective of this thesis is to simulate microfluidic two-phase flow, which is motivated by the complexity fluid motion that is confronted by the need to understand and predict the behavior of the fluid interface.

1.1 Scaling laws in Droplet Microfluidics

Physical parameters of a problem are measured in basic units, also called dimensions, e.g. meters, seconds and kilograms. So the parameters are related by their units, a property that we use when non-dimensionalizing equations. By dimensional analysis, as shown in the example for gravity and pressure, the influence of viscous, inertial, gravitational and capillary effects can be roughly estimated.

For a given set-up there is a characteristic length L , fluid velocity U , gravity acceleration g , density ρ , viscosity μ , surface tension γ . Others influences like temperature or wetting properties are not considered in this thesis. What to choose as characteristic value does not matter primarily, the scaling works for any choice but the physical interpretation might be less obvious. For instance for a channel flow, choosing for a length L not the channel length but the width assures that one has the approximate length over which a meniscus forms or a viscous Poiseuille profile is established.

The numerical values of the non-dimensional parameters establish in a more accessible way, which terms are dominant and which are not. Some variables depend on the flow field, like pressure and velocity and some parameters are constant and depend on the liquids chosen. Table 1.1 contains the material parameters for the liquids used, which are taken from material data sheets (3M Fluorinert FC-40 and F2 Chemicals, Perfluorodecalin) or, in the case of surface tension, were measured by the pendant drop method. Deionized water was used either pure

1.1. Scaling laws in Droplet Microfluidics

or with 2% in weight of a water solvable surfactant (Migros dish washing liquid). Surface tension for the liquid-liquid system are given in table 1.2.

	Perfluorodecalin	Fluorinert FC-40	water	water with surfactant
ρ	$1917 \frac{kg}{m^3}$	$1855 \frac{kg}{m^3}$	$1000 \frac{kg}{m^3}$	$1000 \frac{kg}{m^3}$
μ	$5.1 \cdot 10^{-3} Pa s$	$4.1 \cdot 10^{-3} Pa s$	$10^{-3} Pa s$	$10^{-3} Pa s$
γ (air)	$19.6 \cdot 10^{-3} Pa m$	$16 \cdot 10^{-3} Pa m$	$72 \cdot 10^{-3} Pa m$	$34.5 \cdot 10^{-3} Pa m$

Table 1.1: Material parameters of fluids used in this work.

	water	water with surfactant
Perfluorodecalin	$56.2 \pm 2 \cdot 10^{-3} Pa m$	$13.7 \pm 0.7 \cdot 10^{-3} Pa m$
Fluorinert FC-40	$54.1 \pm 2 \cdot 10^{-3} Pa m$	$13.6 \pm 0.5 \cdot 10^{-3} Pa m$

Table 1.2: Surface tension for liquid-liquid two-phase fluids.

A force has the dimension Newton, that is $N = \frac{kg m}{s^2}$. For any of the hydrodynamic contributions a force scale can be established:

Viscous force:

$$F_v \propto \mu UL.$$

Inertial force:

$$F_a \propto \rho U^2 L^2.$$

Gravitational force:

$$F_g \propto \rho g L^3.$$

Capillary force:

$$F_c \propto \gamma L.$$

The force is not equal but proportional to the characteristic dimensions, there is a proportionality constant that reflects the individual set-up.

We see that in the regime of small L the gravitational forces and inertial forces decrease faster than the viscous and capillary forces. The objective of scaling arguments is to obtain a dominant balance between at least two terms. One term that drives the fluid and another that opposes the driving force. For instance a deformed bubble with surface tension in a medium without viscosity nor inertia would relax infinitely fast because there is nothing that balances the interfacial force. A balance with viscosity fixes a characteristic time, $T \propto \mu L / \gamma$, and a balance with inertial fixes $T \propto \sqrt{\rho L^3 / \gamma}$.

The comparison between the different forces is obtained by dividing one by the other as to obtain a non-dimensional number. Minimum and maximum values are estimated using the material parameters (Table 1.1 & 1.2) and assuming a fluid velocity between $U = 0.1 \cdots 10 mm/s$ and length scale $L = 10 \cdots 100 \mu m$.

$$\text{Eötvös number } Eo = \frac{F_g}{F_c} = \frac{\Delta\rho g L^2}{\gamma}, \quad 2 \cdot 10^{-5} < Eo < 7 \cdot 10^{-3}. \quad (1.1)$$

$$\text{Reynolds number } Re = \frac{F_a}{F_v} = \frac{\rho UL}{\mu}, \quad 4 \cdot 10^{-4} < Re < 1 \quad (1.2)$$

$$\text{Capillary number } Ca = \frac{F_v}{F_c} = \frac{\mu U}{\gamma}, \quad 2 \cdot 10^{-6} < Ca < 4 \cdot 10^{-3}. \quad (1.3)$$

The Eötvös number is approximately zero, so gravitational effects can be neglected compared to capillary effects. As for the Reynolds number, it is small but a tie with viscosity is possible. In our model consideration we neglect also inertial terms because the Reynolds number is assumed small. This example shall serve as warning that the Reynolds number is to be estimated carefully.

At last the capillary number is small as well, which indicates that surface tension forces dominates over viscous forces and therefore over all forces. In that case a droplet inside a channel will find a static equilibrium position and remain at rest. However viscous forces does manage to compete with capillary forces, an example is a droplet that moves in a wide channel. The droplet is squeezed between the top and bottom walls, floor and ceiling, as the channel rigidity wins over surface tension¹ and impose a "pancake" shape. Confined between two walls the droplet can still glide between the parallel walls when pushed by a pressure gradient. Should it reach a constriction and would partially block the channel, the viscous fluid flows past the droplet in a narrow gap. The resulting pressure gradient over the droplet deforms the droplet and pushes it past the constriction. Hence although the low capillary number indicates dominance of the surface tension, viscosity can locally supersede.

1.2 Fields of application for microfluidics

From Microhydrodynamics to Physiochemical Hydrodynamics It follows from the aforementioned scaling arguments that microhydrodynamics is a simplification of hydrodynamics because in the description of fluid motion we may neglect inertia. With decreasing size however one approaches contributions of different nature that were neglected before. These contributions are for instance described by physiochemical hydrodynamics, they include the effects of repulsion and attraction by electrostatic or magnetic forces, migration of charged or uncharged particles and the influence of walls in terms of affinity to be wetted by a fluid (Probstein, 1989). Wetting and surface tension play an important role in this work because they interact particularly strong with the fluid motion. The monograph by de Gennes et al. (2004) elucidates these capillary phenomena.

¹For thin films of PDMS this is not the case and led to the development of capillary origami (Py et al., 2007)

From Physiochemical Hydrodynamics to Microfluidics Physiochemical hydrodynamics is the entry gate of fluid dynamics to touch research of the soft matter community. Softmatter combines research areas from biology, chemistry and physics and a number of books have been dedicated to this topic. A concise description was given by de Gennes (1992).

In order to study these nanometric to micrometric phenomena, the idea to encapsulate and probe at a confinement level of the object was a natural strategy. Advantages of small sizes are summarized in the article by Bartolo and Aarts (2012). The adopted strategy to transport and manipulate material was to drive it by a carrier fluid through microchannels, which is seen as the advent of microfluidic Lab-on-a-chip whose origin and a number of examples are given by Whitesides (2006). A lot of techniques have been developed to manufacture devices, perform probing and manipulation of which a concise summary has been compiled in a review by Squires and Quake (2005). A brief overview of Lab-on-a-chip applications was written by Lindstrom and Andersson-Svahn (2010).

From Microfluidics to Droplet Microfluidics As pointed out by Cahill (2014) in a recent monograph on applications of micro-segmented flow, single phase flow can yield strong limitations. For instance biological material, like proteins are subject to spontaneous binding to channel walls and so further encapsulation is needed to prevent contamination of the channel or modification of the material by uncontrolled interaction. Hence a methodology was developed where droplets streamed in microchannels encapsulate the investigated material, which were reviewed by Baroud et al. (2010) and Seemann et al. (2012). Although the fluid motion is laminar in the regime of microhydrodynamics, the fluid control becomes complex due to the liquid-liquid interface in two-phase flows.

In parallel digital microfluidics has been developed where droplets are moved on a substrate by electrowetting without an external carrier fluid. There is a direct control on a droplet specimen with this technique but the platform for electrowetting is more complicated and the throughput slower. A review on this method has been written by Choi et al. (2012).

Microfluidic applications today span from PCR (polymerase chain reaction) for DNA amplification, to in vivo immunoassays on cells and microchemistry. We will complement the motivation here by describing an example that demonstrates how microfluidics can increase screening of yeast, being 1000 times faster and 10-million times less expensive than when performed on a state-of-the art automated platform. This work has been done by Agresti et al. (2010) and aimed for directed evolution of a horseradish peroxidase that is bound to the surface of yeast cells.

A dense solution of yeast cell coated from a library of horse radish enzymes is injected into the microfluidic chip. The solution, aq1 shown in figure 1.1 (a), is slightly diluted with a costream of water containing a substrate for the yeast cells, aq2. When adding water to the dense yeast solution the flow rates can be adapted such that mostly droplets with only a single yeast cell is formed. Coflowing oil partitions the aqueous thread into a dense stream of droplets at a

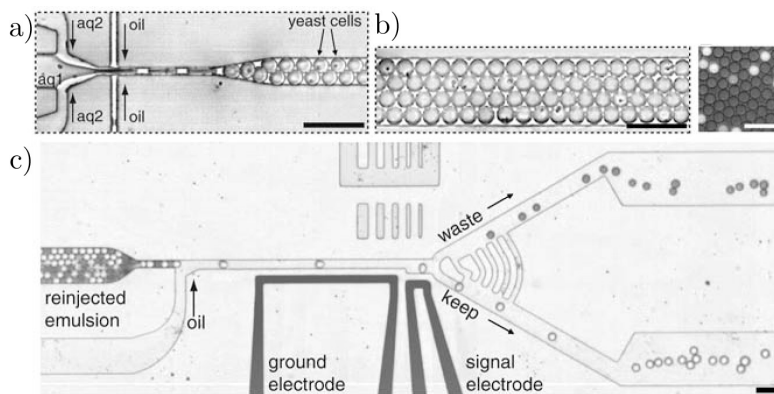


Figure 1.1: Example of Lab-on-a-Chip application for yeast selection, image taken from (Agresti et al., 2010). a) Encapsulation of yeast cells in water droplets in an oil stream. b) Incubation and development of fluorescence. c) Selection of droplets according to the fluorescence signal.

frequency of 2000Hz and $23\mu m$ in diameter. A bio-compatible surfactant coats the droplet interface to stabilize the emulsion whose volume consist to 67% of the aqueous yeast solution.

In every second 2000 droplets are created, which contain only a few picoliters of liquid and each a single yeast cell. Such yield is only possible if the channel geometry, flow rates and surfactant has been optimized, mostly by time consuming trial and error.

In a wide channel the droplets flow slowly and surface absorption of the fluorescent molecules allows to estimate the activity of the enzymes, shown in figure 1.1 (b). Volume and residence time is well controlled in a homogeneous emulsion.

When the emulsion is recovered at the end of the chip the droplets align in a narrow channel and become spaced by a costream of oil such that fluorescence measurement can be performed on a single droplet using laser a monochromatic light source. The signal is automatically analyzed and upon reaching a designated threshold the droplet is kept or discarded. This sorting step is done by dielectrophoresis, where an electric field is created between two electrodes shown in figure 1.1 (c). The channel layout favors droplet transport in the waste channel when no electric field is applied. A 20kHz square wave signal creates a inhomogeneous charge distribution at the droplet interface and deviates the droplet into the keep channel. Here again the channel and electrode layout is crucial for a function sorting device.

The advantages of the system are on one hand the low consumption of liquids and yeast cells, no need for well plates and pipette tips. And on the other hand high specificity using only a single yeast cell and high frequency. In analogy to computer chips it is apparent that microfluidics has the capacity to out-perform traditional lab platforms similarly as integrated semiconductor circuits, which replaced the vacuum tube in the first computers.

1.2.1 Running a microfluidic experiment

For typical applications the literature reports the size of microchannels to be in the range of tens to hundreds of micrometers. In most cases these channels are created by Soft-Lithography, whose basic concepts were developed in the 1950's and 1960's when the first micro-chips were produced since Lithography allowed for small, reliable and mass producible semi-conductors. A documentation of the fabrication techniques for microfluidic devices is given in annex A.7. The structures produced by this process are layers of uniform height, where a structure could be additively, built onto a substrate, or subtractively, etched into a substrate. Structures of multiple layers exist and in some cases structures of variable height have been achieved (Chen et al., 2003) but this is rare yet.

The layout of a channel that is used in this work is shown in figure 1.2 (a) and a photo of a chip with the same layout on an inverted microscope shown in (b).

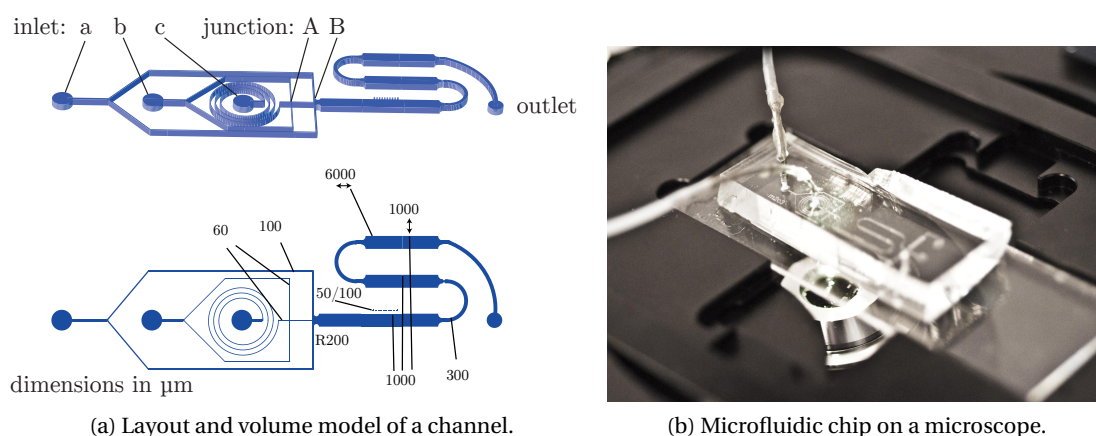


Figure 1.2: An example of a microfluidic chip.

The following chapter shall provide the unfamiliar readers with a Lab-on-a-chip experiment, similar to those described in the literature. Since 2001 the Royal Society of Chemistry has dedicated a journal to such applications, which is called Lab-on-a-Chip.

Preparation Starting point for the microfluidic chip is a PDMS block that has a channel circuit molded in PDMS², shown in figure 1.2b. The PDMS block with the circuit and a glass slide are placed in a plasma chamber and exposed to a pressure of about 0.6mbar, then an oxygen plasma is activated in the chamber at 100W for 6s. Thereafter the PDMS block and the glass slide are taken and pressed together, with the side where the channels have been molded against the glass slide. This seals the channel by a bonding, which is due to activation of the surface.

The microchannels are connect to the outside by holes, which have been punched before

²For prior production steps look up appendix A.7, which explains how the PDMS block is produced.

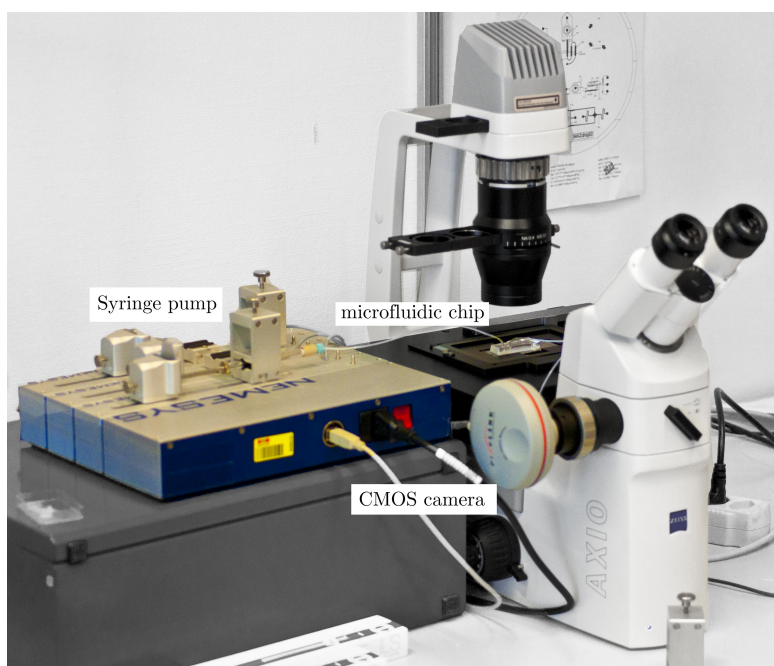


Figure 1.3: A microfluidic chip placed on an inverted microscope, equipped with a digital camera. A syringe pump provides drives the liquid into the chip.

through the PDMS block into the wide area, inlet a, b & c.

The chip is filled with deionized water from a plastic syringe whose plastic tip is placed in the outlet of the chip. With a little gas in the back of the syringe, slowly pressing down the plunger increases gently the pressure and fills the chip. The plasma treatment has rendered the PDMS surface hydrophilic so the microchannel fill almost automatically once wetted with water. Water is injected till liquid domes have formed on each of the inlet holes and no air bubbles are left in the channel, these air bubbles could block a channel. Thereafter the chip is placed on an inverted microscope, which is seen in the photograph in figure 1.3. The inverted microscope has the advantage of offering a clearing above the chip where the tube is to be connected because the objectives are located below the object. The focal length of the microscope, depending on the magnification, is few a millimeters, so the feature channels appear after a slide of glass, to which the chip is bound. A slide of glass at least is the usual distance in bright field microscopy.

A syringe pump next to the microscope has been loaded with three syringes, two 1 ml syringes with deionized water and one $100\mu\text{l}$ syringe with fluorinated oil, FC-40. The syringe pump can advance the plunger with a certain precision as to provide an accurate amount of fluid to the chip. If the syringe is too big the precision may degrade at low flow rates, on the contrary if the syringe is too small the reservoir may be empty before the end of the experiment.

Syringes and tubing must contain no gas bubbles because minute amount of gas can represent relatively large volumes compared to the volume inside the micro channels, hence when the

pressure increases and the gas becomes compressed the apparent volume changes. The same kind of apparent compressibility comes from the elasticity of the tubing. The tubes need to be elastic in order not to break when the microscope stage moves but raising the pressure level stretches the tubing. Before tubing connection to the chip, the syringe pump drives the fluid slowly till a pendant drop is created at the tip of the tubing or connector needle. Pushing the tubing/connector through the pendant drop and through the liquid dome on the PDMS chip ensures that the connection is made without introducing air bubbles in the channel.

Operation First driving the surrounding fluid, water from inlet a & b, water, then gently raising the flow rate of the inner fluid, oil from inlet c, till a steady dripping regime is attained in junction A, shown in figure 1.4a. The fluid-fluid interface appears dark because of the curved meniscus, which deviates the incident light from the microscopes condenser away from the objective. This meniscus forms because the oil, does not wet the PDMS wall. This is curious because the liquid-liquid interface area would be minimal in a wetting configuration. However water is attracted to the PDMS while the fluorinated oil is repelled such that a liquid film of water always remains. Impurities or dust could make oil stick to the wall but as long as the FC-40 glides on a film of water it will not get in contact with impurities. One danger of gas bubbles is that they might enable oil to touch the wall and stick to impurities.

Adjusting the flow rate b & c at the flow junction A allows to influence the volume of the droplets. When the droplets reach the second flow junction B they become immersed in the outer flow from inlet a, shown in figure 1.4b. The droplets move in the wide channel advected by the outer flow. On their top and bottom face, the oil droplets slide on a thin film of water, whose height is in the order of 1/100 of the channel height.

The surface tension keeps the droplet apparently cylindrical, only when they reach a constriction at the end of the channel the droplet deforms as it becomes squeezed by the outer flow. Leaving the construction the droplet is stretched by the outer flow as the streamlines expand. Finally the droplets reach the outlet of the channel and leave the microfluidic chip.

Changing the flow rate ratio at the first fluid junction influences the aspect ratio of the droplet, radius divided by height, while changing the flow rate ratio at the second junction influences the droplet velocity and therefore the balance between viscous to surface tension forces, the capillary number. The viscosity ratio, that is the ratio of inner fluid viscosity to outer fluid viscosity remain unaltered and would require to use fluids with different viscosities.

In this relatively simple set-up the droplet velocity was measured, which will be shown in chapter 5.3. In this narrative illustration only a fraction of the physics that is present in microchannel flow has been detailed. In some chapters more mechanisms will be elucidated but the thesis is far from giving a complete picture of the physics of microhydrodynamic droplet flows.

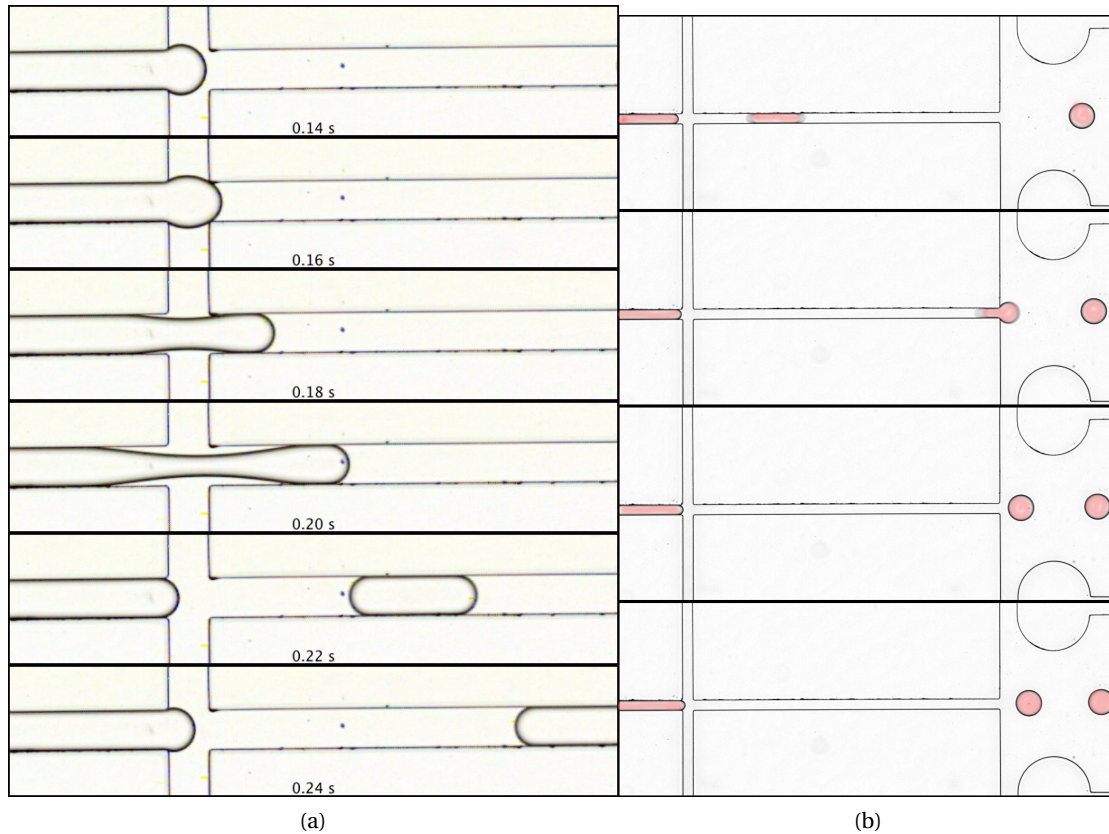


Figure 1.4: (a) Droplet shedding at junction A in figure 1.2a. (b) Droplet is transported into the wide channel after junction B in figure 1.2a.

1.3 From microfluidic experiments to microhydrodynamic simulations

Despite the illustrative example of an experiment, the nature of this work is rather theoretical. Nevertheless the tools that were developed are inspired by a close regard onto experiments, whether home-made or more often, conducted by other researchers.

The theoretical and numerical tools are built on the principle to include only the very necessary into the problem formulation but to remain as close as possible in the parameter space of the microfluidic community.

1.3.1 Challenges in droplet microhydrodynamics

The means to control droplets in micro channels are more or less indirect, apart from kinematic control like valves and switches (Geertz et al., 2012). Design of indirect control by electric fields, local modification of surface tension or passive control due to an intelligent channel geometry requires a neat prediction of the outcome of an indirect intervention or a passive

1.3. From microfluidic experiments to microhydrodynamic simulations

channel layout.

Single phase flow is rather predictable, the flow rate in most cases can be calculated by the Hagen-Poiseuille law (Bruus, 2008) but in two-phase flow the fluid motion is more complex and so are the models that are proposed for a variety of standard flow geometries.

At the present state of the literature experimentalists provide the lion's share of results in the domain of droplet microfluidics, numerical results are few and often restricted to droplets under weak confinement, reflecting the difficulties that are encountered in these small scale flows.

In a review Cristini and Tan (2004) presented numerical approaches to simulate 3D two-phase flows in microfluidics. There are Finite Volume/Finite Elements Methods (Carlson et al., 2010) based on the Navier-Stokes equation or Lattice-Boltzmann Methods (Liu and Zhang, 2011) based on the Boltzmann equation. While the Navier-Stokes equation provides a classical framework, Lattice-Boltzmann methods are very well suited for massive parallelization, but they suffer from an ambiguous macroscopic significance of the microscopic parameters, in particular in two-phase flows. Parallelization is a key issue because the simulations are costly in computation time, running often for hours on hundreds of processors.

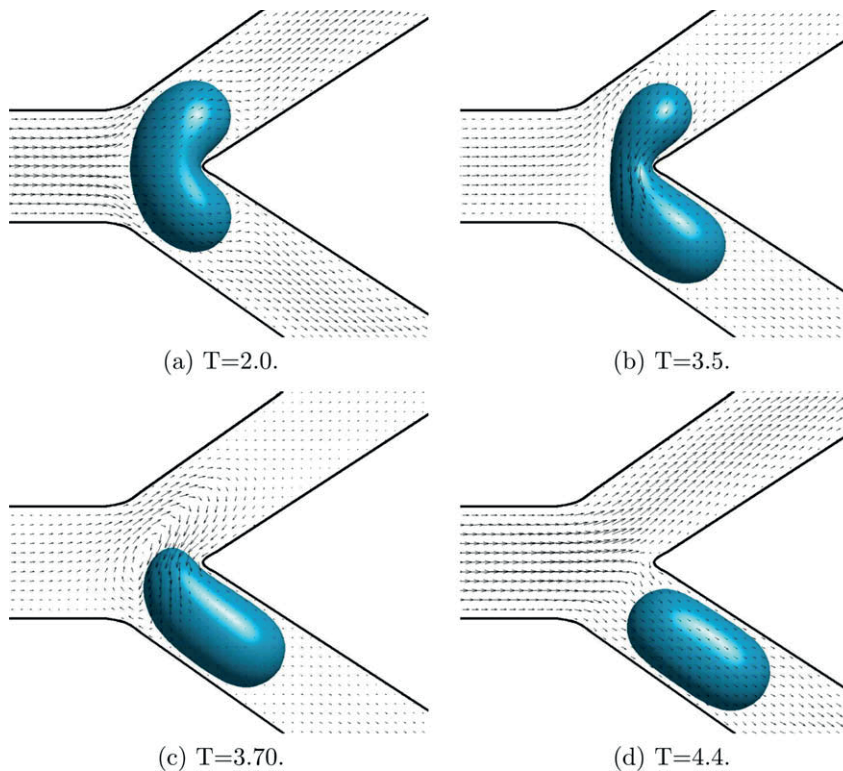


Figure 1.5: Four images at different time steps of a droplet entering a Y-junction at capillary number $Ca = 1.8 \cdot 10^{-3}$.

A remarkable work that illustrates this point was done by Carlson et al. (2010) who studied

droplet break-up of droplets entering a Y-junction. Their numerical study used the Volume-of-Fluid method to solve in three spatial dimensions for capillary numbers as low as 10^{-3} . The influence of droplet volume and capillary number allowed to estimate if break-up occurs or not.

The inlet channel has a square cross section and the droplet is visibly confined by the channel wall and adopts an elongate shape. The domain has been discretized with 7.5 million tetrahedrons and the time step was 10^{-7} , which amounts to iteration of several 10-millions of time steps for one simulation. Hence the solution on a parallel computer is necessary, with 1024 processors the computation time is reduced to 24h.

Long computation times are usually thought as the the flaw of high Reynolds number simulations, where the numerical discretization needs to be fine enough to capture the turbulent vortices. However, they are also the signature of creeping two-phase flows, where the free interface introduced nonlinearity and stiffness. The interface needs to be accurately described by being either captured or tracked by the numerical scheme, leading to two different methodologies:

1. Interface tracking , where the interface is represented by faces of the discretizing mesh. The interface representation is excellent but the mesh around the interface has to evolve with the fluid, leading to complex algorithm that needs to create and delete nodes automatically in order to avoid too dense, sparse or skewed cells (Rabello Dos Anjos, 2012).
2. Interface capturing , where the mesh increases the resolution around the interface without conforming to the interface shape. For this method the mesh can be structured, for instance consist of cubic boxes that can be subdivided into smaller and smaller boxes, called octree mesh refinement. The interface is represented by a Level-Set or Volume-of-Fluid and smeared over several cell (Tryggvason et al., 2011).

Interface tracking requires a robust remeshing algorithm and includes a time consuming remeshing step, while interface capturing schemes are less precise due to the diffuse interface. In microfluidic simulations the terms related to surface tension are the dominant force and lead to a numerically stiff problem. Hence a fine spatial resolution is accompanied by a small restrictive time step.

The Boundary Element Method (BEM) is a so-called meshless methods, where the mesh has one dimension less, so only surfaces are meshed. BEM approaches have been followed for 3D Stokes flows Janssen and Anderson (2007), for 2D Stokes flow Wrobel et al. (2009) and Darcy flow Gupta et al. (2002).

For free interfaces the 3D BEM method is an efficient approach but still demands a high numerical effort, which explains why only few results in confined two-phase flows have been reported so far. The prohibitive numerical cost results in particular from the inherent

1.3. From microfluidic experiments to microhydrodynamic simulations

multiscale character of droplet flow in thin microchannels: the drop size R , the channel depth H and the lubricating film thickness g with $g \ll H \ll R$.

In this work we exploit the confinement of top and bottom walls that is due to the high aspect ratio, $H \ll R$. Thus assuming that the confinement constraints the fluid motion to a planar flow, we depth-average the fluid equations and reduce them from three to two spatial dimensions. Influences due to the thin direction over which we average are to be reintroduced by lumped parameter models. Averaging in the thin-direction is furthermore tempting since the 2D problem adopts the natural perspective that one observes through the microscope. Meaning that the channel layout, see for instance figure 1.2a, shows only lateral confinement due to the side walls. When applying the boundary element method to the depth-averaged problem in 2D, it leads to a numerical problem that is discretized only on the boundaries and therefore simplifies to a quasi 1D problem.

1.3.2 Objective of this work

Physics is about the description of nature. Although micro and macro sized objects inherit their properties from elementary particles, knowledge of their laws does not reveal us immediately their behavior and mechanisms. An appropriate level of description needs to be chosen.

Three dimensional methods for microfluidic simulation exist and have been described in the literature. The results treat only few mechanisms and the flows are not as much confined as in the scenarios addressed in this work. The choice made in this work was not to reproduce the rather complex framework of a 3D solver, which are intense in terms of calculation time, but to explore a new method.

Microfluidic flow problems often have many free parameters, material properties and geometrical parameters. Therefore solving in three spatial dimensions on a parallel computer in a few days might shed less light on a problem, than a 2D simulation that runs on a desktop computer in a couple of hours. Although 2D in physical space the phase space of geometrical or material parameters can be explored in much higher dimension than feasible for 3D simulation due to the shorter calculation time. Without denying that results from three-dimensional simulation might be very interesting to compare to, the results obtained in this work treat confined flows at low capillary number that are not yet explored by 3D simulations.

With the objective to simulate scenarios of applied microfluidics the possibility to simulate rotating devices is included in the fluid model. Spinning devices, similar to a CD or DVD with microfluidic circuits present a robust and low cost way to drive fluids in commercial microfluidic applications (Gorkin et al., 2010). Imaging of fluid flow in a spinning disc ($\sim 30 Hz$) is not always possible and therefore simulation techniques are a good complementary tools for design of channel layout and understanding of fluid flow mechanisms.

1.3.3 Idea of this work

It is common sense in mathematical physics to replace a complex problem that one can not solve by a simplified problem that can be solved. In this tradition the original set of equations that describe fluid motion have been replaced by a simpler equation that is supposed to show the same qualitative behavior and differs only slightly in quantitative terms. Such an approach requires an *a posteriori* justification as well as *a posteriori* proofs of effectiveness, which will be brought by this work.

Our model lies in terms of complexity and ability somewhere between cost-prohibitive computational tools that solve 3D³ equations and simple model equations that researchers develop to explain certain mechanisms observed in experiments. With respect to simple model equations our approach is more general because it allows for more complexity. With respect to 3D computations our model is much faster and in certain cases might give results, while 3D codes can fail when the number of degrees of freedom goes beyond reasonable. This model is derived from the governing 3D equations but with the help of physically motivated order of magnitude arguments, rather than mathematical ones. Main assumption is that the microchannel is much wider than deep.

In the microscopy plane or lateral direction the channels expose a geometrical complexity with various channel shapes. While in the perpendicular direction, perpendicular to the microscopy plane, the geometrical variation is low but the influences are rather strong, more dissipation and strongly curved meniscus. Therefore solving the problem in the plane of variance and modeling the direction of dominance is the key ingredient to this work. I will also refer to directions that lie in the microscopy plane as the in-plane direction and to everything perpendicular to this plane as out-of-plane direction.

1.3.4 Structure of this work

The first part of this thesis is dedicated to the basic concepts and problems within the 2D depth-averaged framework. First the model equations are derived in chapter 2 and some analytical solutions are provided for simple geometries in section 2.3.

A cornerstone of this work is the development of a numerical scheme that solves the model equations for evolving boundaries. The scheme and a number of acceleration techniques are presented in chapter 3.

With this numerical tool at hand, a few scenarios are investigated in chapter 4, some classical like the Saffman-Taylor instability and some novel like recent microfluidic tensiometry devices. In most cases comparison to experiments is undertaken.

The second part of this thesis is dedicated to modified boundary conditions that include 3D phenomena that the basic model equations can not reproduce, like the dynamic meniscus

³In all three spatial dimensions, opposed to 2D which considers only two spatial dimensions.

1.3. From microfluidic experiments to microhydrodynamic simulations

in chapter 5 or deformations due to kinematic constraints for instance by a 3D channel topography, discussed in chapter 6. Modeling 3D effects also made it possible to simulate the motion of rigid objects, shown in chapter 7.

In the last chapter a conclusion discusses the results obtained by the method and perspectives are drawn for future applications.

1.3.5 A word on notation

Scalar values or scalar valued function is written in plain letters. In most cases upper-case letters stand for dimensional parameters, like the height of the microchannel H or the radius of a droplet R . Their non-dimensional homologues usually carries the same letter in lower-case, like the non-dimensional channel height $h = H/L$. Except for the radius, which is \mathcal{R} , because small r denotes the radial component in polar coordinates.

Vectors are denoted by bold lower-case letters and matrices, 2nd order tensors, by bold upper-case letters. Components of a vector or matrix are written in regular letters (non-bold) and carry indices. An exception will be encountered in chapter 2.3, where also 3rd order tensors are used. The notation will be introduced in the respective chapter. Greek letters are never used in bold face and shall carry one or two overbars when denoting a vector or a matrix.

For the velocity vector and position vector, principal quantities in this work, the elements of \mathbf{x} are x, y & z . And for \mathbf{u} the first element is u_x or simply u , its second and third members are u_y and u_z .

A list of variables is found in the nomenclature. Some variables that appear only within a section are omitted from the list. Exceptions are special functions like the Bessel function.

Theory and 2D model description Part I

This part of the thesis explains the two-dimensional methodology for microhydrodynamic two-phase flows. A fluid flow model for shallow confined flows is developed in chapter 2. Using the superposition of singularities two analytical two-phase flow solutions for this model are presented: The solution for a cylinder and for an undeformable droplet.

One of the main novelties of this work with respect to microfluidic simulation is the boundary element method for the Brinkman equation. All numerical results were obtained using this method, which marks the importance of chapter 3. There is an intimate connection between the method of singularities and the boundary element method, since both require the Green's function. Validation and demonstration of convergence is provided in the respective sections.

Chapter 4 presents at first results of deformable interfaces in infinite domains, the expanding interface of a Saffman-Taylor instability with finger formation and the relaxation of a deformed droplet. The latter has been investigated together with Dr. Pierre-Thomas Brun and was published in *Physical Review E* (Brun et al., 2013). Following results show different types of droplet motion, driven by a carrier flow, centrifugal forces or Marangoni stresses, and droplet interaction with walls in comparison to two studies on droplet stretching.

2 A depth-averaged fluid model for confined shallow flows

2.1 Dimensional analysis of the Navier-Stokes equation

Fluid dynamics is traditionally a domain that makes extensive use of mathematics to describe or express related phenomena. When describing the motion of fluids one uses conservation laws like the conservation of mass, momentum and energy. The most widely spread formulations of these laws are field equations that treat the fluid like a continuum. Although fluids are made of particles, the interactions average to continuous distribution of particles with continuous interaction, even in the case of microhydrodynamics, where the length scale of interest approaches that of the molecules. It was shown that even in channels that are tens of nanometers wide the fluid behaves still like a continuum, when averaged over sufficient time (Bocquet and Charlaix, 2010).

The Navier-Stokes equation is the most common fluid description and for later use we write the equations in a Cartesian coordinate system (x , y and z axis) and include terms due to a rotating frame of reference such as centrifugal force and Coriolis force. Choosing a rotational frame of reference was motivated in the introduction and corresponds to fluid actuation on spinning devices. The equation describes a balance of forces and its SI unit is N/m^3 , Newton per meter cube. Following Batchelor (1967), p.140 and p.177.

$$\rho \left(\frac{\partial \tilde{\mathbf{u}}}{\partial \tilde{t}} + \tilde{\mathbf{u}} \cdot \nabla \tilde{\mathbf{u}} \right) + \nabla \tilde{p} = -\rho \tilde{\omega}^2 \tilde{\mathbf{x}} + 2\rho \tilde{\omega} \times \tilde{\mathbf{u}} + \mu \nabla^2 \tilde{\mathbf{u}} - \rho g \mathbf{e}_z. \quad (2.1)$$

acceleration pressure centrifugal Coriolis viscosity gravity

The variables in this equation are time \tilde{t} , position $\tilde{\mathbf{x}}$, vectorial velocity $\tilde{\mathbf{u}}$ and pressure \tilde{p} . The problem parameters and material coefficients are density ρ , viscosity μ , gravitational acceleration g and angular velocity $\tilde{\omega}$ of the reference frame.

All the variables carry dimensions, for the field variables this has been highlighted with tilde \sim , for the material parameters dimensions are understood. Throughout this work only non-

Chapter 2. A depth-averaged fluid model for confined shallow flows

dimensional variables shall be used in calculation. The given scales are:

$$\tilde{\mathbf{u}} = U\mathbf{u}, \quad \tilde{p} = \frac{\gamma_{\text{ref}}}{L}p, \quad \tilde{t} = \frac{L}{U}t \quad \text{and} \quad \tilde{\mathbf{x}} = L\mathbf{x}. \quad (2.2)$$

For the time scale $T = L/U$ is selected and the pressure is expressed with the surface tension $P = \gamma_{\text{ref}}/L$. Surface tension $\tilde{\gamma}$ is considered as a field variable in order to express a possibly non-constant surface tension. The reference surface tension γ_{ref} in contrast is considered as a material parameter. Substituting the variables in eq.(2.1) and yields for each terms a characteristic dimension:

$$\frac{\rho U^2}{L} : \frac{\gamma_{\text{ref}}}{L^2} : \rho \dot{\omega}^2 L : \rho \dot{\omega} U : \frac{\mu U}{L^2} : \rho g. \quad (2.3)$$

acceleration pressure centrifugal Coriolis viscosity gravity

The length scale of the centrifugal force is given by L but can be arbitrary large, depending on the distance to the center of rotation. In order to obtain non-dimensional groups one multiplies by $L^2/(\mu U)$ and obtains,

$$\frac{\rho UL}{\mu} : \frac{\gamma_{\text{ref}}}{\mu U} : \frac{\rho \dot{\omega}^2 L^3}{\mu U} : \frac{\rho \dot{\omega} L^2}{\mu} : 1 : \frac{\rho g L^2}{\mu U}. \quad (2.4)$$

acceleration pressure centrifugal Coriolis viscosity gravity

Using the established non-dimensional parameters Reynolds number, capillary number, Rossby number and Eötvös number,

$$\text{Re} = \frac{\rho UL}{\mu}, \quad \text{Ca} = \frac{\mu U}{\gamma_{\text{ref}}}, \quad \text{Rb} = \frac{U}{\dot{\omega} L} \quad \text{and} \quad \text{Eo} = \frac{\rho g L^2}{\gamma_{\text{ref}}}.$$

The non-dimensional groups for each term are given as:

$$\text{Re} : \frac{1}{\text{Ca}} : \frac{\text{Re}}{\text{Rb}^2} : \frac{\text{Re}}{\text{Rb}} : 1 : \frac{\text{Eo}}{\text{Ca}}. \quad (2.5)$$

acceleration pressure centrifugal Coriolis viscosity gravity

Discussing the influence of the terms based on the order of magnitude considerations in section 1.1 shows that the first term is negligible because the Reynolds number is small. The second term is important because the inverse of the capillary number is big. Whether the third and fourth term are important depends on the Rossby number. In microfluidics the centrifugal force is more important than the Coriolis force. By definition the fifth term is important because we base our analysis on this quantity, this is advantageous because this term is associated with the highest derivatives in the equation. The last term, measured by the

2.2. Depth-averaging the Stokes equation

Eötvös number, is generally small even though Ca is small.

By dimensional analysis we conclude that in the microfluidic range of parameters the Navier-Stokes equation can be simplified to the Stokes equation with an optional extension of centrifugal terms. For the velocity we pick a scale built on surface tension and viscosity, $U = \frac{\gamma_{\text{ref}}}{\mu}$, resulting in capillary number $Ca = 1$,

$$\nabla^2 \mathbf{u} - \nabla \hat{p} = \frac{Re}{Rb^2} \mathbf{x} - 2 \frac{Re}{Rb} \times \mathbf{u} = \frac{\rho L^3 \dot{\omega}^2}{\gamma_{\text{ref}}} \mathbf{x} - 2 \frac{\rho L^2 \dot{\omega}}{\mu} \times \mathbf{u}. \quad (2.6)$$

Defining an augmented pressure,

$$p = \hat{p} + \dot{\Omega} \frac{x^2 + y^2}{2} - 2 \frac{\rho L^2 \dot{\omega}}{\mu} \psi, \quad \text{with} \quad \dot{\Omega} = \frac{\rho L^3 \dot{\omega}^2}{\gamma_{\text{ref}}}, \quad (2.7)$$

where the stream function ψ has been used, which is defined as

$$\nabla \psi = \begin{pmatrix} -u_y \\ u_x \end{pmatrix}. \quad (2.8)$$

Here \hat{p} is the purely hydrodynamic pressure and p a combination of hydrodynamic and centrifugal pressure. In the case of a non-rotating frame of reference, which is the case for most of the studies performed here $p = \hat{p}$.

Thus one can rewrite eq.(2.6) as:

$$\nabla^2 \mathbf{u} - \nabla p = 0. \quad (2.9)$$

2.2 Depth-averaging the Stokes equation

The equation for fluids at low Reynolds number has a similarity in its description with the equation for solid bodies. A solid or liquid body in the absence of inertial forces has to verify continuity of stresses. Additionally the stresses field has to contains no sources or drains,

$$\nabla \cdot \boldsymbol{\sigma} = 0. \quad (2.10)$$

This is equivalent to imposing the conservation of forces, and therefore the expression is similar to the conservation of mass, the so called incompressibility condition:

$$\nabla \cdot \mathbf{u} = 0. \quad (2.11)$$

In a Newtonian fluid the stress $\boldsymbol{\sigma}$ is:

$$\sigma_{ij} = -\delta_{ij} p + \frac{\partial u_i}{\partial x_j} + \frac{\partial u_j}{\partial x_i}, \quad \text{or equivalently} \quad \boldsymbol{\sigma} = \begin{pmatrix} -p + 2 \frac{\partial u_x}{\partial x} & \frac{\partial u_x}{\partial y} + \frac{\partial u_y}{\partial x} \\ \frac{\partial u_x}{\partial y} + \frac{\partial u_y}{\partial x} & -p + 2 \frac{\partial u_y}{\partial y} \end{pmatrix}. \quad (2.12)$$

Chapter 2. A depth-averaged fluid model for confined shallow flows

Inserting the definition eq.(2.12) into eq.(2.10) with the help of eq.(2.11), we obtain the Stokes equation eq.(2.9).

For order of magnitude estimation we re-equip the Stokes equation with characteristic scales or gauges for velocities, pressure and length. The Laplacian ∇^2 is expanded in three spatial directions and we consider shallow channels where the height in the z direction is much smaller than the extension in the x, y direction. Hence for channels whose aspect ratio $L/H \gg 1$ and the non-dimensional height $h = H/L$ is small.

One establishes: $\tilde{u} = Uu, \tilde{v} = Uv, \tilde{w} = Ww, \tilde{p} = Pp, \tilde{x} = Lx, \tilde{y} = Ly$ and $\tilde{z} = Hz$. Although formally identical to the characteristic dimensions defined in the previous chapter, the significance of these gauges is to compare the order of magnitude between units of the same dimension.

Writing eq.(2.9) with gauges:

$$\frac{U}{L^2} \left(\frac{\partial^2 u}{\partial x^2} + \frac{\partial^2 u}{\partial y^2} \right) + \frac{U}{H^2} \frac{\partial^2 u}{\partial z^2} - \frac{P}{\mu L} \frac{\partial p}{\partial x} = 0, \quad (2.13)$$

$$\frac{U}{L^2} \left(\frac{\partial^2 v}{\partial x^2} + \frac{\partial^2 v}{\partial y^2} \right) + \frac{U}{H^2} \frac{\partial^2 v}{\partial z^2} - \frac{P}{\mu L} \frac{\partial p}{\partial y} = 0, \quad (2.14)$$

$$\frac{W}{L^2} \left(\frac{\partial^2 w}{\partial x^2} + \frac{\partial^2 w}{\partial y^2} \right) + \frac{W}{H^2} \frac{\partial^2 w}{\partial z^2} - \frac{P}{\mu H} \frac{\partial p}{\partial z} = 0, \quad (2.15)$$

$$\frac{U}{L} \left(\frac{\partial u}{\partial x} + \frac{\partial v}{\partial y} \right) + \frac{W}{H} \frac{\partial w}{\partial z} = 0. \quad (2.16)$$

Dominant balance requires to determine the scales U, W and P in order to retain as many terms as possible of the same scale and to discard those that are smaller. An unsuitable choice of scale leads to too few dominant terms, where essential physical mechanisms will be lost. For the above system a choice of $W = \frac{H}{L}U$ equilibrates the continuity equation, eq.(2.16). For the pressure gradient $P = \frac{\mu UL}{H^2}$ is a suitable choice, other definitions will leave the system degenerated.

A direct consequence of this choice for W and P is that eq.(2.15) has a pressure that is much larger than any of the viscous terms. However this is not degenerate because the boundary conditions will have a constant pressure over the channel height. Would one have chosen $P = \frac{\mu W}{H}$ then eq.(2.13) and eq.(2.14) would have a pressure much smaller than $\frac{\partial^2 u}{\partial z^2}$, which would be non-physical because when $\frac{\partial^2 u}{\partial z^2} = 0$ then $u = 0$. Neglecting all terms that are $\frac{H^2}{L^2}$

2.2. Depth-averaging the Stokes equation

smaller than the dominant terms one retains:

$$\frac{\partial^2 u}{\partial z^2} - \frac{\partial p}{\partial x} = 0, \quad (2.17)$$

$$\frac{\partial^2 v}{\partial z^2} - \frac{\partial p}{\partial y} = 0, \quad (2.18)$$

$$\frac{\partial p}{\partial z} = 0, \quad (2.19)$$

$$\frac{\partial u}{\partial x} + \frac{\partial v}{\partial y} = 0. \quad (2.20)$$

From eq.(2.19) follows that the pressure being only a function of x and y . There is no dependency anymore on the vertical velocity, which becomes $w = 0$ at leading order. As the pressure does not depend on z the velocity profiles can be depth-averaged in the z direction. Using the no-slip boundary conditions at $z = \pm h/2$ in eq.(2.17 & 2.18) and the definition of the mean velocity,

$$\mathbf{u}_{\parallel} = \frac{1}{h} \int_{-h/2}^{h/2} \mathbf{u} dz, \quad (2.21)$$

we obtain:

$$\mathbf{u}(\mathbf{x}) = \mathbf{u}_{\parallel}(x, y) \frac{3}{2} \left(1 - \frac{4z^2}{h^2} \right) \Rightarrow \frac{\partial^2 \mathbf{u}}{\partial z^2} = -\frac{12}{h^2} \mathbf{u}_{\parallel} = -k^2 \mathbf{u}_{\parallel}, \quad (2.22)$$

where we introduce the permeability¹ parameter $k = \sqrt{12}/h = \sqrt{12} \frac{L}{H}$.

Using the 2D stream function,

$$\mathbf{u}_{\parallel} = \begin{pmatrix} \frac{\partial \psi}{\partial y} \\ -\frac{\partial \psi}{\partial x} \end{pmatrix}, \quad (2.23)$$

the continuity equation is always satisfied. Inserting eq.(2.22) into eq.(2.17) and eq.(2.18) leads to the Cauchy-Riemann differential equations:

$$k^2 \frac{\partial \psi}{\partial y} - \frac{\partial p}{\partial x} = 0, \quad (2.24)$$

$$k^2 \frac{\partial \psi}{\partial x} + \frac{\partial p}{\partial y} = 0. \quad (2.25)$$

In turn these can be reformulated in a Laplace equation, either $\nabla^2 \psi = 0$ or $\nabla^2 p = 0$, also called

¹Permeability because the equation is also used to model porous media (Barenblatt et al., 1989).

Darcy's law:

$$\nabla^2 p = 0, \quad \nabla p = -k^2 \mathbf{u}. \quad (2.26)$$

Darcy's law is widely used for flows in porous media. In shallow channels it corresponds to the limit of very high aspect ratio L/H . It is a potential flow and relatively easy to solve and there is an exhaustive theory since potential flow appears also in the limit of inviscid flow. Just like in inviscid flow, boundary conditions for Darcy's law are only needed for normal velocity and normal stresses.

In order to get to an improved approximation that applies to flows at moderate aspect ratio, we acknowledge that the perpendicular velocity profile is approximated by the Poiseuille flow and $\frac{\partial^2 u}{\partial z^2} = -k^2 \mathbf{u}_{\parallel}$, but instead of neglecting the in-plane derivatives in eq.(2.13 - 2.14) we retain these and obtain:

$$\frac{\partial^2 u_{\parallel}}{\partial x^2} + \frac{\partial^2 u_{\parallel}}{\partial y^2} - k^2 u_{\parallel} - \frac{\partial p}{\partial x} = 0, \quad (2.27)$$

$$\frac{\partial^2 v_{\parallel}}{\partial x^2} + \frac{\partial^2 v_{\parallel}}{\partial y^2} - k^2 v_{\parallel} - \frac{\partial p}{\partial y} = 0, \quad (2.28)$$

$$\frac{\partial u_{\parallel}}{\partial x} + \frac{\partial v_{\parallel}}{\partial y} = 0. \quad (2.29)$$

This equation is called Brinkman equation and can be written in a more compact form:

$$\nabla_{\parallel}^2 \mathbf{u}_{\parallel} - k^2 \mathbf{u}_{\parallel} - \nabla_{\parallel} p_{\parallel} = 0, \quad (2.30)$$

$$\nabla_{\parallel} \cdot \mathbf{u}_{\parallel} = 0. \quad (2.31)$$

An immediate improvement is that the equations are of 2nd order² and therefore normal and tangential velocities and stresses can be imposed. The Brinkman equation unites 2D Stokes equation and Darcy's law not in a fully justified way since close to walls the in-plane velocity gradients are in fact larger than Darcy contribution $k^2 \mathbf{u}_{\parallel}$, therefore the velocity profile in the z direction is by no means a parabola. However the velocities are low near the walls and the influence of the Darcy term becomes small and so the Brinkman equation gives better results than Darcy or 2D Stokes equation. The reason is that 2D Stokes flow does not account for the perpendicular confinement and solves only for viscous stress in the flow plane, that means in the lateral direction. Darcy's law includes only stresses due to the perpendicular confinement but is unable to impose tangential stresses or continuity of tangential velocities.

After a brief historical note follows a discussion in section 2.2.2 on how appropriate the Brinkman model is for confined flows.

²It is a partial differential equation, where the highest derivatives are or 2nd order.

2.2.1 Historical note

When deriving a simplified two-dimensional law of fluid motion by depth-averaging we obtained the Brinkman equation. In fact one should say that the model equation is only formally identical to the Brinkman equation but is phenomenologically quite different.

H. C. Brinkman derived the equation for the first time when he was solving for fluids with suspended particles (Brinkman, 1949). These particles favor a high momentum exchange when in motion, therefore he modelled the rheology of a mixture of liquid and solid particles or colloids by eq.(2.30). At the walls the fluid is at rest but in the bulk the velocity is almost constant. Because his model describes a fluid property it also extends to three-dimensional space, which has no analogy in the sense of depth-averaged fluid dynamics.

Various authors used depth-averaged contributions to simplified fluid models but to my knowledge Boos and Thess (1997) and Bush (1997) were the first to combine low Reynolds number fluid dynamics with depth-averaged friction. They studied the motion of a confined droplet under the action of surface tension gradients, namely the Marangoni effect. The Marangoni names the phenomenon when fluid is brought to motion due to a varying surface tension and is a phenomenon where Darcy's law is invalid because the principal motion is tangential to the droplet interface. The elegance in their approach lies in the analytic solution that can be obtained when the interface shape is fixed to a circle.

2.2.2 An *a posteriori* evaluation of the Brinkman model

There are two major flaws in the Brinkman model: I. There will be no vertical velocity component and II. The velocity profile near boundaries will be parabolic. Phrasing the reason in one sentence:

The solution of the averaged Stokes equation is not the averaged solution of the Stokes equation.

A prominent 3D Stokes solution is the Poiseuille flow in a rectangular cross section. For a channel of homogenous cross section $y = -w/2 \dots w/2$ and $z = -h/2 \dots h/2$ the 3D Stokes equation is:

$$\frac{\partial^2 u}{\partial y^2} + \frac{\partial^2 u}{\partial z^2} - \frac{\partial p}{\partial x} = 0. \quad (2.32)$$

The pressure gradient $\frac{\partial p}{\partial x}$ is constant everywhere and the velocity $u = 0$ at $y = \pm w/2$ and $z = \pm h/2$. The solution is obtained by a separation of variables, where $u = f(y)g(z)$ and a series expansion of $f(y)$ as a sum of $\cosh((2n+1)\pi y/h)$ and $g(z)$ as a sum of $\cos((2n+1)\pi z/h)$. Except for the first element of $g(z)$, which is a 2D Poiseuille shape that compensates the pressure gradient. The solution is obtained by determining the coefficients A_n of the Ansatz

function u in eq.(2.32).

$$u = -\frac{1}{8} \frac{\partial p}{\partial x} (h^2 - z^2) \sum_{n=0}^{\infty} A_n \cosh\left(\frac{2n+1}{h} \pi y\right) \cos\left(\frac{2n+1}{h} \pi z\right). \quad (2.33)$$

For brevity the result is given, details can be found in the book *Slow Viscous Flow* by Langlois and Deville (2014):

$$u_{3D} = -\frac{3}{2} \frac{\partial p}{\partial x} \left(h^2 - 4z^2 + \frac{32h^2}{\pi^3} \sum_{n=0}^{\infty} \frac{(-1)^{n+1} \cosh\left(\frac{2n+1}{h} \pi y\right) \cos\left(\frac{2n+1}{h} \pi z\right)}{(2n+1)^3 \cosh\left(\frac{2n+1}{2h} \pi w\right)} \right). \quad (2.34)$$

In correspondence, the solution of the depth-averaged problem using the Brinkman equations is obtained solving:

$$\frac{\partial^2 u_{\parallel}}{\partial y^2} - \frac{12}{h^2} u_{\parallel} - \frac{\partial p}{\partial x} = 0, \quad u(y = \pm w/2) = 0. \quad (2.35)$$

Whose solution is obtained as:

$$u_{2D} = -\frac{\partial p}{\partial x} \frac{h^2}{12} \left(1 - \frac{\cosh(\sqrt{12}y/h)}{\cosh(\sqrt{12}w/(2h))} \right). \quad (2.36)$$

With the 2D Brinkman profile one can construct a pseudo-3D solution when equipping u_{2D} with a profile in the z -direction like u_{\parallel} in eq.(2.22).

In figure 2.1 a) & c) we compare the velocity profiles in the z direction for different aspect ratios using the 3D Stokes and Brinkman solution. One can see that the profile of the 3D Stokes solution still resembles a parabola close to the wall ($y = 0.484375$), although it is more dissipative, which marks the major difference between 3D Stokes and 2D Brinkman.

In b) the depth-averaged velocity profile along the y direction is plotted for several aspect ratios. The agreement improves for increasing aspect ratios, but even for $W = H$ it is a fair approximation.

The earlier mentioned Darcy equation, eq.(2.26) gives a parabolic velocity profile in the z direction:

$$u_{\text{Darcy}} = -\frac{3}{2} \frac{\partial p}{\partial x} \left(1 - \frac{4z^2}{h^2} \right), \quad (2.37)$$

whose average velocity in the z direction is 1 for all y . Far away from the walls the Darcy equation gives correct results for high aspect ratios but fails near walls or for a moderate confinement.

If one were to seek an improved approximation a perspective might be to tune the friction coefficient in the Brinkman equation according to the in-plane strain. It is an open question how much this would improve a solution in an arbitrary plane channel. For the following work

2.2. Depth-averaging the Stokes equation

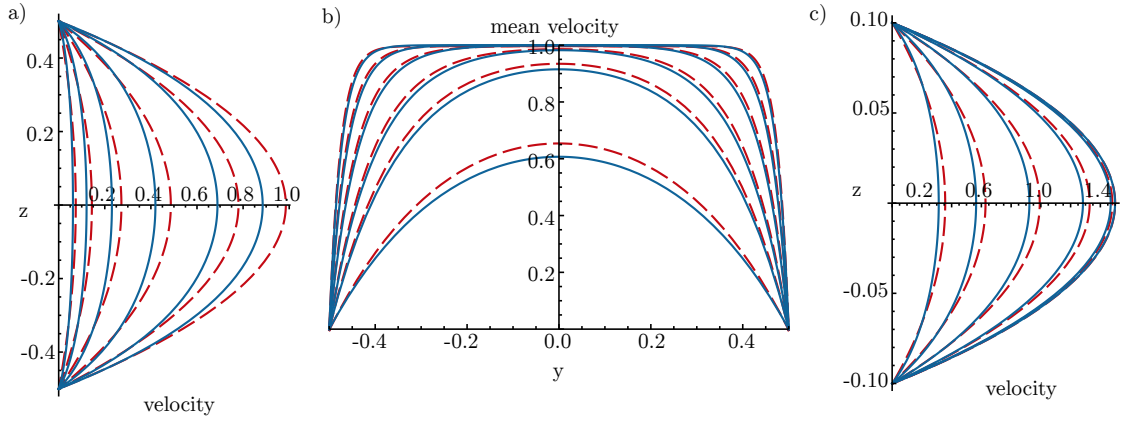


Figure 2.1: Velocity profiles for $\partial p/\partial x = 12/h^2$ of a flow in a rectangular channel with changing aspect ratio using 3D Stokes (blue line) and 2D Brinkman equations (red dashed line). a) and c) Velocity profile in the thin z direction at different positions in $y = 0, 0.25, 0.375, 0.4375, 0.46875, 0.484375$. Aspect ratio a) $W/H = 1$ and c) $W/H = 5$. b) Depth averaged velocity profiles in the wide plane. Profiles shown from bottom up, $W/H = 1, 2, 3, 5, 8, 12$.

the Brinkman equation shall suffice but comments will be made when appropriate on the validity of the model.

2.2.3 Boundary conditions for depth averaged flows

Boundary conditions of the single-phase problem prescribe either the stress or the velocity.

No-slip The typical no-slip boundary condition on a wall is $\mathbf{u} = \mathbf{0}$. In contrast to Darcy flow, for the Brinkman model normal and tangential velocity are imposed. The normal and tangent are given by a vector that contains their projections on the x and y axis, e.g. $\mathbf{n} = (n_x, n_y)^T$.

In-flow As typical inflow boundary condition the solution of the Brinkman equation in a straight channel flow is used. For a straight inflow boundary of length w parametrized by s , whose origin is in the middle of the boundary:

$$u_{\text{in}}(s) = Ca \frac{\cosh(kw/2) - \cosh(ks)}{\cosh(kw/2) - 1}, \quad \text{with } k = \frac{\sqrt{12}}{h}. \quad (2.38)$$

It is worth observing that the dimensionless inflow velocity is represented as the capillary number Ca because the velocity is non-dimensionalized by γ_{ref}/μ . Integration of the velocity field along the inflow boundary relates the dimensional flow rate Q to the inflow capillary

number.

$$Ca = \frac{Q\mu_c}{2HL\gamma_{\text{ref}}} \frac{\cosh(\sqrt{3}W/H) - 1}{\cosh(\sqrt{3}W/H) - \sinh(\sqrt{3}W/H)/(\sqrt{3}W/H)}. \quad (2.39)$$

Out-flow The outflow boundary of parallel channel flow with constant pressure is imposed by zero tangential velocity, $\mathbf{u} \cdot \mathbf{t} = 0$ and constant normal stress $\mathbf{n} \cdot \boldsymbol{\sigma} \cdot \mathbf{n} = p_0$.

Interface conditions for depth-averaged two-phase flows

Interface conditions on the droplet are continuity of velocity and jump of interface stresses on the fluid-fluid interface. The surface or interface stresses shall also be denoted by $\mathbf{f} = \boldsymbol{\sigma} \mathbf{n}$, whose components are f_x, f_y .

The jump condition of the stress at the interface is twofold, coming from rotational effects and surface tensions. In a rotating frame of reference there is a pressure jump due to centrifugal and Coriolis forces in the augmented pressure in eq.(2.7).

For those we write:

$$[[p_{cf}]] = \dot{\Omega} \frac{x^2 + y^2}{2} - 2 \frac{\rho L^2 \dot{\omega}}{\mu} \psi \approx \dot{\Omega} \frac{x^2 + y^2}{2}, \quad \text{with} \quad \dot{\Omega} = \frac{\Delta \rho \dot{\omega}^2 L^3}{\gamma_{\text{ref}}}. \quad (2.40)$$

In the following we restrict our analysis to $\frac{\rho L^2 \dot{\omega}}{\mu} \ll 1$, which means the last term in eq.(2.6) that is due to the Coriolis force is much smaller than the other terms.

There are maybe cases when the Coriolis force is important but such can not be computed in the described framework because the stream function is not directly accessible from the velocities. However when using Darcy's law as a fluid model the boundary integral equation is based on the stream function and therefore the Coriolis force can be included. Leonard W. Schwartz used this in a simulation of a instability in a rotating Hele-Shaw cell based on Darcy's law with centrifugal and Coriolis force reported in a Letter to Physics of Fluids (Schwartz, 1989). To my knowledge, apart from practical aspects like ease of implementation and computational time, a rotating Hele-Shaw cell with Coriolis force is the only case where Darcy's law is superior to the Brinkman equation.

The stress boundary condition due to surface tension contains a jump in normal stress, due to the curvature, and in tangential stresses, due to varying surface tension, also called Marangoni effect. The varying surface tension is introduced by $\gamma = \tilde{\gamma}/\gamma_{\text{ref}}$. The two principal curvatures are the in-plane curvature κ_{\parallel} and the meniscus curvature in the thin direction κ_{\perp} .

$$[[\boldsymbol{\sigma} \mathbf{n}]] = \gamma \left(\kappa_{\parallel} \frac{\pi}{4} + \kappa_{\perp} \right) \mathbf{n} + \frac{d\gamma}{ds} \mathbf{t} = \frac{d(\gamma \mathbf{t})}{ds} - \gamma \left(1 - \frac{\pi}{4} \right) \frac{d\mathbf{t}}{ds} + \gamma \kappa_{\perp}. \quad (2.41)$$

In accordance with real droplet microfluidic systems we assume a non-wetting dispersed phase so the out-of-plane meniscus is approximately a half-circle, $\kappa_{\perp} = \frac{2}{h}$, and the in-plane curvature κ_{\parallel} is corrected by a $\frac{\pi}{4}$ term, which was derived by Park and Homay (1984).

Anticipating the discretization of the interface, the curvature is also expressed in terms of Frenet equations, which was proposed by Tryggvason et al. (2011).

In this formulation of the jump of interface stresses we neglect the effect of dynamic film formation, which changes the out-of-plane curvature κ_{\perp} . This effect, which depends in a non-linear way on the capillary number (Park and Homay, 1984), will be discussed in chapter 5.

The total traction force discontinuity at the interface is therefore:

$$[[\mathbf{f}]] = [[\boldsymbol{\sigma}\mathbf{n}]] + [[p_{cf}\mathbf{n}]]. \quad (2.42)$$

In all following chapters only planar fluid flow in two dimensions is considered. So for ease of notation the \parallel symbol as a suffix for velocity, pressure and operators is omitted and it shall be understood that 2D operators and variables are considered.

2.3 Solutions for undeformable droplets

The previous section presented the Brinkman equation, which models fluid motion in shallow channels. In this section we solve this equation analytically to study the motion of droplets in wide channels at low capillary number ($Ca < 10^{-2}$) when the deformation is negligible. The analytical solution provides elegant closed-form expressions, which will be at the heart of one important result of this thesis: the estimation of the velocity of a flat droplet.

We recall the Brinkman equation from eq.(2.30), which is a 2D equation with variables in two dimensions, where λ represents the viscosity ratio.

$$\lambda(\Delta\mathbf{u} - k^2\mathbf{u}) - \nabla p = 0, \quad k = \frac{\sqrt{12}L}{H} = \frac{\sqrt{12}}{h}, \quad (2.43)$$

$$\nabla \cdot \mathbf{u} = 0. \quad (2.44)$$

The solution is developed with fundamental solution that are also called Green's functions or singularities. An introduction to singularity methods is found in the book *Microhydrodynamics* by Kim and Karrila (1991) or in the book *Boundary integral and singularity methods for linearized flow* by Pozrikidis (1992). These books treat only Stokes and potential flow and their fundamental solutions. For the Brinkman equation Gallaire et al. (2014) used the singularity method to derive droplet solutions.

As an alternative to the following derivation for the Brinkman equation, I propose also a droplet model based on Darcy's law found in the appendix A.2. The description is much simpler and for didactic purposes it might be clearer to look at the procedure there.

Introduction to fundamental solutions

Fundamental solutions are also called Green functions when they refer to the solution of an equation with Dirac forcing³. Green's functions tend to zero when evaluated at infinity, but diverge at the origin. Because of the divergence at the origin they are also referred to as singularities. Some of these solutions will reappear in the numerical solution scheme, where they allow to transform field equations into boundary equations.

Apart from Green functions there is a second family of solutions, which are not forced by a Dirac but have a divergent behavior at infinity. These are referred to as internal flow solutions because they need to be in a bounded domain due to their divergent terms at infinity.

2.3.1 Fundamental solutions of the Brinkman equation

The solutions are given with subindices a, b, c where $a = 1, 2$ stands for a forcing in x or y direction and the other indices address the components of a vector $b = 1, 2$ or a matrix b, c . Some fundamental solutions use the modified Bessel functions of first and second kind of order 0 and 1, written $I_0(kr)$, $I_1(kr)$, $K_0(kr)$ and $K_1(kr)$.

These solutions have one or more degrees of freedom. When the fundamental solution of the velocity is given as a vector it has one degree of freedom and when it is given as a 2nd order tensor it has two degrees of freedom. For the fundamental solutions a slight change in notation makes the appearance more harmonic. All velocities of fundamental solutions are given by a capital letter where over bars denote the tensorial order, e.g. one bar corresponds to a vector. The pressures and stresses associated are named P and T with a superscript letter that marks the corresponding velocity field.

For the sake of clarity, the velocity for a given fundamental solution $\overline{\overline{D}}$ is obtained by multiplication with a vectorial weight \overline{d} :

$$\mathbf{u} = \overline{\overline{D}} \overline{d}.$$

The stress tensor and pressure are obtained from fundamental stress function $\overline{\overline{\overline{T}}}$ and pressure field $\overline{\overline{P}}^D$:

$$p = \overline{\overline{P}}^D \cdot \overline{d}, \quad \overline{\overline{\sigma}} = \overline{\overline{\overline{T}}} \overline{d}.$$

³The Dirac distribution is a distribution that takes the value infinity in one point and zero everywhere else.

Internal solutions

These are solutions that do not tend to zero for $r \rightarrow \infty$. For compact notation the Kronecker delta is used δ_{ab} , which is defined as $a = b \rightarrow \delta_{ab} = 1$ and $a \neq b \rightarrow \delta_{ab} = 0$.

Parallel flow: The most simple solution to Stokes and Brinkman equations is a constant unidirectional flow:

$$\bar{\bar{C}} = \begin{pmatrix} 1 & 0 \\ 0 & 1 \end{pmatrix}, \quad \text{or equivalently in component wise notation } C_{ab} = \delta_{ab}. \quad (2.45)$$

Whose pressure field is:

$$\bar{P}^C = -k^2 \begin{pmatrix} x \\ y \end{pmatrix}, \quad \text{or } P_a^C = -k^2 x_a. \quad (2.46)$$

The stress tensor contains only the pressure contribution:

$$T_{abc}^C = k^2 \delta_{bc} x_a. \quad (2.47)$$

For $\mathbf{u}^c = \bar{\bar{C}} \begin{pmatrix} 1 \\ 0 \end{pmatrix}$ the velocity field represents parallel flow in the x direction and $\begin{pmatrix} 0 \\ 1 \end{pmatrix}$ parallel flow in the y direction.

Linear flow The following configuration is called linear flow because it depends linearly on the spatial variables x and y .

$$\bar{\bar{L}} = \begin{pmatrix} x & y \\ -y & x \end{pmatrix} \quad (2.48)$$

with

$$\bar{P}^L = -k^2 \begin{pmatrix} \frac{x^2 - y^2}{2} \\ xy \end{pmatrix}. \quad (2.49)$$

For illustrative purposes the velocity field \mathbf{u}^L is plotted in figure 2.2a for a forcing vector \mathbf{l} .

$$\mathbf{l} = \begin{pmatrix} -1 \\ 0 \end{pmatrix} \Rightarrow \mathbf{u}^L = \bar{\bar{L}} \mathbf{l} = \begin{pmatrix} -x \\ y \end{pmatrix},$$

$$p^L = \bar{P}^L \mathbf{l} = k^2 \frac{x^2 - y^2}{2}. \quad (2.50)$$

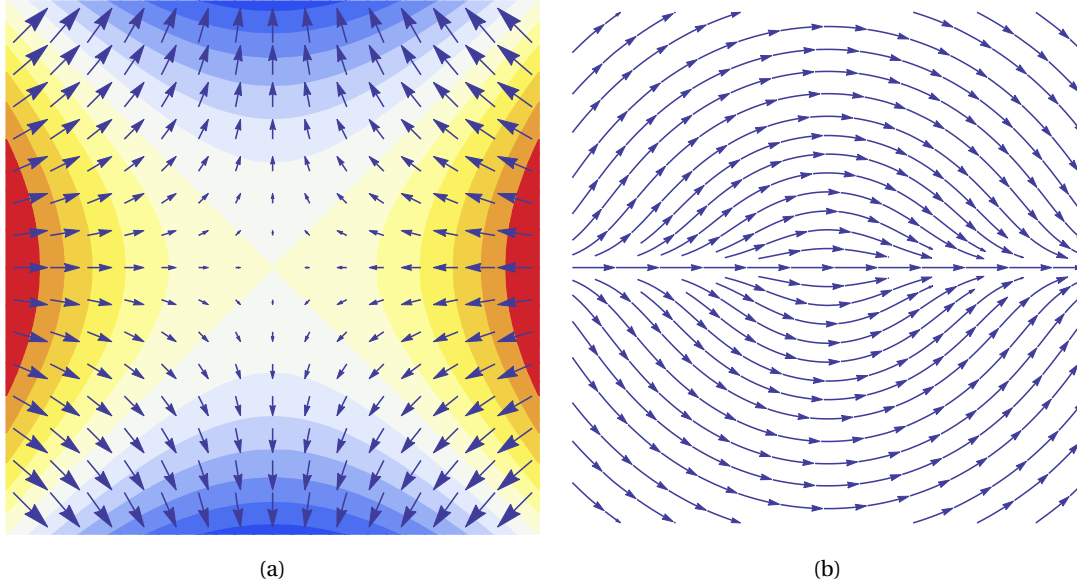


Figure 2.2: Examples of fundamental solutions. a) Vector field of a linear flow field with coloring according to pressure levels. b) Stream lines of a "Brinkmanon", where the pressure is constant.

The linear flow will be reused as a boundary condition in a future case study. Its degrees of freedom determine its orientation. For Stokes flow there is one more linear flow that corresponds to solid rotation where $\mathbf{u} = (y, -x)^T$ this is not a valid solution neither for Brinkman nor for the Darcy equation.

"Brinkmanon" The less trivial solution in analogy to the Stokeson termed "Brinkmanon", which uses modified Bessel functions of first kind. For shorter notation the following substitutions are proposed, with $r = \sqrt{x^2 + y^2}$,

$$B_1(kr) = I_0(kr) - \frac{I_1(kr)}{kr}, \quad B_2(kr) = 2\frac{I_1(kr)}{kr} - I_0(kr) \quad \text{and} \quad B_3 = I_1(kr)kr. \quad (2.51)$$

This defines the Brinkmanon:

$$E_{ab} = B_1(kr)\delta_{ab} + B_2(kr)\frac{x_a x_b}{r^2}. \quad (2.52)$$

Surprisingly the pressure field associated to this flow is constant. The flow represents a case where the fluid is sheared from infinity to overcome the friction from top and bottom plates.

The stress tensor is:

$$\begin{aligned}
 T_{abc}^E &= \frac{1}{r^2} (\delta_{ab}x_c + \delta_{ac}x_b) (B_3(kr) + 2B_2(kr)) + \frac{2x_a}{r^2} \delta_{bc}B_2(kr) \\
 &- \frac{x_ax_bx_c}{r^4} (8B_2(kr) + 2B_3(kr)).
 \end{aligned} \tag{2.53}$$

with the symmetries:

$$T_{111}^E = -T_{122}^E \text{ and } T_{222}^E = -T_{211}^E.$$

Free-space solutions

We name Green functions also free-space solutions since they can represent a solution in an infinitely wide domain. For free-space Stokes flow there are two families Poles and Stokeslets, depending if the Dirac distribution is applied on the force balance (Stokeslet) or on the mass balance (Pole).

Poles are harmonic solutions of the Laplace operator (i.e. $\Delta \vec{u} = 0$). In the Stokes equation there is no pressure contribution for these flows. For Brinkman flows the added velocity component, $k^2 \mathbf{u}$ is compensated by the pressure.

Stokeslets and what is termed here "Brinkmanlets" are solutions with a Dirac in the force balance. Close to the singularity the Brinkman solution tends to the Stokes solution, which reflects the fact that if k goes to zero the Brinkman equation turn into the Stokes equation. Far from the singularity the Brinkmanlet tends to the Green's function of the Darcy equation, apart from a multiplicative constant. This again reflects the dual nature the Brinkman equation.

At first we look at the poles, whose velocity field solves 2D Stokes, Brinkman and Darcy equation because it corresponds to a forcing in the continuity equation which is the same for all these equations. One could say that it is a fundamental solution of kinematic nature. Apart from the velocity field, the stress and pressure are quite distinct between all these solutions and only the Brinkman solution will be given here.

Monopole Corresponds to a radial injection with only one degree of freedom from the center of the domain . Velocity vector:

$$M_b = \frac{x_b}{r^2}, \tag{2.54}$$

Chapter 2. A depth-averaged fluid model for confined shallow flows

Pressure field:

$$P^M = -\frac{k^2}{2} \ln(r^2). \quad (2.55)$$

Stress tensor:

$$T_{bc}^M = k^2 \ln(r) \delta_{bc} + 2 \left(\frac{\delta_{bc}}{r^2} - 2 \frac{x_b x_c}{r^4} \right). \quad (2.56)$$

Dipole The Dipole is the derivative of the monopole and represents injection and suction at an infinitely small distance. It creates a recirculation and its degree of freedom allows to orient the sense of circulation. Velocity vector:

$$D_{ab} = \frac{1}{r^2} \delta_{ab} - \frac{2x_a x_b}{r^4}, \quad (2.57)$$

Pressure field:

$$P_a^D = -k^2 \frac{x_a}{r^2}. \quad (2.58)$$

Stress tensor:

$$T_{abc}^D = k^2 \delta_{bc} \frac{x_a}{r^2} - \frac{4}{r^4} (\delta_{ab} x_c + \delta_{ac} x_b + \delta_{bc} x_a) + \frac{16x_a x_b x_c}{r^6}. \quad (2.59)$$

Monopole and Dipole are plotted in figure 2.3a and 2.3b, higher order poles like Quadpole etc. can be derived but will not be of importance in this work.

Brinkmanlet Another class of free space fundamental solutions are "Brinkmanlets", analogous to Stokeslets. They show a similar flow field as the dipole but behave quite different. For the Brinkmanlet and its stress tensor we will use the following three substitutions:

$$A_1(kr) = 2 \left(K_0(kr) + \frac{K_1(kr)}{kr} - \frac{1}{k^2 r^2} \right),$$

$$A_2(kr) = 2 \left(-K_0(kr) - 2 \frac{K_1(kr)}{kr} + \frac{2}{k^2 r^2} \right),$$

and

$$A_3 = K_1(kr) kr.$$

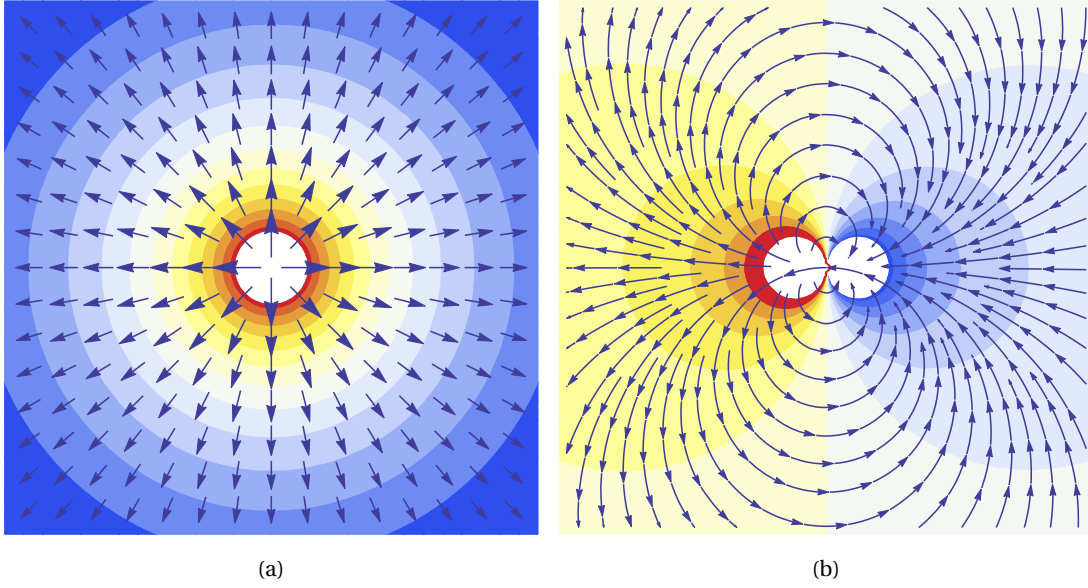


Figure 2.3: Examples of fundamental solutions. a) Vector field of a Monopole or source, with coloring according to pressure levels. b) Streamlines of a Dipole with coloring according to pressure levels.

Velocity vector:

$$G_{ab} = A_1(kr)\delta_{ab} + A_2(kr)\frac{x_ax_b}{r^2}, \quad (2.60)$$

Pressure field

$$P_a^G = \frac{2x_a}{r^2}. \quad (2.61)$$

Stress tensor:

$$T_{abc}^G = \frac{2}{r^2}(A_2(kr) - 1)\delta_{bc}x_a + \frac{2}{r^2}(A_2(kr) - A_3(kr))(\delta_{ab}x_c + \delta_{ac}x_b) \quad (2.62)$$

$$- \frac{2x_ax_bx_c}{r^4}(4A_2(kr) - 2A_3(kr)). \quad (2.63)$$

The Brinkmanlet is plotted in figure 2.4a, it resembles the dipole but its recirculation pattern is different.

Combination of singularities: A cylindrical obstacle

The combination of Brinkmanlet, Dipole and constant flow yields the flow around a solid disc of radius R in a flow parallel to the x axis in a liquid of velocity V_∞ . The set-up can be

Chapter 2. A depth-averaged fluid model for confined shallow flows

imagined to be like a cylindrical pillar that spans from the floor to the ceiling of an infinitely wide channel. The aspect ratio, that is the radius of the pillar divided by the height of the channel should be bigger than 1 to respect the prerequisite of the Brinkman equation.

The flow field at infinity is represented by a constant flow with a forcing of V_∞ in the x direction. Since the initial forcing is in the x direction we assume that all forcings in the y direction are zero, that is the second components of \mathbf{g} and \mathbf{d} .

We shall recall that we non-dimensionalized the equations with a length scale, viscosity and surface tension, which is paradoxical in this case where there is no surface tension. Here we chose the velocity scale $U = V_\infty$, viscosity μ and length scales are $L = R$ for non-dimensionalization. In the equations we keep the non-dimensional velocity $v_\infty = 1$ in order to illustrate the dependency. Writing the superposition of $\overline{\overline{C}}$, $\overline{\overline{D}}$ and $\overline{\overline{G}}$:

$$\mathbf{u} = \begin{pmatrix} v_\infty + \left(\frac{1}{r^2} - \frac{2x^2}{r^4} \right) d_1 + \left(A_1(kr) + A_2(kr) \frac{x^2}{r^2} \right) g_1 \\ - \frac{2xy}{r^4} d_1 + A_2(kr) \frac{xy}{r^2} g_1 \end{pmatrix}. \quad (2.64)$$

On the cylinder the fluid has zero velocity, it therefore follows from the no-slip condition: $\mathbf{u}(\mathbf{r} = \mathbf{1}) = \mathbf{0}$. The elegance of the method can be appreciated right away, although no-slip is imposed everywhere it lies in the power of two adjustable parameters g_1 and d_1 . From the balance in y direction of eq:(2.64) follows immediately that:

$$d_1 = \frac{A_2(kr) g_1}{2}. \quad (2.65)$$

Hence in the x direction one obtains:

$$u_1(r = 1) = v_\infty + \left(\frac{A_2(k)}{2} + A_1(k) \right) g_1 = v_\infty + K_0(k) g_1 = 0, \quad (2.66)$$

$$g_1 = -\frac{v_\infty}{K_0(k)} \quad \text{and} \quad d_1 = -\frac{v_\infty A_2(k)}{2K_0(k)}. \quad (2.67)$$

Inserting these values for g_1 and d_1 in eq.(2.64) solves the problem, whose solution is shown in figure 2.4b.

Since the stress tensor for the problem is known it is possible to calculate the force on the cylinder by integration around its circumference. Details of this calculation will be given in section 2.3.2.

$$F_{\text{disc}} = -\frac{\pi v_\infty h}{K_0(k)} \left(2 + 2A_3(k) - k^2 \frac{A_2(k)}{2} + k^2 K_0(k) \right). \quad (2.68)$$

For the comfort of the reader the dimensional force is given as well. Constructing a force from

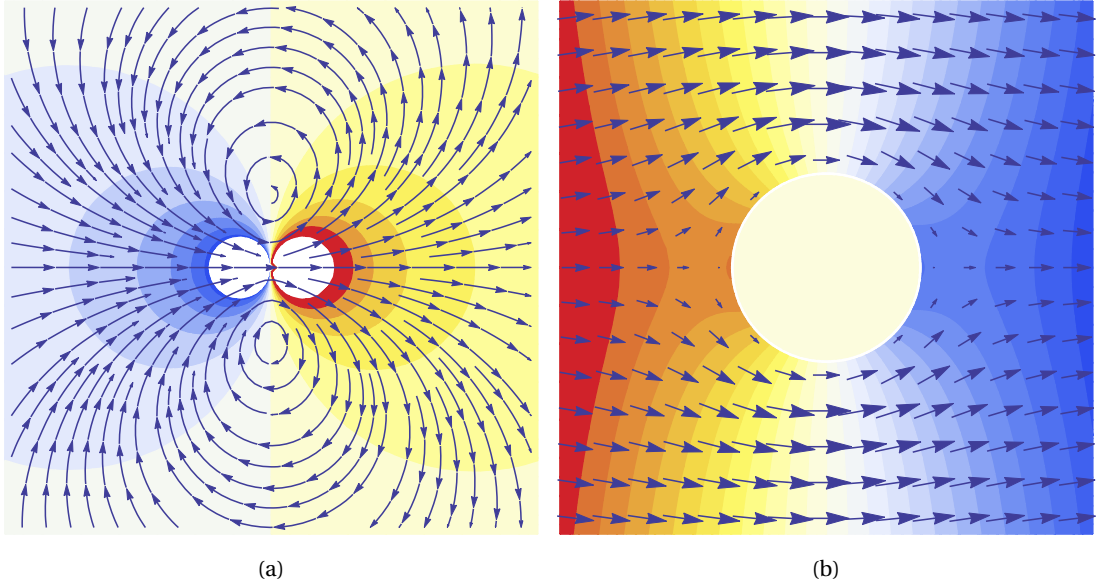


Figure 2.4: a) Streamlines of a Brinkmanlet with coloring according to stress levels. b) Motion around a cylindrical obstacle, shown as vector field and pressure.

the basic dimensions U, μ and R expresses $\tilde{F} = U\mu R F$, thus

$$\tilde{F}_{\text{disc}} = -V_{\infty}\mu \frac{\pi H}{K_0(k)} \left(2 + 2A_3(k) - k^2 \frac{A_2(k)}{2} + k^2 K_0(k) \right). \quad (2.69)$$

2.3.2 Combination of singularities: An undeformable droplet

A combination of internal and free-space solution reproduces the flow inside and outside of a droplet moving in a liquid. This requires the computation of surface stresses and involves the stress tensors associated with the fundamental solutions.

Non-dimensionalizing with the droplet radius $L = R$ and inflow velocity $U = V_{\infty}$, we consider a droplet of radius $\mathcal{R} = 1$ with viscosity ratio λ , being the ration between droplet viscosity and carrier fluid viscosity. The droplet is in a shallow channel of aspect ratio of R/H , so $k = \sqrt{12}R/H$ and velocity far from the droplet $v_{\infty} = 1$.

The solution will be made out of a constant flow field and the superposition of four Brinkman singularities, two for the outer flow and two for the inner flow. We restrict ourselves at first to a unidirectional flow along the x-axis. For reasons of symmetry there will be no forcing component in the y-direction.

The outer flow shall be represented by

$$\mathbf{u}_o = v_\infty + \overline{\overline{G}} \begin{pmatrix} g_1 \\ 0 \end{pmatrix} + \overline{\overline{D}} \begin{pmatrix} d_1 \\ 0 \end{pmatrix}. \quad (2.70)$$

where we chose only singularities with x-forcing and the unknowns are therefore scalars. The vector v_∞ is the streamed velocity in the x-direction.

And the stress field is given by:

$$\overline{\overline{\sigma}}_o = \mathbf{I} k^2 x v_\infty + \overline{\overline{T}}^G \begin{pmatrix} g_1 \\ 0 \end{pmatrix} + \overline{\overline{T}}^D \begin{pmatrix} d_1 \\ 0 \end{pmatrix}, \quad \text{with } \mathbf{I} = \begin{pmatrix} 1 & 0 \\ 0 & 1 \end{pmatrix}. \quad (2.71)$$

The inner flow inside the droplet is represented by

$$\mathbf{u}_i = \mathbf{I} \begin{pmatrix} c_1 \\ 0 \end{pmatrix} + \overline{\overline{E}} \begin{pmatrix} e_1 \\ 0 \end{pmatrix}, \quad (2.72)$$

and

$$\overline{\overline{\sigma}}_i = \mathbf{I} k^2 x c_1 + \overline{\overline{T}}^E \begin{pmatrix} e_1 \\ 0 \end{pmatrix}. \quad (2.73)$$

Boundary conditions of a deformable droplet are equality of inner and outer velocity at the droplet interface and stress discontinuity described Laplace's law (see section 2.2.3). For 2D and 3D Stokes flow far from boundaries, completely unconfined unlike in this work, the deformable solution does not deform, see Young et al. (1959). That can be guess by intuition because the driving force for the unconfined droplets comes from buoyancy, a body force, and the viscous interaction around the droplet is harmonic.

In the case of a droplet that is confined in a shallow channel there is no body force, the drag component in the thin direction decelerates the droplet, whereas the stresses around the circumference accelerate. Hence a non-uniform stress distribution, which is unlikely to yield perfect balance of normal stresses in a cylindrical configuration.

For the second order differential equation two boundary conditions can be applied for the inner problem and two for the outer problem. In the case of a deformable droplet that is equality of normal and tangential velocities and stresses.

In the case of an undeformable droplet equal tangential velocities and stresses are imposed, together with zero normal velocity in the reference frame of a moving drop, for inner and outer flow. Hence one loses control of the normal stress boundary condition. Since in reality small deformations, for which we can not account in the undeformable model, are equilibrating the normal stress balance everywhere we shall impose only a global force balance over the whole droplet.

The numerical study in section 5.2.3 will prove that droplets at low capillary number are only slightly deformed.

Boundary conditions: The normal along a circle is written as: $n_x = x/r$ and $n_y = y/r$. The tangent is then defined as: $t_x = -y/r$ and $t_y = x/r$. In the reference frame of the displacing droplet the normal velocities become:

$$(\mathbf{u}_o - \mathbf{u}_d) \cdot \mathbf{n} = (\mathbf{u}_i - \mathbf{u}_d) \cdot \mathbf{n} = 0, \quad (2.74)$$

Where by symmetry the second component of \mathbf{u}_d is zero. Inserting in eq.(2.74) the superposition of fundamental solutions eq.(2.70) & (2.72) determines the outer flow:

$$d_1 = \left(2 \left(\frac{1}{k^2} - \frac{K_1(k)}{k} \right) g_1 + v_\infty - u_d \right). \quad (2.75)$$

And for the inner flow:

$$c_1 = u_d - \frac{I_1(k)}{k} e_1. \quad (2.76)$$

The third boundary condition is equality of tangential velocity:

$$\mathbf{u}_o \cdot \mathbf{t} = \mathbf{u}_i \cdot \mathbf{t}, \quad (2.77)$$

With the fundamental solutions this becomes:

$$2 \left(K_0(k) + \frac{K_1(k)}{k} - \frac{1}{k^2} \right) g_1 + d_1 + v_\infty = c_1 + \left(I_0(k) - \frac{I_1(k)}{k} \right) e_1. \quad (2.78)$$

We eliminate d_1 with eq.(2.75):

$$e_1 = \frac{2u_d - 2v_\infty + \left(\frac{K_1(k)}{k} - \frac{1}{k^2} \right) g_1}{B_2}. \quad (2.79)$$

And at last the equality of tangential stresses:

$$\mathbf{t} \bar{\bar{\sigma}}_o \mathbf{n} = \mathbf{t} \bar{\bar{\sigma}}_i \mathbf{n}. \quad (2.80)$$

Inserting the superposition of fundamental stress tensors eq.(2.71, 2.73).

$$4d_1 + 2 \left(K_1(k)k + 2K_0(k) + 4 \frac{K_1(k)}{k} - \frac{4}{k^2} \right) g_1 = \lambda \left(2I_0(k) - 4 \frac{I_1(k)}{k} - I_1(k)k \right) e_1. \quad (2.81)$$

Then eliminating d_1 with eq.(2.75):

$$4(v_\infty - u_d) + (4K_0(k) + 2K_1(k)k)g_1 + \lambda \left(\frac{4I_1(k)}{k} - 2I_0(k) + I_1(k)k \right) e_1 = 0. \quad (2.82)$$

And further eliminating e_1 with eq.(2.79):

$$g_1 = \frac{4 \left(2 \frac{I_1(k)}{k} - I_0 \right) - 2\lambda \left(4 \frac{I_1(k)}{k} - 2I_0(k) + I_1(k)k \right)}{(4K_0(k) + 2K_1(k)k) \left(2 \frac{I_1(k)}{k} - I_0 \right) - 2\lambda K_0(k) \left(\frac{I_1(k)}{k} - 2I_0(k) + I_1(k)k \right)} (u_d - v_\infty). \quad (2.83)$$

In return one can determine e_1 :

$$e_1 = \frac{2K_1(k)k(u_d - v_\infty)}{(K_1(k)k + 2K_0(k)) \left(\frac{2I_1(k)}{k} - I_0 \right) + \lambda K_0(k) \left(2I_0(k) - \frac{4I_1(k)}{k} - I_1(k)k \right)}. \quad (2.84)$$

The remaining coefficients d_1 and c_1 are determined from equation (2.75) and (2.76).

For a droplet velocity $u_d = 1.55$, viscosity ratio $\lambda = 1/4$ and aspect ratio $R/H = 3$ the resulting flow field is then plotted in figure 2.5.

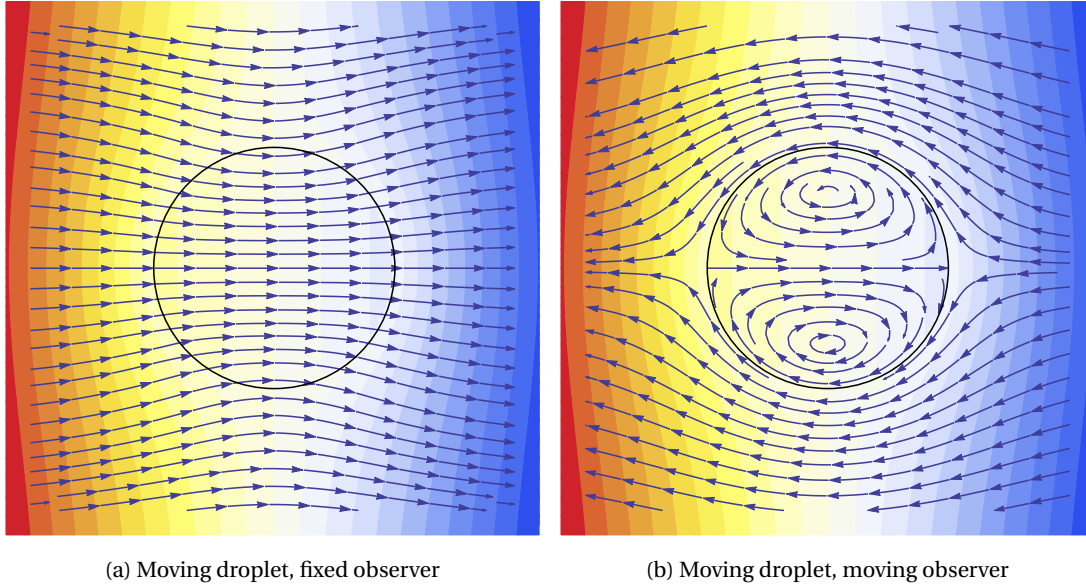


Figure 2.5: Vector and pressure field of a droplet of viscosity $\lambda = \frac{1}{4}$ and aspect ratio $R/H = 3$. The droplet velocity U_D is about $1.55V_\infty$.

Forces on the droplet

Since the displacement velocity u_d was imposed the system is overdetermined and the global force balance is not verified. Surface deformations that compensate the normal stress balance are in the order of Capillary number. Hence the droplet stays approximately cylindrical for

2.3. Solutions for undeformable droplets

$Ca < 10^{-2}$. It just remains to impose that the integral of traction forces along the interface is zero to determine the streaming velocity u_d .

The force is obtained by integration of the fundamental stress tensor around the interface and multiplication the height of the channel h . Without forcing in the y direction, the forces in the y direction are zero, which was checked and results are only given for the x direction.

$$F_x = h \int_0^{2\pi} (T_{111} n_x + T_{112} n_y) d\theta, \quad n_x = \mp \cos(\theta), \quad n_y = \mp \sin(\theta).$$

The sign changes because the sense of integration is different for the inner and outer domain. For the outer domain the normal points to the origin, being defined as pointing outwards of the domain. For the inner domain the normal points outwards. We will proceed one by one for the fundamental solutions and sum up the resulting forces with the coefficients

$$F_x^G = -2h\pi(1 + A_3(k))g_1, \quad F_x^D = k^2 h\pi d_1, \quad (2.85)$$

$$F_x^C = -\lambda h\pi k^2 c_1, \quad F_x^E = -\lambda h\pi I_1(k)k e_1. \quad (2.86)$$

The force on the droplet from the outside is:

$$F_{\text{drop,out}} = -h\pi k^2 v_\infty + F^G g_1 + F^D d_1 = -\pi k \left(2k v_\infty - u_d k + 4K_1(k)g_1 \right). \quad (2.87)$$

Calculating the force on the droplet from the inside is done either keeping the 2D perspective adding the force of the inner stress to the interface or adopting the 3D point of view. In 3D one integrates the velocity gradient in the z direction on the top and bottom surface using the prescribed Poiseuille profile from eq.(2.22). In 2D we impose zero sum of forces on an interface ring and in 3D we impose zero sum of forces on the droplet surface from the outside. Both approaches give the same result, which is expected because the fluid inside has zero sum of force so its force on the channel floor and ceiling equals the force on the lateral fluid interface demonstrated in appendix A.3.

$$F_{\text{drop,int}} = F^E e_1 + F^C c_1 = -\lambda\pi \left(I_1(k)k e_1 + k^2 \left(u_d - \frac{I_1(k)}{k} e_1 \right) \right) = -\lambda\pi k^2 u_d. \quad (2.88)$$

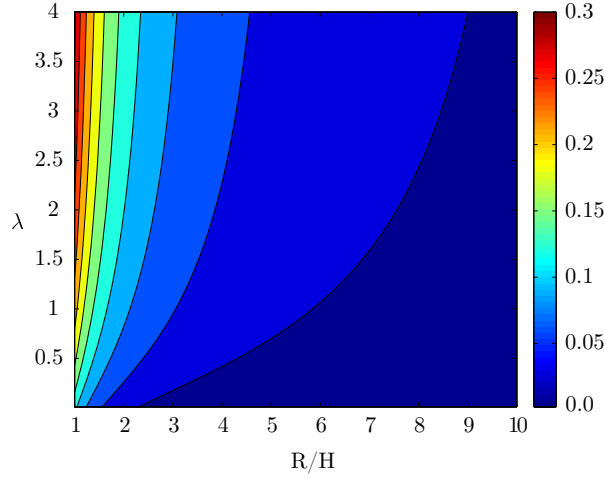


Figure 2.6: Value of χ/k for changing viscosity ratio and aspect ratio.

So the total force on the interface is

$$\begin{aligned}
 F_{\text{interface}} &= F^G g_1 + F^D d_1 + F^C v_\infty - F^C c_1 - F^E e_1, \\
 &= \pi k^2 \left((u_d(1 + \lambda) - 2v_\infty) - \frac{4K_1(k) g_1}{k} \right), \\
 &= \pi k^2 \left((u_d(1 + \lambda) - 2v_\infty) - \frac{\chi}{k} (v_\infty - u_d) \right), \quad \text{with } \chi = \frac{4K_1(k) g_1}{(v_\infty - u_d)}. \quad (2.89)
 \end{aligned}$$

$$(2.90)$$

For brevity χ has been introduced, which depends only on λ and k , the dependence on the droplet velocity u_d has been cancelled off from g_1 , eq. (2.83).

The Brinkman equation introduces a contribution that scales like k instead of k^2 so its influence becomes small for droplets of high aspect ratio. Its effect is also bigger for viscous droplets than for inviscid ones. The correction introduced by the Brinkman equation χ/k is plotted in figure 2.6.

Velocity of a streaming droplet

Flow at low Reynolds number is force and torque free, which follows from the divergence of the stress tensor, which is zero. Setting F_x to zero in eq.(2.89) leads to an expression that relates U_d to V_∞ for free streamed droplets in wide channels. We solve for the non-dimensional droplet streaming coefficient $u_d = U_d/V_\infty$ and obtain:

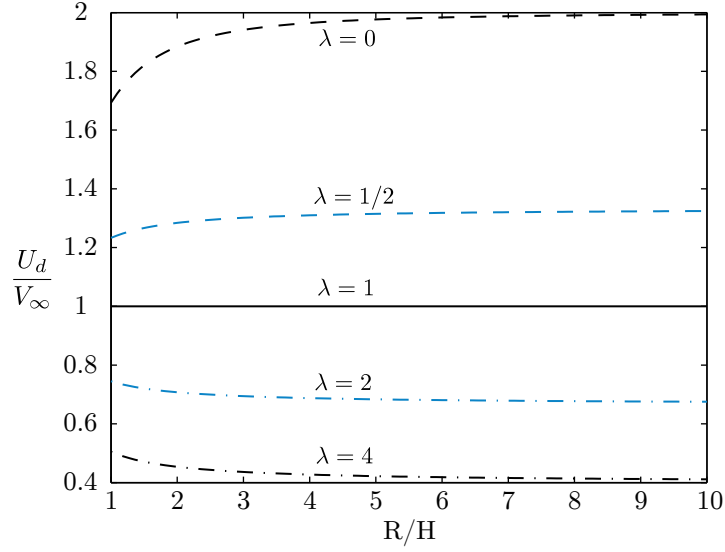


Figure 2.7: Relative traveling velocity of streamed droplets for $\lambda = 0, 1/2, 1, 2$ and 4 .

$$\begin{aligned}
 F_{\text{interface}} &= \pi k (\chi(v_{\infty} - u_d) + k(v_{\infty} - u_d(1 + \lambda))) = 0, \\
 u_d &= \frac{\chi + 2k}{\chi + (1 + \lambda)k}.
 \end{aligned} \tag{2.91}$$

For $R/H \rightarrow \infty$ the velocity approaches the result of Darcy's law. The streaming velocity is plotted in figure 2.7 against the aspect ratio for different viscosity ratios. It shows that a droplet with lower viscosity travels faster than the carrier flow. For $\lambda = 1$ we find $u_d = 1$ or $U = V$, which equals the result for parallel flow without droplet. A droplet with higher viscosity travels slower and comes to rest in the limit of an infinitely high viscosity ratio. When setting $\lambda \rightarrow \infty$ we observe $u_d \rightarrow 0$ and recover the result of the disc.

Using Darcy's law a similar relation can be obtained ($\chi \rightarrow 0$), where tangential velocity and tangential stress do not match. The result is derived in the appendix A.2.

$$u_{\text{Darcy}} = \frac{2}{1 + \lambda}. \tag{2.92}$$

One observation is that the aspect ratio changes the behavior only slightly. Of course this result is furnished by the Brinkman equation, which is obtained by simplifications like depth-averaging and the assumption of homogeneous out-of-plane meniscus. The result tells us that droplets, where the inner viscosity is lower than the outer viscosity show a higher velocity

than the mean flow. This result contradicts most experimental findings (Kopf-Sill and Homsy, 1988). Up to here the calculation did not use the capillary number, assuming only that it is very small for the sake of undeformability. In chapter 5 the force balance will be reevaluated using a modification due to three dimensional effects.

Summary

Vertical confinement in a microchannel allowed a depth-averaged formulation that reduced the fluid problem from three to two dimensions. The 2D plane in which the fluid motion is considered captures the complex channel layout and the varying fluid interface geometry. Perpendicular to this plane, in the direction that was averaged out, there is a dominant contribution of viscosity and surface tension due to the confinement, which yields high velocity gradients and a highly curved meniscus. Despite the dominant contribution this out-of-plane direction shows no variation since the ceiling height is kept fixed.

Thus modelling the dominant contribution by a lumped parameter model, allows to solve in the plane with high geometric variations. Since the in-plane stresses were retained the depth-averaged equation has a much wider range of aspect ratio where the solution is physically meaningful.

Analytical solutions for disc shaped obstacles or droplets could be obtained. These analytical solutions will be reused to cross check the numerical algorithm that will be used to solve for deformable fluid interfaces.

3 Numerical solution of the deformable interfaces

In order to solve the two-phase flow numerically the domain has to be discretized. It is desirable to apply an interface-tracking scheme, as the interface represents a localized force. This force is relatively high because it competes with viscous forces that scale like the capillary number, which is small. In order to avoid numerical difficulties we discretize the interface with mesh elements for the sake of precision and stability of the numerical algorithm.

In order to avoid remeshing the whole domain as the interface evolves, a Boundary Element Method is implemented, where only boundaries are discretized. The following paragraph demonstrates how the Brinkman equation can be reformulated in boundary integral form. A more detailed presentation of the method applied to Stokes flow is found in Pozrikidis (1992). For a general introduction to the method the book *The Boundary Element Method* by Wrobel and Aliabadi (2002) offers an general introduction into a variety of problems.

3.1 Transformation to boundary integrals

As a first step we perform the transform to boundary integrals. Integrating the Brinkman equation (2.30) and continuity equation over a vector field \mathbf{v} and a scalar field q on a domain Ω one obtains:

$$\int_{\Omega} \left(\lambda (\Delta \mathbf{u} - k^2 \mathbf{u}) - \nabla p \right) \cdot \mathbf{v} + \lambda \nabla \cdot \mathbf{u} q \, dA = 0. \quad (3.1)$$

Here \mathbf{v} and q can be seen as test functions, as in the Finite Elements Method. The continuity equation has been multiplied by the viscosity ratio λ , which will be necessary later on for the droplet interface condition. If the velocities \mathbf{u} and pressure p fulfill this equation for whatever choice of test function they also solve the initial equation system eq.(2.30).

Performing integration by parts on eq.(3.1),

$$\begin{aligned} & \int_{\Omega} (\lambda (-\nabla \mathbf{u} : \nabla \mathbf{v} - k^2 \mathbf{u} \cdot \mathbf{v}) + p \nabla \cdot \mathbf{v} + \lambda \nabla \cdot \mathbf{u} q) dA \\ & + \oint_{\omega} \left(\begin{array}{cc} 2\lambda \frac{\partial u_x}{\partial x} - p & \lambda \left(\frac{\partial u_x}{\partial y} + \frac{\partial u_y}{\partial x} \right) \\ \lambda \left(\frac{\partial u_x}{\partial y} + \frac{\partial u_y}{\partial x} \right) & 2\lambda \frac{\partial u_y}{\partial y} - p \end{array} \right) \mathbf{n} \cdot \mathbf{v} ds = 0. \end{aligned} \quad (3.2)$$

The term that appears as a boundary integral on the boundary ω of the domain Ω can also be expressed as a surface stresses $\sigma \mathbf{n}$ or \mathbf{f} . Performing integration by parts once more makes \mathbf{u} and \mathbf{v} exchange roles.

$$\begin{aligned} & \int_{\Omega} (\lambda (\Delta \mathbf{v} - k^2 \mathbf{v} - \nabla q) \cdot \mathbf{u} + \nabla \cdot \mathbf{v} p) dA \\ & + \oint_{\omega} \sigma \mathbf{n} \cdot \mathbf{v} - \lambda \left(\begin{array}{cc} 2 \frac{\partial v_x}{\partial x} - q & \frac{\partial v_x}{\partial y} + \frac{\partial v_y}{\partial x} \\ \frac{\partial v_x}{\partial y} + \frac{\partial v_y}{\partial x} & 2 \frac{\partial v_y}{\partial y} - q \end{array} \right) \mathbf{n} \cdot \mathbf{u} ds = 0. \end{aligned} \quad (3.3)$$

After integrating by parts twice the Laplace operator that acted on the velocity \mathbf{u} has been transferred to \mathbf{v} . Since the vector field \mathbf{v} takes the role of a velocity in a reappearing Brinkman equation, q can be interpreted as a pressure and the new boundary term as a surface stress $\tau \mathbf{n}$.

$$\tau = \left(\begin{array}{cc} 2 \frac{\partial v_x}{\partial x} - q & \frac{\partial v_x}{\partial y} + \frac{\partial v_y}{\partial x} \\ \frac{\partial v_x}{\partial y} + \frac{\partial v_y}{\partial x} & 2 \frac{\partial v_y}{\partial y} - q \end{array} \right).$$

When \mathbf{v} , q and τ solve the Brinkman equation the domain integral disappears and only boundary integrals are left. The Green's functions of the Brinkman equation are used as test functions because they have a Dirac like forcing, which ensures that in a numerical discretization of the problem the highest elements are usually the diagonal elements of the matrix, leading to a low condition number of the problem. A Dirac forcing on the boundary also allows for a domain integral being solely dependent on the velocities at the location of the Dirac distribution.

3.1.1 Green's functions

In order to solve for the unknown velocities and stresses two Green's functions are necessary. A third Green's function can be used to compute the pressure in the domain. As a consequence of the Dirac forcing the velocity, pressure and stress fields have singularities at $\delta(\mathbf{x}_0)$, where their respective values go to infinity.

In the following we recall the two Green's function of the Brinkman equation with a Dirac forcing of the stress equation in x or y direction, which were presented previously in chapter

3.1. Transformation to boundary integrals

2.3.1. In this chapter the Dirac is normalized by $-\frac{1}{4\pi}$, where the area integral $\int_{\Omega} \delta(\mathbf{x}_0) dA = 1$.

Taking two velocity vectors \mathbf{G}_a , two pressures P_a and two stress tensor fields \mathbf{T}_a , with $a = 1, 2$ and which verify:

$$\nabla \cdot \mathbf{T}_a - k^2 \mathbf{G}_a = \Delta \mathbf{G}_a - \nabla P_a - k^2 \mathbf{G}_a = \mathbf{w}_a \delta(\mathbf{x}_0) \quad \text{and} \quad \nabla \cdot \mathbf{G}_a = 0. \quad (3.4)$$

The Dirac forcing occurs at the position \mathbf{x}_0 with a vectorial weight \mathbf{w}_a . We are interested in two linear independent weight vectors $\mathbf{w}_1 = \begin{pmatrix} 1 \\ 0 \end{pmatrix}$ and $\mathbf{w}_2 = \begin{pmatrix} 0 \\ 1 \end{pmatrix}$.

The solutions are given in indexed form, first index a for the corresponding weight function \mathbf{w}_a and b, c for the b^{th} component of a vector or the (b, c) component in a matrix. The Green's function velocity field is taken from Kohr et al. (2008).

$$G_{ab} = \frac{1}{4\pi} \left(A_1 \delta_{ab} + A_2 \frac{x_a x_b}{r^2} \right). \quad (3.5)$$

Introducing A_1 and A_2 , which are functions of aspect ratio times distance kr and are expressed by modified Bessel functions of second kind $K_0(kr)$ and $K_1(kr)$. Bessel functions are transcendental functions and their development is shown in appendix A.1. In the above and following definitions δ_{ab} is the Kronecker delta and not to be confused the Dirac distribution $\delta(\mathbf{x}_0)$.

$$A_1 = 2 \left(-K_0(kr) - \frac{K_1(kr)}{kr} + \frac{1}{k^2 r^2} \right), \quad A_2 = 2 \left(K_0(kr) + 2 \frac{K_1(kr)}{kr} - \frac{2}{k^2 r^2} \right) \quad (3.6)$$

The function $A_1(kr)$ behaves like a $\log(kr)$ close to $r \approx 0$ and is therefore weakly singular. Using this result in eq. (3.4) leads to the associated pressure field P_a .

$$P_a = -\frac{x_a}{2\pi r^2}. \quad (3.7)$$

From velocity and pressure fields one derives the associated stress tensor, $T_{abc} = -P_a \delta_{bc} + \frac{\partial G_{ab}}{\partial x_c}$:

$$T_{abc} = \frac{\delta_{bc} x_a}{2\pi r^2} (A_2 + 1) + \frac{\delta_{ab} x_c + \delta_{ac} x_b}{2\pi r^2} (A_2 + K_1(kr) kr) - \frac{x_a x_b x_c}{\pi r^4} (2A_2 + K_1(kr) kr). \quad (3.8)$$

Inserting now $\mathbf{v} = \mathbf{G}_a$ and $\boldsymbol{\tau} = \mathbf{T}_a$ with $a = 1$ or 2 into eq.(3.3) gives two independent boundary integral equations with a forcing either in the x or y direction. Because of the Dirac forcing the domain integral does not disappear completely but is confined to a single point and eq.(3.3) becomes:

$$\lambda \int_{\Omega} \delta(\mathbf{x}_0) \mathbf{w}_a \cdot \mathbf{u} dA = \oint_{\omega} \lambda \mathbf{T}_a \mathbf{n} \cdot \mathbf{u} - \sigma \mathbf{n} \cdot \mathbf{G}_a ds. \quad (3.9)$$

The domain integral over the Dirac selects the value of \mathbf{u} at \mathbf{x}_0 , the position where the Green's functions was forced. Depending on whether \mathbf{x}_0 is in the domain, on the boundary or outside

the prefactor S is λ , $\frac{\lambda}{2}$ or 0.

A third fundamental solution has a Dirac distribution forcing of the continuity equation, which corresponds to a point source in the continuity equation at \mathbf{x}_0 . Instead of eq.(3.4) the Green's function solves:

$$\nabla \cdot \mathbf{T}_3 - k^2 \mathbf{G}_3 = \Delta \mathbf{G}_3 - \nabla P_3 - k^2 \mathbf{G}_3 = 0 \quad \text{and} \quad \nabla \cdot \mathbf{G}_3 = \delta(\mathbf{x}_0). \quad (3.10)$$

This point source solution is also solution of the Darcy equation and its fields are:

$$P_3 = -\frac{k^2}{4\pi} \log(r^2), \quad G_{3b} = \frac{x_j}{2\pi r^2}, \quad T_{3bc} = \frac{1}{4\pi} \left(\left(k^2 \log(r^2) + \frac{4}{r^2} \right) \delta_{bc} - 8 \frac{x_b x_c}{r^4} \right). \quad (3.11)$$

Inserting $\mathbf{v} = G_3$ and $\boldsymbol{\tau} = \mathbf{T}_3$ in eq.(3.3) this gives:

$$\int_{\Omega} \delta(\mathbf{x}_0) p dA = S p(\mathbf{x}_0) = \oint_{\omega} \lambda \mathbf{T}_3 \mathbf{n} \cdot \mathbf{u} - \boldsymbol{\sigma} \mathbf{n} \cdot \mathbf{G}_3 ds. \quad (3.12)$$

Again the prefactor S depends whether \mathbf{x}_0 is in the domain, on the boundary or outside, $S = (1, \frac{1}{2}, 0)$. Evaluating this integral equation allows to calculate the pressure at a given point in the domain once the stresses and velocities at the boundary are known.

3.1.2 Boundary integral for two-phase flow

When dealing with two-phase flows the two fluid domains need to be coupled by their common boundaries. The channels internal boundary is the same as the droplets boundary, except for the sense of orientation. The orientation determines the direction of the normal and therefore changing the sign of one of the normals makes both integral paths identical. One includes the droplet into the boundary integral formulation by summing the contributions of the boundary integral of the droplet η and the channel domain, where the channel domains internal boundary η^* has a reversed integration path, i.e. inverted normals. Boundary integration is performed counter-clockwise around a domain, illustrated in Figure 3.1.

$$\oint_{\omega} \mathbf{T}_a \mathbf{n} \cdot \mathbf{u} - \boldsymbol{\sigma} \mathbf{n} \cdot \mathbf{G}_a ds + \oint_{\eta} -\mathbf{T}_a \mathbf{n} \cdot \mathbf{u} + \boldsymbol{\sigma} \mathbf{n} \cdot \mathbf{G}_a ds = \frac{1}{2} \mathbf{w}_a \cdot \mathbf{u}(\mathbf{x}_0). \quad (3.13)$$

In the channel domain the viscosity ratio is $\lambda_c = 1$ and in the droplet $\lambda_d = \lambda$. The dispersed phase boundary integral problem is:

$$\oint_{\eta} \lambda \mathbf{T}_a \mathbf{n} \cdot \mathbf{u} - \boldsymbol{\sigma} \mathbf{n} \cdot \mathbf{G}_a ds = \frac{\lambda}{2} \mathbf{w}_a \cdot \mathbf{u}(\mathbf{x}_0). \quad (3.14)$$

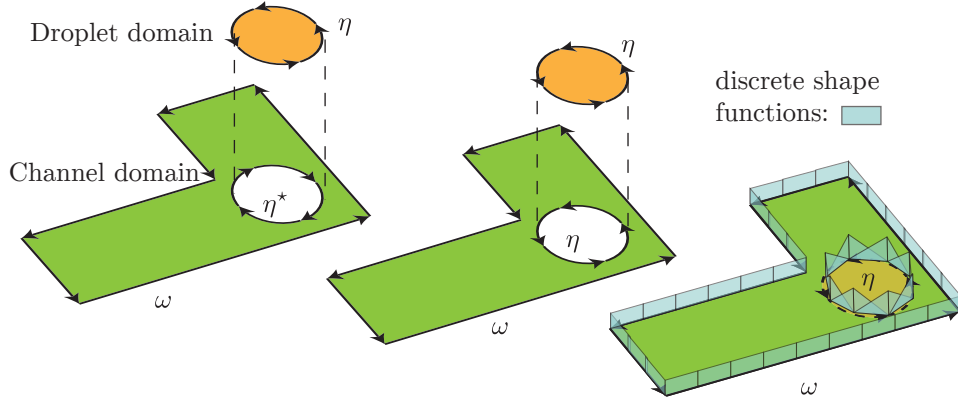


Figure 3.1: Schematic representation of how the two fluid domains are coupled. Arrows depicted boundary integral paths. a) Two separate domains. b) Changing the orientation of the channels internal boundary, $\eta \rightarrow \eta^*$. c) Combination of both integral contributions on the interface using the interface conditions (eq.(2.41)). Piece-wise constant and piece-wise linear shape functions are sketched.

Combining eq.(3.13) and (3.14) by adding the contributions under the integral along η gives,

$$\oint_{\omega} \mathbf{T}_a \mathbf{n} \cdot \mathbf{u} - \sigma \mathbf{n} \cdot \mathbf{G}_a ds + \oint_{\eta} \mathbf{T}_a \mathbf{n} \cdot (\lambda - 1) \mathbf{u} - [[\sigma \mathbf{n}]] \cdot \mathbf{G}_a ds = S \mathbf{w}_a \cdot \mathbf{u}(\mathbf{x}_0). \quad (3.15)$$

If the singularity at \mathbf{x}_0 is located on the outer boundary the coefficient $S = \frac{1}{2}$ and if the singularity is located on the interface $S = \frac{1+\lambda}{2}$. Prescribing the jump in viscosity $(\lambda - 1)$ and jump in surface stresses $[[\sigma \mathbf{n}]]$, see eq.(2.41), specifies the fluid-fluid interface conditions and poses the combined problem.

Simplification for viscosity ratio $\lambda = 1$ A significant simplification is obtained for $\lambda = 1$, where from eq.(3.15) only a diagonal matrix and right hand side remains,

$$\oint_{\eta} [[\sigma \mathbf{n}]] \cdot \mathbf{G}_a ds = -\mathbf{w}_a \cdot \mathbf{u}(\mathbf{x}_0). \quad (3.16)$$

In the absence of walls the velocity at the point \mathbf{x}_0 depends only on known quantities and does not require the solution of a matrix. Even in the presence of outer boundaries the evolution problem can be reduced by one matrix inversion in a problem that involves only matrix vector multiplications, which will be shown in section 3.2.4. We do not restrict our method to $\lambda = 1$ it is worth mentioning that Zhu et al. (2006) have used this in the case of 3D droplet motion.

Infinite and semi-infinite domains Boundary element methods can deal with infinite or semi-infinite¹ domains. For semi-infinite walls the test functions are altered as to account for an infinite wall (Pozrikidis, 1992), which is not used in this work. Infinite domains can be represented in a simple way that follows from the fact that boundaries at infinity are not affected by the fluid interface. In a quiescent fluid the external boundaries at infinity can be simply omitted. Whenever the carrier fluid is in motion and can be expressed by a known solution in the absence of obstacles the contribution of the outer boundaries can be represented by an identity.

The external flow without internal interfaces is given by:

$$\oint_{\omega, \infty} \mathbf{T}_a \mathbf{n} \cdot \mathbf{u} - \sigma \mathbf{n} \cdot \mathbf{G}_a ds = \frac{1}{2} \mathbf{w}_a \cdot \mathbf{u}(\mathbf{x}_0) \quad (3.17)$$

Hence when the velocity field is known one can substitute the boundary integral at infinity by $\frac{1}{2} \mathbf{w}_a \cdot \mathbf{u}(\mathbf{x}_0)$.

3.2 Numerical solution of the boundary integral equation

3.2.1 Spatial discretization

The boundaries are discretized by piece-wise straight line elements with local shape functions whose amplitude is to be determined. Fixed boundary conditions like walls and inflow and outflow boundaries are discretized with piece-wise constant shape functions, whereas the droplet is discretized by piece-wise linear shape functions. The boundary integral form of the Brinkman equation, eq.(3.15) is discretized with a collocation method and integrated by Gauss-Legendre quadrature with 6 nodes.

The quadrature uses 6 weights w_j , which are evaluated at 6 base points s_j . For instance applied to a generic real valued function $f(x)$ integrated between x_1 and x_2

$$\int_{x_1}^{x_2} f(x) dx \approx \frac{|x_2 - x_1|}{2} \sum_{j=1}^6 w_j f\left(\frac{x_2 + x_1}{2} + s_j \frac{x_2 - x_1}{2}\right), \quad (3.18)$$

$$s = \left[-0.932469514203152, -0.661209386466265, -0.238619186083197, \right. \\ \left. 0.238619186083197, 0.661209386466265, 0.932469514203152 \right], \quad (3.19)$$

$$w = \left[0.171324492379170, 0.360761573048139, 0.467913934572691, \right. \\ \left. 0.467913934572691, 0.360761573048139, 0.171324492379170 \right]. \quad (3.20)$$

Discretized normal and tangential vector $\mathbf{n}^i, \mathbf{t}^i$, element length $|\Delta x_i|$ and local variable χ_j^i are

¹A semi-infinite domain is a fluid domain bounded by an infinite straight wall.

3.2. Numerical solution of the boundary integral equation

given as:

$$\mathbf{t}^i = \frac{\mathbf{x}_{i+1} - \mathbf{x}_i}{|\mathbf{x}_{i+1} - \mathbf{x}_i|}, \mathbf{n}^i = \begin{pmatrix} -t_y^i \\ t_x^i \end{pmatrix}, |\Delta x_i| = |\mathbf{x}_{i+1} - \mathbf{x}_i|, \chi_j^i = \frac{\mathbf{x}_{i+1} + \mathbf{x}_i}{2} + s_j \frac{\mathbf{x}_{i+1} - \mathbf{x}_i}{2}. \quad (3.21)$$

The integral equation, eq.(3.15), turns into a double summation, the sum of the quadrature points, summed over all M fixed elements and N droplet elements.

$$\begin{aligned} S_l \mathbf{w}_a \cdot \mathbf{u}^l &= \sum_{i=1}^M \sum_{j=1}^6 \frac{w_j |\Delta x_i|}{2} \left(\mathbf{T}_a^l(\chi_j^i - \mathbf{x}_l) \mathbf{n}^i \cdot \mathbf{u}^i - \mathbf{f}^i \cdot \mathbf{G}_a^l(\chi_j^i - \mathbf{x}_l) \right) \\ &+ \sum_{i=M+1}^{M+N} \sum_{j=1}^6 \frac{w_j |\Delta x_i|}{2} \left(\mathbf{T}_a^l(\chi_j^i - \mathbf{x}_l) \mathbf{n}^i \cdot (\lambda - 1) \left(\frac{1 - s_j}{2} \mathbf{u}^i + \frac{1 + s_j}{2} \mathbf{u}^{i+1} \right) \right. \\ &\left. - \left(\frac{1 - s_j}{2} \llbracket \mathbf{f}^i \rrbracket + \frac{1 + s_j}{2} \llbracket \mathbf{f}^{i+1} \rrbracket \right) \cdot \mathbf{G}_a^l(\chi_j^i - \mathbf{x}_l) \right). \end{aligned} \quad (3.22)$$

There are $2 \times (M + N)$ unknowns to be solved for; $2 \times M$ velocities or surface stresses on the channel boundaries and $2 \times N$ velocities on the drop interface. For each position l of the test functions on one of the $M + N$ nodes, there are two discretized equations, eq.(3.22), for $a = 1$ or 2 . Summing up all known variables in the right hand side and forming a dense $2(M + N) \times 2(M + N)$ matrix with a vector of $2(M + N)$ unknowns, yields a linear equation system.

Due to the weak and strong singularities of the Green's functions, these functions diverge on the collocating element although the integral does not. In numerical integration the singularities need special attention. The test velocity G_{aa} is weakly singular like a logarithm; in fact its asymptotic development in terms of Bessel functions contains a $\log(r)$ as shown in appendix A.1. If the integration interval contains a singularity, the $\log(r)$ contribution is not evaluated in Gauss quadrature but integrated analytically.

The last member of eq.(3.8) for the stress \mathbf{T} contains a $1/r$ singularity but its divergent behavior is perpendicular to the normal \mathbf{n} and vanishes. To show this we consider an element collocating with a singularity, whose normals can be written as: $n_x = y/r$, $n_y = -x/r$.

$$\mathbf{T}_a \mathbf{n} \approx -\frac{x_a}{\pi r^4} \begin{pmatrix} x^2 & xy \\ yx & y^2 \end{pmatrix} \begin{pmatrix} \frac{y}{r} \\ -\frac{x}{r} \end{pmatrix} + \mathcal{O}(k^2 r^2) = -\frac{x_a}{\pi r^5} \begin{pmatrix} x^2 y - x^2 y \\ xy^2 - xy^2 \end{pmatrix} + \mathcal{O}(k^2 r^2) = \mathcal{O}(k^2 r^2).$$

Hence the strongly singular contribution cancels out, which allows to set them to zero on a collocating element and leaves an expression that can be numerically integrated. Details on the extraction are shown in appendix A.1.3.

Velocities at the droplet interface are unknown and the provided interface conditions are the

jumps in surface stresses, which we discretize from eq.(2.41).

$$[[\mathbf{f}_i]] = \frac{\gamma_{i+1/2} \frac{\mathbf{x}_{i+1} - \mathbf{x}_i}{|\mathbf{x}_{i+1} - \mathbf{x}_i|} - \gamma_{i-1/2} \frac{\mathbf{x}_i - \mathbf{x}_{i-1}}{|\mathbf{x}_i - \mathbf{x}_{i-1}|}}{\frac{1}{2}|\mathbf{x}_{i+1} - \mathbf{x}_i| + \frac{1}{2}|\mathbf{x}_i - \mathbf{x}_{i-1}|} - \gamma_i \left(1 - \frac{\pi}{4}\right) \frac{\frac{\mathbf{x}_{i+1} - \mathbf{x}_i}{|\mathbf{x}_{i+1} - \mathbf{x}_i|} - \frac{\mathbf{x}_i - \mathbf{x}_{i-1}}{|\mathbf{x}_i - \mathbf{x}_{i-1}|}}{\frac{1}{2}|\mathbf{x}_{i+1} - \mathbf{x}_i| + \frac{1}{2}|\mathbf{x}_i - \mathbf{x}_{i-1}|} + \frac{2\gamma_i}{h}, \quad (3.23)$$

where γ is defined on vertices and midpoints.

Validation: Marangoni flow of Boos and Thess

We demonstrate the convergence of the method by comparison to an analytical solution. A droplet placed in a Hele-Shaw cell and subject to a surface tension gradient was studied by Boos and Thess (1997). The gradient in surface tension will lead to a motion that is tangential to the interface, which is named Marangoni effect. In their theoretical study they assumed a cylindrical droplet that is exposed to a linearly changing surface tension gradient. Their result is particularly of interest because it provides a test case with a shear stress boundary condition, something impossible when using the Darcy equation. The boundary conditions for a droplet of radius $r = 1$ and surface tension gradient in the y-direction $\frac{d\gamma}{dy} = 1$ are radial velocity $u_r = 0$ and tangential stress discontinuity $[[f]] = \mathbf{t}x$. In a recent article Gallaire et al. (2014) showed that the 2D Brinkman solution of the thermo-capillary problem is in fact a close approximation to the full 3D solution.

The 2D Brinkman solution by Boos *et al.* is given as:

$$u_\theta = \frac{(1 + \lambda)k I_2 K_0 \sin \theta}{\lambda K_0(k^2 I_1 - 2k I_2) + I_2(k^2 K_1 + 2k K_0)}. \quad (3.24)$$

Comparing theoretical velocity u_θ against numerically obtained velocity u_t shows a decrease of the maximum error with second order, shown in figure 3.2. Two aspect ratios $R/H = 3$ and 6 and two viscosity ratios $\lambda = 1/3$ and 5 were used.

3.2.2 Discretization of wall bounded interfaces

A special case of a liquid interface is encountered when the interface is bound to a wall. In microfluidic application this is typically encountered at a junction, where channels carrying different immiscible liquids meet.

The interface is fixed to a point on the wall boundary with unknown velocity on all nodes of the interface that do not lie on the wall. If fluids have different viscosity eq.(3.15) changes to account for a part of the outer boundary ω_s being immersed into the fluid of viscosity λ ,

3.2. Numerical solution of the boundary integral equation

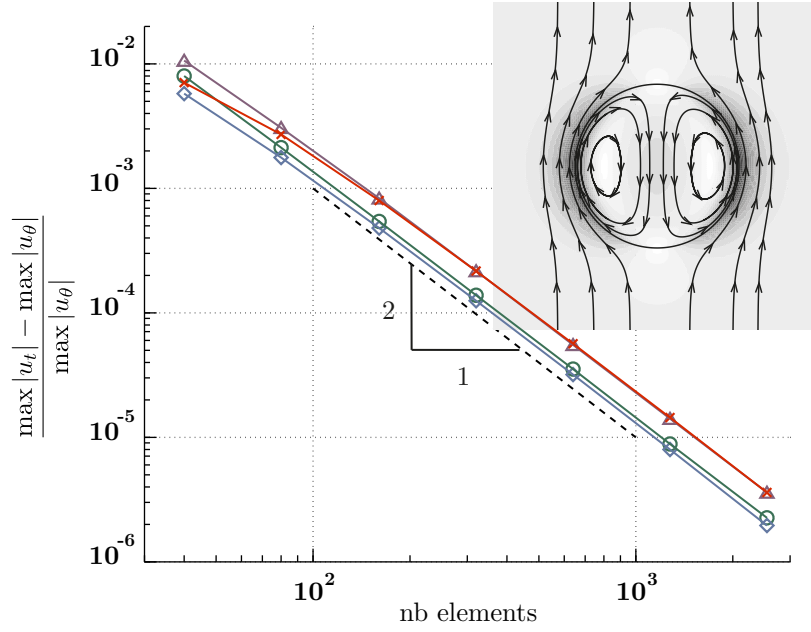


Figure 3.2: Convergence for a cylindrical droplet exposed to a surface tension gradient. The error is given as $(\max|u_t| - \max|u_\theta|) / \max|u_\theta|$ and plotted against the number of elements on the circumference. \circ $R/H = 3$, $\lambda = 1/3$, \triangle $R/H = 6$, $\lambda = 1/3$, \diamond $R/H = 3$, $\lambda = 5$, \times $R/H = 6$, $\lambda = 5$. The inset visualizes the flow field.

whereas the remaining part of the boundary ω_u is still in contact with a fluid of viscosity 1.

$$\oint_{\omega, u} \mathbf{T}_a \mathbf{n} \cdot \mathbf{u} - \sigma \mathbf{n} \cdot \mathbf{G}_a ds + \oint_{\omega, s} \mathbf{T}_a \mathbf{n} \cdot \lambda \mathbf{u} - \sigma \mathbf{n} \cdot \mathbf{G}_a ds \quad (3.25)$$

$$+ \oint_{\eta} \mathbf{T}_a \mathbf{n} \cdot (\lambda - 1) \mathbf{u} - [[\sigma \mathbf{n}]] \cdot \mathbf{G}_a ds = S \mathbf{w}_a \cdot \mathbf{u}(\mathbf{x}_0). \quad (3.26)$$

Figure 3.3 illustrates the discretization with a sketch and a simulation of an interface in a rectangular channel, where fluid enters on the left and leaves on the right. The capillary number is $Ca = 10^{-2}$ and the viscosity ratio $\lambda = 2$, with a more viscous fluid to the left. Walls are discretized with 500 elements and the interface with initially 100 elements. The channel aspect ratio $R/H = 0$, which means we consider Stokes, the reason for this choice is that curiously this case will serve as an example for a paradox that will be discussed in section 5.1.

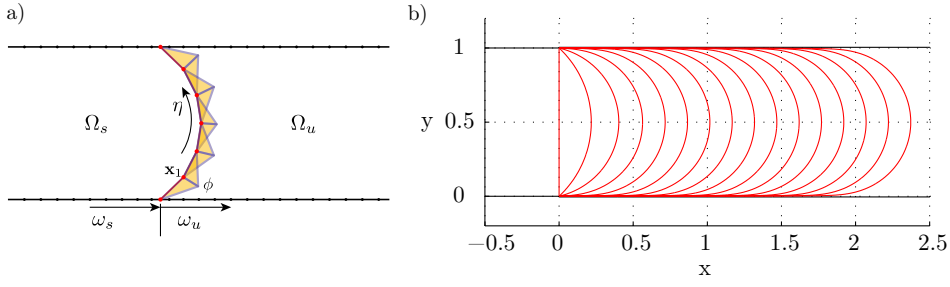


Figure 3.3: a) Discretization of a wall bounded interface η , separating a domain Ω_s of viscosity λ from domain Ω_u of unit viscosity. b) Simulation of a wall bounded interface with $R/H = 0$, $Ca = 10^{-2}$ and $\lambda = 2$. The interface is shown for every 10 time steps with a $\delta t = 1$.

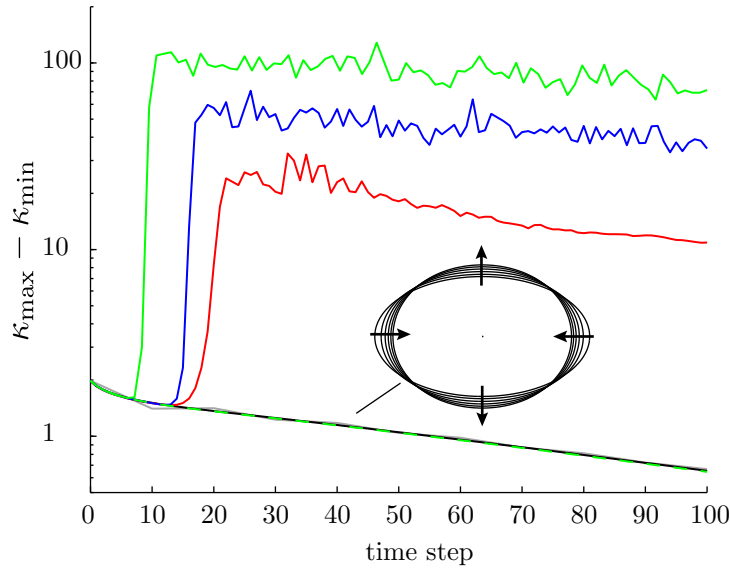


Figure 3.4: Relaxation of a droplet with eccentricity $e = 0.83$, area π , aspect ratio $R/H = 4$ and viscosity ratio $\lambda = 1/2$. The black (resp. gray) line represents the stabilized scheme with $N = 400$ elements and $\Delta t = 1$ (resp. $\Delta t = 10$). The non-stabilized scheme is represented by the green line $N = 400, \Delta t = 0.125$, blue $N = 200, \Delta t = 0.25$, red $N = 100, \Delta t = 0.5$ and green dashed line $N = 400, \Delta t = 0.0625$.

3.2.3 Temporal discretization and stabilization of the fluid-fluid interface

The droplet is advanced in discrete time steps using either an explicit Euler scheme:

$$d\mathbf{x} = \mathbf{u} dt \Rightarrow \mathbf{x}^{n+1} = \int_{t=n}^{t=n+1} \mathbf{u}(\mathbf{x}) dt \Rightarrow \mathbf{x}^{n+1} \approx \mathbf{u}^n \Delta t + \mathbf{x}^n. \quad (3.27)$$

Where \mathbf{u}^n is the velocity field obtained by solving the boundary element problem eq.(3.22) using the nodes at \mathbf{x}^n . Or advanced alternatively by a two-step Runge-Kutta scheme (Heun's

3.2. Numerical solution of the boundary integral equation

method):

$$\mathbf{x}^* = \mathbf{x}^n + \mathbf{u}^n \Delta t, \quad (3.28)$$

$$\mathbf{x}^{n+1} = \mathbf{x}^n + \frac{\Delta t}{2} (\mathbf{u}^n + \mathbf{u}^*). \quad (3.29)$$

With \mathbf{u}^* being the intermediate velocity field obtained using the nodes at \mathbf{x}^* .

During evolution, when the element size on the interface is twice as big or twice as small as the initial size, the points are redistributed equidistantly with the help of a 3rd order polynomial fit.

The time step is limited as a consequence of the mobile interface and non-linearities associated to surface tension and coupling domains of possibly different viscosities. In the limit of low capillary numbers when the surface tension dominates over viscous dissipation the limiting time step for stable integration decreases like capillary number times element size.

For instance the circular interface of a droplet at rest, which is physically stable, develops nevertheless divergent oscillations when solving the evolution problem for a time step larger than some factor multiplied by the discrete element length Δs . For a viscosity ratio $\lambda = 1/2$ and aspect ratio $R/H = 4$ the maximal time step is about $\Delta t < 8\Delta s$. This stiff constraint has also been observed by Dai and Shelley (1993) when analyzing finger formation in a Hele-Shaw cell at low capillary numbers.

The numerical instability is illustrated here on the dynamic problem of an elliptic droplet, which relaxes to a circular interface. Initial shape is an ellipse of eccentricity $e = 0.83$ and area π . A discretization of 100, 200 and 400 elements is tried with time steps on the threshold of instability of $\Delta t = 8 \Delta s$, so $\Delta t = 0.5, 0.25$ and 0.125 . In figure 3.4 the difference between maximal and minimal in-plane curvature is plotted, which starts near two and goes to zero for the perfectly cylindrical droplet. In plotting the curvature, oscillations will appear much more pronounced. A time steps on the threshold leads to oscillations due to deformations on the evolving interface. As the time step is divided by two the scheme becomes stable, as shown by the green dashed line with $N = 400$ and $\Delta t = 0.0625$.

Interface stabilization technique

A semi-implicit scheme is used to stabilize these numerical capillary waves and therefore allow for larger time-steps. For a discrete interface the in-plane interface stress is derived from eq.(3.23) at the vertex i at time step n as:

$$\left. \frac{d\gamma \mathbf{t}}{ds} \right|_i^{t=n} = \frac{\gamma_{i+1/2} \frac{\mathbf{x}_{i+1} - \mathbf{x}_i}{|\mathbf{x}_{i+1} - \mathbf{x}_i|} - \gamma_{i-1/2} \frac{\mathbf{x}_i - \mathbf{x}_{i-1}}{|\mathbf{x}_i - \mathbf{x}_{i-1}|}}{\frac{1}{2} |\mathbf{x}_{i+1} - \mathbf{x}_i| + \frac{1}{2} |\mathbf{x}_i - \mathbf{x}_{i-1}|} \Big|^{t=n}. \quad (3.30)$$

Chapter 3. Numerical solution of the deformable interfaces

Stabilization is achieved when the interface is "made aware" of its displacement by providing a feedback loop. The position of the points \mathbf{x}^* a discrete time step Δt after time n is approximated by eq.(3.28) to be $\mathbf{x}^* = \mathbf{x}^n + \Delta t \mathbf{u}(\mathbf{x}^n)$. Presuming the change in distance between two points to be negligible ($|\mathbf{x}_{i+1}^* - \mathbf{x}_i^*| \approx |\mathbf{x}_{i+1}^n - \mathbf{x}_i^n|$), the linearized expression for the interface stress after a time increment Δt is then given by:

$$\left. \frac{d\gamma \mathbf{t}}{ds} \right|_i^* = \left. \frac{d\gamma \mathbf{t}}{ds} \right|_i^n + \frac{\gamma_{i+1/2} \frac{\mathbf{u}_{i+1} - \mathbf{u}_i}{|\mathbf{x}_{i+1} - \mathbf{x}_i|} - \gamma_{i-1/2} \frac{\mathbf{u}_i - \mathbf{u}_{i-1}}{|\mathbf{x}_i - \mathbf{x}_{i-1}|}}{\frac{1}{2} |\mathbf{x}_{i+1} - \mathbf{x}_i| + \frac{1}{2} |\mathbf{x}_i - \mathbf{x}_{i-1}|} \Delta t \Big|_{t=n}. \quad (3.31)$$

A similar stabilization is applied to the second term in eq.(3.23). Using the stabilization scheme for the relaxing droplet allows for much larger time step. Computing the droplet relaxation with 400 nodes and a time step of $\Delta t = 1$ and 10 agrees with the non-stabilized solution that was computed at a time step that is 16 and 160 times smaller, respectively. For the stabilized scheme no oscillations are observed and stabilization is achieved independent of the discretization.

Convergence study: Deformable droplet in flow focusing

In lack of an analytical solution for the convergence study of deformable droplets we resort to comparison with a numerical result of increased spatial and temporal resolution. For this study a cross flow junction is simulated, where a fluid stream is focused by flow from two side channels. A droplet of diameter $R = \frac{1}{2}$ submitted to that flow is deformed and accelerated, figure 3.5 shows the numerical set-up with time lapsed droplet position. The left inflow condition is chosen to be $Ca = 0.005$ and the inflow velocity from the side channels is $Ca = 0.015$.

The droplet viscosity is half the viscosity of the surrounding fluid, $\lambda = \frac{1}{2}$ and droplet aspect ratio $R/H = 3$. Variables that are observed are the displacement x_c of the center of mass of the droplet and its perimeter.

The displacement error is measured by the root-mean-square (rms) of the difference in position at $n = 68$ time steps normalized by the total distance. The perimeter error is the rms of the difference of the droplet perimeter, sampled at 68 time steps, normalized by the perimeter for an undeformed droplet π .

Spatial discretization varies between $\Delta x = \frac{1}{100}, \dots, \frac{1}{10}$ as element size for the walls and $\Delta x = \frac{1}{300}, \dots, \frac{1}{30}$ for the droplet to account for the importance of the mobile interface. Temporal discretization ranges between $\Delta t = \frac{10}{16}, \dots, 10$. The reference solution uses $\Delta t = \frac{1}{10}$ and $\Delta x = \frac{1}{200}$ and $\Delta x_{\text{drop}} = \frac{1}{600}$, respectively.

Figure 3.6 a) shows the errors for a fixed temporal resolution of $\Delta t = \frac{1}{10}$ and confirms second order convergence as expected from the previous study in section 3.2.1. In fact the error

3.2. Numerical solution of the boundary integral equation

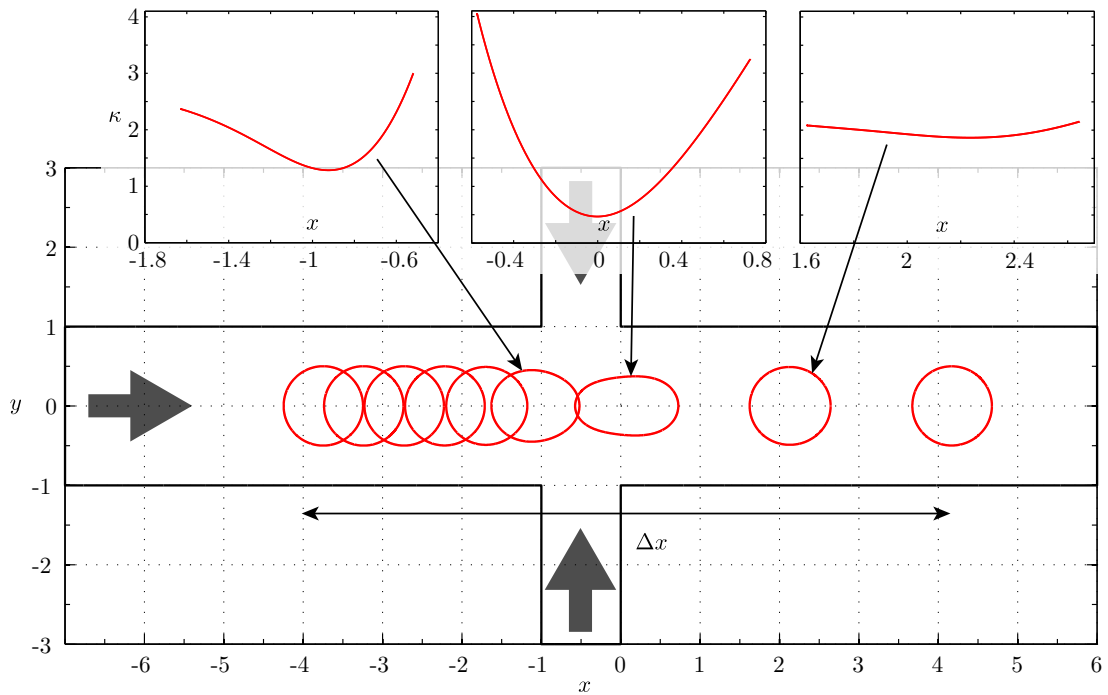


Figure 3.5: The figure shows the computational domain with the droplet interface at several time steps. The three inset figures show the in-plane curvature at three selected time steps around the most deformed. The interface is free of any spurious oscillations.

decreases almost with 3rd order, which maybe due to the symmetries in the configuration. Figure 3.6 b) shows for a fixed spatial resolution of $\Delta x = \frac{1}{200}$ the temporal convergence. The convergence of the stabilized Euler scheme is of order 1 as expected. However the second order Runge-Kutta scheme (Heun's method) shows also first order convergence although with smaller error, which is likely due to the fact that an intermediate time step was performed. The semi-implicit interface stabilization scheme incorporates a first order Euler scheme and thus spoils any higher order scheme.

Without interface stabilization the spatial convergence, done with $\Delta t = \frac{1}{10}$ would fail for $\Delta x < 0.04$ on the droplet, which follows from the empirical formula above $\Delta t < 8\Delta s$. Likewise the temporal convergence with fixed spatial discretization of $\Delta x = \frac{1}{200}$ would require a time step as low as 0.013 that is eight times lower than the time step in the refined solution.

Due to incompressible flow the area of the droplet, initially $A_0 = \pi/4$ is theoretically conserved. In the worst case, the scheme with the lowest resolution finished the simulation loosing 3.4% of the area, whereas the scheme with the highest resolution lost $8 \cdot 10^{-4}\%$.

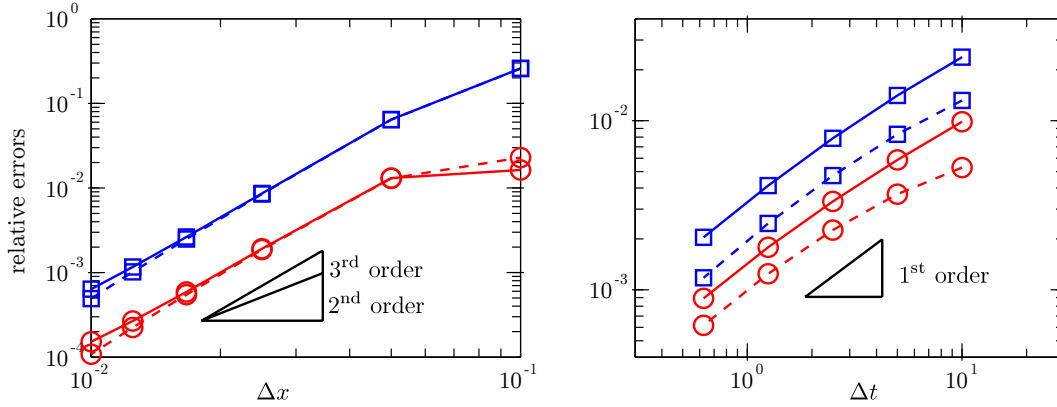


Figure 3.6: Left figure a) convergence for varying element size Δx , right figure b) convergence for varying time step Δt . The blue line represents the displacement error ϵ_x and the red line the perimeter error ϵ_p . Full line for 1-step integration and dashed line for 2nd order Runge-Kutta scheme.

3.2.4 Block pre-elimination and parallel scaling

The discretized problem results in a dense matrix \mathbf{A} with right-hand-side \mathbf{b} and vector of unknowns \mathbf{u} (velocities and stresses). The degrees-of-freedom (DOF) of the problem are $2(M + N)$. $2M$ DOF associated to the static interface, the outer walls, and $2N$ DOF associated to the dynamic interface, the droplet. If the droplet is surrounded by walls one generally finds that the DOF, $2M$, of the walls are larger than the DOF, $2N$, of the droplet. The problem without droplet is without evolution and independent of time. One therefore splits the matrix into blocks, where the block matrix \mathbf{W} represents the wall problem.

Looking at the matrix in detail:

$$\mathbf{A}\mathbf{u} = \mathbf{b} \Rightarrow \begin{pmatrix} \mathbf{W} & \mathbf{R} \\ \mathbf{P} & \mathbf{D} \end{pmatrix} \begin{pmatrix} \mathbf{u}_w \\ \mathbf{u}_d \end{pmatrix} = \begin{pmatrix} \mathbf{b}_w \\ \mathbf{b}_d \end{pmatrix} \quad (3.32)$$

Here \mathbf{W} is the influence of the static walls on themselves, \mathbf{R} like a resistance, is the influence of the droplet on the outer walls, \mathbf{P} like propulsion, is the influence of the outer walls on the droplet and \mathbf{D} the influence of the droplet on itself.

Matrix sizes are \mathbf{W} is $4M^2$, \mathbf{R} and \mathbf{P} are $4MN$ and \mathbf{D} is $4N^2$. The matrix \mathbf{W} is always the same because its boundary conditions and its element distribution does not change. We invert the matrix and save the inverse \mathbf{W}^{-1} .

Applying the inverse to the upper part of the eq. 3.32:

$$\mathbf{W}\mathbf{u}_w + \mathbf{R}\mathbf{u}_d = \mathbf{b}_w \Rightarrow \mathbf{u}_w = -\mathbf{W}^{-1}\mathbf{R}\mathbf{u}_d - \mathbf{W}^{-1}\mathbf{b}_w.$$

3.2. Numerical solution of the boundary integral equation

Then replacing \mathbf{u}_w in the lower part of eq. 3.32:

$$\mathbf{P}\mathbf{u}_w + \mathbf{D}\mathbf{u}_d = \mathbf{b}_d \Rightarrow -\mathbf{P}\mathbf{W}^{-1}\mathbf{R}\mathbf{u}_d - \mathbf{P}\mathbf{W}^{-1}\mathbf{b}_w + \mathbf{D}\mathbf{u}_d = \mathbf{b}_d.$$

And finally:

$$(\mathbf{D} - \mathbf{P}\mathbf{W}^{-1}\mathbf{R})\mathbf{u}_d = \mathbf{P}\mathbf{W}^{-1}\mathbf{b}_w + \mathbf{b}_d. \quad (3.33)$$

With $\mathbf{D} - \mathbf{P}\mathbf{W}^{-1}\mathbf{R}$ called the Schur complement. These matrix-matrix and matrix vector multiplications reduce the problem from a dense $4(M + N)^2$ matrix to a dense $4N^2$ matrix. In the case of equal viscosities $\lambda = 1$, $\mathbf{R} = \mathbf{0}$ and \mathbf{D} is the identity matrix, so the velocity at the droplet interface is given explicitly by: $\mathbf{u}_d = \mathbf{P}\mathbf{W}^{-1}\mathbf{b}_w + \mathbf{b}_d$.

A direct matrix solver for general matrices implemented in LAPACK (Anderson et al., 1999) solves the matrix. Dense matrices in contrast to sparse matrices have stronger limitations for parallelism on distributed computers. A rather efficient way is to use OpenMP (OpenMP Architecture Review Board, 2008), which allows shared memory parallelism on a multiprocessor and multicore environment. LAPACK routines automatically use these features, whereas the loop for matrix filling has been parallelized by OpenMP pragma.

Scaling for parallelism and pre-condensation The speed-up is demonstrated solving for a droplet advected in a rectangular channel using pre-condensation and multiple cores. The boundaries were discretized with 1440 DOF and its multiple by five and ten (7200 and 14400 DOF). The ratio between DOF on the droplet and on the fixed geometry, M/N was changed between 3, 5, 9, 14 and 19.

The performance tests were performed on a Dell Server with 16 cores at 1.8 GHz. The computation time for a single iteration of 1440 DOF on a single core was 0.57s with 7200 DOF 25.91s and with 14400 DOF 161.62s. Practically all the time is spent either on matrix filling and matrix solving. There is an almost perfect scaling of computation time $T \propto \text{DOF}^2$ for matrix filling and $T \propto \text{DOF}^3$ for matrix solving.

In the presence of outer walls the fixed boundary problem can be pre-condensed and therefore reduces the time to fill and solve the matrix. In assessing the speed-up we ignore the time associated to pre-condensation, which includes one matrix inversion. The matrix inversion is more costly than direct solving of a matrix but it is done only once and becomes negligible to the overall time. Increasing the number of cores shows a good scaling up to 16 cores for the problems with 7200 and 14400 unknowns, which achieve a speed-up of about 11 compared to the single core case. The problem with 1440 unknowns shows more waiting time and achieves only a speed-up of 7. We shall exclude the results so the trends are uniform but apply only to the large scale problems, which are in fact the ones that have the highest need for acceleration. Figure 3.7 a) shows the speed-up time on a single core divided by time on multiple cores.

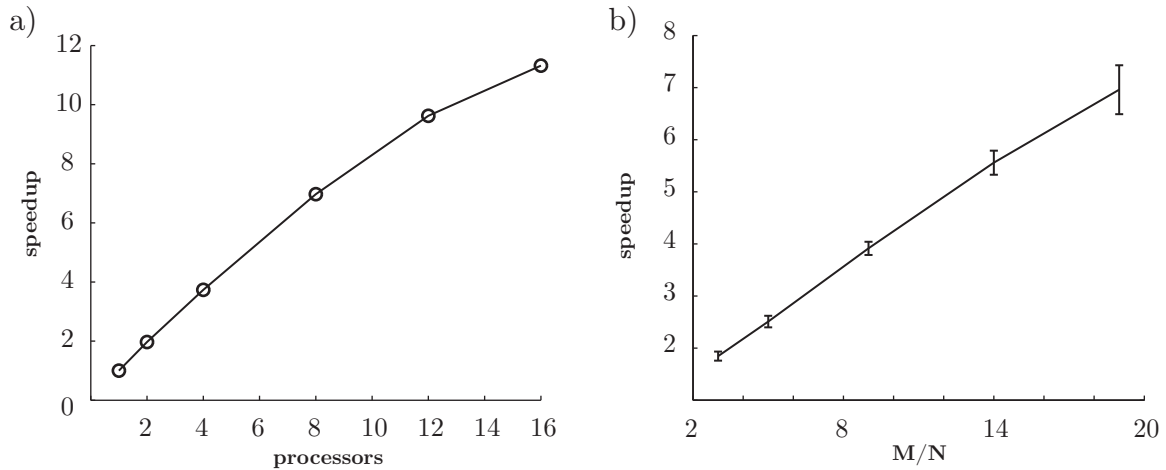


Figure 3.7: Speed-up of calculation by: a) OMP implementation, where the speed-up increases almost linearly to the number of cores, mean of 7200 and 14400 DOF shown. b) Pre-condensation, where the speed-up increases approximately linearly with the ratio of droplet to wall degrees-of-freedom.

Comparing problems of varying ratio M/N in figure 3.7 b) shows the mean speed-up out of four configurations, from 7200 DOF on single core and 16 cores and 14400 DOF on a single core and 16 cores. The error bars are computed from configurations different DOF with and without parallelism and indicate that the speed-up is quite uniform even when using OpenMP. The problem with 1440 DOF was stagnant at a speed-up by factor 3.

3.3 Boundary integrals to solve for field variables

Key feature of the boundary integral method is that only unknowns on the boundary are necessary, which is the reason for its efficiency for moving boundary problems. However once the equation is solved only values on the boundary are known and if one is interested in velocity or pressure in the domain, these values have to be computed first. For a large number of points this can be equally expensive than solving for the boundary values. However, in general this is not a problem because for an evolving problem there is hardly ever a need to know the complete velocity field with a high resolution at every time step.

Under some circumstances field values are needed for the simulation, as would be the case for example when advecting marker points, which one correlates with the surface tension. This has not been done in this thesis but instead passive markers have been advected and their position was updated at every time step using the velocity at their respective position. The mixing example in section 6.3.2 has been simulated with this method.

A lot of points in the domain are usually needed when the velocity and pressure field has to

3.3. Boundary integrals to solve for field variables

be visualized. In this case it is a costly procedure but only performed once every few time steps. Once surface stresses and velocities on the boundaries are known, integrating along the boundary over a Green's function at a chosen position \mathbf{x}_0 gives the velocity and pressure at that point.

$$\begin{pmatrix} \lambda u_x(\mathbf{x}_0) \\ \lambda u_y(\mathbf{x}_0) \\ p(\mathbf{x}_0) \end{pmatrix} = \oint_{\omega} \mathbf{T}_a \mathbf{n} \cdot \mathbf{u} - \sigma \mathbf{n} \cdot \mathbf{G}_a ds + \oint_{\eta} \mathbf{T}_a \mathbf{n} \cdot (\lambda - 1) \mathbf{u} - [[\sigma \mathbf{n}]] \cdot \mathbf{G}_a ds \quad (3.34)$$

Visualizing the flow field on a structured set of equidistant points demands the knowledge whether the point is in the continuous or dispersed phase, because the velocities are multiplied by λ . In order to figure out if a point is in the dispersed phase we integrate swept angle θ_d along the closed interface.

$$\theta_d = \oint_{\omega_d} \arcsin \left(\frac{\mathbf{x}_1 - \mathbf{x}_0}{|\mathbf{x}_1 - \mathbf{x}_0|} \times \frac{\mathbf{x} - \mathbf{x}_0}{|\mathbf{x} - \mathbf{x}_0|} \right) \approx \sum_1^m \arcsin \left(\frac{\mathbf{x}_i - \mathbf{x}_0}{|\mathbf{x}_i - \mathbf{x}_0|} \times \frac{\mathbf{x}_{i+1} - \mathbf{x}_0}{|\mathbf{x}_{i+1} - \mathbf{x}_0|} \right). \quad (3.35)$$

When the angle $\theta_d = 2\pi$ the point lies inside the droplet, for $\theta_d = \pi$ it lies on the boundary and for $\theta_d = 0$ it lies outside.

For points that are very close to the boundary the integration of eq.(3.34) will prove to be difficult because of the singular behavior of the Green's function. There exist approaches for the evaluation of these integrals, see Helsing and Ojala (2008). In this work we simply set the velocity of a point to the velocity of his nearest neighbor on the boundary if that one is closer than the sampling distance.

It is more involved to calculate the pressure close to a boundary. On the droplet the pressure is multiply defined and up to now no method is known to me that could determine a one-sided pressure.

On solid walls the singularity associated to the third Green's function is hyper-singular and can not be integrated but can be subtracted as shown in the appendix A.6. The Hadamard finite part integral over a singular element and the domain integral becomes:

$$\begin{aligned} & \oint_{\omega, \text{sing.}} \mathbf{T}_3 \mathbf{n} \cdot \lambda \mathbf{u} - \sigma \mathbf{n} \cdot \mathbf{G}_3 ds + \int_{\Omega} (\lambda (\Delta \mathbf{v} - k^2 \mathbf{v} - \nabla q) \cdot \mathbf{u}) dA \\ & = \frac{2}{\pi} (u_1 \sin(\theta) - u_2 \cos(\theta)) \left(\frac{1}{\epsilon} - k^2 \epsilon (\ln(\epsilon) - 1) \right) + \frac{p(\mathbf{x}_0)}{2}. \end{aligned} \quad (3.36)$$

With ϵ being half the element length.

Velocity or pressure gradients in the domain can be approximated by finite differences. A more accurate way would be to obtain them directly from a boundary integral. Such might be possible when differentiating the expression in eq.(3.15) for the base point of the forcing. In elasticity the gradients of the displacement are often used, which provides a similar frame

work (Wrobel and Aliabadi, 2002).

Unlike the Stokes equation, whose Green's functions are rational functions, the Green's function of the Brinkman equation involves transcendental functions, modified Bessel functions of 2nd kind. Higher order Green's functions become more and more complicated. Hence evaluating the gradient of a stress at the interface is possible but maybe frustrating to derive and implement.

3.4 Implementation

An efficient implementation of the solver was achieved by programming the discretized scheme in the programming language C++. Although high-level programming languages like MATLAB offer fast matrix solvers and parallelism it was found that achievable computation times were much shorter using C++. The aim was to provide classes that contain high-level functions of the mathematical schemes described in this chapter. In a similar fashion as the Finite Element Code FreeFEM++, developed by the Laboratoire Jacques-Louis Lions at UMPC in Paris. A programming environment of high-level functions is a trade-off between flexibility and a user-friendly interface.

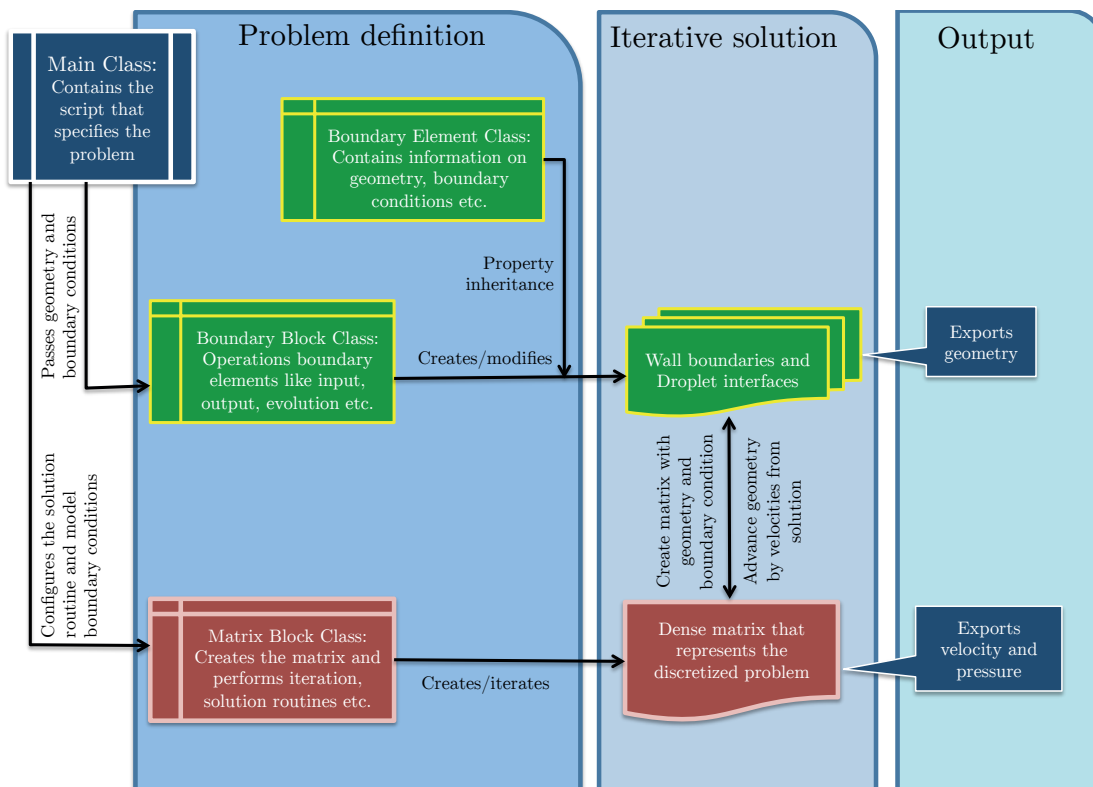


Figure 3.8: Working principle among the Boundary Element Class, Boundary Block Class and Matrix Block Class that are used by the Main class to set up and solve the discretized problem.

C++ is an object oriented programming language, in the realm of object oriented programming three classes provide the routines and variables that are separated according to their field of application. Names of the functions are generic. A Boundary Element class contains all variables and functions to access information of a closed boundary curve. Several objects or boundaries can be created from this class. These boundaries are created by function calls from the Boundary Block class object, one object of this class is created and provides all function that are necessary to read and edit boundary information, e.g. advance the droplet interface, write the geometry and pass boundary conditions to the Matrix Block class object. From the Matrix Block class one object is created that manages the memory of the matrix, unknowns and right hand side. It furthermore provides all function and routines necessary to set-up the matrix from the boundary conditions and geometry of the boundaries.

On top of these three classes is the Main class, which is edited by the user and which specifies the problem parameters ($Ca, \lambda, k, \Delta t$), geometry, boundary conditions, solution method and output routines. After creating the Boundary Block object and Matrix Block object, the Main class calls the respective functions in the Boundary Block object to set up the geometry and boundary conditions as instances of the Boundary Element class. Then the Main class calls the respective routines of the Matrix Block object and sets up the matrix. Thereafter, by calling the defined solution method of the Matrix Block object, the solution is advanced iteratively. The dependence and working principle is sketched in figure 3.8.

Summary

After reducing the three-dimensional physical problem into a two-dimensional depth-averaged problem, we applied a boundary integral transform in this chapter, which reduces the discretization to one-dimensional lines that lie in a common plane. Hence reducing the discretization to the essential, while maintaining a sharp representation of the mobile fluid interface.

As a consequence of discretizing only the boundaries, the number of unknowns is relatively small, nevertheless the resulting matrix is dense and may require a considerable computational effort on a desktop computer. The acceleration that we proposed is threefold:

Interface stabilization allows for larger time steps, which is important at low capillary numbers. Mathematically speaking the problems at a very low flow rate and at low capillary number are equivalent. Hence when solving problems whose evolution is very slow a lot of iterations are needed to simulate a significant physical time. Stabilization could make the limiting time step independent of the spatial discretization and allows for more than 10 times larger time steps.

Chapter 3. Numerical solution of the deformable interfaces

Block pre-elimination is essentially a block Gauss algorithm performed on a matrix consisting of four blocks. In large problems usually the channel walls make up for the biggest part of the matrix but since the channel walls do not move the associated block can be pre-eliminated and so a few matrix multiplications reduce the computational effort. Examples showed a speed-up of up to seven times short computation times.

Shared memory parallelization has been applied on a multi-processor and multi-core server. The speed-up scaled almost proportional to the number of cores with a speedup of eleven on sixteen cores.

Considering the cumulative speedup the computational time can be reduced by a factor about 1000. Therefore the numerical tool is able to perform simulations of a variety of complex problems on a single computer within minutes or hours.

4 Liquid interface evolution in theory and experiment

4.1 Saffman-Taylor Instability

The linear-stability analysis that follows in this chapter has been published together with François Gallaire in the journal Physics of Fluids and is mostly a facsimile of Nagel and Gallaire (2013). For this chapter an adaptation of notation is needed. Here the viscosity ratio is expressed by η instead of λ , while λ takes the role of a wave number.

Viscous fingering, also called Saffman-Taylor instability, is considered as an archetype of pattern forming instability, which has been explained in an insightful review by Couder (2000). It has also been widely studied in the context of industrial research, such as petroleum extraction in particular. The phenomenon belongs to the broad family of instabilities of growth in Laplacian fields, which includes solidification, aggregation, etc... It was first studied by Saffman and Taylor (1958), who investigated the formation of patterns upon injection of a fluid into a shallow rectangular channel filled with a different immiscible and more viscous fluid. They had observed that the formation of fingers was dependent on the ratio of channel height to channel width. The extension to radial geometry, depicted in figure 4.1, dates back to Bataille (1968) and Paterson (1981).

Viscous and capillary forces govern the mechanism of this instability. The viscosity difference drives the formation of fingers, because emerging fingers enhance the pressure gradients acting in the tip region. This is illustrated by isocontours of the pressure field in figure 4.1, where the inner fluid is assumed inviscid and at constant pressure. Since the interface moves with a velocity proportional to the pressure gradient, the feedback loop is closed. In presence of a positive radial gradient of viscosity across the interface, any minute initial displacement will turn unstable, as it increases the pressure gradient and further accelerates a protruding finger, which in turn becomes steeper and steeper as it continues to develop.

This instability is damped by surface tension, which acts to minimize the interface area and opposes the formation of curved fingers. One key parameter that determines the number

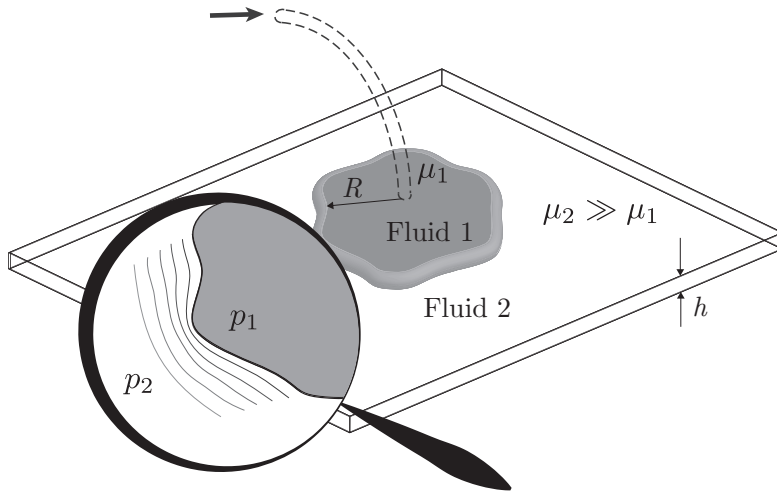


Figure 4.1: Sketch of a Hele-Shaw cell with an inviscid liquid, injected amid a viscous liquid. A close-up shows schematically the isocontours of the pressure field.

of fingers is therefore the ratio between viscous effects, represented by the product of the interface velocity U and the viscosity μ , against capillary effects represented by the surface tension γ . This ratio is called the capillary number $Ca = \frac{U\mu}{\gamma}$.

A second influential parameter is the aspect ratio R/H , because the viscous drag is mainly created by the velocity gradients in the small direction H , whereas the capillary forces act on fingers formed along the circumference whose length scales with the radius R .

In the circular injection case, as shown by Paterson (1981), who determined the wave number of the fastest growing perturbation:

$$n = \sqrt{\frac{1}{3} \left(12 Ca \frac{R^2}{H^2} + 1 \right)}, \quad (4.1)$$

where, for brevity, the injected fluid is considered inviscid. Maxworthy (1989) showed experimentally that this prediction works well for low capillary numbers but does not reproduce the behavior at elevated capillary numbers ($Ca > 10^{-2}$).

Paterson's predictions are based on the Darcy equation, which is the classical Hele-Shaw limit of the Stokes equation for large aspect ratios. In this limit only viscous terms in the thin direction are retained. The flow in the thin direction is approximated by a Poiseuille profile and the equations can be depth-averaged in the shallow direction. This leads to the Darcy equation, which is a two-dimensional potential flow, where the pressure represents the potential. One paradox of this model was pointed out by Dai and Shelley (1993), who argued that for zero surface tension the fingers would form infinitely sharp cusps.

Paterson (1985) assumed that for zero surface tension flows, for instance with two miscible fluids, the interface is influenced by the full three-dimensional stress tensor. He used a

potential flow for which he derived the 3D stress tensor at the fluid-fluid interface and looked for the perturbation wavelength that minimizes the dissipated energy, thereby using the property that low Reynolds number flows minimize the dissipation. In this limit, where the capillary number Ca goes to infinity, Paterson found that the wavelength λ depends only on the cell height H in the form $\lambda \approx 4H$. This matches quite well with Maxworthy's results: $\lambda \approx 5H$, found in figure 2 in his article (Maxworthy (1989)).

This result indicates that at high capillary number the wavelength scales like $\lambda \sim H$ and therefore the wave number $n = \frac{2\pi R}{\lambda}$ scales like $n \sim R/H$. Taking an interface perturbation of wave number n the potential flow eigenfunction in the outer fluid of viscosity μ_2 can be found for instance in Paterson (1981), $\phi = \left(\frac{r}{R}\right)^{-n} \exp(in\theta)$. This potential relates to the pressure as $p = 12\mu_2/H^2\phi$ and velocity as $\mathbf{u} = -\nabla\phi$. For Newtonian fluids the radial component of the stress tensor is $\sigma_{rr} = -p + 2\mu_2 \frac{\partial u}{\partial r}$, hence the normal stress at the interface $r = R$ becomes:

$$\sigma_{rr} = -\frac{12\mu_2}{h^2}\phi - 2\mu_2 \frac{\partial^2 \phi}{\partial r^2} = -\mu_2 \exp(in\theta) \left(\frac{12}{h^2} + \frac{2(n^2 + n)}{R^2} \right). \quad (4.2)$$

When inserting R/H for n in the limit of high wave numbers the viscous normal stress gains the same order of magnitude as the pressure. It is therefore important to include the normal stress into potential flow as proposed by D.D. Joseph, who introduced the concept of viscous potential flow (VPF), where the flow is governed by potential flow but the boundary conditions include viscous normal stress. Kim et al. (2009) determined the most unstable mode using VPF and their result showed improved agreement with Maxworthy's experiment even at capillary numbers of order one.

Although normal stress has been accounted for, there is no reason to discard tangential stress *a priori*. With normal and shear stresses equally important as the stresses in the thin direction the validity of the Hele-Shaw approximation is likely to break down near the interface. In order to increase the validity of the flow model we resort to the Brinkman equation that represents shallow flows in a depth averaged manner and retains in-plane stresses. The Brinkman equation retains in-plane stress terms and is therefore a PDE of second order, which allows boundary conditions for the normal and tangential velocities at the fluid-fluid interface. Following the same steps as Paterson (1981) in his article for radial fingering using Darcy equations, we are able to show that the finger prediction in the range from low to high capillary numbers is improved.

In a recent work Logvinov et al. (2010) used the Brinkman equation to describe the Saffman-Taylor instability of miscible fluids, hence with zero surface tension, in rectangular channels and demonstrated the influence of viscous effects in the flow plane. They found a wavelength dependence that is about $\lambda \approx 2.5h$, which is still by a factor 2 too small compared to the experiment.

4.1.1 Mathematical formulation of the problem

The flow geometry under consideration is a Hele-Shaw cell, a space confined between two plates, whose distance is in the order of a millimeter. The cell is filled with a viscous liquid and in the center is a second fluid of smaller viscosity with a uniformly circular interface. As the injection of more fluid in the center is started the front advances and the instability is triggered. This configuration is schematically depicted in figure 4.1.

Upon radial injection with constant flux Q , the interface evolves as $R(t) = \sqrt{Qt/H\pi}$. We use the undisturbed initial radius R of the interface, the flow rate Q and the viscosity of the outer fluid μ_2 for non-dimensionalization. This defines the following velocity and pressure gauges:

$$U = \frac{Q}{2\pi RH} \quad \text{and} \quad P = \frac{U\mu_2}{R}. \quad (4.3)$$

Recalling the non-dimensional Brinkman equation, which reads:

$$\eta_j(\Delta \mathbf{u}_j - k^2 \mathbf{u}_j) - \nabla p_j = 0, \quad (4.4)$$

$$\nabla \cdot \mathbf{u}_j = 0. \quad (4.5)$$

Herein the bottom index corresponds to $j = 1$ for the inner fluid and $j = 2$ for the outer fluid. The velocity components of vector \mathbf{u}_j and pressure p_j are only two-dimensional, as all the operators. All quantities are dimensionless including the viscosity ratio η_i , which is defined as $\eta_1 = \mu_1/\mu_2 = \eta$ and $\eta_2 = 1$. Given the radial geometry of the problem it is convenient to write the Brinkman equation in polar coordinates:

$$\eta_j \left(\frac{\partial^2 u_j}{\partial r^2} + \frac{1}{r} \frac{\partial u_j}{\partial r} + \frac{1}{r} \frac{\partial^2 u_j}{\partial \theta^2} - \frac{u_j}{r^2} - k^2 u_j - \frac{2\partial^2 v_j}{r^2 \partial \theta^2} \right) - \frac{\partial p_j}{\partial r} = 0 \quad (4.6)$$

$$\eta_j \left(\frac{\partial^2 v_j}{\partial r^2} + \frac{1}{r} \frac{\partial v_j}{\partial r} + \frac{1}{r^2} \frac{\partial^2 v_j}{\partial \theta^2} - \frac{v_j}{r^2} - k^2 v_j + \frac{2\partial^2 u_j}{r^2 \partial \theta^2} \right) - \frac{1}{r} \frac{\partial p_j}{\partial \theta} = 0, \quad (4.7)$$

where u_j and v_j denote the radial and azimuthal velocity components, respectively. With help of the stream function, $\mathbf{u}_j = \left(\frac{\partial \psi_j}{r \partial \theta}; -\frac{\partial \psi_j}{\partial r} \right)$, a more compact form is obtained by taking the curl of eq.(4.6) and eq.(4.7):

$$\left(\frac{\partial}{r \partial r} r \frac{\partial}{\partial r} + \frac{\partial^2}{r^2 \partial \theta^2} \right) \left(\frac{\partial}{r \partial r} r \frac{\partial}{\partial r} + \frac{\partial^2}{r^2 \partial \theta^2} - k^2 \right) \Psi = 0. \quad (4.8)$$

The kinematic boundary conditions at the interface are equality of normal and tangential velocity and normal velocity equal to interface velocity $\partial \rho / \partial t$, with ρ being the non-dimensional

interface position:

$$\nabla \times \Psi_1 = \nabla \times \Psi_2 \quad \text{and} \quad \frac{\partial \rho}{\partial t} = \frac{\partial \Psi_1}{r \partial \theta}. \quad (4.9)$$

Since the interfacial stress component in the shallow direction is averaged out, only the radial stress σ_{rr} and the in-plane tangential stress $\sigma_{r\theta}$ are matched. The dynamic boundary conditions are continuous tangential stress:

$$\mathbf{t} \cdot \bar{\bar{\sigma}}_1 \cdot \mathbf{n} = \mathbf{t} \cdot \bar{\bar{\sigma}}_2 \cdot \mathbf{n}, \quad (4.10)$$

and jump in normal stress according to Laplace's law:

$$\mathbf{n} \cdot \bar{\bar{\sigma}}_1 \cdot \mathbf{n} - \mathbf{n} \cdot \bar{\bar{\sigma}}_2 \cdot \mathbf{n} = \frac{1}{Ca} \left(\frac{\pi}{4} + \frac{2R}{H} \right), \quad (4.11)$$

where the two curvatures have been non-dimensionalized with $1/R$. The second curvature, $2R/H$, is due to the curvature of the rim in the thin direction with radius $h/2$.

Maxworthy observed that the apparent contact angle is nearly zero, which corresponds to quasi-static total wetting and therefore we neglect specific dynamical effects linked to the moving contact lines. Boundary conditions for an advancing meniscus with dynamic film formation in the case of perfect wetting have been derived by Park and Homsy (1984). In this study we will only consider the corrections introduced by the in-plane curvature, via the $\pi/4$ coefficient, and not the asymptotic corrections accounting for dynamic film formation.

4.1.2 Linear perturbation theory

The unperturbed interface position is $\rho(t_0) = 1$ and the base flow for the radially evolving liquid is simply obtained using the incompressibility equation. Since the base flow depends only on the radial direction the pressure can be integrated using eq. (4.6), which gives:

$$u_{0j} = \frac{1}{r}, \quad v_{0j} = 0 \quad \text{and} \quad p_{0j} = -\eta_j k^2 \ln(r) + P_j. \quad (4.12)$$

The solution for the pressure field depends on the constant $P_1 - P_2 = \frac{1}{Ca} \left(\frac{\pi}{4} + \frac{2R}{H} \right) - 2(1 - \eta)$, which matches the jump due to surface tension and normal stress at the interface.

Let us assume a perturbation expansion of the interface position $\rho = \rho_0 + \epsilon f_n(t) e^{i n \theta}$ and stream function $\Psi_j = \Psi_{0j} + \epsilon \Psi_{1j}$, with a time dependent amplitude $f_n(t)$ and normal mode Ansatz of wave number n .

The Brinkman equation being linear, the general solution for eq. (4.8) is used.

$$\Psi_{11} = i \left(a_n \frac{I_n(kr)}{I_n(k)} + b_n r^n \right) e^{i n \theta}, \quad (4.13)$$

$$\Psi_{12} = i \left(c_n \frac{K_n(kr)}{K_n(k)} + d_n r^{-n} \right) e^{i n \theta}. \quad (4.14)$$

The general solution is build of powers of r and modified Bessel functions of first and second kind, I_n and K_n . The parameters a_n , b_n , c_n and d_n have to be determined from the boundary conditions at the interface. The structure of eq. (4.8) shows that the classical solutions of the Laplace equation are also solutions of the Brinkman equation. The two additional solutions of the Brinkman equation are modified Bessel functions that decay exponentially away from the interface.

An immediate improvement to (viscous) potential flow is that this solution allows to impose continuous tangential velocities and stresses. In contrast, the potential flow solution has a discontinuity of tangential velocity and tangential stress. This is illustrated in figure 4.2 by plotting the perturbation of potential flow and Brinkman flow applying all possible matching conditions at the interface.

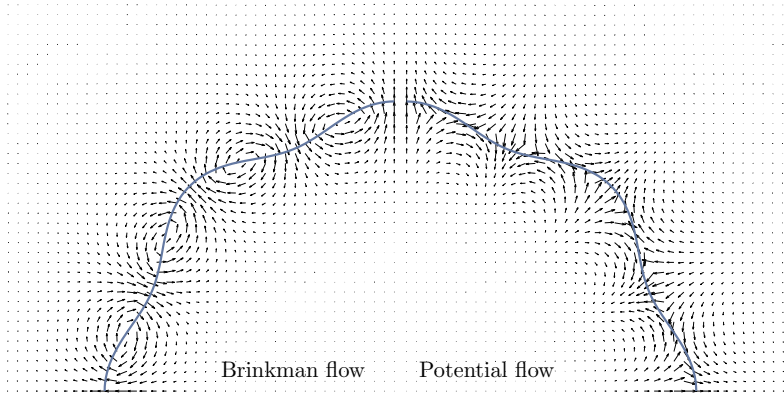


Figure 4.2: Flow fields for perturbation of wave number $n = 8$ and amplitude 0.05 for the Brinkman model and viscous potential flow, at $k = 16\sqrt{12}$, $\eta = 1/2$ and $Ca = 1$. Tangential velocities vary continuously only for the Brinkman solution. The interface is represented as a grey line.

We apply the flattened boundary conditions at the interface that consider the first order Taylor expansions around the original interface position.

Impermeability: The interface moves with the inner radial velocity such that $\frac{\partial \rho}{\partial t} + \epsilon \frac{\partial f_n}{\partial t} e^{i n \theta} = u_{01} + \epsilon \frac{\partial u_{01}}{\partial r} f_n e^{i n \theta} + \epsilon u_{11}$. Cancelling dominant terms yields at order ϵ ,

$$\frac{\partial f_n}{\partial t} e^{i n \theta} = \frac{\partial u_{01}}{\partial r} f_n e^{i n \theta} + \frac{i}{r} \frac{\partial \Psi_{11}}{\partial \theta}, \quad (4.15)$$

which further leads to:

$$n(a_n + b_n) + f_n + \frac{\partial f_n}{\partial t} = 0. \quad (4.16)$$

Continuity of radial velocity: Matching the outer velocity to the inner velocity at the interface, $u_{11} = u_{12}$:

$$\frac{\partial \Psi_{11}}{\partial \theta} = \frac{\partial \Psi_{12}}{\partial \theta}, \quad (4.17)$$

leads to

$$a_n + b_n - c_n - d_n = 0. \quad (4.18)$$

Continuity of tangential velocity: The equality of tangential velocities on the flattened interface, $v_{11} = v_{12}$:

$$\frac{\partial \Psi_{11}}{\partial r} = \frac{\partial \Psi_{12}}{\partial r}, \quad (4.19)$$

leading to:

$$a_n k \frac{I_{n+1}(k)}{I_n(k)} + c_n k \frac{K_{n+1}(k)}{K_n(k)} + n(a_n + b_n - c_n + d_n) = 0. \quad (4.20)$$

Continuity of tangential stress: To ensure continuity of the tangential stress at the interface eq. (4.10):

$$\eta \left(-\frac{\partial^2}{r^2 \partial \theta^2} \Psi_{11} + r \frac{\partial}{\partial r} \left(\frac{\partial}{r \partial r} \Psi_{11} \right) \right) = \left(-\frac{\partial^2}{r^2 \partial \theta^2} \Psi_{12} + r \frac{\partial}{\partial r} \left(\frac{\partial}{r \partial r} \Psi_{12} \right) \right), \quad (4.21)$$

which becomes:

$$\begin{aligned} & \eta \left(2a_n n^2 + 2b_n n^2 + a_n k^2 - 2a_n k \frac{I_{n+1}(k)}{I_n(k)} - 2a_n n - 2b_n n \right) \\ & - 2c_n n^2 - 2d_n n^2 - c_n k^2 - 2c_n k \frac{K_{n+1}(k)}{K_n(k)} + 2c_n n - 2d_n n = 0. \end{aligned} \quad (4.22)$$

Laplace law: The jump of the normal stress balance is more involved since it requires to recover the pressure from the perturbation, which had been left out due to use of the stream function. Integrating eq. (4.7) for θ relates the pressure perturbations to the general solutions.

$$p_{1j} = \eta_j r \int_0^\theta \left(\left(\frac{n^2}{r^2} + k^2 + \frac{1}{r^2} \right) \frac{\partial \Psi_{1j}}{\partial r} - \frac{\partial^3 \Psi_{1j}}{\partial r^3} - \frac{\partial^2 \Psi_{1j}}{r \partial r^2} - \frac{2n^2}{r^3} \Psi_{1j} \right) d\theta, \quad (4.23)$$

which simplifies to:

$$p_{11} = \eta b_n r^n k^2 e^{in\theta} \quad \text{and} \quad p_{12} = -d_n r^{-n} k^2 e^{in\theta}.$$

The radial stress balance in order ϵ for the flattened interface according to eq. (4.11):

$$p_{11} + \frac{\partial p_{01}}{\partial r} f_n e^{in\theta} + 2\eta \frac{\partial}{\partial r} \left(\frac{i \partial}{r \partial \theta} \Psi_{11} \right) - 2\eta \frac{\partial^2 u_0}{\partial r^2} f_n e^{in\theta} - p_{12} - \frac{\partial p_{02}}{\partial r} f_n e^{in\theta} - 2 \frac{\partial}{\partial r} \left(\frac{i \partial}{r \partial \theta} \Psi_{12} \right) + 2 \frac{\partial^2 u_0}{\partial r^2} f_n e^{in\theta} = - \frac{\pi}{4 Ca} (1 - n^2) f_n e^{in\theta}. \quad (4.24)$$

Recalling that the factor $\pi/4$ in front of $1/Ca$ stems from the corrected boundary condition by Park and Homsy (1984). Inserting the expressions for velocity and pressure results in:

$$\eta \left(-k^2 f_n + b_n k^2 - 2a_n n - 2b_n n + 2a_n n k \frac{I_{n+1}(k)}{I_n(k)} + 2a_n n^2 + 2b_n n^2 - 4f_n \right) + d_n k^2 + f_n k^2 + 2c_n n + 2d_n n + 2c_n n k \frac{K_{n+1}(k)}{K_n(k)} - 2c_n n^2 + 2d_n n^2 + 4f_n = - \frac{\pi}{4 Ca} f_n (1 - n^2). \quad (4.25)$$

Using the boundary condition equations (4.16), (4.18), (4.20), (4.22) and (4.25) the unknowns f_n, a_n, b_n, c_n, d_n have to solve an eigenvalue problem, with $\frac{1}{f_n} \frac{df_n}{dt}$ as an Eigenvalue.

Assuming that the growth of the instability is much faster than the evolution of the base flow, it is assured that the aspect ratio k and capillary number Ca do not change significantly with time. Hence this leads to the possibility to express the function $f_n(t) = f_n \exp(\sigma t)$ and consequently $df_n/dt = \sigma f_n$.

4.1.3 Growth rates for linear theory

The dispersion relation that is obtained from the Eigenvalue problem is for brevity given only for the case where the inner viscosity is zero and the general expression is given in the appendix of the article (Nagel and Gallaire, 2013).

For the case of an inviscid inner fluid the growth rate σ becomes:

$$\sigma = \frac{A(k, n) + \frac{\pi}{4} Ca^{-1} B(k, n)}{C(k, n)}. \quad (4.26)$$

In this form it can be easily seen that the growth rate depends on a parameter pair, where $A(k, n)/C(k, n)$ weights the flow rate and $B(k, n)/C(k, n)$ weights the influence of surface tension. The parametric functions are:

$$A(k, n) = k^4 n - k^4 - 8n^2 - 8n^4 + 4k^2 n - 8k^2 n^2 + \frac{K_{n+1}(k)}{K_n(k)} (-2k^3 + 2k^3 n + 4kn + 4kn^3), \quad (4.27)$$

$$B(k, n) = k^2 n - k^2 n^3 + 4n^4 - 4n^2 + \frac{K_{n+1}(k)}{K_n(k)} (2kn - 2kn^3), \quad (4.28)$$

$$C(k, n) = k^4 - 8n^2 + 8n^4 + 4k^2 n^2 + \frac{K_{n+1}(k)}{K_n(k)} (2k^3 - 4kn^3 + 4kn). \quad (4.29)$$

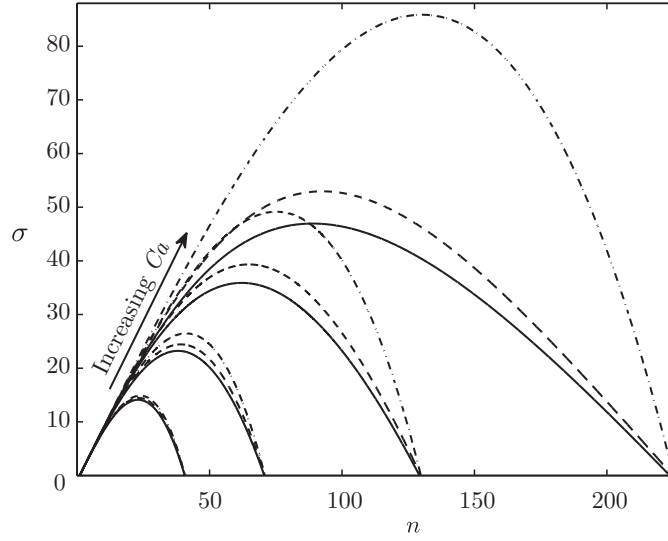


Figure 4.3: Dispersion relations using different models: - · - Potential flow, - - - Viscous potential flow and — Brinkman model. The aspect ratio is fixed to $k = 200$, while the capillary number changes between $\frac{1}{30}$, $\frac{1}{10}$, $\frac{1}{3}$ and 1.

For a better comparison with existing results the growth rate σ obtained by Paterson (1981) is decomposed in the same way. Correcting only the influence of the curvature in Paterson's result by factor $\pi/4$, which is done for the corrected boundary condition.

$$\hat{\sigma} = \left((n-1) - \frac{\pi}{4} \frac{n(n^2-1)}{\text{Ca} k^2} \right). \quad (4.30)$$

Reorganizing the equation in the form of eq. (4.26) gives:

$$\hat{A}(k, n) = (n-1)k^4, \quad \hat{B}(k, n) = n(1-n^2)k^2, \quad \hat{C}(k, n) = k^4.$$

This rephrasing shows that the results of Paterson (1981) are recovered in the limit of large aspect ratio k . However it is apparent that for zero surface tension, where the growth rate increases linearly with n , our relation has stabilizing terms that grow faster in wave number n than the destabilizing terms. This ensures that for finite aspect ratio k , there will always be a finite cut-off wave number n .

Figure 4.3 shows the growth rate σ for different capillary numbers as a function of the wave number at constant aspect ratio $k = 200$ for potential flow, VPF and Brinkman model. Curves for other values of k are not presented because they only depart one from the other at low aspect ratio $k^2 \ll Ca^{-1}$.

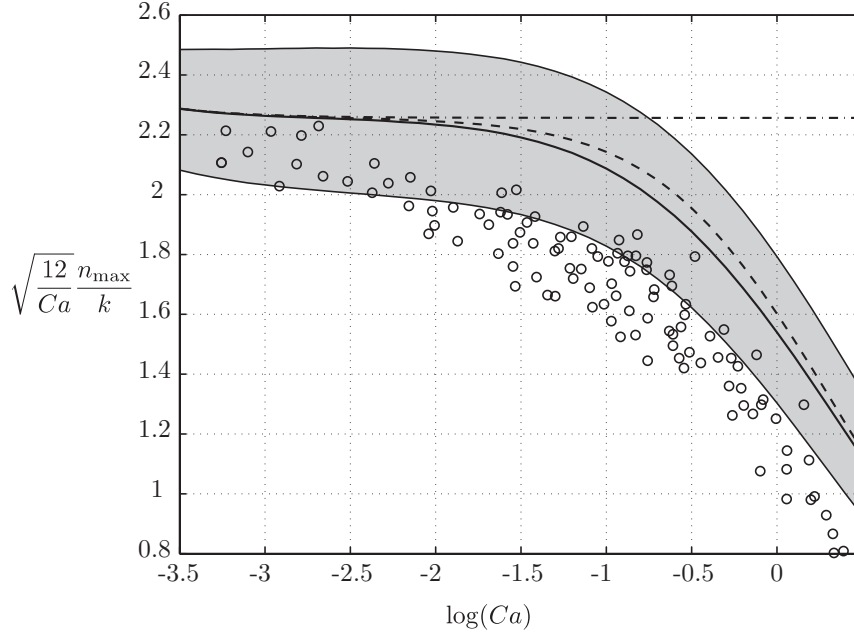


Figure 4.4: Most unstable modified wave number plotted against logarithm of capillary number. Plotted results are: - · - Potential flow, - - - VPF and — Brinkman model with aspect ratio $k = 200$. Maxworthy's experimental results are also shown, indicated by \circ symbols. The grey shaded region includes all wave numbers of the Brinkman model, where the growth rate is within 1 % of the maximal growth rate.

This example reveals two properties in the dispersion relation induced by the Brinkman model: The growth rates are smaller for all wavelengths and the maximum growth rates shift to lower wave numbers as higher modes receive larger damping. For small capillary numbers the difference is small but becomes large for high capillary numbers ($Ca \approx 1$). In the intermediate range of $Ca \approx 0.1$ the difference between Brinkman model and VPF is comparable to the difference between VPF and potential flow.

Furthermore one is interested in the wave number n with the highest growth rate σ for given parameters k and Ca . In figure 4.4 the most unstable wave numbers are plotted in the same way as done by Maxworthy (1989), including the results from our stability analysis. Maxworthy chose to plot the results for a modified wave number being:

$$A_{max} = \sqrt{\frac{12}{Ca}} \frac{n_{max}}{k},$$

because then Paterson's theoretical most unstable wave number is approximately represented as a straight line. With the corrected boundary conditions of Park and Homsy (1984) this line

should be constantly $4/\sqrt{\pi}$ for all capillary numbers. Maxworthy showed, as the capillary number approaches 1, the observed number of fingers becomes much smaller than predicted. Our findings are represented by the full line and show an improved agreement. Despite the clear difference in growth rate there is a relatively small improvement of the maximal growth rate between Brinkman and VPF.

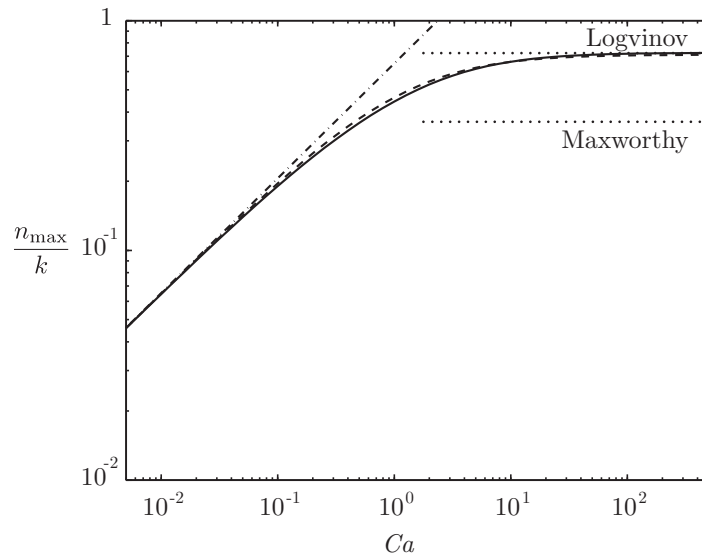


Figure 4.5: Most unstable finger number as a function of capillary number: - · - Potential flow, - - - Viscous potential flow and — Brinkman model. Dotted lines show the experimental result of Maxworthy (1989) for low surface tension and the theoretical result of Logvinov et al. (2010) who used the Brinkman model for zero surface tension fingering of a flat interface with aspect ratio $k = 200$. For higher capillary number the number of fingers becomes inversely-proportional to the gap width.

Maxworthy's data is spread, which can be explained by the relatively flat peak of the dispersion relation, as seen figure 4.3, which does not cause a sharp wavelength selection. Displaying also possible fingers that have a growth rate of no less than 1% of the maximal growth rate, the spread takes an almost symmetric shape about the maximal growth rate.

The number of fingers for zero surface tension when $Ca \rightarrow \infty$ was shown to depend only on the gap width, in other words the aspect ratio. In order to highlight this we plot the number of most unstable finger divided by the aspect ratio k against capillary number in figure 4.5. For $k^2 \gg Ca^{-1}$ the results approximately collapse on a single curve. For large capillary numbers the prediction tends asymptotically to the result of Logvinov et al. (2010) who studied zero surface tension flows in rectangular channels using the Brinkman equation. Their result in wavelength $\lambda = 2.5h$ is reformulated in wave number $n = \frac{2\pi R}{2.5H} = \frac{2\pi}{2.5\sqrt{12}}k$. The experimental result, identified from Maxworthy's data, is missed by a factor 2, $n = \frac{2\pi}{5\sqrt{12}}k$. Not surprisingly the result of Paterson (1981) gives a far too high number of fingers.

4.1.4 Simulation of non-linear finger formation

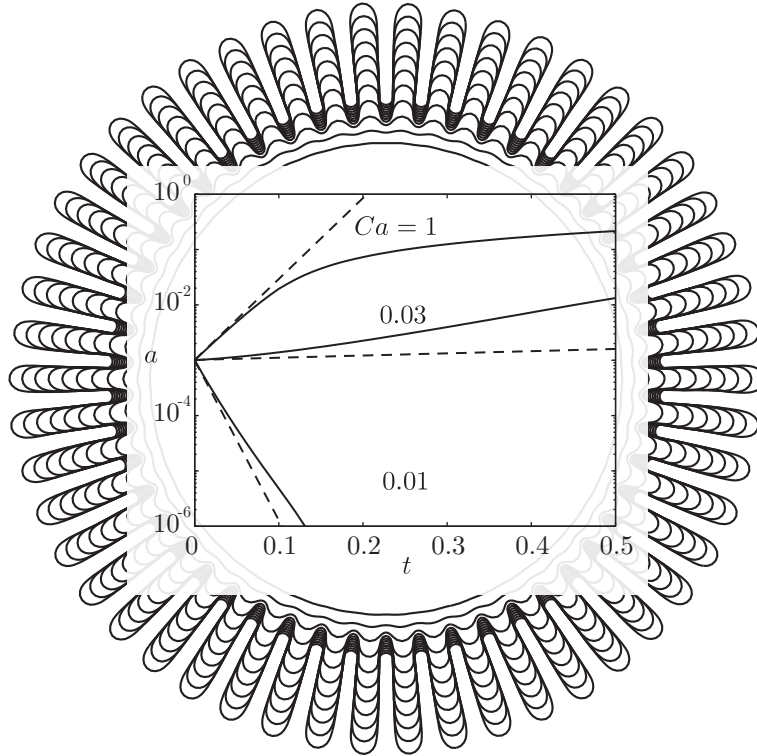


Figure 4.6: Plotting the growth of a sinusoidal perturbation of wave number 50 while injection of a liquid that is 10 times less viscous than the surrounding liquid. The evolution of the interface for $Ca = 1$ is depicted at several instances in time. The graph in the center compares prediction by linear stability analysis - - against numerical simulation —.

The instability is numerically simulated with an interface of 500 elements and a time step of $\Delta t = 10^{-3} \cdot Ca^{-1}$. Introducing a sinusoidal perturbation of the interface, the theoretical growth of the perturbation is given as $a(t) = a_0 \exp(\sigma t)$. The initial perturbation amplitude is chosen $a_0 = 10^{-3}$ and σ is determined from eq.(4.26). The initial aspect ratio was set to $R/H = 80$, the viscosity ratio to $\eta = \frac{1}{11}$ and the capillary number was varied between $Ca = 1, 0.03$ and 0.01 as to obtain unstable, neutral and stable modes.

Plotting perturbation amplitude $a(t)$ against time for analytical and numerical results $a^n = \frac{1}{2}(R_{max}^n - R_{min}^n)$ in figure 4.6 shows perfect agreement in the beginning of the simulation, which then is slightly deviating as the radius evolves. The background illustration in the figure shows the interface evolution for every 50th time step. Deviation for large t at $Ca = 1$ is due to non-linear saturation and at $Ca = 0.03$ because the aspect ratio changes with the radius and therefore the solution shifts into the unstable regime.

When starting from stochastic initial conditions these simulations have allowed to observe tip splitting and opens perspectives to study the selection of number of fingers. When adding

Marangoni stresses it is also possible to analyze the evolution of fingering in a medium of variable surface tension, like in a Hele-Shaw with thermal gradients.

4.1.5 Conclusion

A dispersion relation for the Saffman-Taylor instability modeled by the Brinkman equation covers a wide range of capillary numbers and shows a good agreement with experiments. We showed that viscous stresses become important when the number of fingers increases. This decreased wave number of the maximal growth is achieved by the in-plane stresses. When the surface tension has only little influence, the in-plane stresses decrease the growth rate for high wave numbers, as these create large velocity gradients and thus normal and tangential stresses at the interface. Darcy's law cannot account for them, in contrast to the Brinkman model, which allows for a cut-off wave number even with zero surface tension.

The finger size for zero surface tension is found to scale like the cell height h , as found by Logvinov et al. (2010) who considered a rectangular cell and by Kim et al. (2009) for radial injection. In the contrast to the latter study, based on viscous potential flow, our solution satisfies continuity of tangential velocity and shear stress perturbations.

Under what circumstances the use of only normal stress boundary conditions in a potential flow is justified is an open question. In our Brinkman model normal and tangential stresses are present throughout the flow domain, nevertheless we reveal a result that is similar to VPF. Having matched boundary condition in the tangential direction influences the growth rate but changes only weakly the selectivity of the radial growth rate σ . Even for viscosity ratios η different from zero. Furthermore the velocity field of the Brinkman model differs by terms that decrease exponentially in r away from the interface, therefore having only a limited zone of contribution.

Comparison to numerical data provided an important test case to validate the evolving algorithm and check whether unstable, neutral and stable solutions can be accurately reproduced.

4.2 The relaxation of an ellipse

This chapter is a facsimile of an article by Pierre-Thomas Brun, François Gallaire and myself, which has been published in Physical Review E (Brun et al., 2013).

Herein we report the study of an idealized, yet representative, case of relaxation: an initially flattened cylindrical droplet of fluid #1 with an elliptical cross section of area \mathcal{A} is placed in a Hele-Shaw cell at $t = t_0$ where the surrounding fluid #2 is at rest (Fig. 4.7-I). The two fluids, of viscosity μ_1 and μ_2 are immiscible and subject to surface tension (denoted $\tilde{\gamma}$) that drives the relaxation of the droplet at a typical speed $U = \tilde{\gamma}/\mu_2$ obtained when balancing surface tension effects and viscous dissipation such that $U(\mu_1 + \mu_2) = \tilde{\gamma}$. Preferring $\mu_1 + \mu_2$ to μ_1 or μ_2 is quite arbitrary at this point and will be discussed later on. The investigation we propose is twofold.

Firstly, a numerical simulation for this ellipse is performed using the algorithm presented in chapter 3.

What is the geometry of the relaxing droplet? and does the droplet remain elliptic? are two questions that naturally arise when considering this problem. Secondly, we tackle the relaxation analytically with a linear stability analysis that helps build a predictive reduced model of the dynamics as well as a geometric theory for droplets relaxation.

4.2.1 A non monotonous relaxation

At low Reynolds numbers the 3D-Stokes equations prevail and can advantageously be averaged along the cell small direction h assuming $H \ll R$, where $R = \sqrt{\mathcal{A}/\pi}$ is the characteristic length of the problem (\mathcal{A} is the area of the droplet). The resulting equations, are the Brinkman equation derived in section 2.2.

$$\eta_j(\Delta \mathbf{u}_j - k^2 \mathbf{u}_j) - \nabla p_j = \mathbf{0} \quad (4.31)$$

$$\nabla \cdot \mathbf{u}_j = 0 \quad (4.32)$$

where $\mathbf{u}_j = u_j \mathbf{e}_r + v_j \mathbf{e}_\theta$ and p_j are respectively the fluid # j dimensionless speed in the xy -plane (expressed in polar coordinates) and dimensionless pressure field using U and $P = \tilde{\gamma}/R$ as gauges. The parameters of this equation write $k = \sqrt{12}R/H$ and $\eta_j = \mu_j/(\mu_1 + \mu_2)$. In this section η is used instead of λ because the viscosity is normalized by the sum of viscosities and not just the outer flow viscosity.

Note that the differential operators and the variables are implicitly restricted to the cell plane and that we work with dimensionless variables. These equations go along with five scalar boundary conditions expressing (i) the impermeability of the interface, the continuity of both fluids (ii) normal and (iii) tangential speeds at the interface as well as (iv) the tangential stress continuity and (v) normal stress discontinuity. For the latter writing:

$$\mathbf{n} \cdot \llbracket \overline{\overline{\boldsymbol{\sigma}}} \rrbracket \cdot \mathbf{n} = \gamma \left(\frac{\pi}{4} \kappa + \frac{2}{h} \right) \quad (4.33)$$

where κ denotes the in plane curvature of the interface, $\overline{\overline{\boldsymbol{\sigma}}}$ is the Cauchy stress tensor, \mathbf{n} is the normal to the interface and $\llbracket \cdot \rrbracket$ denotes a discontinuity.

Taking advantage of the predominance of interfaces in this problem we used a boundary element method algorithm (BEM hereafter) to solve this set of equations.

Note that the surface tension γ actually sets the time scale $T = R(\mu_1 + \mu_2)/\gamma$ of this evolution but does not affect the successive shapes of the interface. They solely depend on the two parameters: η_1 and k (or equivalently $\eta_2 = 1 - \eta_1$ and k). Given the generalized Laplace law for the normal stress jump (4.33) at the interface we anticipate that the planar geometry of

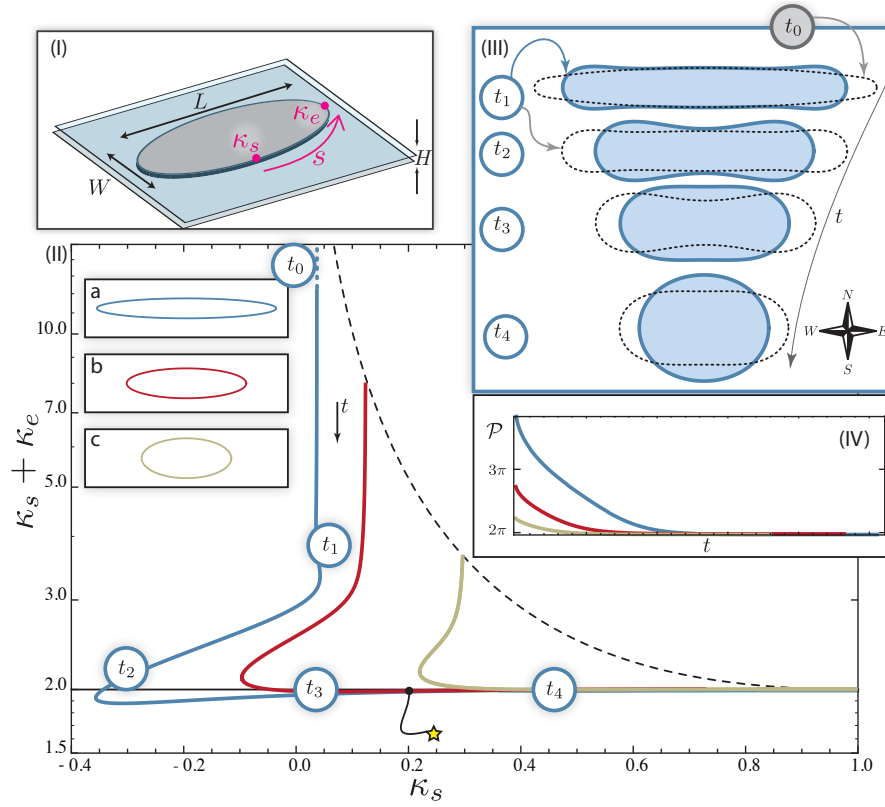


Figure 4.7: **I** Idealized case study: an elliptical droplet of typical size R and initial deformation $D_f = \frac{L-W}{W}$ is placed in an Hele-Shaw cell of height $H \ll R$. **II** Relaxation pathways in the plane $(\kappa_n + \kappa_e, \kappa_n)$ respectively corresponding to the ellipses of initial deformations $D_f = 8$ (a), 3 (b), $5/4$ (c). **III** Time evolution of the drop interface for $D_f = 8$ (plain lines). At $t = t_i$ the dotted line recalls the drop at $t = t_{i-1}$. **IV** Shown is the perimeter as a function of time in each case.

the interface parametrized by its arc-length $\mathbf{r}(s)$ as well as the interface curvature $|\mathbf{r}_{,ss}| = \kappa$ are of interest in this study. In particular, we define the south and east curvatures respectively denoted $\kappa_s = \kappa(0)$ and $\kappa_e = \kappa(\mathcal{P}/4)$, where \mathcal{P} is the flattened drop perimeter (Fig. 4.7-I).

Without loss of generality we consider the relaxation of elliptic droplets of area $\mathcal{A} = \pi$ (*i.e.* $\mathcal{R} = 1$ and all variables are dimensionless) that have a different initial deformation $D_f(t=0)$ where $D_f = (L - W)/W$ denotes the deformation coefficient and L and W are respectively the drop length and width (see Fig. 4.7-I). As a first step both viscosities are assumed equal ($\eta_1 = 1/2$) and the dimensionless height of the channel is chosen to be $h = \frac{1}{4}$ a typical value for microfluidic systems yielding $k = 8\sqrt{3} \approx 13.86$ a sufficiently large value for the depth averaged model to be accurate (section 2.2.2). Shown in Figure 4.7 is the relaxation diagram of three elliptic droplets obtained with our BEM. As regards of the perimeters (Fig. 4.7-IV), they all monotonously relax towards the value of 2π that corresponds to the perimeter of a circle of curvature $\kappa = 1$ minimizing \mathcal{P} – therefore the "surface" energy – for a given area \mathcal{A} . \mathcal{A} may be

interpreted as the droplet "volume" in our depth averaged formalism. Unlike \mathcal{P} some other variables evolutions are non-monotonous and are of particular interest for the rest of this section.

In the following, the droplets path of relaxation is described in terms of curvature. Ellipses verify the relation $\kappa_s = 1/\kappa_e$. Therefore they fall on the curve $1/\kappa_s + \kappa_s$ in the parameters space $(\kappa_e + \kappa_s, \kappa_s)$ and thus, the $t = t_0$ extremities of the three relaxation trajectories are found on that very curve. One could expect these ellipses to relax while remaining elliptic *i.e.* to follow the dotted line in Figure 4.7-II. On the contrary the heel shaped relaxation curves as well as the successive shapes of the droplets reported in Figure 4.7 strongly suggest a different and non-monotonous scenario. This scenario is depicted in the case of the ellipse **a** verifying $D_f(0) = 8$. Shown in Figure 4.7-III is the superimposition between the time t_0 and t_1 where one may observe that the most curved parts of the ellipse (east and west) initiate their relaxation while the least curved parts (south and north) remain motionless. As a consequence κ_e decreases while κ_s remains constant and the relaxation curve decreases vertically. The inflections of the interface induced by the east and west parts respective relaxations then reach the north and south poles and cause the curvature there to decrease and possibly change sign (at $t = t_2$ for the ellipse **a**). This is responsible for the heel like shape of these relaxation curves. Of particular interest is the third and last part of relaxation in which the droplets then enter. Remarkably, all relaxation curves eventually collapse on a master curve defined by $\kappa_e + \kappa_s = 2$ (\star) (this event occurs at $t = t^\star$ and is marked by a star in Fig. 4.7 for the ellipse **a**). It is crucial to note that the value 2 is reached before the relaxation is complete (that is when $D_f = 0$). Therefore, from t^\star onwards both curvatures trade for each other, their evolutions balance each other while their sum remains constant and equal to 2. Everything happens as if the curvature was "flowing" from areas of excess (east and west) to deprived areas (north and south). A quantitative analysis of such a relaxation is reported next and is generalized to different aspect ratios k as well as different viscosity ratios η_1 .

4.2.2 Quantitative analysis of the relaxation

Shown in Figure 4.8-I is the time evolution of the deformation $D_f(t)$ for different aspect ratios $4 \leq R/H \leq 10$ and $\eta_1 = 1/2$ in the case of the ellipse **c** ($D_f(0) = 5/4$, see Fig. 4.7). After the earlier described initial stage of relaxation the deformations appear to be exponentially decreasing. Note that the overall time of relaxation is an increasing function of the ratio R/H (and thus k) as explained next.

The relaxation is driven by surface tension effects that induce a pressure field scaling as $\gamma(\frac{2}{H} + \frac{\pi}{4R})$ derived by Park and Homay (1984) where $\frac{1}{R}$ is the typical in plane curvature of the droplet. This pressure term is dominated by the factor $\frac{2}{H}$ as we consider a confined environment ($H \ll R$). However this term is fixed by the channel geometry. Consequently, only the in plane curvature is meant to evolve while the droplet relaxes. A proper evaluation of the active term of the pressure field imposed by surface tension is therefore γ/R . This driving

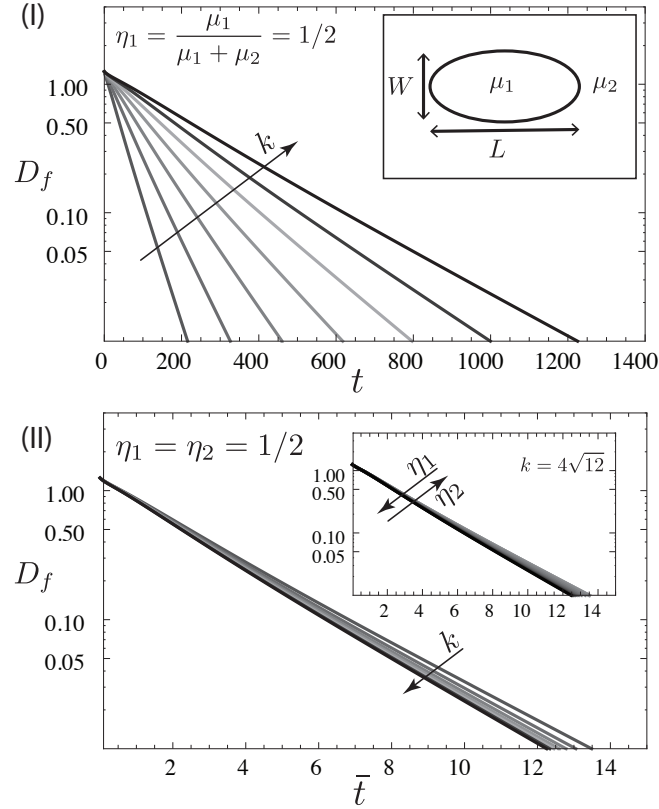


Figure 4.8: **I** Shown is the deformation coefficient $D_f = (L - W)/W$ as the function of the time t for several values of $k = \sqrt{12} \frac{R}{H}$ ($4\sqrt{12} \leq k \leq 10\sqrt{12}$) and $\eta_1 = 1/2$. **II** The same data plotted as a function of T shows a collapse. The insert shows that a similar collapse is possible when varying η_1 while k is fixed ($0 \leq \eta_1 \leq 10/11$).

mechanism is counterbalanced by the viscous damping, itself dominated by terms in the normal direction yielding to $\mu \bar{v}/H^2 \sim \frac{1}{R} \gamma/R$ where \bar{v} is the yet undermined characteristic velocity and $\mu = \mu_1 + \mu_2$ is a typical viscosity. Note that the extra $\frac{1}{R}$ in the right end side denotes the gradient of the pressure field. One eventually obtains:

$$\bar{v} = \frac{\gamma H^2}{\mu R^2} = U \frac{H^2}{R^2} \quad (4.34)$$

where U was the first speed gauge established earlier in the introduction that was built on the classical construction of the capillary number. Equation (4.34) suggests the rescaling $T = \tilde{t} \frac{H^2}{R^2}$ that leads to the collapse of the relaxation plots in Figure 4.8-**II**. Note that the use of $\mu = \mu_1 + \mu_2$ as a viscosity gauge is consistent as shown by the collapse in the insert of Figure 4.8-**II** obtained when varying η_1 .

We now concentrate on the axial curvatures κ_s, κ_e and in particular compare their evolutions to the one of the deformation $D_f(T)$. As the ellipse relaxes towards a circle it is obvious that

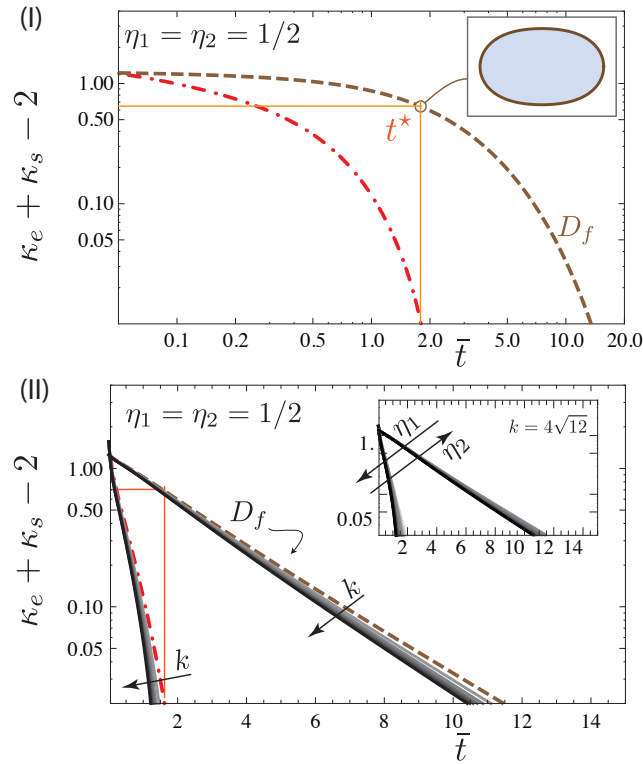


Figure 4.9: **I** Shown in dotted-dashed line is the convergence of $\kappa_s + \kappa_e$ towards 2 for $\eta_1 = 1/2$ and $k = 4\sqrt{12}$. t^* is the time when the sum of curvatures has converged with 0.05% of error. Note that $t^* \sim 2$ is way smaller than the time needed for the droplet to become almost circular ($T \sim 15$, the dashed curve represents the deformation). Insert: droplet at t^* . **II** Generalization of the previous plot varying k and showing the collapse obtained with T . The insert shows that a similar collapse is possible when varying η_1 while k is fixed ($0 \leq \eta_1 \leq 10/11$).

κ_s and κ_e both tend to 1. However their sum $\kappa_s + \kappa_e$ and especially its deviation to the value 2 is now investigated for $R/H = 4$, with equally viscous fluids and $D_f(0) = 5/4$ (Fig. 4.9). The convergence of $\kappa_s + \kappa_e$ towards 2 is insured (with an error of 0.05%) at a time denoted t^* while the deformation is still large $D_f \approx 0.7$ (insert of Fig. 4.9). For $T > t^*$ the droplet relaxes while the sum of its south and east curvature is conserved and their respective evolutions balance each other (κ_s is increasing and κ_e decreasing). This result is remarkably general in the sense that it does not depend neither on k nor η_1 as shown by the collapses in Figure 4.9-II.

We now derive a model to shed lights on the earlier reported observations.

4.2.3 Two complementary models for the relaxation

A linear model

To explain the vertical part of the curvature relaxation trajectories above reported – that is to explain why ellipses do not remain as such while relaxing – we proceed with a linear analysis. This linear analysis is the same as in the stability analysis of the Saffman-Taylor instability in section 4.1 but without a baseflow. We consider a weak elliptical deformation of a circle ($D_f \ll 1$). Over time this ellipse relaxes and writes $r(\theta, t) = \alpha_0 + \sum_{n \geq 1} \epsilon \alpha_n(t) \cos(n\theta)$ in polar coordinates using a cosine Fourier decomposition where $\epsilon \ll 1$ and the values of α_0 and $\alpha_n(0) = \alpha_n^0$ for $n \in \mathbb{N}^+$ are chosen to match the initial shape of the ellipse. The time evolution is assumed to write $\alpha_n(t) = \alpha_n^0 \exp(\tau_n t)$. The values of τ_n , that may be complex, are obtained

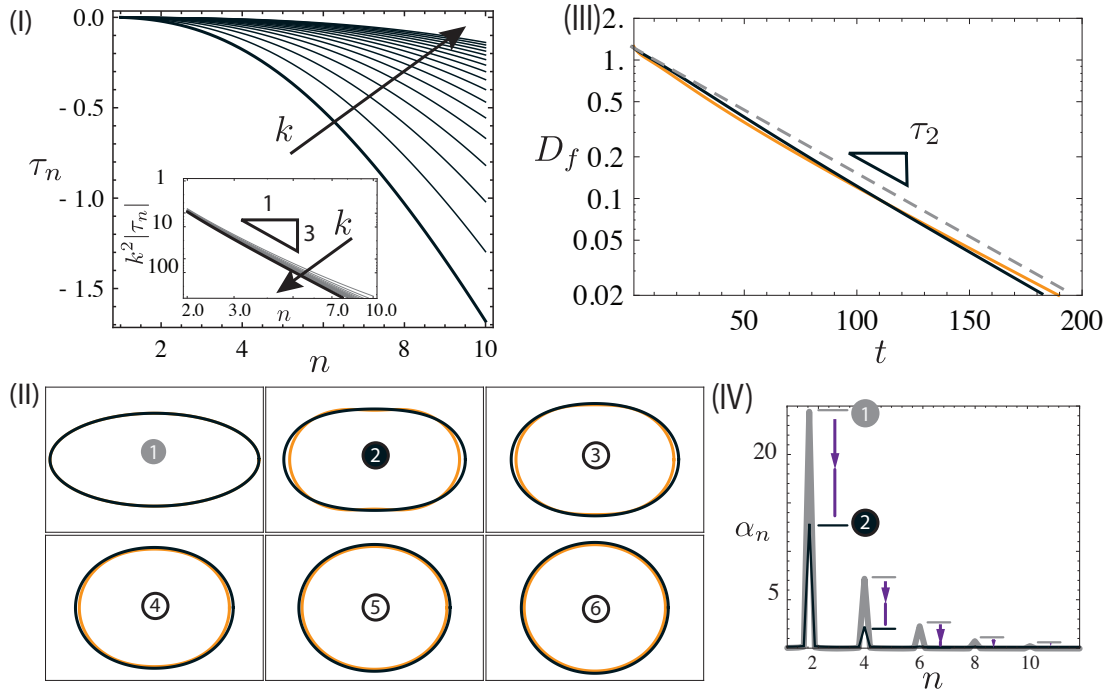


Figure 4.10: **I** Shown is $\tau_n(n)$ for increasing values of k . **II** Superposition of relaxation shapes calculated by BEM (black) and the one obtained with the linear stability analysis (orange). **III** Plot of the deformation D_f respectively shown for the BEM ($k = 4\sqrt{12}$ in black) and the linear stability analysis (orange). In dashed is the result found with one mode only. **IV** FFT of the oscillating part of $\kappa(\theta)$ corresponding to the state denoted (1) (resp. (2)).

through a linear stability analysis that we now briefly outline. A complex stream function Ψ_j is introduced for each fluid $\#j$. In polar coordinates they relate to the speed \mathbf{u}_j through the relation: $\mathbf{u}_j = \frac{1}{r} \frac{\partial \Psi_j}{\partial \theta} \mathbf{e}_r - \frac{\partial \Psi_j}{\partial r} \mathbf{e}_\theta$ and may be expressed in a generic form, see section 4.1,

eq.(4.13) & (4.14):

$$\Psi_1(r, \theta) = \mathbf{i} \left(a_n \frac{I_n(kr)}{I_n(k)} + b_n r^n \right) \exp i n \theta \quad (4.35)$$

$$\Psi_2(r, \theta) = \mathbf{i} \left(c_n \frac{K_n(kr)}{K_n(k)} + d_n r^{-n} \right) \exp i n \theta \quad (4.36)$$

where I_n and K_n respectively denote the n^{th} Bessel I and K functions and a_n, b_n, c_n and d_n are coefficients that are yet to be determined. The earlier expressed 5 boundary conditions (i) to (v) (see section 4.2.1) may be rewritten using these stream functions and form a linear problem:

$$\overline{\overline{M}}(\tau_n) \cdot \mathcal{V} = \mathbf{0} \quad (4.37)$$

where $\mathcal{V} = (a_n, b_n, c_n, d_n, \alpha_n^0)$ and $\overline{\overline{M}}$ may be seen as the impedance of the system. Non trivial solutions are found only if $\det(\overline{\overline{M}}(\tau_n)) = 0$. Shown in Figure 4.10-I is a plot of the corresponding values of τ_n for different values of k in the case of equally viscous fluids. Note that these values are all negative real numbers, thus no instability arises. More importantly is that the higher the mode, the faster its decrease as pointed out by the negative slope of the curves. This will prove to have a large impact on the dynamics of relaxation as explained later. Let us first point out that from the exact solution of (4.37) one may derive the following scaling law: $\tau_n \sim -\frac{n(n^2-1)\pi}{4k^2}$ for large values of k (insert Fig. 4.10-I). Note that this scaling is independent of the viscosity ratio and therefore confirms that the choice of $\mu_1 + \mu_2$ as a viscosity gauge is consistent. It also explains why the earlier proposed scaling $T = \tilde{\tau} \cdot H^2 / R^2$ provided a collapse in Fig 4.8 and 4.9 (since $\tau_n \propto H^2 / R^2$).

The earlier obtained modes τ_n are now used to model the dynamics of relaxation of the ellipse such that $r(\theta, t) = \alpha_0 + \sum_{n \geq 1} \alpha_n^0 \exp(\tau_n t) \cos(n\theta)$. Shown in Figure 4.10-III is the time evolution of the deformation coefficient $D_f(t)$ for this model as well as the one obtained with our BEM for the ellipse **c**. Even for such a reasonably large initial deformation the agreement between the full calculation and the linear model remains acceptable (Figure 4.10-II-III). Note that symmetry is conserved over time while the ellipse relaxes towards a circle. Note also the "volume" conservation is only granted in the linear approximation yielding $\alpha_0 = 1 - \mathcal{O}(e^2)$ for ellipses of area π . Consequently the final shape predicted by the model in Fig. 4.10-II has a radius α_0 slightly smaller than 1.

Differentiating the previous expression for $r(\theta, t)$ one finds that the linearized curvature Fourier modes scale as $(n^2-1)\alpha_n^0 \exp \tau_n t$. Therefore the higher a Fourier mode of the curvature the more it is damped. Shown in Fig. 4.10-IV are the FFT spectra of the oscillating part of the curvature $\kappa(\theta)$ computed at two different times with our BEM and corresponding to the interfaces denoted (1) and (2) in Figure 4.10-II. As suggested by the analysis the highest modes vanish in the time interval between the two shots. Consequently only two low order peaks remain after some time and this type of spectra does not coincide with the one of an ellipse. On the contrary they correspond to a family of ovals that we introduce next.

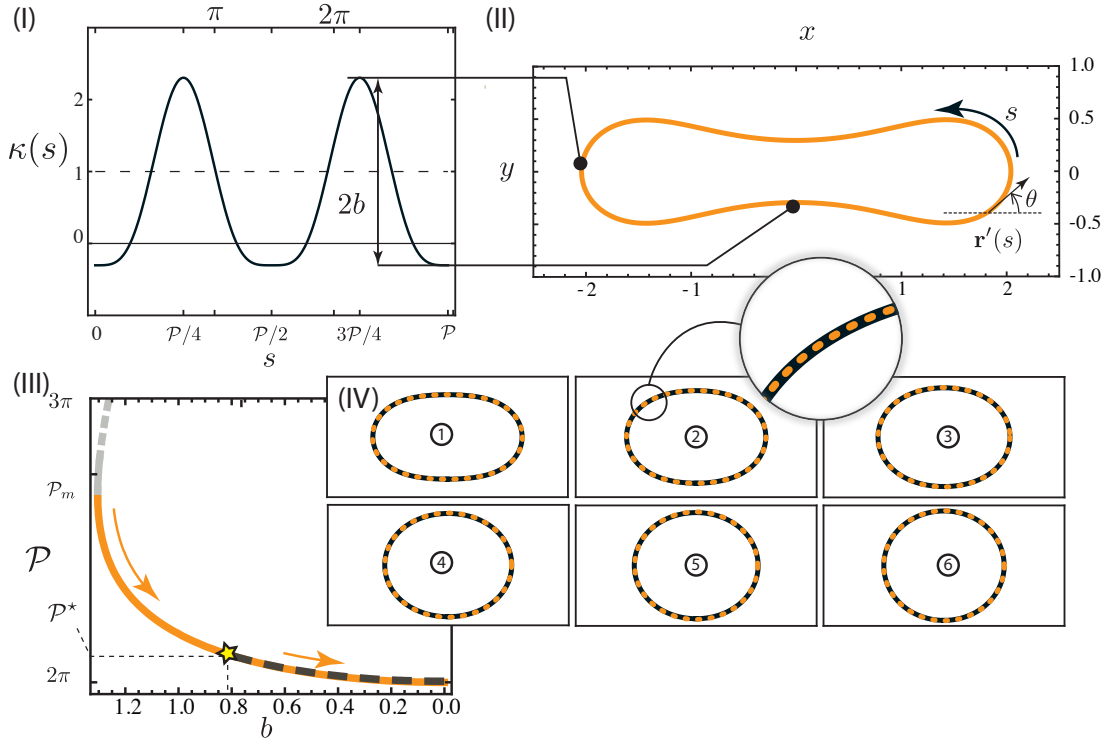


Figure 4.11: **I** Plot of the Ansatz of the curvature in the particular case of the κ_2 oval shown in **II**. **III**: Shown is the relation between the two parameters \mathcal{P} and b that characterize the κ_2 ovals. **IV**. Comparison between the full BEM numerical simulation (black) with the corresponding κ_2 ovals (dotted orange line).

The κ_2 ovals

A geometrical model for the droplet relaxation shapes is developed below using the relation: $\kappa_e + \kappa_s = 2$ (\star). The modeled shapes are coined κ_2 ovals after the equation (\star). They additionally follow some more conventional geometrical constraints, namely:

- (i) the periodicity ensuring a closed interface,
- (ii) the symmetry along both cartesian axes and
- (iii) the conservation of the droplet "volume" \mathcal{A} .

Building upon the linear analysis results and (i) we propose the following Ansatz for the droplet curvature profile: $\kappa(s) = a - b \cos(\frac{4\pi}{\mathcal{P}} s) - c \cos(2\frac{4\pi}{\mathcal{P}} s)$ where \mathcal{P} is the drop perimeter, s the interface arc length, and the minus signs help anticipate the inequality $\kappa_s \leq \kappa_e$. Note that four degrees of freedom (a, b, c and \mathcal{P}) are *a priori* necessary to satisfy the four stated geometrical constraints. Applying (\star) and (ii) leads to $\kappa(s) = \frac{1}{\mathcal{P}} (2\pi - b\mathcal{P} \cos(\frac{4\pi}{\mathcal{P}} s) + (\mathcal{P} - 2\pi) \cos(\frac{8\pi}{\mathcal{P}} s))$ and leaves two parameters in the model, the perimeter \mathcal{P} and b that may be interpreted as a

coefficient of deformation. These two parameters are actually tied together by the remaining constraint (*iii*) that writes $\mathcal{A} = \frac{1}{2} \int xy' - yx' = \pi$ in cartesian coordinates. This relation explicitly depends on the shape of the drop that we integrate with a numerical shooting method solving the system:

$$\left(\frac{d\theta}{ds}, \frac{dx}{ds}, \frac{dy}{ds} \right) = (\kappa(s), \cos\theta(s), \sin\theta(s)) \quad (4.38)$$

$$(\theta(0), x(0), y(0)) = (0, 0, 0) \quad (4.39)$$

where the main unknown is the position of the droplet interface (x, y) reconstructed from θ that tracks the orientation of the tangent to its interface. The unknowns b and \mathcal{P} (both found in the expression of κ) are the shooting parameters. The recovered interface is centered around the origin after integration. A typical result and the corresponding curvature function are displayed in Figure 4.11-I-II. This solution is not unique, there is a 1D family of such ovals that may be represented in the parameters plane (\mathcal{P}, b) . The branch for which the perimeter is an increasing function of the deformation ($\partial\mathcal{P}/\partial b > 0$) is shown in Figure 4.11-III (orange). This curve describes the so called κ_2 ovals family.

These ovals, solely obtained with geometrical considerations, are now compared to the shapes found when solving the full dynamics of relaxation (BEM) for $t > t^*$, that is when the droplets verify $\kappa_e + \kappa_s = 2$. Some of the BEM shapes are shown in Figure 4.11-IV (black) working with the ellipse of initial deformation $D_f = 8$ (denoted **a** in Fig. 4.7). For each BEM shape, the easternmost position of the interface is used to select the corresponding κ_2 oval among the family obtained earlier so that no adjustable parameter is used. This κ_2 oval is plotted for comparison in Figure 4.11-IV (orange) and the agreement is excellent. Consequently, under a certain level of deformation (corresponding to a perimeter \mathcal{P}^* and the time t^*) the droplet continuously explores the κ_2 ovals family while relaxing towards the limiting circle (as shown in Figure 4.11-III). Similar results are obtained when investigating ellipses of different eccentricities that lead to diverse values of \mathcal{P}^* . Since the branch $\mathcal{P}(b)$ has a turning point, the existence of an upper bound for the matching point between the relaxation shapes and the κ_2 ovals is anticipated, yielding $\mathcal{P}^* < \mathcal{P}_m$ where \mathcal{P}_m is the fold point of the solutions family shown in Figure 4.11-III.

We show in the following discussion that these results are not limited to ellipses but extend to broader cases.

4.2.4 Discussion

As explained earlier the occurrence of κ_2 ovals is supported by the fast damping of high order deformation modes that keeps the lower ones afloat. Therefore this type of result may apply to other symmetrical shapes relaxing to a circle. To illustrate this generic aspect we explore a different and ubiquitous type of relaxation: the coalescence of two identical droplets of area

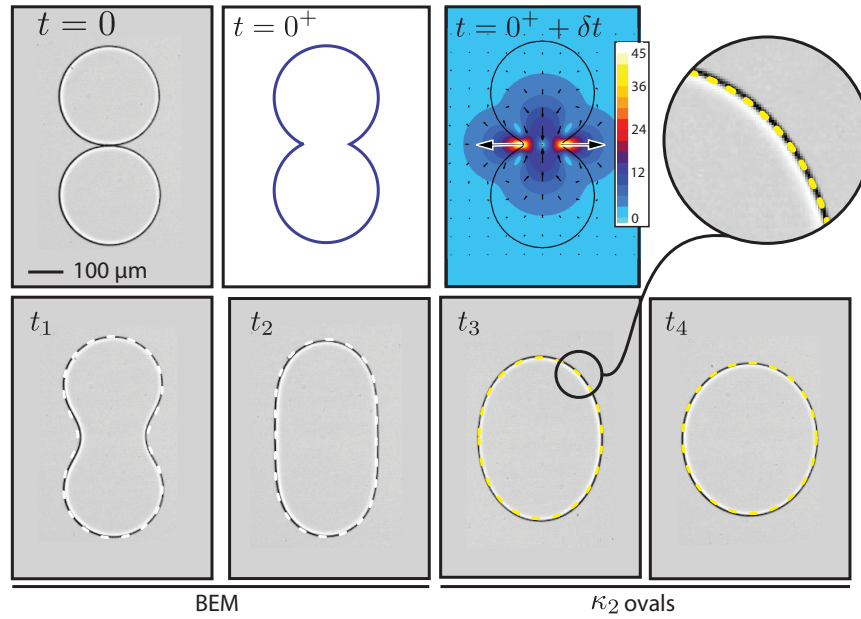


Figure 4.12: Two droplets before coalescence ($t=0$) and the initial configuration used in our numerically investigation ($t=0^+$). Velocity map of the droplet at $t=0^+ + \delta t$. Comparison with experimental pictures, BEM shapes (dashed white) and κ_2 ovals (dashed yellow) at $t = 0.18\text{ms}, 1.57\text{ms}, 7.15\text{ms}, 13.63\text{ms}$

$$\mathcal{A}_i = \pi/2.$$

This coalescence is achieved experimentally in polydimethylsiloxane (PDMS) microchannels fabricated using a silicon wafer that has been etched with soft lithography methods, and then bonded by plasma to a glass slide. Water is used as the external phase and fluorinated oil (FC40) as a dispersed phase. Both liquids are injected via syringe pumps (cetoni Nemesys) into the chip. The micro-channel of height $H = 25\mu\text{m}$ consists of a T-junction followed by a straight channel of width $160\mu\text{m}$. Far from the T-junction the channel width then increases linearly to reach $600\mu\text{m}$ where coalescence by separation is performed (Bremond et al., 2008). A typical sequence observed with a Zeiss AxioVert A.1 microscope coupled to a Miro M310 high speed camera is shown in Figure 4.12.

The early times of coalescence are a 3D-phenomenon, see Eggers et al. (1999); Bremond et al. (2008); Yokota and Okumura (2011), that we do not attempt to solve here. Instead, we consider the configuration at $t = 0^+$ shown in Figure 4.12 as a starting point for our simulations. As inferred from the velocity map in Figure 4.12 only the most curved parts of the interface relax initially (that is κ_e). The dimensionless speed of the interface at these points is about 40 times greater than anywhere else. The droplet relaxes going through a wealth of shapes such as peanut like shape, race-tracks, ovals and ends up circular. These shapes are accurately recovered by our numerical simulations $\kappa_s + \kappa_e = 2$ as seen in Figure 4.12. Remarkably, as soon as the the sum of both curvatures verify $\kappa_s + \kappa_e = 2$ the droplet enters a final stage of relaxation

where both curvatures evolve while satisfying the κ_2 ovals criterion. A comparison between experimental pictures and the κ_2 ovals is provided as an illustration and shows a very good agreement.

Note that the κ_2 ovals, found here after coalescence, are generic. They will appear as soon as an initially symmetrical form relaxes to a circle. Indeed their presence is insured by a faster damping of higher modes of deformations and this is always true for relaxing droplets in a confined environment.

In summary we have considered the relaxation of symmetrically shaped droplets in Hele-Shaw cells and have found a novel generic behavior. In contrast with what classically occurs in 3-D bulk flows, the droplet shapes are attracted by a family of ovals, which verify $\kappa_s + \kappa_e = 2$. These κ_2 ovals are then constructed geometrically and are of valuable help to predict the interface shapes and flows in diverse events such as coalescence.

4.3 Free space droplet migration

Following the exploration of free interfaces in quiescent fluids, we turn to locomotion of droplets driven by different mechanisms, including streaming current, density difference and gradients of surface tension.

4.3.1 Velocity of an advected droplet

Here we establish a link with the calculation of the droplet velocity obtained from singularities in section 2.3.2, when comparing the droplet velocity between undeformable and deformable droplets. In infinitely wide channels we vary the viscosity ratio between $\lambda = 0.2, 2, 4, 9$ and the permeability between $k = 6, 9, 12, 16, 20$, which corresponds roughly to aspect ratios from $R/H = 1.7$ to 5.7 . The numerical method solves for a domain of infinite size with a deformable droplet. Capillary number 10^{-2} ensures that the deformations are little, with variations of curvature κ around 10^{-3} .

Figure 4.13 shows the traveling velocity of a droplet moving in a liquid stream. We plot the speed of the droplet scaled by the background flow against the viscosity ratio λ for different aspect ratios k . A good agreement between the numerical results and the analytical prediction is observed. Note that both approaches use the Brinkman equation as a fluid model. The result seems to be fairly independent of the permeability k .

A numerical analysis can be employed to estimate the influence of lateral walls. As the lateral walls approach a circular droplet the droplet behaves like a piston and approaches the mean in-flow velocity. Figure 4.14 shows the droplet velocity U_d normalized by V_∞ for increasing lateral confinement. Results for two viscosity ratios $\lambda = 0.01, 2$ and aspect ratios $R/H = 2, 6$ are presented. The capillary number $Ca = 0.01$ was kept constant and only small deformations were observed in the most confined cases.

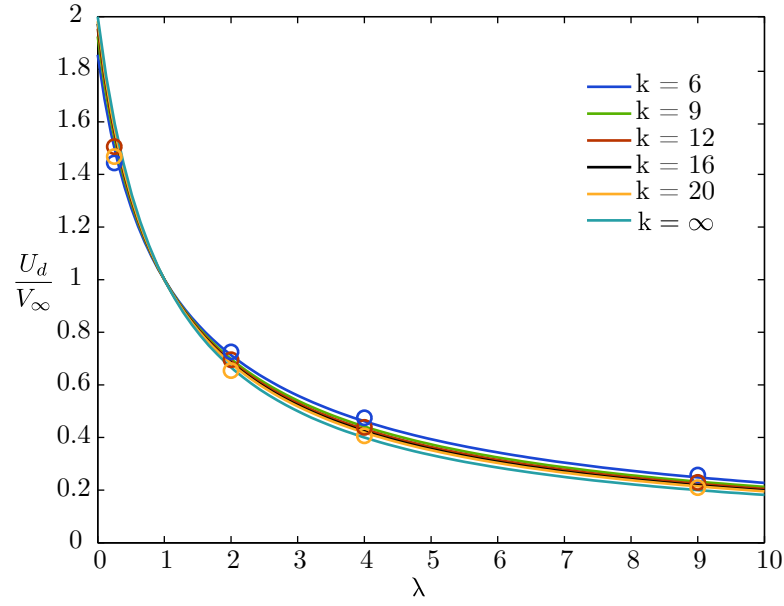


Figure 4.13: Relative traveling velocity of streamed droplets, where circles mark numerical results. The solid lines correspond to the model equation, where cyan represents Darcy's law corresponding to $k = \infty$. Numerical simulations used $Ca = 10^{-2}$.

The channel width W has been reduced from 10 times the droplet diameter down to the diameter. The capillary number $Ca = 10^{-2}$ plays a role in this case because it hinders deformation and reduces leakage past the droplet.

4.3.2 Droplet motion in a rotating frame

In a rotating reference frame centrifugal forces act on the liquid body of two liquids of different density, which are then submitted to an imbalanced surface force driving the denser fluid outwards. Injecting a sample of a denser fluid of density difference $\Delta\rho$, near the center of a microfluidic disc provides thus by simple rotation a driving force that can easily range from milli Pascals to thousands of Pascals.

The force on a liquid sample at a given position S from the center of rotation and angular velocity $\dot{\omega}$ is given by :

$$\tilde{F}_\omega = \Delta\rho S \dot{\omega}^2 A H. \quad (4.40)$$

In the realm of flattened objects the fluid volume is decomposed into an apparent area A and height H .

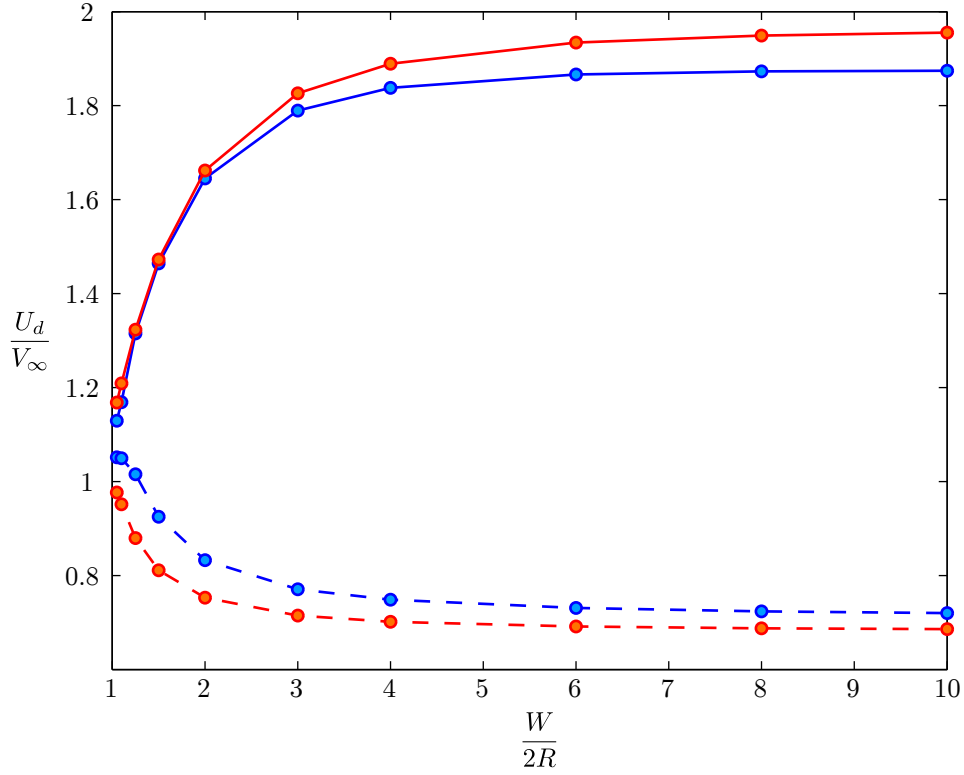


Figure 4.14: Influence of lateral wall confinement. Blue line, aspect ratio $R/H = 2$ and red line $R/H = 6$. Full line viscosity ratio $\lambda = 0.01$ and dashed line $\lambda = 2$.

The non-dimensional force is thus normalized by γL ,

$$F_\omega = \frac{\Delta\rho\dot{\omega}^2 L^3}{\gamma} \mathcal{A} h s = \dot{\Omega} \mathcal{A} h s, \quad (4.41)$$

with $s = S/L$ being the non-dimensional distance from the center of rotation.

Replacing the viscous force in the force balance for undeformable droplets, eq. (2.91) with $v_\infty = 0$, by the centrifugal force supplies an alternative driving moment and leads to the droplet velocity:

$$\begin{aligned} F_{\text{interface}} + F_\omega &= -h\pi k(\chi(u_d) + k(u_d(1 + \lambda))) + \dot{\Omega} \mathcal{A} h s = 0, \\ u_c &= \frac{\dot{\Omega} \mathcal{A} s}{\pi k(\chi + (1 + \lambda)k)}. \end{aligned} \quad (4.42)$$

For a cylindrical droplet of radius $\mathcal{R} = 1$ the area $\mathcal{A} = \pi$. For a numerical example the droplet radius is $R = 100\mu\text{m}$, the density difference $\Delta\rho = 10^{-3}\text{g/mm}^3$, surface tension $\gamma = 16\text{Pa}\cdot\text{m}$ and angular velocity $\dot{\omega} = 30\text{Hz}$. Inserted in eq.(2.7) this results in $\dot{\Omega} = 56.25 \cdot 10^{-6}$. The forcing

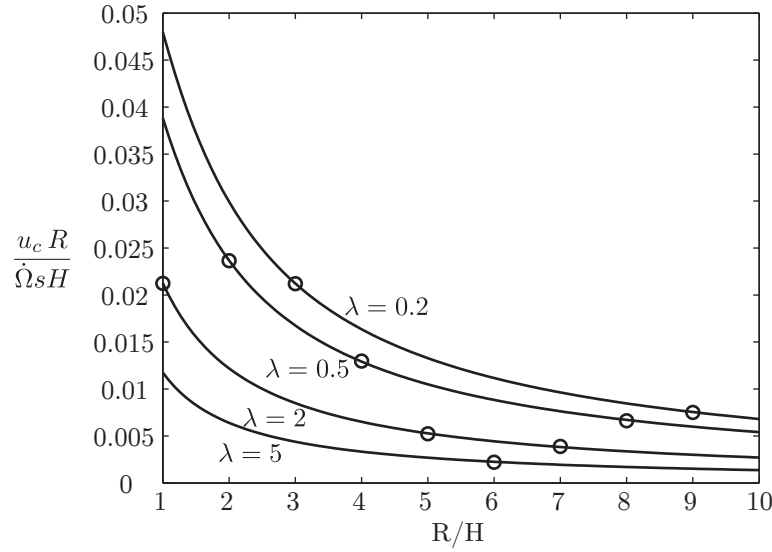


Figure 4.15: Velocities of droplets in a rotating reference frame plotted against aspect ratio R/H for different viscosities λ .

is levered by s . So for a droplet positioned at a distance of 4 cm from the center of rotation, $s = 4\text{ cm}/L = 400$. A theoretical prediction yields a velocity of $u_c = 2.2 \cdot 10^{-5}$.

The velocities are maybe low but they are measured in a capillary scale, where $U = \frac{\gamma}{\mu}$. Having water with surfactant as an external liquid: $U = 16 \frac{\text{Pa}\cdot\text{m}}{\text{Pa}\cdot\text{s}} = 16\text{ m/s}$. For the example, the resulting dimensional velocity is about $U_c = 0.35\text{ mm/s}$.

The theoretical prediction of the droplet velocity is shown in figure 4.15. A simulation using the pressure boundary condition for a moving frame of reference in eq. (2.40) demonstrates agreement between the two approaches. The aspect ratio was varied between $R/H = 1 \dots 10$ and four viscosity ratios were applied $\lambda = 0.2, 0.5, 2, 5$. The resulting velocity is rescaled by $\dot{\Omega} s$ because of the linear dependence of the forcing, and by R/H to help the reader distinguish results at elevated R/H .

Low aspect ratio and low viscosity lead to higher droplet velocities. Centrifugal transport has the particularity that the body force increases as the droplet travels away from the center.

4.3.3 Droplet in a surface tension gradient

Manipulating droplets in closed microchannels is a challenge and a compromise is to be found that allows for the desired interaction by maintaining a channel design that is easy to reproduce. A nonintrusive way of interaction is provided by focussed laser heating. Baroud et al. (2007) developed an optical toolbox that was able to drive, block and merge droplets in microchannels.

Chapter 4. Liquid interface evolution in theory and experiment

In this study a droplet in a fluid with a fixed temperature gradient is simulated, similar to the droplet under Marangoni stresses in the convergence study and illustrated in figure 3.2. Changing the boundary conditions to that of a deformable droplet with a free interface the droplet moves in the direction of the lower interfacial tension, because the droplet tends to minimize its interface energy $E_\gamma = A \cdot \gamma$.

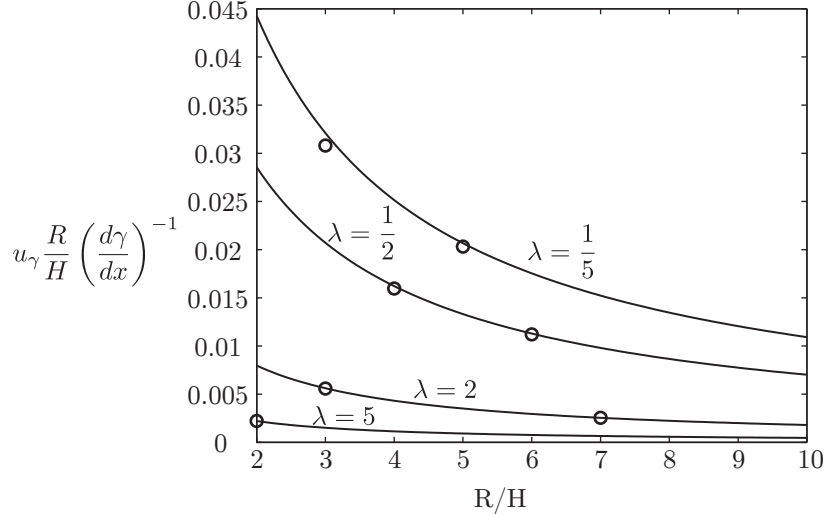


Figure 4.16: Droplet velocity in field of linear surface tension distribution. The analytical solution given eq.(4.43) is shown by solid lines and numerical data is presented by circles.

The velocity of a droplet in a infinitely wide Hele-Shaw cell was derived by Gallaire et al. (2014) using the Brinkman equation.

$$u_\gamma = \frac{2K_1(k)I_2(k)\frac{d\gamma}{dx}k\frac{1+\lambda}{k(1+\lambda)^2+4\lambda}}{I_2(k)(2kK_0(k)+k^2K_1(k))+\lambda K_0(k)(k^2I_1(k)-2kI_2(k))}. \quad (4.43)$$

The solution depends on the aspect ratio, represented by the permeability k , the viscosity ratio λ and the surface tension gradient $\frac{d\gamma}{dx}$. The velocity scale is $U = \gamma_{\text{ref}}/\mu$ and the length scale L is given by droplet radius R .

For a numerical computation the droplet is discretized with 400 elements and the time step $\Delta t = 0.1$ is chosen. For the surface tension gradient $d\gamma/dx = -1/10$ is picked to compare to the theory. The theory considers a flat interface in the thin direction, so Laplace law becomes:

$$[[\mathbf{f}]] = \frac{1-x}{10}\kappa_{\parallel}\mathbf{n} - \frac{1}{10}t_x\mathbf{t}. \quad (4.44)$$

Comparison between the analytical solution in eq.(4.43) and numerical data in figure 4.16 shows good agreement. We observe that the droplet shape remained circular even when the surface tension gradient was raised to 1/2, which leads to the conclusion that droplets in wide channels may not deform under Marangoni stresses, unless the gradient is much higher.

4.4. Droplet deformation driven by the channel geometry

Higher gradients can only be generated locally, because the surface tension is never negative.

The boundary condition in eq. (4.43) that was used in to derive the Marangoni effect driven droplet velocity (Gallaire et al., 2014) did not use the out-of-plane curvature but only the contribution due to recirculation on the interface. A change in surface tension induces also a force on the droplet, which is due to the normal stress pressure jump. Because of the high perpendicular curvature over the channel height, this contribution is dominant for large aspect ratios.

4.4 Droplet deformation driven by the channel geometry

Previous sections have studied the motion of droplets in the absence of walls, e.g. in one of the preceding section droplet relaxation was investigated in an infinite Hele-Shaw cell. Experimentally the initial deformation has been obtained by coalescence of two droplets. In this section we investigate the deformation of droplets due to the channel geometry, where we march numerically in the foot steps of two different experimental studies. At first we consider the deformation in a wide cross channel, investigated by Ulloa et al. (2014) and then a linear setup of multiple serial deformations, investigated by Brosseau et al. (2014).

4.4.1 Viscous droplet stretching in cross flow

Recently Ulloa et al. (2014) experimentally studied droplet deformation in diverging flow, shown in figure 4.17. Their set-up is a microfluidic cross-junction with fluid injected from two opposite sides, where the fluid leaves the junction in two channels, oriented 90° to the inlet channels.

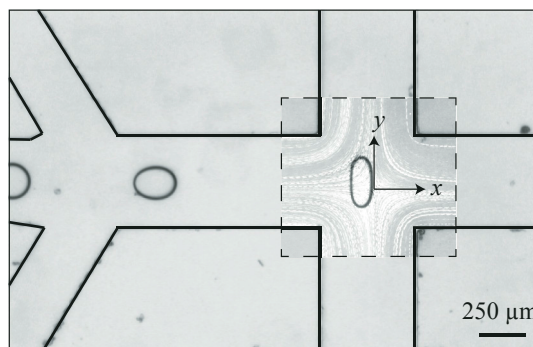


Figure 4.17: Photo of the microchannel geometry taken from (Ulloa et al., 2014). The droplet is stretched in the cross junction by fluid coming from the left and right side and leaving to the upper and lower side.

From left inlet channels droplets enter the junction and get advected to the center of the junction, a stagnation point, and stretched by the flow. This stagnation point is a saddle point and due to imperfect alignment and the unstable nature of the equilibrium position the droplet

gets streamed away after some time. Before getting streamed away the droplets have deformed in the flow field to an equilibrium shape. Ulloa *et al.* characterized the deformation D by the difference in major and minor axis length a and b , normalized by their sum, $D = (a - b)/(a + b)$. They investigated the influence of channel geometry, shear rate and droplet radius on the deformation.

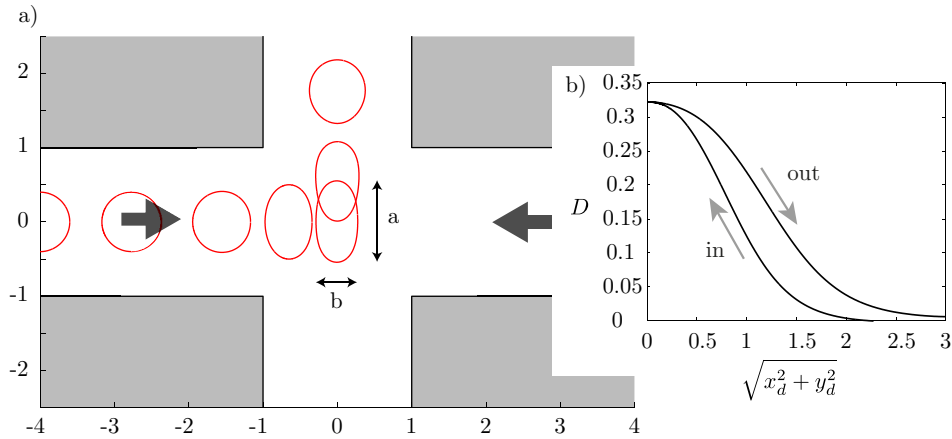


Figure 4.18: Multiple snapshots of a droplet that enters a junction from the left. Gray arrows indicate the incoming flow. Capillary number $Ca = 0.048$, channel width $W/H = 7.5$ and droplet radius $2R/W = 0.4$. The inset b) shows droplet deformation, plotted against the distance between droplet center and the center of the junction.

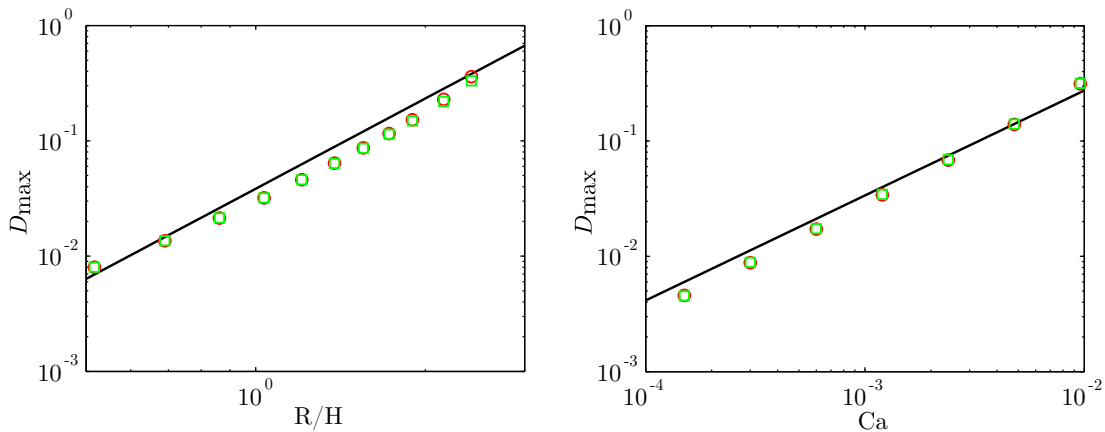


Figure 4.19: Maximum deformation D_{\max} against a) droplet aspect ratio R/H at capillary number $Ca = 0.0126$ and channel aspect ratio $W/H = 6.9$ and b) against capillary number Ca for droplet aspect ratio $R/H = 1.5$ and channel aspect ratio $W/H = 7.5$. The black line is the trend extracted from the experimental data, circles (red) correspond to simulation in cross-junction and squares (green) to hyperbolic flow that stretches to infinity.

Choosing a length scale $L = W/2$, a junction of width 2 and extending from -6 to 6 in the x -direction and -4 to 4 in the y -direction is simulated. For illustrative purposes figure 4.18

4.4. Droplet deformation driven by the channel geometry

shows a simulation with one droplet at several instances. One sees the droplet coming from the left, stretching in the center and leaving the junction on the top. A maximum deformation of $D = 0.323$ is reached at the center as shown in the inset.

In figure 4.19 we compare the scaling of maximum deformation D_{\max} with droplet radius normalized by the channel height R/H in a channel of width $W/H = 6.9$, at constant capillary number $Ca = 0.0252$. Furthermore we compare to the shear rate G that has been non-dimensionalized by the viscosity, surface tension and channel width $Ca = \frac{\mu_c GW}{\gamma_{\text{ref}}}$ in a Channel of $W/H = 7.5$. Numerical simulation shows a dependence in $R/H^{2.57}$ and in $Ca^{1.01}$. Experimentally Ulloa *et al.* found $D \propto (R/H)^{2.59} Ca^{0.91}$. The graphs are shown in figure 4.19. The viscosity ratio of inner fluid to outer fluid is $\lambda = 0.008$ in all their experiments as well as in our simulations.

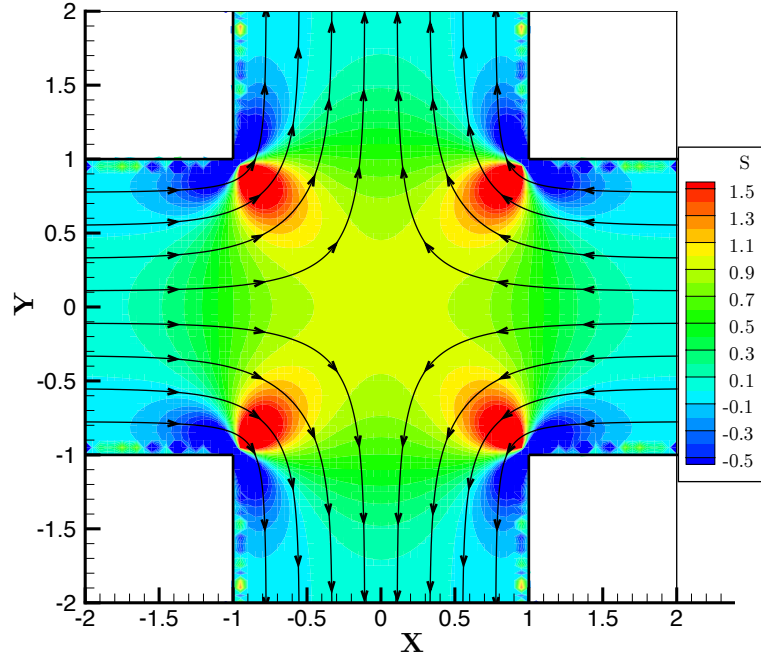


Figure 4.20: The strain in the cross section is plotted. At the center of the cross section the strain is about 0.92.

Ulloa *et al.* provide a simplified calculation of a droplet in an infinite extensional flow to underline the scalings found in the experiments. The scaling law in free space can be reasoned to be based on the surface tension and curvature balancing a pressure field. In the Hele-Shaw limit the pressure gradient scales like: $\frac{p}{R} \propto \frac{\mu U}{H^2}$. At the interface the pressure differences is given by Laplace law and so surface tension and curvature scale like: $p \propto \gamma/R$. Substituting the pressure leads to a non-dimensional term: $\frac{\mu U}{\gamma} \frac{R^2}{H^2}$, substituting $U = GR$, establishes a characteristic non-dimensional relation in $D \propto GR^3$.

When simulating the droplet stretching in an infinite flow field, it can be shown that the cross-

junction provides a suitable hyperbolic flow. Undisturbed from the droplet the velocity field is $\mathbf{u} = Ca^* \begin{pmatrix} -x \\ y \end{pmatrix}$. In order to determine the free space capillary number Ca^* that corresponds to the confined capillary number Ca we simulate a confined single-phase flow with mean inflow velocity $Ca = 1$ in a cross junction and extract the mean strain $S = -\frac{1}{2}(\frac{\partial u}{\partial x} - \frac{\partial v}{\partial y})$, which remains approximately constant in a region close to the center, $S = 0.907$ for $W/H = 7.5$ and $S = 0.913$ for $W/H = 6.9$. In the case of free space flow the strain $S = 1$ for $Ca^* = 1$ and we therefore set the free space capillary number $Ca^* = 0.91Ca$ for a given Ca . Running the same simulations as before in the absence of walls the same scaling laws are reproduced. Therefore using the corrected capillary numbers reproduces almost the same results as in the presence of walls, supporting the hypothesis that the channel does indeed provide a region of constant strain.

4.4.2 Viscous droplet stretching in expanding-contracting flow

The idea of a microfluidic tensiometer was brought up by Cabral and Hudson (2006), who proposed to measure the surface tension by the observation of a droplet in an extensional flow in a micro channel.

In a recent work Brosseau et al. (2014) extended this idea in order to investigate the influence and absorption of surfactants. Influence of surfactants in dynamic systems is difficult to determine experimentally and microfluidics might help to investigate characteristics that are inaccessible by established means. When surfactants are absorbed on the fluid interface they change the surface tension and introduce surface tension gradients. Modeling surfactants in numerical simulations is a formidable task and the flow solver we developed is able to simulate deformable interfaces and surface tension gradients, while being computationally inexpensive as to run many simulations in order to fit surfactant models to experiments aiming at reverse engineering.

The length scale $L = 100\mu m$, viscosity ratio is $\lambda = 0.8$ and channel aspect ratio $W/H = 1$, as in the experiments. Figure 4.21 shows that the numerical method is able to simulate the deformation of droplets and retrieve a behavior close to those observed in the experiments. Illustration of the extensional flow together with the resulting deformation for $Ca = 0.1$ and $Ca = 0.01$ and radius $R/W = 0.55$ is shown in figure 4.21 b) and c). At capillary number $Ca = 0.1$ the droplet is more stretched in the small channel, till $x = 0$ and then also expands much wider than the droplet at $Ca = 0.01$. In figure d) one can see this behavior in the deformation curve, where the initial deformation is negative, which corresponds to elongation. At $x = 0$ the flow expands and shortly after the droplets reach their maximum deformation.

It shall be stressed that although the channel aspect ratio $W/H = 1$ is not in the regime of flat micro channels we recover a scaling law for $D_{\max} \propto Ca^{0.6}$ for droplets of aspect ratio $R/W = 0.5...0.55$, where the experiments showed $D_{\max} \propto Ca^{2/3}$. These results are shown in figure 4.21 e). Our numerical results overestimate the deformation by about 30%. A droplet with a slightly higher aspect ratio $R/W = 0.6$ showed a dependence of the maximum deformation on Ca as $D_{\max} \propto Ca^{0.5}$. Three-dimensional effects like gutter formation in the corners between

4.4. Droplet deformation driven by the channel geometry

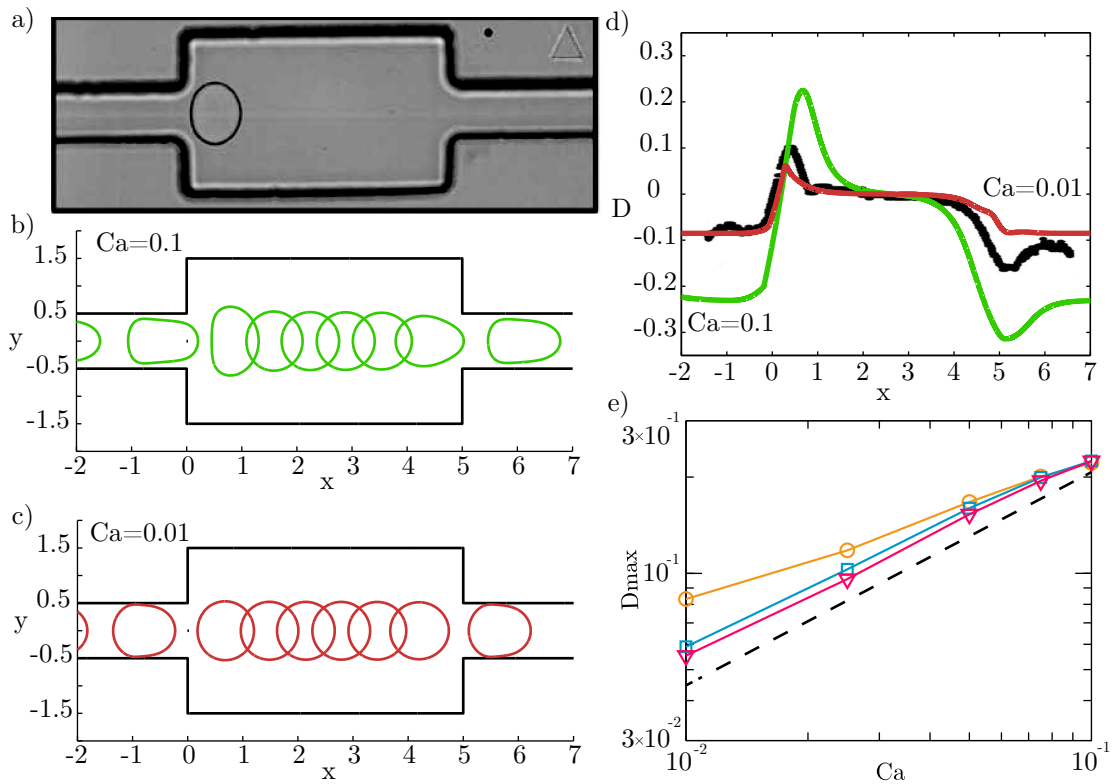


Figure 4.21: a) Photo of a droplet entering in a wide channel, taken from (Brosseau et al., 2014). b) Droplet stretching at capillary number $Ca = 0.1$ and c) at $Ca = 0.01$. Droplet contour at several moments in time are plotted. The graph d) shows the evolution of the deformation at different positions of the droplet. Black dots, Experimental data from Brosseau *et al.* for $Ca = 0.037$. In figure e) the maximum deformation is plotted for different aspect ratios R/W , ∇ 0.5, \square 0.55 and \circ 0.6. Experimental results by Brosseau *et al.* for $R/W = 0.5$ are drawn by a dashed line.

lateral and top/bottom walls, might explain the difference between our numerical model and experiments.

Summary

The variety of problems that have been studied in this chapter demonstrated the versatility of the implemented boundary element method and validated the physical significance of the method. The interface dynamics in the absence of an outer flow field were studied in sections 4.1 and 4.2.

The relevance of the Brinkman equation was highlighted by a study of the Saffman-Taylor instability, where an infinitely small perturbations of the interface showed to evolve differently when solving Darcy's law or the Brinkman equation. Since the Brinkman equation was intro-

Chapter 4. Liquid interface evolution in theory and experiment

duced for confined two-phase flow in the presence of surface tension gradients it is important to mark that improvement is also made by the Brinkman equation when considering constant surface tension. Some of the methods of the linear stability analysis were then transposed to study the relaxation of droplets, which showed fast relaxation towards an attractor that has a constant sum of maximum and minimum curvature.

In section 4.3 different microfluidic displacement techniques were simulated and the results agreed well with the analytical results. Section 4.4 introduced confinement by lateral walls, where deformation is observed. The simulations reproduce in detail different experiments although the aspect ratio R/H is only between 1/2 and 2 and therefore far from the highly confined state the was initially used to depth-average the equations. Hence apart from being versatile and computationally inexpensive the method also shows robustness.

Modified theory and 3D influences **Part II**

In the previous part of the thesis the basics of a fluid dynamic description was laid out, the restriction to two-dimensional flow was motivated and the feasibility to model confined channel flow was shown. Furthermore the boundary element method was presented, which allows to solve for two-phase phenomena of arbitrary interface shape by solving discretized equations on a line.

In this part of the thesis a more critical look shall be undertaken in order to point out what inherently three-dimensional effects occur in two-phase flows and if solutions to overcome possible insufficiencies can be found.

In the following three chapters model boundary conditions for 3D interface phenomena are developed and applied in comparative studies to experiments. Revisiting dynamic film formation in chapter 5 investigates the effect of a moving meniscus on its curvature. The effect of dynamic film formation is the answer to one important question: What is the velocity of droplets in a Hele-Shaw cell? In previous chapters the droplet velocity was addressed but failed the observed velocity in experiments. Since no data in the regime of interest are found in the literature the droplet velocity in wide channels is investigated experimentally. This is explained in section 5.3 and compared to the velocities obtained by model droplets with dynamic meniscus formation.

A model boundary condition is proposed in chapter 6 that takes into account geometric features in microchannels, which extend in the perpendicular direction and violate the assumption that channels have a constant height. A detailed study on anchoring and deformation of droplets on anchors and rails is undertaken in section 6.1 to 6.3, followed by an example for droplet formation in channels with linearly changing confinement in section 6.4.

A departure from the topic of liquid interfaces is made in chapter 7, where the transport of rigid objects in microchannels is investigated. For rigid discs and fibers there was need to investigate the flow behavior in the vertical direction, out of the flow plane, in order to be physically meaningful.

5 Dynamic Film formation

Dynamic film formation is closely related to coating or lubrication problems. Coating films are formed when a liquid body is entrained under the shear motion of a solid boundary. In the case of a droplet motion the movement of the wall, relative to the droplet, entrains liquid from the surrounding carrier fluid into a gap between the droplet interface and the top/bottom walls.

In the next section the classical results by Bretherton are numerically reproduced in 2D Stokes flow. These results assume flow around a bubble at constant pressure. This motivates to simulate the effect of film formation on droplets with a finite viscosity ratio. In section 5.2 a model is devised that treats the thin films, which are no longer resolved but modelled. In section 5.3 the velocity of model droplets is then compared to droplet velocities measured in experiments.

5.1 Origin of dynamic film formation

In order to appreciate the role of dynamic films, figure 5.1 depicts the assumptions from previous chapters where the velocity profile is parabolic and the interface spans from the bottom to the top. This configuration displays a paradox: if the interface is displaced with a parabolic velocity profile, its shape turns into a stretched parabola and it does not stay flat.

The cure to that incompatibility comes from surface tension, when the capillary number is low the surface withstands deformation. In that case the velocity of the interface remains zero because the interface at the walls has still a no-slip velocity constraint.

In reality the solution is a compromise, the resistance of the interface leads to a zone of high shear near the channel wall, where viscous forces equal surface tension forces. This happens in a thin layer on the boundary, similar to boundary layers in high Reynolds number fluid dynamics, where viscosity competes with inertia. In fact the situation of an interface sticking to a wall with an incoming Poiseuille flow was simulated in section 3.2.2 when wall bounded interfaces were presented.

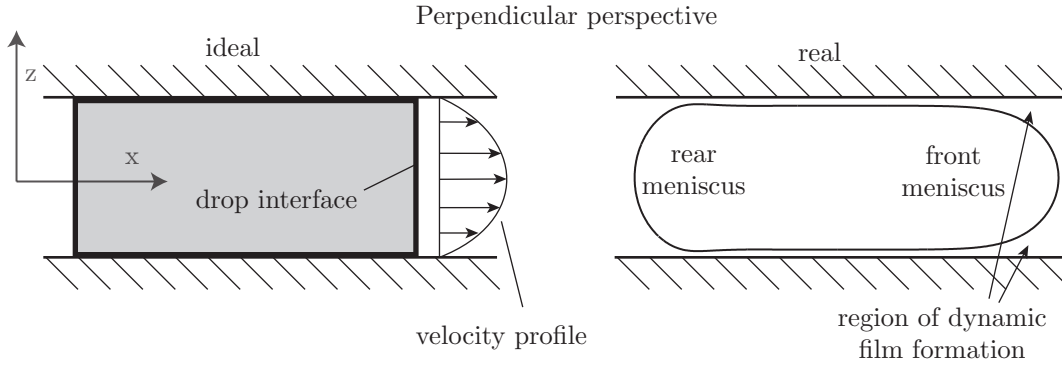


Figure 5.1: Left: A droplet and the velocity profile based on the assumptions drawn in chapter 2. The droplet interface is incompatible with the velocity profile. Right: A droplet interface for $Ca = 0.025$, deformed under the shear stresses on the interface.

5.1.1 Revisiting Bretherton's law in 2D

The solution to this capillary boundary layer was worked out by Landau and Levich in the 40's in the USSR for coating problems and was later applied by Bretherton (1961) to film formation on a rising bubble in a cylindrical tube.

A comprehensive explanation and derivation is found in chapter 9.3 of the book *Physicochemical Hydrodynamics* by Probstein (1989). The solution is obtained by matched asymptotics, where a small region of balanced viscous and capillary terms is matched to a static meniscus.

The thickness b_f of the thin films between droplet and wall is asymptotically constant far from the menisci and was obtained as:

$$b_f = 0.643 \frac{h}{2} (3\mu U_d / \gamma)^{2/3} = 0.669 h C a_d^{2/3}. \quad (5.1)$$

The film thickness b_f depends on the $2/3$ power of the capillary number.

Bretherton furthermore determines the changes of the pressure jump over the leading and receding meniscus, which comes from the curvature that increase or decreases, respectively, in the dynamic film formation region. The curvatures are asymptotically given according to Bretherton for a bubble to be:

$$\kappa_f = \frac{2}{h} (1 + 3.80 C a^{2/3}) \quad \text{and} \quad \kappa_r = \frac{2}{h} (1 - 1.13 C a^{2/3}). \quad (5.2)$$

For flattened bubbles the same results have been derived by Park and Homsy (1984) in a more rigorous way, including also the leading order effects of the in-plane curvature. Also Burgess and Foster (1990) have reached the same conclusions, using no more than 7 asymptotic regions.

Improvements to the theory have been proposed by Taylor (1961), Reinelt (1987) and Aussillous and Quere (2000) for an increased capillary number. For finite viscosity ratios, $\lambda > 0$, Hodges

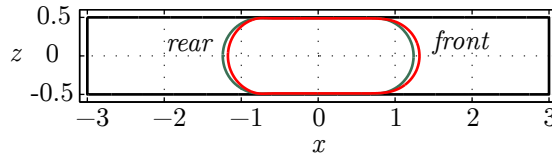


Figure 5.2: Domain for simulation of dynamic films, shown are droplet at initial position (green) and final position (red) for $Ca = 0.0025$ and $\lambda = 0.1$.

et al. (2004) developed a multi-zone asymptotic solution of the film thickness but no indication of the influence on the curvature are given. Since droplet microfluidics operates with fluids of finite viscosity ratio an extension of the Bretherton law is needed. With a solver for free interface flows at hand we will use the boundary element method to solve the 2D Stokes equation for dynamic films.

The boundary element method described in chapter 3 solves the Brinkman equation when integrating over the Green's function of the Brinkman equation. In the following we use the Green's function of the 2D Stokes equation, given in Pozrikidis (1992) or appendix A.4, with the objective to solve in the out-of-plane direction for an infinitely wide droplet. Therefore in the remaining part of this section we consider the x, z plane with a droplet slice. Since the droplet is now in a configuration where $H_y \gg L_z$, 2D Stokes is indeed appropriate.

The boundary condition on the liquid interface is now:

$$[[\mathbf{f}]] = \kappa_{\perp}. \quad (5.3)$$

Where \perp stands from the x, z plane in contrast to the x, y plane denoted by \parallel . The discontinuity of interface stresses is equal to the curvature in the x, z plane.

The wall boundaries shown in figure 5.2 have been discretized with 3000 elements and the droplet with 1000 elements. A time step of $\Delta t = 0.25$ was chosen and the simulation ran till the results converged. Interface evolution in time for an example at $Ca = 0.0025$ and $\lambda = 0.1$ is shown in figure 5.3. A close-up near the wall of the interface and the evolution of the curvature is shown. A film thickness of 0.0118 is obtained and a front and rear meniscus curvature of $\kappa = 2.145$ and 1.953 respectively.

Bretherton's matched asymptotic solution describes the interface close to the wall by an exponential function for the front meniscus and by an exponential with an oscillating contribution for the receding meniscus, which can be observed in the simulations.

In practice the viscosity of the droplet is not always much smaller than that of the carrier fluid. Although the dissipation takes place in a thin region with high velocity gradients it is not certain whether a droplet of superior viscosity exhibits the same scaling law as predicted by Bretherton.

Performing the simulation for $\lambda = 0.1$, varying the capillary number $Ca = 2.5 \cdot 10^{-4} \dots 10^{-1}$

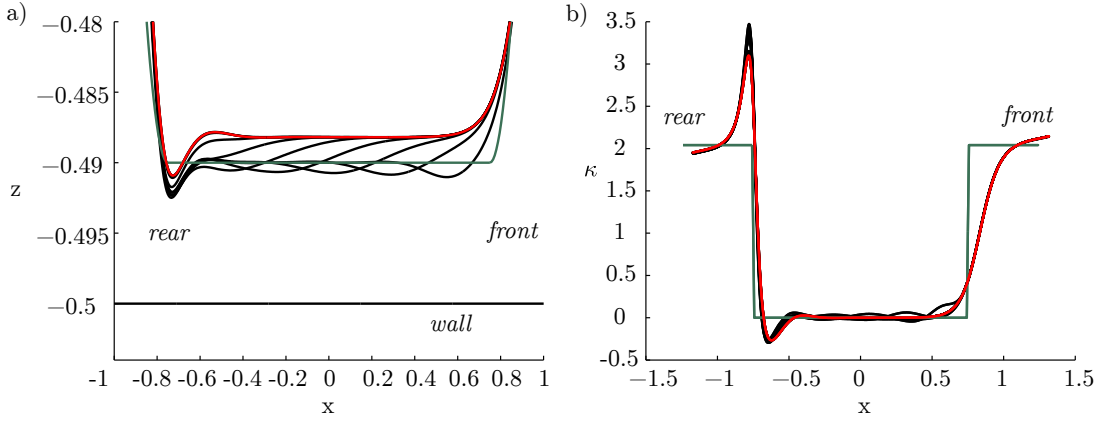


Figure 5.3: Evolution of the droplet interface with $Ca = 0.0025$ and $\lambda = 0.1$ showing increments in time $\Delta t = 10$. The droplet is moving from left to right but is recentered in x . Droplet at initial position (green) and final position (red). a) Zoom into film region; b) Plot of curvature κ against position x .

and for $\lambda = 10$, varying the capillary number $Ca = 10^{-3} \dots 2.5 \cdot 10^{-2}$ reveals the classical $Ca^{2/3}$ dependence for the curvatures for both viscosity ratios, $\lambda = 0.1$ and $\lambda = 10$. In fact the validity of the $2/3$ exponent was shown to apply for the film thickness for finite viscosity ratios (Hodges et al., 2004). Using this data one fits model parameters of a Bretherton model:

$$b_f = m h Ca^\alpha, \quad \kappa_f = \frac{2}{h}(1 + k_f Ca^\beta) \quad \text{and} \quad \kappa_r = \frac{2}{h}(1 - k_r Ca^\gamma). \quad (5.4)$$

For Bretherton's law $\alpha = \beta = \gamma = 2/3$, $m = 0.669$, $k_f = 3.80$ and $k_r = 1.13$. From the numerical solution with $\lambda = 0.1$ one obtains: $\alpha = 0.65$, $\beta = 0.66$, $\gamma = 0.65$, $m = 0.58$, $k_f = 3.71$ and $k_r = 1.13$. While for $\lambda = 10$ one gets: $\alpha = 0.64$, $\beta = 0.65$, $\gamma = 0.58$, $m = 0.61$, $k_f = 4.42$ and $k_r = 1.16$. These results are shown in figure 5.4. For $\lambda = 0.1$, they confirm the suitability of the BEM implementation to solve the 2D free interface Stokes equation and to describe such lubricating flows, even at low Ca . The results at $\lambda = 10$ show that Bretherton's scaling remains a reasonably accurate approximation of viscous droplets.

At fixed capillary number $Ca = 10^{-3}$ the viscosity ratios between $\lambda = 0.02$ and 10 are investigated. The results plotted in figure 5.5 show that the film thickness increases only slightly, whereas the front meniscus curvature increases, κ_f changing from 2.076 to 2.097 and the rear meniscus curvature decreases, κ_r going from 1.975 to 1.959. Also shown is the change of parameters k_f and k_r with λ , assuming a $Ca^{2/3}$ dependence,

$$k_f = \frac{\kappa_f/2 - 1}{0.001^{2/3}}, \quad k_r = \frac{1 - \kappa_r/2}{0.001^{2/3}}. \quad (5.5)$$

For viscosity ratios below $\lambda = 0.5$ the parameters k_f, k_r remain unaffected but increase steadily for higher viscosity ratios. A refined fitting procedure to a more complete numerical data-set

5.2. Dynamic meniscus boundary condition

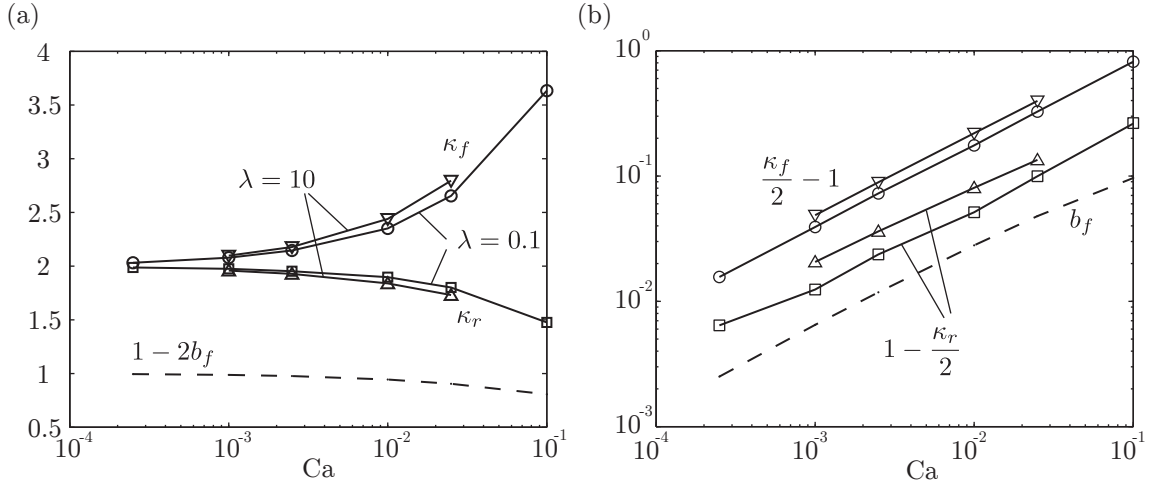


Figure 5.4: (a) Changes in the curvature for the advancing meniscus κ_f and the receding meniscus κ_r for two viscosity ratios, $\lambda = 0.1$ and $\lambda = 10$. Also shown the normalized droplet height, being channel height 1 minus twice the film thickness b_f . (b) Plotting the deviation from the equilibrium curvature at rest and film thickness against the capillary number.

could provide a dynamic meniscus model for droplets with arbitrary inner viscosity. For the purpose of this thesis only data for $Ca = 10^{-3}$ is tabulated in table 5.1. A viscosity ratio of $\lambda = 4$ will be needed to compare to experiments, which are conducted with fluorinated oil droplets in water.

λ	0.5	1.0	2.0	4.0	10.0
k_f	3.97	4.08	4.27	4.61	4.87
k_r	1.30	1.42	1.75	1.93	2.06

Table 5.1: Dynamic meniscus parameters as a function of viscosity ratio λ , assuming a $Ca^{2/3}$ dependence.

As can be seen in the table the coefficient for k_f for $\lambda = 10$ is higher than 4.42, which was obtained when fitting the data of constant viscosity ratio λ and varying capillary number. Small deviations of the exponent (here 0.65 instead of 0.66) induce sensible variations of the prefactors when the scaling laws are used in a wide range of capillary numbers.

5.2 Dynamic meniscus boundary condition

For a simulation that includes the presence of a dynamic meniscus and still remains in a 2D depth-average perspective, one needs to incorporate the film formation as a lumped parameter model, where the out-of-plane curvature at every point on the interface depends on the local capillary number. This model is based on the assumption that what takes place in the flow plane is happening on a length scale that is much bigger than the gap width, allowing the decoupling of the perpendicular and parallel planes.

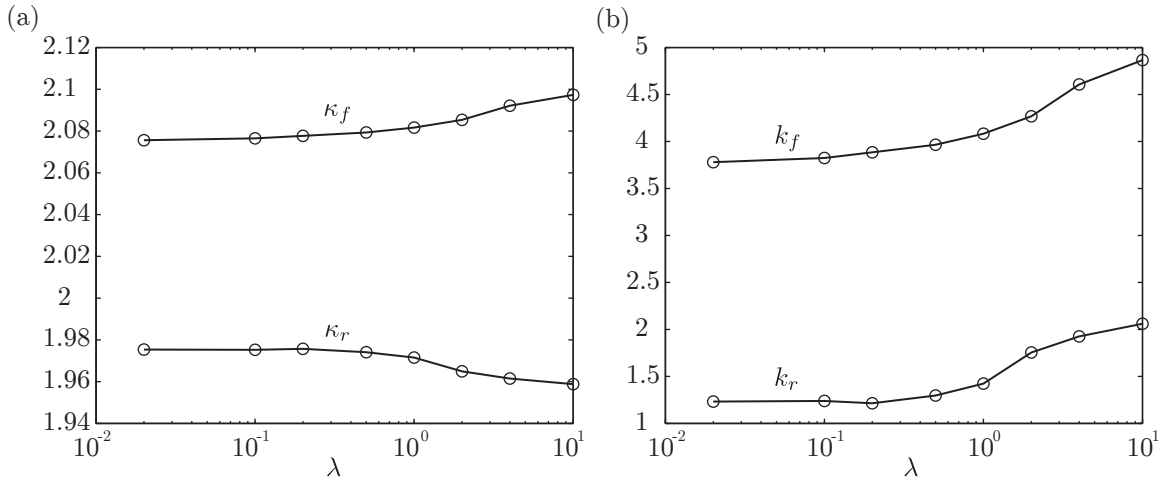


Figure 5.5: (a) Dependence of the curvature on the viscosity ratio λ . (b) Variation of dynamic film parameters k_f and k_r for changing viscosity ratio.

When experimental studies showed that the bubble velocity in a Hele-Shaw cell did not agree with the Darcy theory (Kopf-Sill and Homay, 1988) there were efforts to correct the transport equations by corrections on the boundary conditions. Numerical simulation by Meiburg (1989) determined velocities for very large aspect ratios. Quantitative agreement was rather poor and research began to focus on bubble shapes instead (Saffman and Tanveer, 1989). An asymptotic approach using different boundary layers to all sides of a bubble was pursued by Burgess and Foster (1990) but did not allow for comparison with experiments.

The lumped parameter model for now consists only of eq.(5.2). The height of the films becomes negligible for $Ca \ll 1$. In contrast the influence of the dynamic meniscus on the curvature increases with decreasing capillary number, which follows from eq.(2.6) because the pressure scales like Ca^{-1} . Hence a contribution of $Ca^{2/3}$ to the curvature affects the pressure like $Ca^{-1/3}$.

In the following section the lumped parameter model is first applied to the flow of an undeformable droplet, analyzed in the absence of lubricating film formation in section 2.3. It shall be noticed that this has important implications on the terminal velocity in a wide channel.

Thereafter the lumped parameter model is used in the boundary element algorithm for deformable droplets that was described in section 3.

5.2.1 Dynamic film formation for undeformable droplets

In order to determine the terminal velocity of an undeformable droplet only viscosity ratio λ and aspect ratio R/H appeared as parameters. Because the transverse curvature was assumed constant everywhere, all terms involving the capillary effects were found to be zero.

5.2. Dynamic meniscus boundary condition

An evaluation of the out-of-plane curvature in Laplace law in eq.(2.41) with the effect of a dynamic meniscus reveals that the resistance increases. The normal stress correction is written as follows:

$$[[\mathbf{f}]] = Ca^{-1} \left(\frac{\pi}{4} + \frac{k}{\sqrt{3}} (1 + \beta Ca_d^{2/3}) \right). \quad (5.6)$$

One finds κ_{\parallel} still constant on the interface of the cylindrical droplet but κ_{\perp} has an additional term, which depends on the local capillary number power 2/3. Here β is a numerical parameter accounting for the deformation of the advancing and receding meniscus. Ca_d is the local capillary number based on the normal velocity at the droplet interface. The polar coordinate system has been redefined such that the normal vector $\mathbf{n} = [\sin\theta; -\cos\theta]$ because then β changes at $\theta = 0$ and π , see figure 5.6. Using the symmetry of the problem we integrate the difference between front and rear meniscus of β between 0 and π in order to make the calculation more concise.

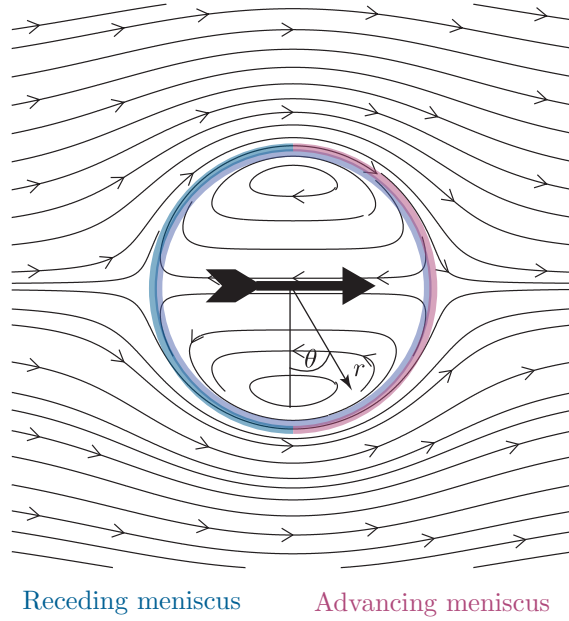


Figure 5.6: View of streamlines moving with a droplet. Advancing and receding meniscus are shown. The advancing meniscus has an increased curvature due to dynamic film formation and its coefficient for $\lambda = 0$ is $\beta = 3.80$, the receding meniscus has a decreased curvature and its coefficient is $\beta = -1.13$.

$$Ca_d = Ca |\mathbf{u} \cdot \mathbf{n}| = Ca |u_d \sin(\theta)|. \quad (5.7)$$

The stress contribution due to surface tension in eq.(5.6) has terms that give zero when integrated along the interface, these are the first two terms that are due to the undeformed

Chapter 5. Dynamic Film formation

interface. We therefore retain only the last contribution $\beta k u_d^{2/3} |\sin(\phi)|^{2/3} / Ca^{1/3} \sqrt{3}$:

$$F_{\text{menisc}} = \oint \frac{\beta k u_d^{2/3}}{\sqrt{3} Ca^{1/3}} |\sin(\phi)|^{2/3} \mathbf{n} d\phi. \quad (5.8)$$

At first one demonstrates that the capillary force in the y-direction (perpendicular to the droplet motion) stays zero. Since we integrate only on half of the circle, because of symmetry we take into account the front and rear film coefficient $\Delta\beta = \beta_f - \beta_r = 3.8 + 1.13 = 4.93$ ¹.

$$F_{\text{menisc},y} = - \oint \frac{\beta k u_d^{2/3}}{\sqrt{3} Ca^{1/3}} |\sin(\phi)|^{2/3} \cos\phi d\phi = - \frac{\Delta\beta k u_d^{2/3}}{\sqrt{3} Ca^{1/3}} \int_0^\pi |\sin\phi|^{2/3} \cos\phi d\phi = 0. \quad (5.9)$$

We turn then to the force in x-direction:

$$F_{\text{menisc},x} = \int_0^\pi \frac{\Delta\beta k u_d^{2/3}}{\sqrt{3} Ca^{1/3}} |\sin(\phi)|^{2/3} \sin\phi d\phi = 0.31\pi k \Delta\beta Ca^{-1/3} \quad (5.10)$$

The force balance equation 2.91 that was used before for streaming droplets without dynamic meniscus is now reevaluated and becomes:

$$F_{\text{interface}} + F_{\text{menisc}} = \pi k^2 \left(\frac{\chi(u_d - 1)}{k} + (u_d(1 + \lambda) - 2) + 0.31 \frac{Ca^{-1/3}}{k} u_d^{2/3} \Delta\beta \right) = 0, \quad (5.11)$$

Where χ is defined in eq. 2.89, and where the dynamic meniscus parameter $\Delta\beta = k_f - k_r$, which are listed in table 5.1. This equation can be solved analytically after transformation to a third order polynomial in u_d , as follows

Analytical solution

$$\chi + 2k - u_d((1 + \lambda)k + \chi) = 0.31\Delta\beta \frac{u_d^{2/3}}{Ca^{1/3}}. \quad (5.12)$$

We rewrite with the substitutions a, b , function of λ, Ca, k .

$$a = \frac{(1 + \lambda)k + \chi}{2k + \chi}, \quad b = \frac{0.31\Delta\beta}{Ca^{1/3}(2k + \chi)}. \quad (5.13)$$

The resulting equation system is taken to the power of 3.

$$1 - u_d a = b u_d^{2/3} \Rightarrow 1 - 3u_d a + 3u_d^2 a^2 - u_d^3 a^3 = b^3 u_d^2. \quad (5.14)$$

Expansion in powers of u_d :

$$u_d^3 + \left(\frac{b^3}{a^3} - \frac{3}{a} \right) u_d^2 + \frac{3}{a^2} u_d = \frac{1}{a^3}. \quad (5.15)$$

¹For viscosity ratio $\lambda = 4$ the coefficient changes to $\Delta\beta = 6.53$.

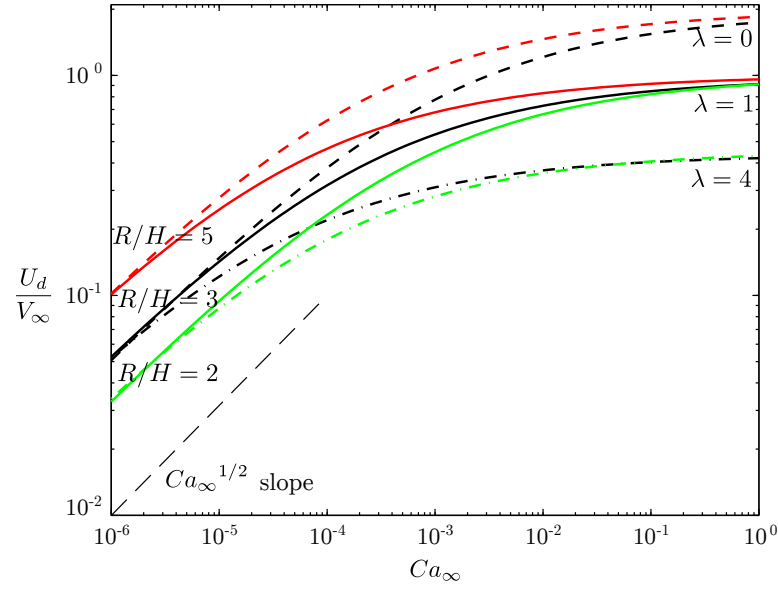


Figure 5.7: Droplet velocity for varying capillary number. Influence of viscosity ratio $\lambda = 0, 1, 4$ and aspect ratio $R/H = 2, 3, 5$

Substituting again,

$$A = \left(\frac{b^3}{a^3} - \frac{3}{a} \right), \quad B = \frac{3}{a^2}, \quad C = \frac{1}{a^3},$$

then solving the cubic equation 5.15 analytically:

$$u_d = \frac{1}{6} \left(-2A + \frac{16^{1/3}(A^2 - 3B)}{D^{1/3}} + 2^{2/3} D^{1/3} \right), \quad (5.16)$$

$$D = 27C - 2A^3 + 9AB + 3\sqrt{3} \sqrt{27C^2 - 4A^3C + 18ABC - A^2B^2 + 4B^3}.$$

A, B and C are composed of a and b , which are composed of k, λ and Ca . This closes the problem and yields a relation for the droplet velocity in wide channels from viscosities, droplet radius, channel height, surface tension and inflow velocity. In the Darcy limit the factor χ is neglected.

Figure 5.7 shows the droplet velocity normalized by the mean incoming velocity for a wide range of capillary numbers, with an initial slope of $u_d \propto Ca_\infty^{1/2}$. In the regime of low capillary numbers the droplet motion becomes independent of the viscosity ratio as all the dissipation is done in the dynamic meniscus region which only weakly depends on the viscosity ratio. The aspect ratio is still important since it reflects the influence of the in-depth curvature effects around the circumference competing with viscous drag of the droplet surface.

In the limit of high capillary numbers the droplet velocity in the absence of films is recovered, where the aspect ratio has only a small influence and the viscosity ratio dominates.

5.2.2 Dynamic film formation for deformable droplets

The preceding section elucidated the ample influence of dynamic meniscus on the droplet velocity. In the simulation of deformable liquid interfaces the curvature needs to be adapted according to the local capillary number. In contrast to the calculation of the undeformable droplet, where the local normal velocity can be obtained from the droplet displacement, the normal velocity of deformable droplets has to be obtained from the local velocities at the interface.

Equation (5.6) states that the out-of-plane curvature is modified depending on the local capillary number accounting for the normal velocity. Hence the jump in normal stresses at the interface depends on the velocity.

$$[[\mathbf{f}]] = \left(\kappa_{\parallel} \frac{\pi}{4} + \frac{2}{h} (1 + \beta \hat{C} a^{2/3}) \right) \mathbf{n} = \left(\kappa_{\parallel} \frac{\pi}{4} + \frac{2k}{\sqrt{12}} (1 + \beta (\mathbf{u} \cdot \mathbf{n})^{2/3}) \right) \mathbf{n}, \quad (5.17)$$

With channel height h , local Capillary number $\hat{C}a$ and β , a parameter that depends whether it is an advancing or receding meniscus (3.80 front, -1.13 back for $\lambda = 0$).

The case distinction for advancing or receding meniscus was implemented using a hyperbolic tangent:

$$\beta = -1.13 + (3.80 + 1.13) \frac{\tanh(20Ca^{-1}u_n) + 1.0}{2}. \quad (5.18)$$

Due to the stiff nature of the problem and the non-linearity of the interface condition, the velocity has to be determined iteratively till the forcing has converged and the time step can be advanced.

Approximation by fix point iteration A fix point iteration method has a slow convergence and needs a relaxation parameter in order to converge smoothly to the final solution. Convergence was measured by the root-mean-square (rms) of the difference in velocity between two iteration steps. The iteration stopped once the rms was below $Ca \cdot 10^{-3}$.

The relaxation parameter ϵ is initially set to 0.3 and increased by 10% at every iteration when the rms decreased till $\epsilon = 1$ and ϵ was decreased by factor 2 when the rms increased.

At the next iterative time step the velocity \mathbf{u} is modified by the solution \mathbf{u}^* :

$$\mathbf{u} = \mathbf{u} + \epsilon(\mathbf{u}^* - \mathbf{u}). \quad (5.19)$$

From the updated velocity a new right-hand-side is created with forcing due to the dynamic meniscus by inserting \mathbf{u} in eq.(5.17).

The advantage of the fix point iteration is that it can be rather fast because only the right-hand-side is modified at every time step. Hence after block pre-condensation the remaining matrix can be inverted and the updated velocity is obtained by matrix-vector multiplication. In average 20 iterations are needed till convergence is achieved and this method is preferred here.

Approximation by Newton iteration A Newton algorithm provides a faster convergence rate and improved stability. At every iteration step the matrix for the droplet problem is altered, which in turn demands at every time step to write and solve the matrix, unlike fixpoint iteration.

The forcing is linearized:

$$[[\mathbf{f}]] = \frac{2\beta}{h} \left(|u_n^{2/3}| + \frac{2}{3} \left(\frac{|u_n^*|}{|u_n^{1/3}|} - |u_n^{2/3}| \right) \right) \mathbf{n} = \frac{2\beta}{h} \left(\frac{1}{3} |u_n^{2/3}| + \frac{2}{3} \frac{|u_n^*|}{|u_n^{1/3}|} \right) \mathbf{n} \quad (5.20)$$

Where u_n is the former time step (prediction) and u_n^* the unknown velocity. As probably anticipated because of the fractional exponent there is a problem if u_n is very small. We relax thus this approximation with the following identity using a relaxation parameter ϵ .

$$\frac{u^*}{|u_n|^{1/3}} = \frac{u^*}{|u_n|^{1/3} + \epsilon} + \frac{\epsilon}{|u_n|^{1/3} + \epsilon} \quad (5.21)$$

Therefore close to a vanishing normal velocity the Newton algorithm turns into fixpoint iteration.

5.2.3 Droplet velocity including films

We have seen that the dynamic meniscus introduced the capillary number as a new parameters in the calculation of the droplet velocity. A comparison of the droplet velocity of deformable and undeformable droplets is proposed in figure 5.8 for three values of the viscosity ratios $\lambda = \frac{1}{4}, \frac{1}{2}$ and 2 and aspect ratio $R/H = 5$. It reveals a very weak dependence when comparing to the frozen circular shape assumed in the undeformable model equation, pointing to the excellent predictive power of the analytical formula eq(5.16). Hence the model for undeformable droplets is in good agreement with the simulation of deformable droplets.

In figure 5.9 droplets with a variety of parameters have been simulated and only in few cases did the deformation become clearly visible. The aspect ratio was varied on the diagonal from bottom left to top right from $R/H = 2.5 \dots 7.5$. On the diagonal from bottom right to top left the viscosity ratio was varied from $\lambda = 0.25 \dots 2$. For all positions on the diagonal the capillary

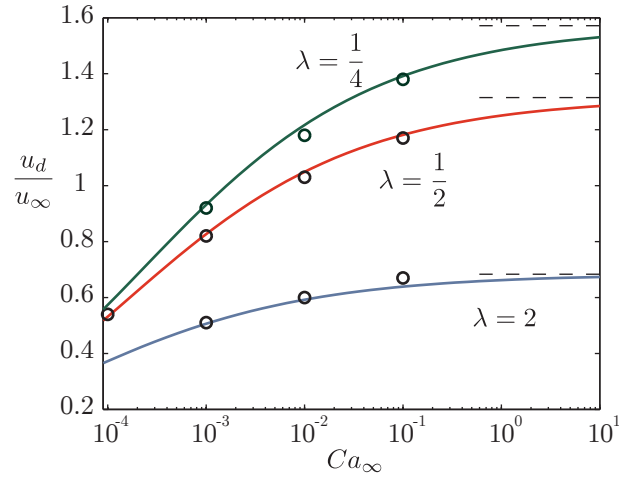


Figure 5.8: Droplet velocities for different inflow capillary numbers Ca at constant aspect ratio $R/H = 5$. The line represents the model for undeformable droplets and the circles simulation of deformable droplets.

number was also varied. The strongest deformation is reached for large capillary number $Ca = 0.1$, large aspect ratio $R/H = 5$ and large viscosity ratio $\lambda = 2$.

5.3 Experimental study on droplet velocity

Measurements of droplet velocity were obtained by imaging of the droplet interface motion in a PDMS microchannel. The channel layout was presented in the introduction in figure 1.2a, where the velocities were measured in a wide channel of width 1 mm and the channel height was either $H = 53\mu\text{m}$ or $24\mu\text{m}$. The free stream velocity is obtained by the sum of the volume flows from the syringe pump. The viscosity ratio is obtained from the fluid mixtures, water and FC-40, $\lambda = 4.1$, see table 1.1 and the viscosity of water $\mu = 10^{-3}\text{ Pa s}$ from table 1.2.

For an imaged sequence of a droplet, the inflow capillary number $Ca = \frac{V_\infty \mu}{\gamma}$ is known and the radius estimated from the droplet area. Determination of Ca , R/H and λ allows to calculate an expected droplet velocity using eq.(5.16). From the imaged data the droplet velocity is estimated as well and normalized by the free stream velocity V_∞ .

In figure 5.10 the experimental droplet velocity is compared to the expected velocity from the model using eq. (5.16). One observes the influence of the droplet radius on the velocity and that the velocity increases for increasing capillary number. The experiments have not yet matured and some more should be performed for a wider range of aspect ratios and also with an less viscous inner phase.

Figure 5.11 the dependence of the relative droplet velocity against the capillary number is shown for one data set of droplets with a radius $R/H = 1.3$. The data points follow closely the prediction of the analytical model.

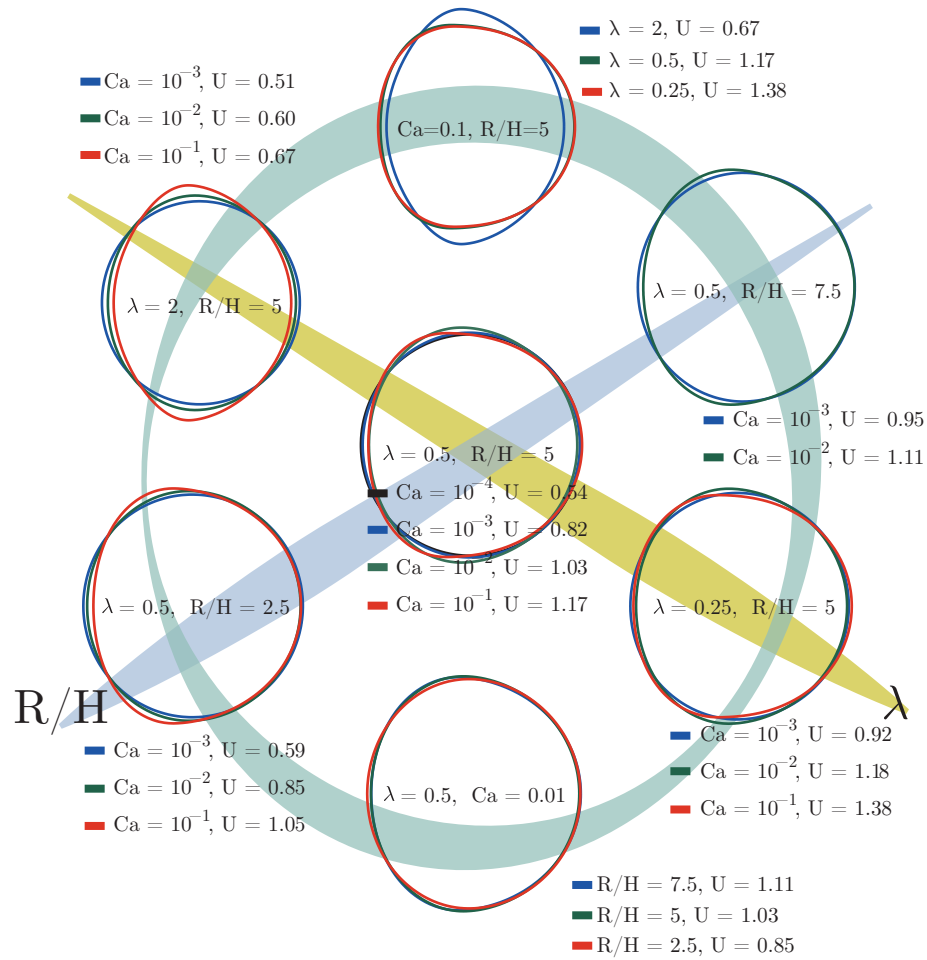


Figure 5.9: Deformable droplet shapes and velocities for varying parameters λ , R/H and Ca . Here U denotes the mobility ratio $\frac{u_d}{u_\infty}$

Summary

The deformation of the meniscus in a capillary tube or Hele-Shaw cell has been known for bubbles and the study was extended here to viscosity ratios ranging from $\lambda = 0.1$ to 10. Knowing about the deformation and therefore about the pressure jump enabled us to devise a lumped parameter model for the meniscus, or in other words, the out-of-plane curvature.

The presence of thin films itself did not introduce a reasonable resistance but the relative contribution due to the surface tension that acts on the meniscus becomes increasingly important as the capillary number decreases. The resistance due to the dynamic meniscus is the key ingredient to correctly estimate the velocity of a streaming droplet

The necessity to predict the correct velocity shall be elucidated by an example of droplet interaction, which is footed on the concept of a peloton (Shen et al., 2014). A peloton, well

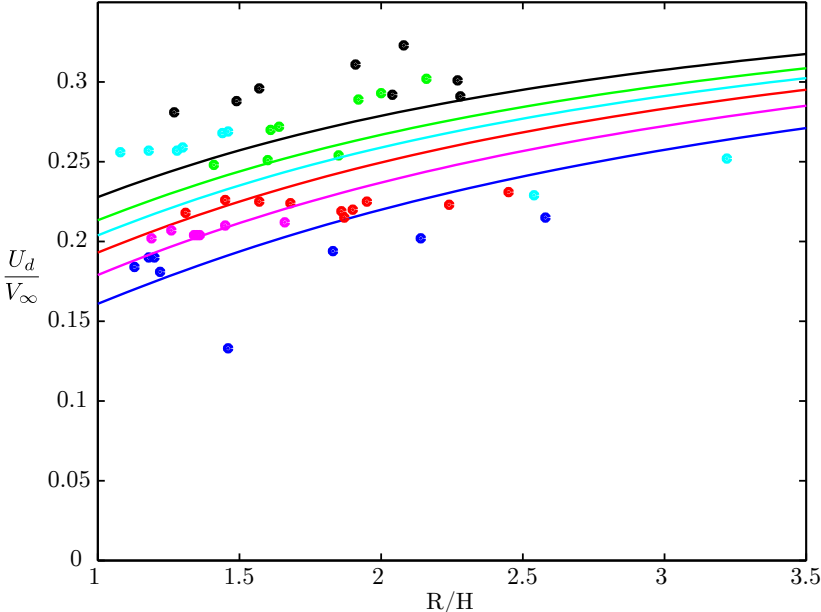


Figure 5.10: Relative droplet velocities plotted against their aspect ratio. Grouped according to their capillary number: $Ca = 2.45 \cdot 10^{-4}$ blue, $Ca = 3.54 \cdot 10^{-4}$ magenta, $Ca = 4.71 \cdot 10^{-4}$ red, $Ca = 5.83 \cdot 10^{-4}$ cyan, $Ca = 7.03 \cdot 10^{-4}$ green and $Ca = 9.35 \cdot 10^{-4}$ black.

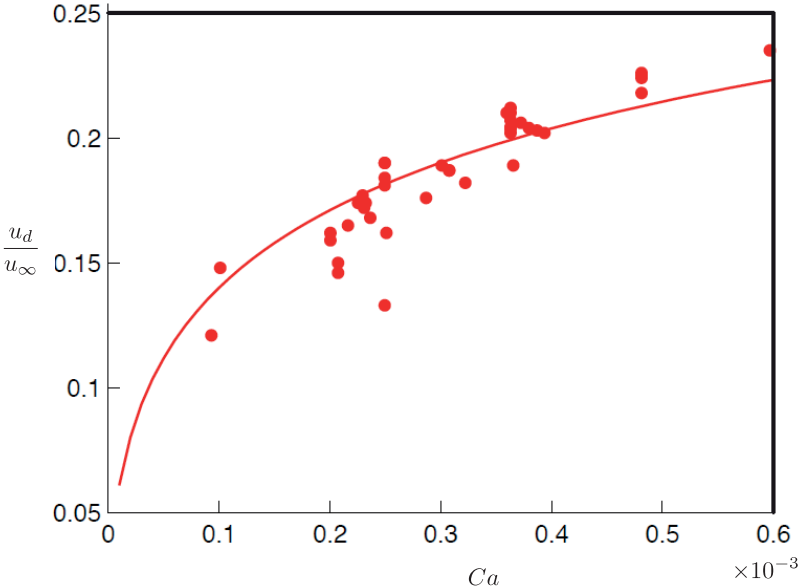


Figure 5.11: Relative droplet velocity plotted against the capillary number for a viscosity ratio $\lambda = 4.1$ and aspect ratio $R/H = 1.3$.

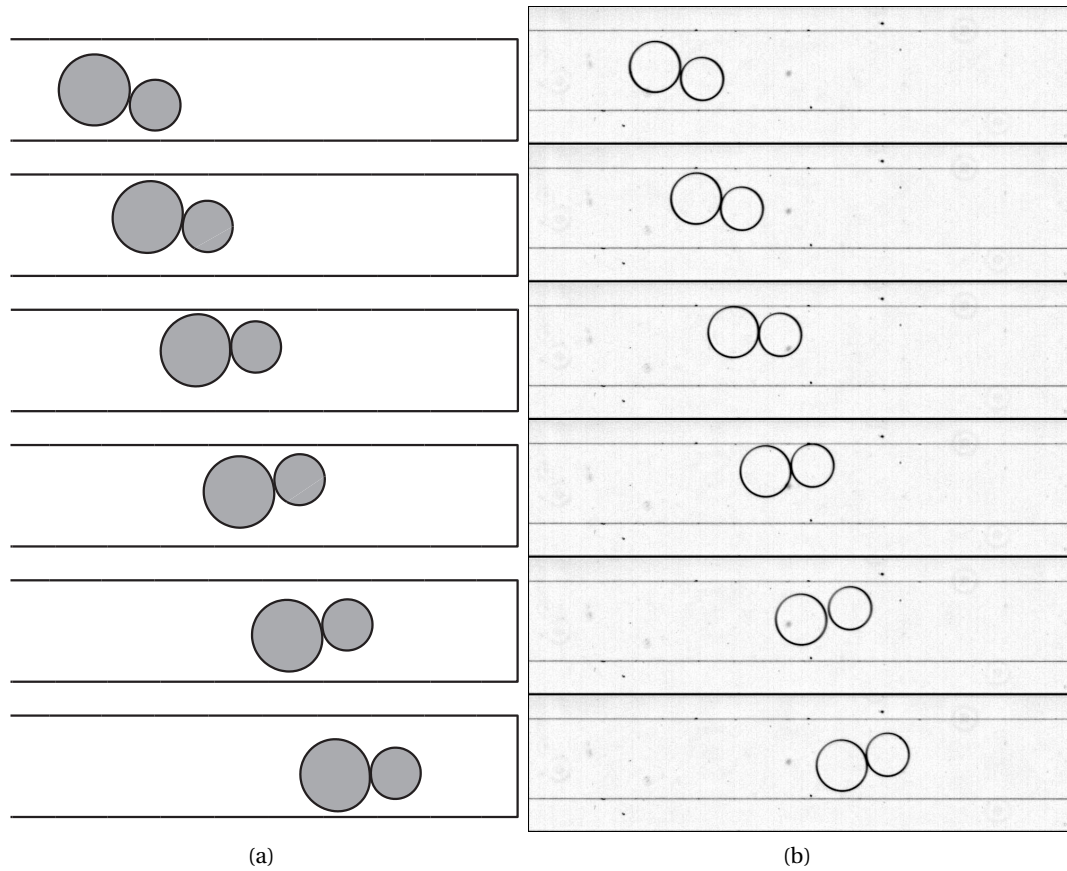


Figure 5.12: Droplet oscillation in narrow channel. The flow comes from the left, the droplets group, touch the top wall and move downwards. (a) Simulation, (b) Images taken from (Shen et al., 2014)

known to cycling aficionados, allows a group of droplets or cyclists to move at a higher velocity when the ratio of combined driving force to combined drag is bigger than one. In the case of two droplets moving faster than the mean flow the arrangement of two droplet centers aligned parallel to the flow leads to a higher velocity than for a single droplet. With droplet centers situated perpendicular to the flow their velocity lower than that of a single drop. The effect of moving slower in a group than alone is called anti-peloton . This behavior is inversed when the droplet moves slower than the mean flow. A configuration of two droplets parallel to the flow is slower than a single drop, while a configuration of droplet centers perpendicular to the flow moves faster. In neglecting the dynamic meniscus the droplet

Table 5.2: Peloton and anti peloton regimes

	pair in parallel	single	pair perpendicular
$u_{\text{solo}} > u_{\infty}$	$u_{\text{para}} >$	u_{solo}	u_{perp}
$u_{\text{solo}} < u_{\infty}$	$u_{\text{para}} <$	u_{solo}	u_{perp}

velocity is overestimated. For a single droplet this may result only in a time discrepancy between experiments and numerics. But considering two or more droplets can change the dynamic interaction completely depending when the droplets are considered faster than the mean flow, which is shown in figure 5.12. Droplets in presence of film formation do not find their homologue in droplets with a high inner viscosity, to which one might want to resort as a similar substitute. Because as was shown the droplets velocity with a dynamic meniscus depends on the aspect ratio R/H , whereas the droplet without dynamic meniscus has almost no dependence on R/H .

The correction of the boundary condition was introduced to the undeformable model droplets and the numerical algorithm. Both methods agree well as the deformation remains small. Experiments that were performed show relatively good agreement in scaling with aspect ratio and capillary number. Even so the result does not fit perfectly, the agreement improved a lot compared to the velocities predicted without dynamic meniscus. More experiments with a wider range of aspect ratios and also varying viscosity ratio need to be conducted. These experiments should probably be redone in glass chips, which could provide superior results because they are less flexible than PDMS and larger channel aspect ratios could be reached.

Future work could introduce the effect of surfactants on the meniscus and therefore on the droplet velocity. A model for film formation in the presence of a rigid interface, for instance due to Marangoni stress, was derived by Cantat (2013).

6 Topographical boundary conditions

Apart from meniscus deformation caused by film formation at the liquid interface, a liquid interface deformation can be caused by a topographical modification of the top or bottom wall in the channel. In principle all of our analysis is based on the prerequisite that the channel's top/bottom walls are parallel and of uniform distance. Hence any modification of this confinement should be applied with great care. Here I allow only for either small or localized deviation from the uniform channel height. The influence is not reflected by the viscous terms of the Brinkman equation but only by the capillary effects at the interface. On the one hand because a lumped model for the fluid behavior in a 3D channel topology is generally difficult to obtain and on the other hand does the numerical model allow only for domain-wise constant parameters. To privilege capillary effects is justified at low capillary numbers, where capillary effects dominate over viscous effects.

6.1 A topographical model for microfluidic anchors and rails

The following chapter is mostly a facsimile of a published article (Nagel et al., 2014) that followed a study done with Pierre-Thomas Brun and François Gallaire.

Droplet based microfluidic devices are built on the idea of precise flow control of minute volumes. Such control is mostly borne by the small dimension of microfluidic channels, usually their height $H \ll R$, where R is the typical radius of a droplet. These length scales impose low Reynolds number in the flows as $Re = \rho U H / \mu$ where U is the typical flow speed, μ the fluid viscosity and ρ its density. Such a strategy minimizes inertial effects, hence enforces control. A consequence of this choice of parameters is that the droplets are geometrically constrained in-between the walls of the channel and adopt a pancake like shape. In complete wetting and quiescent conditions their exact 3D shape is the one of a Delaunay surface, Delaunay (1841), of uniform mean curvature

$$\kappa = \frac{2}{h} + \frac{\pi}{4} \frac{1}{\mathcal{R}} \quad (6.1)$$

Chapter 6. Topographical boundary conditions

where the curvature κ should write $\kappa C = \left(\frac{2}{h} + \left[\frac{\pi}{4} - 1 \right] \frac{1}{\mathcal{R}} + \frac{1}{\mathcal{R}} \right)$ to better highlight the correction $\left[\frac{\pi}{4} - 1 \right] \frac{1}{\mathcal{R}}$ brought to the $2/h$ term accounting for the difference between such a surface and a torus.

The obtained results are quantitatively validated against experimental data from the literature and help building a physical insight of such a system. Using the numerical scheme presented in chapter 3 to simulate the free liquid interface, the geometric model for the anchor is conveniently introduced into the dynamic boundary condition.

Recent applications have started to make an extensive use of the \mathbf{e}_z direction be it when etching grooves in the top of channels, see Dangla et al. (2011); Dawson et al. (2013) (Fig 6.1) or making their height variable in the flow direction, say $h(x)$ as done by Dangla et al. (2013). In the former case the grooves create an area of reduced confinement that droplets may fill and thus reduce their surface energy (Dangla et al., 2011). These wells of surface energy of depth ΔE_γ act as anchors of force $F_\gamma \approx |\Delta E_\gamma|/\tilde{d}$, where \tilde{d} denotes the diameter of the anchor and the subscript γ refers to the surface tension of the fluid. Consequently, the droplets remain pinned on the anchor when $F_\gamma > F_d$, where F_d is the drag force exerted on the droplets. This is of course possible as the capillary numbers $Ca = \mu U/\gamma_{\text{ref}}$ found in the channel are rather small. However, the evoked anchors violate the hypothesis of uniformity of the channel in the z -direction along which the problem is averaged. Therefore, they call into question the previously stated 2D formalism. Herein, we concentrate on this type of droplet capturing devices and propose a solution to restore an almost two dimensional formalism ($2D^+$) with the Brinkman equation and a generalized Laplace law using a geometrical model. The model accounts for the curvature of the droplet in the groove as the external flow rate is increased from zero to a critical value above which the droplet is detached.

Here I recall the interface conditions that go along with eq.(2.30), which express equality of fluid velocities, the tangential stress continuity and the generalized Laplace law all expressed at the interface. They respectively write:

$$\mathbf{u}_1 = \mathbf{u}_2 \quad (6.2a)$$

$$\mathbf{t} \cdot \overline{\overline{\boldsymbol{\sigma}}}_1 \cdot \mathbf{n} = \mathbf{t} \cdot \overline{\overline{\boldsymbol{\sigma}}}_2 \cdot \mathbf{n} \quad (6.2b)$$

$$\mathbf{n} \cdot \overline{\overline{\boldsymbol{\sigma}}}_1 \cdot \mathbf{n} - \mathbf{n} \cdot \overline{\overline{\boldsymbol{\sigma}}}_2 \cdot \mathbf{n} = [[\mathbf{f}]] = \gamma \left(\frac{2}{h} + \frac{\pi}{4} \bar{\kappa} \right) \quad (6.2c)$$

where κ_{\parallel} denotes the interface in-plane curvature ($\kappa_{\parallel} = 1/\mathcal{R}$ for a pancake droplet at rest), $\overline{\overline{\boldsymbol{\sigma}}}$ is the planar stress tensor, $[[\mathbf{f}]]$ denotes the stress jump at the interface, a subscript i denotes a variable defined for the fluid i and \mathbf{t} and \mathbf{n} respectively denote the interface tangent and normal. The Brinkman equation, eq.(2.30), along with the boundary conditions (6.2) constitute a mathematically well posed problem. The generalized Laplace pressure jump in (6.2c) uses the curvature of a pancake droplet in the channel given in (6.1). We now derive a model to

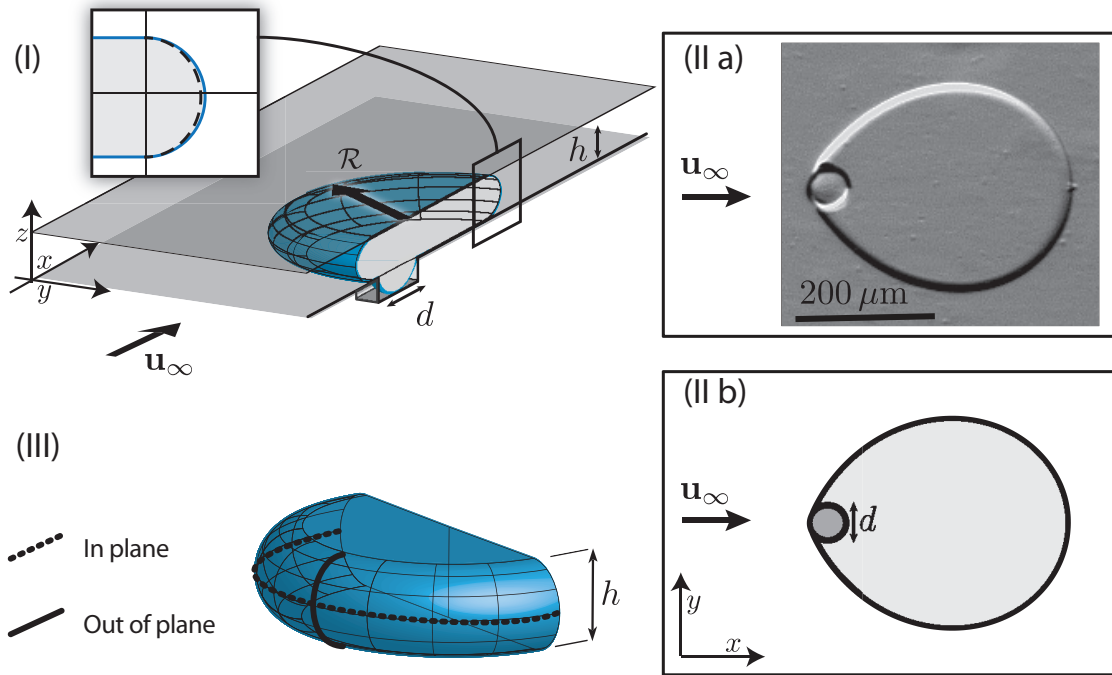


Figure 6.1: (I) - Scheme of an anchor of diameter d holding a confined droplet. Inset: the droplet interface (plain line) compared to a torus (dashed line). (II) Experimental and numerical situations for $Ca = \frac{\mu U_\infty}{\gamma} = 1.9 \times 10^{-4}$, $d/h = 1.8$ and $R/H = 6.25$. Photo courtesy: Remi Dangla. (III) Details of the droplet shape. Out-of-plane (plain lines) and in-plane (dashed) directions of the principal curvatures.

revise (6.2c) when the droplet is anchored onto a groove.

6.1.1 A geometrical model for the anchor

Extension of the generalized Laplace pressure jump (6.2c)

The 3D shape of an anchored droplet in quiescent conditions may be derived using a minimization of surface energy software such as Surface Evolver. The droplet partially fills the groove with a protuberance in the form a spherical cap. In particular, it has been pointed out that the curvature of this cap matches the curvature of the interface elsewhere: $\kappa = \frac{2}{h} + \frac{\pi}{4} \kappa_\parallel$ as stated in eq. (6.1) yielding a uniform pressure jump at each point of the interface. This is in agreement with the fact that the droplet is at rest.

Deriving the exact shape of the droplet in the anchor in the presence of a flow is a complex

3D dynamical problem. It is technically challenging and is beyond the scope of the present work: not only one has to carry out time consuming 3D computations but also account for the details of the contact line at the edge of the groove. The approach we propose is different.

We propose a simple model to account for the out-of plane geometry of the droplet which can adapt to the flow rate. The model is two-fold. First we concentrate on the largest possible state of occupation of the groove. We anticipate that this state corresponds to a limiting situation and is associated to a critical value of the flow rate above which the droplet will be released. Second, we propose a parametrization allowing for the interface geometry to adapt to the flow rate from quiescent conditions up to the critical value of release.

Let us first model the situation where the droplet occupation rate in the groove is maximal. For simplicity, the depth of the anchor is assumed not to be a limiting factor here. The upstream interface is assumed to be a spherical cap (Figure 6.2II). This is a natural hypothesis in the view of the experimental results by Dawson et al. (2013) reported in the literature where bubbles flowing in square cross-section channels with trapping features are studied. As illustrated in Figure 6.2II-b, this spherical cap indentation is assumed to approximate the exact shape of the droplet in the anchor region and to match the rest of the pancake droplet. This idealization cannot be justified *a priori* in absence of any 3D simulations but will be validated against experiments using indirect indicators as done in section 6.2.1.

The (x, z) central view of the droplet is shown in (Figure 6.2II). The corresponding critical radius of curvature writes:

$$\rho_l = \frac{h}{2} \left(1 + \frac{d^2}{4h^2} \right), \quad (6.3)$$

as the circle in the (x, z) plane passes through the three points A, B and C.

Second, let us introduce r defined as the distance from the center of the anchor to the interface and parametrize the curvature at each point of the interface:

$$\rho(r) = \frac{h}{2} \left(1 + \frac{d^2}{4h^2} \exp \left(-\ln(2) \left(\frac{4r^2}{d^2} \right)^4 \right) \right). \quad (6.4)$$

This expression allows for a smooth transition from a free state $\rho = h/2$ (quiescent conditions) to a fully anchored droplet $\rho = \rho_l$ (critical situation). The continuous range of configurations in-between these two limiting configurations are schematized in Figure 6.2 III. Hereafter, each point of the interface is provided with a curvature, which is only a function of its distance to the anchor and equation (6.2c) is discarded in favor of

$$\mathbf{n} \cdot \overline{\overline{\sigma}}_1 \cdot \mathbf{n} - \mathbf{n} \cdot \overline{\overline{\sigma}}_2 \cdot \mathbf{n} = [[\mathbf{f}]] = \gamma \left(\frac{1}{\rho} + \frac{\pi}{4} \kappa_{\parallel} \right) \mathbf{n} \quad (6.5)$$

6.1. A topographical model for microfluidic anchors and rails

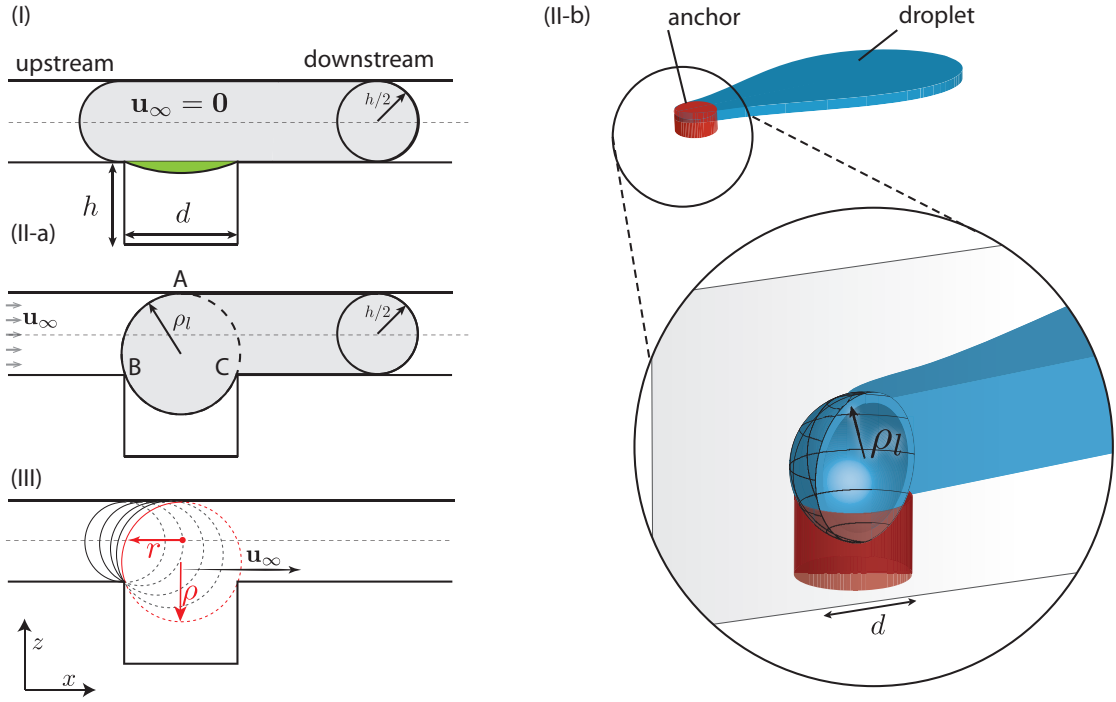


Figure 6.2: (I) (x, z) -view of the droplet in quiescent conditions, the upstream interface curvature remains unchanged despite the spherical cap in the groove (green). (II-a,b) Spherical cap model of a fully anchored droplet. The upstream interface complies geometrically touching the points A,B and C and is modeled by a sphere of radius $\rho_l = \frac{h}{2} \left(1 + \frac{d^2}{4h^2} \right)$. The downstream radius of curvature remains unchanged, $\rho = h/2$. (III) Successive shapes adopted by the droplet front interface when the flow rate is increased. The radius of curvature evolves from $\rho = h/2$ to $\rho = \rho_l$. The variable r denotes the distance from the interface to the center of the anchor.

With this boundary condition we now have a modified set of equations to solve. Prior solving them we briefly draw the physical picture which underpins the anchor mechanism.

A naive scenario for the anchoring mechanism

We now briefly depict a pressure based explanation of the anchoring mechanism. It consists in explaining the possibility of equality between the pressure changes $(\Delta p)_1$ and $(\Delta p)_2$ respectively found when circumnavigating the droplet (path 1 in Figure 6.3) or going through its interface (path 2 in Figure 6.3). $(\Delta p)_1$ simply consists in a linear decrease in pressure (Dangla et al., 2011; Maruvada and Park, 1996).

$(\Delta p)_2$ is evaluated in the following. Let us first denote δp_u and δp_d the upstream and downstream absolute pressure jumps encountered on the path 2 in Figure 6.2. Since the droplet is at rest, the pressure field in the droplet is assumed uniform so that $(\Delta p)_2 = \delta p_d - \delta p_u$

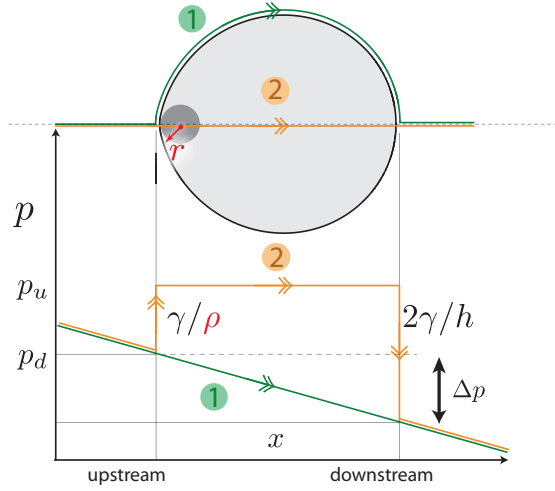


Figure 6.3: Simplified pressure profiles as a function of x respectively for (1) a path circumnavigating the droplet and (2) a path passing right through it.

. In equation (6.5) the pressure jump is dominated by the out-of-plane terms since $\rho \propto h \ll \mathcal{R}$ and $\bar{\kappa} \approx 1/\mathcal{R}$. As a first attempt the in-plane terms of the curvature are discarded yielding $\delta p_u = \gamma/\rho$ and $\delta p_d = 2\gamma/h$ respectively. Consequently $(\Delta p)_2 = \gamma(1/\rho - 2/h)$.

The model we have proposed allows values of $1/\rho_l \leq 1/\rho \leq 2/h$. Such values yield $-\gamma(2/h - 1/\rho_l) \leq (\Delta p)_2 \leq 0$ which adapts to the pressure change $(\Delta p)_1 \leq 0$ dictated by the outer flow and function of u_∞ .

This scenario neglects the in-plane curvature which, to be properly taken into account, requires a determination of the in-plane droplet shape.

6.2 A numerical investigation of anchors

6.2.1 Capture, deformation and release

In the rest of the article we investigate numerically droplets of viscosity $\mu_1 = \mu_2/4$, of radius \mathcal{R} and in a flow of velocity u_∞ . The viscosities ratio is consistent with the fluids usually used in microfluidics such as water in FC40. Note it is also a non-trivial case unlike the choice of $\mu_1 = \mu_2$ which leads to a simplification in eq. (3.15). For simplicity the diameter of the anchor is fixed (unless otherwise specified) and is chosen to be $d = 2h$.

A series of simulations were performed gradually increasing the capillary number $Ca = \frac{\mu_2 u_\infty}{\gamma}$. For each capillary number a droplet was considered to have reached equilibrium when its center of mass was moving 10^{-5} slower than the free stream velocity, the droplet was then declared captured. Next, this last configuration was used as a starting point for a new computation using a capillary number 5% larger. The procedure was repeated until release was

observed. A droplet has therefore two states: captured or released depending on the capillary number. First, we focus on the capture state and in particular study the deformation of the

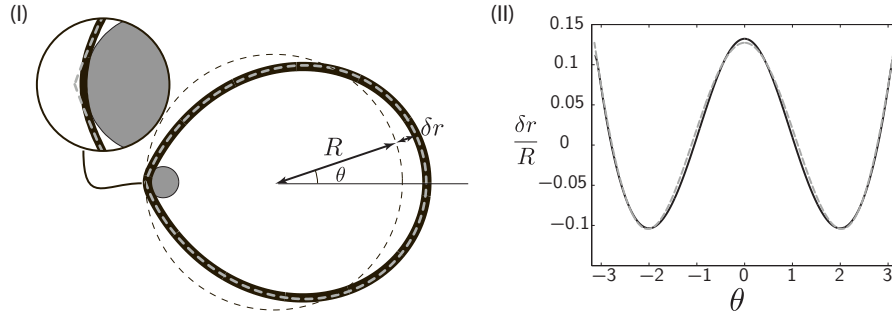


Figure 6.4: (I) Simulation result (black thick) of an anchored droplet for parameters $R/H = 8$ and $Ca = 1.3 \times 10^{-4}$ compared to the deformation model by Dangla et al. (2011) (dashed gray). The black dashed line represents the undeformed circular shape of the droplet. Insert: Zoom on the droplet tip (II) Deformation $\delta r/R$ against the angle θ for $R/H = 8$ and $Ca = 1.3 \times 10^{-4}$ (Black and dotted gray lines for the numerics and theory results respectively).

droplet interface. Second, a state diagram is drawn searching for the separation line between the capture and release state.

Study of the deformation

Shown in Figure 6.4 is the typical pear like shape the droplet adopts when anchored. This shape was obtained numerically for $R/H = 8$ and $Ca = 1.3 \cdot 10^{-4}$ and is compared to the expression derived by Dangla et al. (2011) in the limit of small deformations:

$$\frac{\delta r(\theta)}{R} = \frac{48}{\pi} Ca \frac{R^2}{H^2} (1 - \theta \sin(\theta)). \quad (6.6)$$

where δr is the local deviation from R , the droplet circular radius in absence of flow.

The numerical results are in very good agreement with (6.6). Note the small but significant difference at the front of the droplet. Simulation helps recover a smooth representation of the interface on the anchor unlike the expression (6.6). The droplet interface encompasses the anchor as shown in the insert in Figure 6.4. Similar results, where the droplets interface follows the contour of the anchor, are found when varying the capillary number and the anchor diameter (Figure 6.5). This particular feature is made possible by the use of the parametrization function (6.4). Note additionally that other smoothing functions warranting that $\rho(r)$ evolves from $h/2$ far from the anchor to ρ_l around the $r = d/2$ have proven equally successful.

Let us now quantify the droplets deformations in term of their elongation $\epsilon = \delta r(0)/R$. Shown in Figure 6.5 is a plot of such elongations for different aspect ratios R/H and capillary numbers

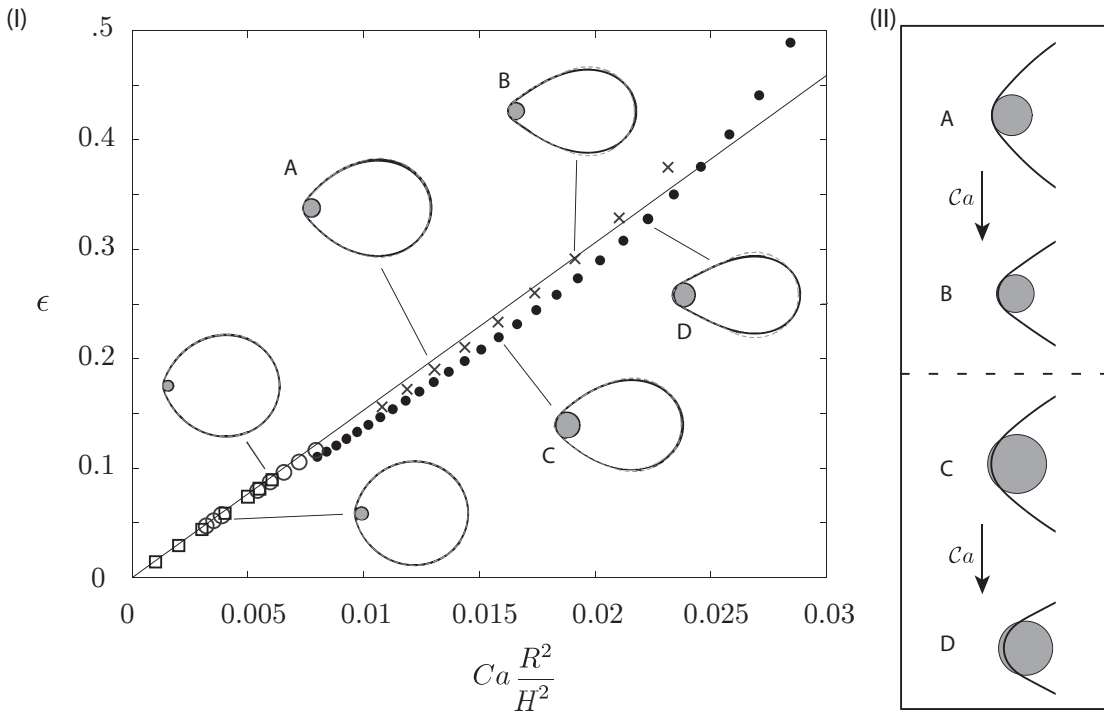


Figure 6.5: (I) Elongation of droplets of aspect ratio R/H : 4 •, 6 ×, 8 ○, 10 □. The solid line gives the trend for small deformations following (6.6): $\epsilon = 48/\pi Ca \frac{R^2}{H^2}$. Some cases are illustrated, where the solid line represents the numerical solution and the dashed grey line the model. (II) Details of the droplet interface that nearly follows the anchor contour.

Ca. The agreement between simulation and theory is very satisfactory, while the theory itself agrees well experiments by Dangla et al. (2011). Note that these deformations are independent of the strength of the anchor embodied by the coefficient ρ_l in (6.3).

Numerical results separate from the theoretical prediction for large capillary numbers. This was anticipated since the validity of equation (6.6) is restrained to weak deformations. More importantly note that the stretching of the droplet is increasing with the capillary number. We will see that such in-plane deformations play a key role in the release of the droplet.

Droplet state diagram

The progressive increase in the carrier fluid velocity u_∞ leads to an increase in the viscous drag which eventually causes the droplet to release from its anchoring site. This may advantageously be captured defining a critical capillary number Ca^* comparing the viscous and surface tension effects acting on the droplet at the release threshold. In Figure 6.6 are shown the critical capillary numbers for droplets of different aspect ratios R/H on holes of diameter

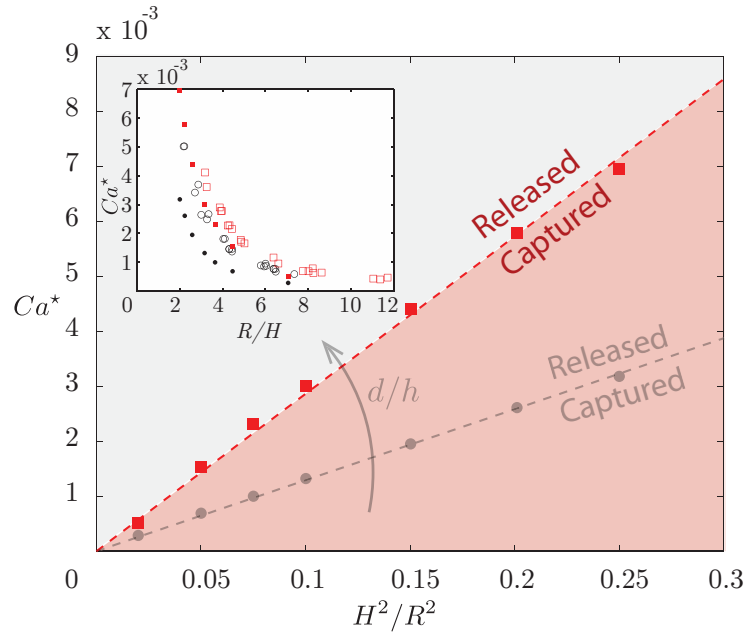


Figure 6.6: Critical capillary number at which droplets are released, plotted against H^2/R^2 . A least square fit of the data exhibits a slope of about 29×10^{-3} for $d = 2h$ (■, red) and 13×10^{-3} for $d = 1.4h$ (○). Inset: same results plotted as a function of R/H compared to experimental data by Abbyad et al. (2011) (□ and ○).

$d = 2h$ and $d = 1.4h$.

The critical capillary number Ca^* is found to be an increasing function of the ratio d/h and the values found numerically are found to be remarkably close to experimental data (Abbyad et al., 2011). In particular the scaling $Ca^* \propto H^2/R^2$ is recovered in agreement with the literature (Dangla et al., 2011). The positive prefactor is a function of both the strength of the anchor, hence of the value of ρ_l in (6.3), and the effective size of the anchor set by (6.4). The overall agreement between numerics and experiments validate the use of (6.3) and (6.4) that were derived with a simplified geometric model of the droplet central slice.

The method is now used to investigate further the anchoring mechanism holding the droplet and the consequences on the droplet dynamics.

6.2.2 Pressure distribution in and out the captured droplets

In this section we take advantage of the numerical simulations to investigate the pressure distribution in the considered problem and in particular revise the scenario depicted in section 6.1.1. In Figure 6.7 is shown the pressure field of a droplet of aspect ratio $R/H = 6$ for $Ca = 4 \cdot 10^{-4}$. As underlined by the closed streamlines the droplet appears to be at rest.

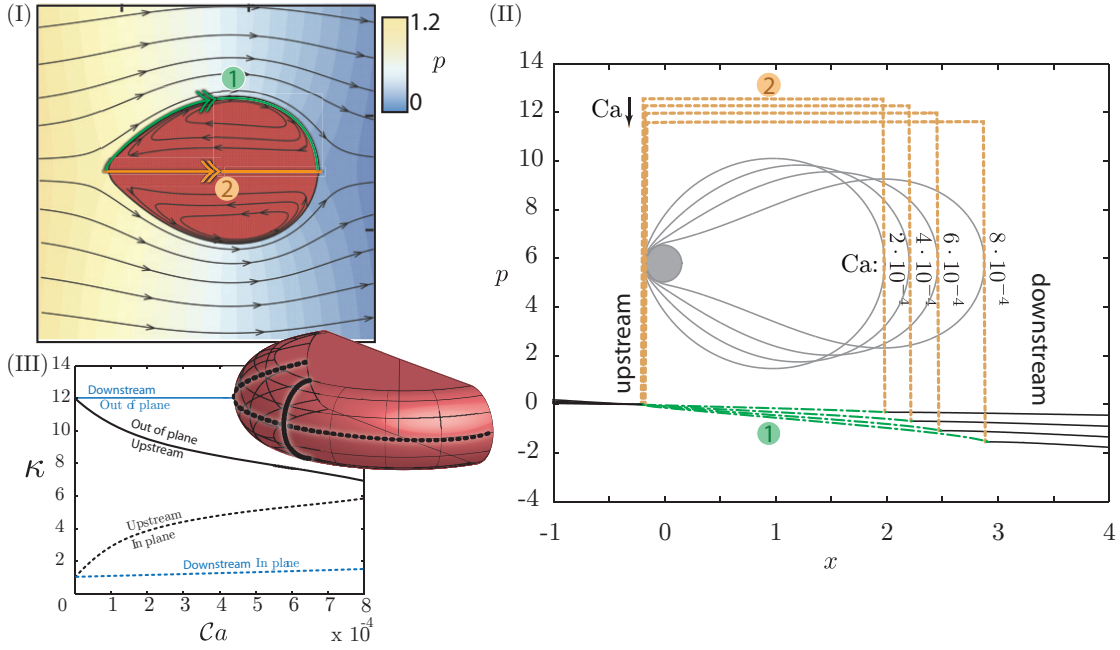


Figure 6.7: (I) Illustration of the pressure field of a droplet at $Ca = 4 \times 10^{-4}$ (II) Pressure distribution of the droplet attached to a hole with aspect ratio $R/H = 6$ and $d = 2h$. The dotted curves (orange) are obtained going through the droplet unlike the dash-dotted ones (green) obtained when circumnavigating the droplet. The corresponding capillary numbers are 2, 4, 6 and 8×10^{-4} . (III) Out-of-plane (plain line) and in-plane (dotted line) components of the upstream (resp. downstream) curvature as a function of the capillary number.

Additionally, a weak recirculating flow is found inside the droplet. It results from the shear exerted by the outer flow through the interface, as underlined by the high density of streamlines in a boundary layer. Nevertheless, the pressure field inside the droplet is approximatively uniform. On the other hand, the pressure decreases almost linearly in the outer flow and may be approximated with

$$(\Delta p)_1 = -48u_\infty\mu_2R/H^2 \quad (6.7)$$

where $(\Delta p)_1$ denotes the pressure drag along the path 1 in Fig 6.7. This pressure drag is equivalent to the classical formulation of the drag force $F_d = 24\pi u_\infty R^2/H^2$ exerted on a cylindrical droplet. Note that the pressure evolutions in (path 2) and out (path 1) of the droplet therefore differ. Such discrepancy is balanced by the difference in the unsigned pressure jumps on the droplet upstream and downstream interfaces. They are respectively denoted δp_u and δp_d and are found over the path 2 in Fig 6.7. Going through this path one may derive an alternative expression of the overall pressure gradient

$$(\Delta p)_2 = \delta p_u - \delta p_d \quad (6.8)$$

The condition for the droplet to remain on the anchor naturally writes

$$(\Delta p)_1 = (\Delta p)_2 \quad (6.9)$$

Of particular interest are the plots of the pressure evolution for different capillary numbers (Figure 6.7-II) where one may observe that the condition (6.9) is fulfilled. To ease the comparison the pressure reference is set to zero exactly on the upstream interface in each case. We recall that the dimensionless pressure jump at the interface of an unperturbed droplet is $\gamma\left(\frac{\pi}{4}\frac{1}{\mathcal{R}} + \frac{2}{H}\right) \simeq 13\frac{\gamma}{\mathcal{R}}$ in the present case. As the droplet gets dragged in the anchor by the surrounding fluid, its upstream edge sinks deeper into the hole leading to a decrease of the effective pressure jump δp_u . The decrease in δp_u outruns the weak evolution of the downstream pressure jump δp_d . As a result, $(\Delta p)_2$ adapts and copes with the pressure drag $(\Delta p)_1$ when Ca is varied.

Let us now detail the evolution of the upstream pressure jump δp_u . The two curvatures found in the Laplace equation (6.5) have opposite effects. The out-of-plane curvature $1/\rho$ decreases when increasing the capillary number (Fig. 6.7-III and equation (6.4)). However, it appears clearly from Figure 6.7-III that the in-plane deformation of the droplet plays an important role too. The more the droplet is dragged the more the upstream interface in-plane curvature $\bar{\kappa}$ increases. This growth undermines the overall effectivity of the anchor which we recall is based on the reduction of the pressure jump in the vicinity of the groove. We now combine and quantify these effects to obtain a pressure based expression of the critical capillary number above which (6.9) fails and the droplet is released from the anchor.

Let us consider the droplet to be on the verge of release. This state is characterized by the critical capillary number Ca^* associated with the velocity u^* . By definition, release is achieved when $(\Delta p)_1$ overcomes $(\Delta p)_2$. This is possible as $(\Delta p)_2$ is bounded by a maximal value $(\Delta p)_2^*$ which is now derived. Each term in $(\Delta p)_2^*$ is evaluated individually.

Downstream the in-plane shape of the droplet is deformed by a quantity denoted $\delta r(\theta = 0)$ following the formalism of section 6.2.1. The induced change in the droplet curvature writes: $-\frac{1}{R}(\delta r(0) + \delta r''(0))$ in linear theory and may be derived recalling (6.6). The out-of-plane curvature remains unchanged yielding:

$$\delta p_d = \gamma \left(\frac{2}{h} + \frac{\pi}{4} \frac{1}{\mathcal{R}} \left(1 + \frac{48}{\pi} Ca^* \frac{R^2}{H^2} \right) \right) \quad (6.10a)$$

Upstream, the droplet is more dramatically deformed and is found to be rather different from the linear prediction (6.6) (Fig. 6.4-I and Fig. 6.7-III). Hereafter, it is modeled by a section of a spherical cap yielding:

$$\delta p_u = \gamma \left(\frac{1}{h} + \frac{1}{h} \right) \quad (6.10b)$$

where both $1/h$ terms respectively denote the contribution of the in-plane and out-of-plane

curvatures. The $\pi/4$ prefactor has been voluntarily omitted to account for the evoked spherical shape. Consequently, using (6.8), the overall difference $(\Delta p)_2 = \delta p_u - \delta p_d$ writes:

$$(\Delta p)_2 = -\gamma \frac{\pi}{4} \frac{1}{\mathcal{R}} \left(1 + \frac{48}{\pi} Ca^* \frac{R^2}{H^2} \right) \quad (6.10c)$$

Balancing (6.7) in the case where $u_\infty = u^*$ and (6.10c) leads to the expression of the critical capillary number above which the droplets are released:

$$Ca^* = \frac{\pi}{144} \frac{H^2}{R^2} \quad (6.11)$$

This analysis helps recover the proper scaling law $Ca^* \propto H^2/R^2$ as found in the numerics and in the experiments by Dangla et al. (2011). A close examination of the numerical results shows that, in the present case $Ca^* \simeq 29 \times 10^{-3} \frac{H^2}{R^2}$ when the theoretical prediction (6.11) is $Ca^* \simeq 22 \times 10^{-3} \frac{H^2}{R^2}$. These results are discussed next.

This theoretical derivation of Ca^* has been done in the representative yet specific case where $d = 2h$ and would need to be refined to account for the dependence in the anchor geometry. However, the prediction (6.11) is commensurable with other sizes of anchor since $Ca^* \simeq 13 \times 10^{-3} \frac{H^2}{R^2}$ in the case of $d = 1.4h$. Second, the droplet is already severely deformed when released and the spherical cap model occults the non-linear effects that may come into play. However this scaling enlightens the main characteristics of the anchor that (i) warrants a decrease in the upstream out-of-plane curvature and its contribution to the Laplace pressure jump which helps holding the droplet and in turn (ii) induces a deformation of the droplet causing an increase the in-plane curvatures and their respective contribution to the Laplace pressure jumps. This increase is moderated downstream but is severe upstream since the droplet bends into the shape of the anchor and eventually escapes.

6.3 Discussion and droplets on rails and anchors

6.3.1 Recirculation

Altering the boundary condition (6.2c) and replacing it by (6.5) in the vicinity of the groove successfully reproduces the main feature of the considered anchors: holding droplets against the flow. The combined use of this method and the Brinkman equation (2.30) allows us to examine the inner recirculating flow inside the droplet. Of particular interest is the tangential velocity u_t found on the droplet interface (Fig 6.8). We propose a scaling argument to estimate u_t and compare the results with numerics. The viscous stress is estimated in the boundary layer at the interface of the droplet. In the outer fluid the velocity evolves from $2u_\infty$ (Taylor and Saffman, 1959) far from the interface to u_t over a length scaling as the boundary layer thickness, that is the height of the channel h . On the other side of the interface the velocity changes from u_t to an approximately nil value over the same length h . The continuity of the

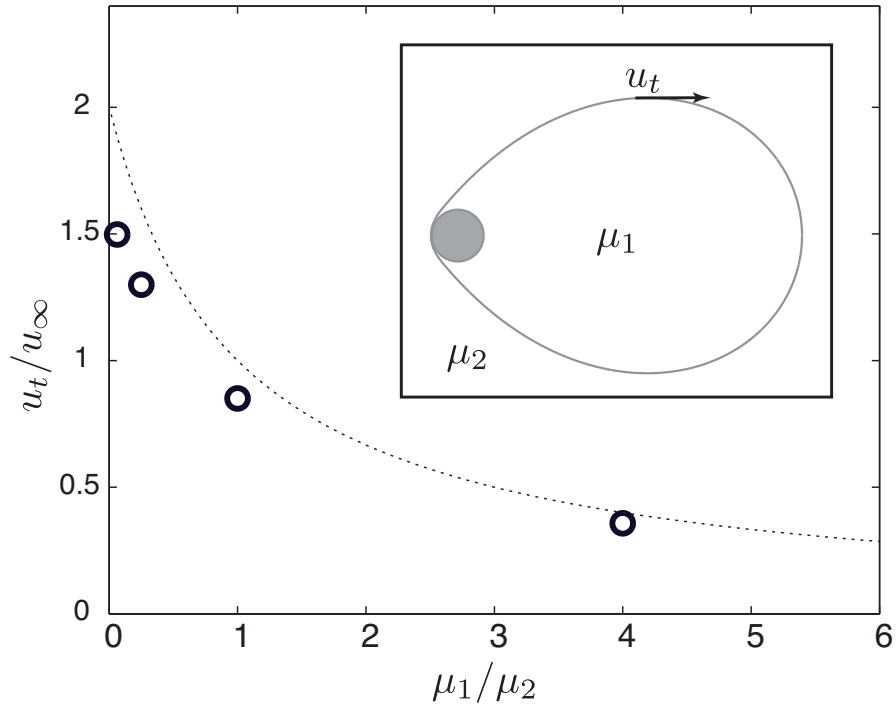


Figure 6.8: Dimensionless tangential velocity u_t/u_∞ on the droplet interface (see insert) as a function of the viscosity ratio ($R/H = 6$ and $d = 2h$).

tangential stress at the interface yields:

$$\mu_2 \frac{2u_\infty - u_t}{h} \sim \mu_1 \frac{u_t - 0}{h} \quad (6.12)$$

which allows for an estimation of u_t :

$$u_t = 2u_\infty \frac{1}{1 + \frac{\mu_1}{\mu_2}} \quad (6.13)$$

Equation (6.13) is plotted in Fig 6.8 and compared to numerical results. The agreement validates the scaling argument, in particular the fact that both boundary layers have the same typical size.

Such recirculating flows have important implications such as the mixing species at low Reynolds numbers investigated next.

6.3.2 Applications

The above described droplets may be seen as the building bricks for Lab-on-a-Chip applications. Two illustrations from the literature by Abbyad et al. (2011) are now simulated using our anchoring model.

Mixing

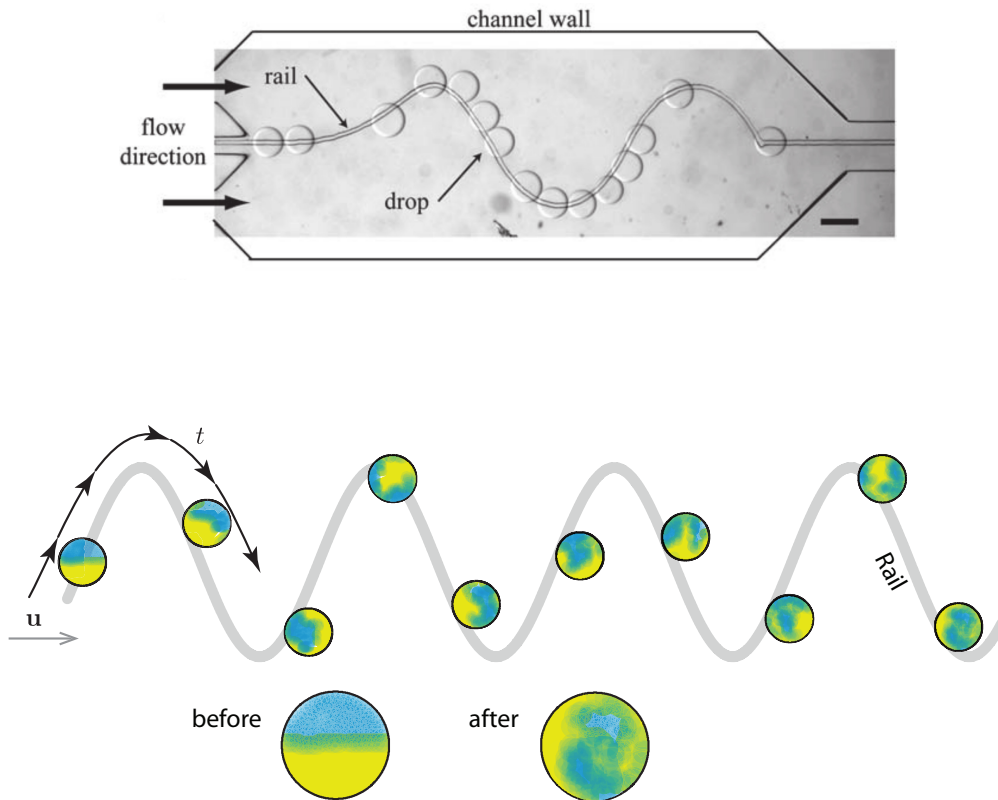


Figure 6.9: A single droplet, $R/H = 3$, is following a rail of width h , amplitude $A = 4R$ and wavelength $\lambda = 10\pi R$. The flow is such that $Ca = 10^{-4}$. Passively convected tracer particles demonstrate the mixing of two species in the droplet.

The anchors may easily be extended to rails, which are etched in the channel wall and force the trajectory of droplets in the flow. The reported numerical method is as versatile as the grooves are. A mere change in the definition of r in eq. (6.4) that is in the definition of the distance from the droplet interface to the anchor, is sufficient to simulate the guiding of a droplet along a rail. For anchors the distance was given by $r = \sqrt{x^2 + y^2}$ where (x, y) are the coordinates of the droplet interface in a system centered in the anchor. This may be traded

for:

$$r = y - A \sin\left(\frac{2\pi}{\lambda_r} x\right) \quad (6.14)$$

in the case of sinusoidal rail of amplitude A in the y direction and wavelength λ_r in the x direction. The typical results obtained when performing a simulation using (6.14) are shown in Figure 6.9 in the form of a time sequence. As in the experiments the droplet is found to follow a path essentially dictated by the rail: its interface intersects the rail twice at all times so that the droplet remains on the rail despite its overall motion along the y -axis.

It is worth noticing there is no privileged anchoring site for the droplet on the rail, unlike what happens when a train follows the railroad. (Figure 6.9). Such an oscillatory motion is an interesting way to enhance mixing inside the droplet. Note that the mixing in a droplet following a straight line trajectory in a micro-channel is in fact quasi nil.

The mixing of two species initially sitting in the 'north' and 'south' hemispheres of the droplet is illustrated in Figure 6.9. In particular, shown are the details of the droplet after just less than 4 periods on the rail. The mixing was found improved when increasing the amplitude of the rail. Another important factor is the viscosity ratio μ_1/μ_2 as the smaller the ratio the better the mixing. This last results is consistent in the view of Figure 6.8 where the velocity transferred to the droplet interface increases as μ_1/μ_2 decreases. On the other hand the capillary number was found to have little influence on the mixing.

Droplets interactions

The second illustration consists in sequentially sending multiple droplets towards a single trap in operating conditions such that $Ca < Ca^*$. A buffering mode may then be obtained: droplets are successively stopped on the groove, since $Ca < Ca^*$, and then chased away by the next incoming droplet repeating the cycle. Consequently, each droplet is stopped in the flow for a limited period without any modification of the flow rate, leaving enough time to perform specific tasks on the droplet. The numerical results are in good qualitative agreement with experimental data previously reported in the literature (Abbyad et al., 2011). The buffering mode is well reproduced in the simulations as shown in Fig 6.10 where the shaded droplet ejects the other one from the anchor when colliding with it. The time of contact $\tau_c \simeq 0.8u_\infty/d$ is found numerically and appears to be shorter than in experiments, where $\tau_c \simeq 1.2u_\infty/d$. This difference is attributable to the fact that our model ignores the dissipation in the volume of fluid residing in the anchor.

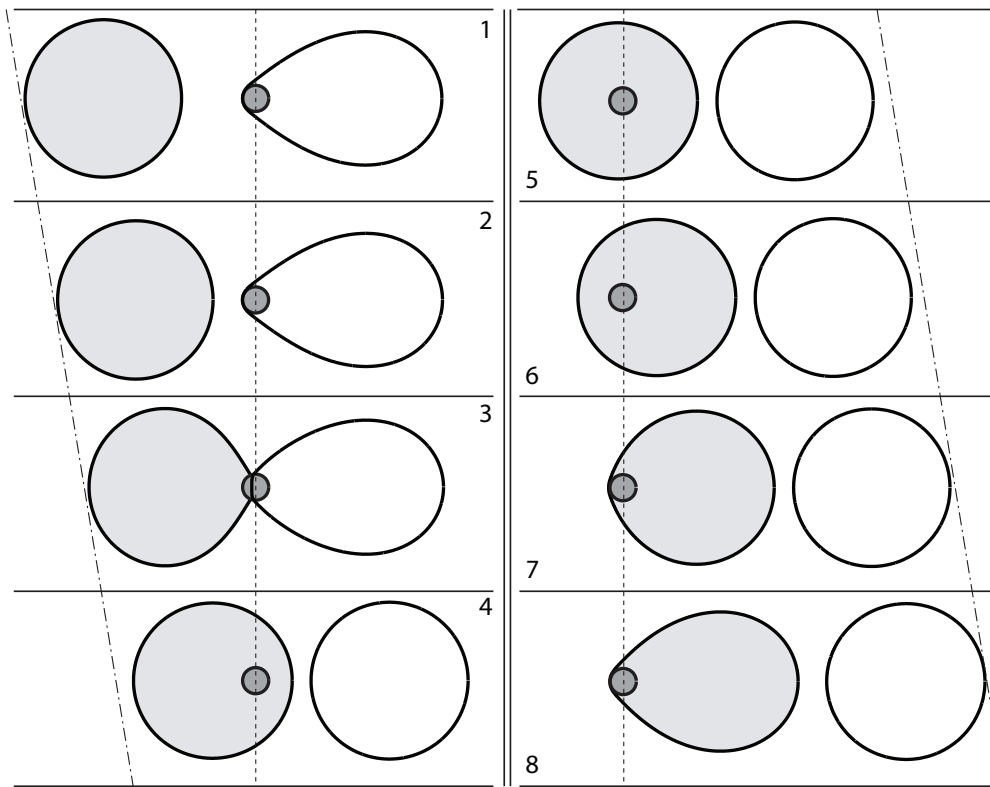


Figure 6.10: Buffering mode where droplets stop on the anchor until they are chased away by an incoming droplet ($Ca = 5 \times 10^{-3}$, $\mu_1 = \mu_2/2$, $R/H = 6$, $d/h = 2$, $dt = 0.35$) The dashed lines indicate the position of the center of the anchor that is a fixed point in the channel. The dotted dashed lines denote the average speed of the droplet arriving onto and leaving the hole

6.4 Droplet formation on a tearing slope

Let us now tentatively use the modified dynamic boundary condition introduced in this chapter to account for the transverse meniscus shape modification induced by topographical features to reproduce another microfluidic device invented by Dangla et al. (2013) in C. Baroud's lab at LadHyX. On an historical note, this technique, as well as the one presented in the previous part of the chapter, are based on earlier observations and experiments by Dangla et al. (2010). The nature of this discovery was, as quite common in science, hazard. A microfluidic channel showed strange symmetry breaking when droplets enter into a wide section and started shift to the side of the channel instead of remaining centered and thus symmetric. The droplet deviation is explained by swelling of the channel, which was made out of PDMS and swells when hexadecane is absorbed. Swelling caused the channel ceiling to deform downwards and thus increasing a meniscus of increased curvature towards the center of the channel.

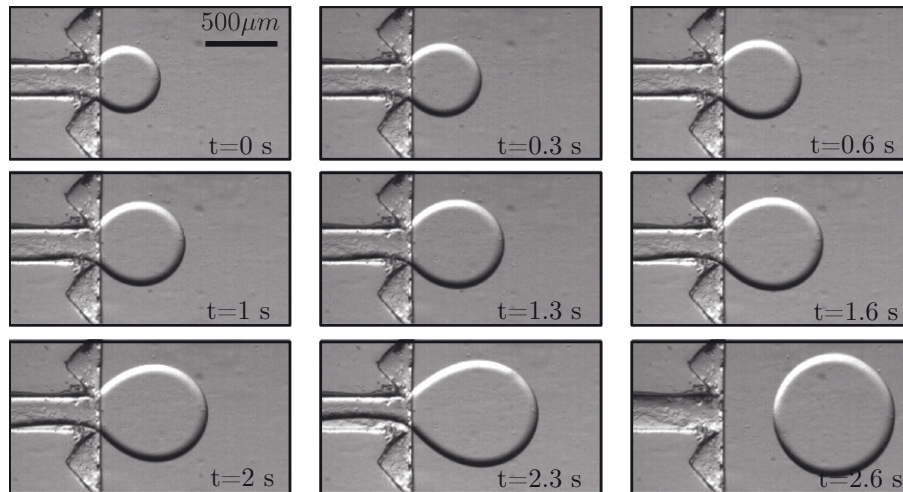


Figure 6.11: Photograph of droplet formation on a slope of 1.2° , taken from (Dangla et al., 2013).

Dangla et al. (2013) used this technique in order to drive droplets in microchannels or initial droplet shedding without coflow channels, as needed in a flow focussing device or T-junction. Without the need of coflow channels the device design becomes much simpler, which is especially important when a lot of these structures are used for parallelized droplet creation.

Droplet creation by channel height gradients is different from the flow focussing device, where a cross flow initiates the shedding process. Dangla's technique uses a liquid thread that enters into a wider channel, which has a constant slope, thus the height on the cell increases constantly. Dangla et al. (2013) explain that the shedding is similar to the dripping instability, where droplets are formed by gravity forces, hence a volume force. Using Gauss theorem one can convert the gradient of surface energy on the boundary, surface tension γ constant but transverse curvature changes, into a body force and show that both problems are mathematically equivalent.

Phenomenologically the liquid interface is accelerated by the the channel height gradient because the capillary force tries to minimize the surface energy of the droplet and therefore it advances in the direction of a higher channel as it reduce its curvature there.

6.4.1 Model boundary condition for varying h

The BEM formulation does not allow for a varying height in the channels. This is because the Brinkman equations incorporate the height into the aspect ratio R/H , which has to be a constant in the fundamental solution or Greens responds of the system. The easiest way to get around this shortcoming at first is to assume that the change in $h(\mathbf{x}) = h_0 + \epsilon \hat{h}(\mathbf{x})$ is very small and does not influence the equation of motion to leading order, $\epsilon \ll 1$. Because of the small capillary number the normal stress jump at the droplet interface still senses the slope

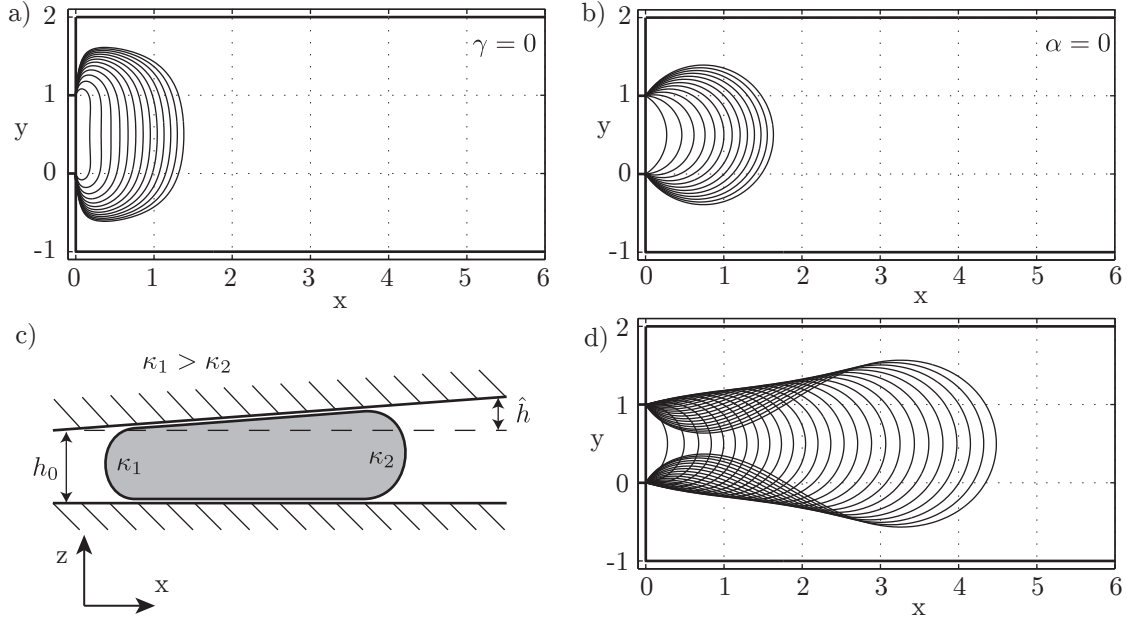


Figure 6.12: a) Injection of fluid into a wide channel with zero surface tension. b) Injection of fluid into a wide channel with with parallel floor/ceiling. c) Sketch of the perpendicular plane in a channel with an angle 11° between ceiling and floor. d) Fluid injected into a wide channel with an angle between ceiling and floor. a) and b) iterated till $t = 2600$, while d) iterated till $t = 5200$.

and therefore the slope enters only in the boundary conditions:

$$\mathbf{f} = \left(\frac{\pi}{4} \kappa_{\parallel} + \kappa_{\perp} \right) \mathbf{n} = \gamma \left(\frac{\pi}{4} \kappa_{\parallel} + \frac{2}{h_0 + \epsilon \hat{h}(\mathbf{x})} \right) \mathbf{n}. \quad (6.15)$$

Herein, according to Laplace's law, \mathbf{f} is are the surface stresses, γ the surface tension and κ the curvature. The κ_{\parallel} designates the in-plane curvature and h the height of the channel. Included is a height deviation \hat{h} .

Numerically the jump of surface tension over the wall bounded interface can pose a problem because unlike droplets a strong forcing on the inner fluid is felt only on one side. This can be circumvented when subtracting the equilibrium out-of-plane curvature $h/2$ because a constant contribution does not affect the interface.

One writes:

$$\mathbf{f} - \frac{2}{h_0} \mathbf{n} = \left(\frac{\pi}{4} \kappa_{\parallel} + \frac{2}{h_0 + \epsilon \hat{h}} - \frac{2}{h_0} \right) \mathbf{n} = \left(\frac{\pi}{4} \kappa_{\parallel} - \frac{2\epsilon \hat{h}}{(h_0 + \epsilon \hat{h}) h_0} \right) \mathbf{n}. \quad (6.16)$$

6.4.2 Simulation of a slope

We consider a rectangular channel with an inflow of a fluid of viscosity $\lambda = 1/2$ coming from a orifice on the left. The simulation is done for three different cases, one without surface tension ($Ca = \infty$), the two others at capillary number $Ca = 10^{-3}$ once without a slope and once with a slope of $\epsilon \hat{h} = \frac{x h_0}{5}$, that is 11.3° . For every time $\Delta t = 100$ the evolution of the interface has been plotted in figure 6.12 till just before break-up.

In the perspectives, chapter 8, we will propose a model allowing for pinch-off through a two-stage numerical procedure. First when a thread becomes thinner than the cell thickness h , a circular thread geometry is accounted for. Second, when two points of facing interfaces become closer than a regularization distance, the interface is opened and the topology changed by creating a new droplet. Combining this technique with the present investigation should allow to recover the scaling of the droplet size as a function of the slope angle and surface tension.

The fluid without surface tension is unaffected by a slope, it accumulates close to the entry channel. Adding surface tension but without a slope, $\alpha = 0^\circ$, makes the fluid advance into the surrounding fluid because the interface adopts a circular shape. However without a slope the interface stays bound to the inflow channel. When adding a slope the droplet advances into the domain driven by a pressure gradient around its interface.

Compared to the experiments the slope used in these tentative simulations is about two times larger. The result is still preliminary but suggests the capability to qualitatively reproduce flows in channels with variable height.

Summary

We described and demonstrated how to simulate droplets in confined channels in the presence of a varying channel height. The strategy consisted in modifying only the generalized Laplace law boundary condition to account for these holes, rails or slopes. This was motivated by the fact that the capillary number is small ($Ca \ll 1$) so that surface tension effects drive the dynamics. The numerical method was compared to experiments where droplets were anchored, deformed and released. More importantly this numerical method allows to visualize the pressure fields and accurately quantify the interface curvature revealing the inner machinery of these anchors. The reported mechanism allowed to recover the experimental result $Ca^* \propto H^2/R^2$. This method reveals to be flexible as well and may be extended to multiple droplets or different geometries for the anchors as the presented rails.

For the simulation of slopes the method provided qualitative agreement but is less appropriate since the steady change of the confinement has an influence on the effective viscous dissipation that is not modelled.

7 Solution of rigid objects

Apart from droplets there are other types of objects that can be transported or deformed in microchannels. In this chapter the implementation of the motion of a rigid object in a microchannel is described. Rigid objects have been studied experimentally in microchannels under the viewpoint of collective hydrodynamic interactions, for instance in the work of H el ene Berthet and co-workers at PMMH in Paris (Berthet et al., 2013). In her work she studied fibers, which are created inside microchannels by photo-polymerization using an UV-source and a mask. Work on deformable fibers has also been carried out by Wexler et al. (2013) who have studied the bending of a single fiber attached to the channel wall, while Wandersman et al. (2010) have analyzed the trajectory of a flexible fiber in an hyperbolic flow. Outside the field of microfluidics the settling behavior of small rods was studied by Russel et al. (1977).

Apart from the fundamental interest of understanding the diversity of fluid/solid behaviors in absence of inertia, rigid or deformable solid objects are also of interest for microfluidic application. For instance red and white blood cells behave like incompressible objects with a given elasticity (McWhirter et al., 2011).

In the next section we tackle the motion of cylindrical objects with flat faces parallel to the top and bottom confining walls. While one avoids computing the flow inside the rigid object, the price to pay is the requirement of modeling the lubricating films. From the rigid body assumption follows that the velocity at each point of the rigid object can be expressed by three values: Object velocities u_f, v_f in x and y direction and rotational velocity $\dot{\theta}$. The rotation $\dot{\theta}$ is performed around the center of area \mathbf{x}_f of the object, whose area is A_f

$$\mathbf{x}_f = \frac{1}{A_f} \int_{\Omega_f} \mathbf{x} dA \quad \Rightarrow \quad 0 = \int_{\Omega_f} (\mathbf{x} - \mathbf{x}_f) dA. \quad (7.1)$$

The rigid body problem can be posed as a linear combination of an external flow on a body at rest and quiescent fluid with a body of unitary x and y displacement and unitary rotation. Imposing force \mathbf{F} and torque M equal to zero for the sum of these four contributions yields one vectorial and one scalar equation, altogether three equations that allow for the determination

of the instantaneous values of u_f , v_f and $\dot{\theta}$.

$$\mathbf{F}_{\text{ext. flow}} + u_f \mathbf{F}_{\text{body},x} + v_f \mathbf{F}_{\text{body},y} + \dot{\theta} \mathbf{F}_{\text{body},\theta} = 0, \quad (7.2)$$

$$M_{\text{ext. flow}} + u_f M_{\text{body},x} + v_f M_{\text{body},y} + \dot{\theta} M_{\text{body},\theta} = 0. \quad (7.3)$$

This requires the solution of four steady Brinkman problems at each time step. By including the x, y displacement and rotation magnitude into the unknowns, a single linear system with three additional degrees of freedom and three additional equations for the force and momentum equations can be formulated.

7.1 Problem formulation for rigid objects

Fluid flow motion is again governed by the 2D Brinkman equation, which will be formulated in a boundary integral equation exactly as described in chapter 3.

As for droplet motion, the outer flow is prescribed by the fixed boundaries. The rigid object is described by the boundary ω_f with a displacement \mathbf{u}_f . We examine the integral equation 3.9 on the rigid object boundary ω_f :

$$\oint_{\omega_f} \mathbf{Tn} \cdot \mathbf{u}_f - \sigma \mathbf{n} \cdot \mathbf{G} ds + \oint_{\omega} \mathbf{Tn} \cdot \mathbf{u} - \sigma \mathbf{n} \cdot \mathbf{G} ds = \frac{\mathbf{w}_a}{2} \cdot \mathbf{u}(\mathbf{x}_0). \quad (7.4)$$

The velocity of the rigid object appears in the first term, while the second term in the integral contains the unknown traction forces on the object. A rigid body in plane motion has three degrees of freedom u_f , v_f and $\dot{\theta}$. Writing therefore the velocity field for a body in the frame of its barycenter:

$$\mathbf{u}_f = \begin{pmatrix} 1 & 0 & -y \\ 0 & 1 & x \end{pmatrix} \begin{pmatrix} u_f \\ v_f \\ \dot{\theta} \end{pmatrix}. \quad (7.5)$$

Forces that the fluid exerts on the rigid object come from viscous stresses and pressure. Again, we adopt the notation for the surface force \mathbf{f} in x and y direction

$$\sigma \mathbf{n} = \begin{pmatrix} \sigma_{11} n_x + \sigma_{12} n_y \\ \sigma_{12} n_x + \sigma_{22} n_y \end{pmatrix} = \begin{pmatrix} f_x \\ f_y \end{pmatrix}.$$

The force and momentum equations write:

$$\mathbf{F} = \oint_{\omega_f} \sigma \mathbf{n} ds = \oint_{\omega_f} \begin{pmatrix} f_x \\ f_y \end{pmatrix} ds, \quad (7.6)$$

$$\mathbf{M} = \oint_{\omega_f} \sigma \mathbf{n} \times \mathbf{x} ds = \oint_{\omega_f} -f_x y + f_y x ds. \quad (7.7)$$

Here, f_x and f_y are unknown surface forces on the object in the x and y directions. Imposing these equations allows to determine $u_f, v_f, \dot{\theta}$ and couples the object to the flow. Observe however that in this 2D averaged approach the viscous contribution in the gap between rigid object and channel top and bottom walls are missing.

The flow profile in the thin gap between rigid object and top/bottom walls needs therefore to be modeled, to restore some three-dimensionality and allow for the computation of the viscous stresses on the upper and lower faces. The model shall be solely based on the solid objects velocity and rotation. In fact, the need for a correct description of the velocity profile is also essential in order to relate the averaged velocity to the objects velocity.

Recalling the pseudo 3D velocity $\hat{u} = \bar{u}f(z)^1$ and applying for this chapter the short notation $f' = \partial f / \partial z|_{z=0}$. The force extracted by the external walls facing the object and films is evaluated from the friction on top and bottom wall at $z = [0, h]$ is:

$$F_{c,x} = 2 \int_{\Omega_f} \frac{\partial \hat{u}_f}{\partial z} \Big|_{z=0} dA \approx 2 \int_{\Omega_f} (u_f - y\dot{\theta}) f' dA = f' \left(u_f A_f - \dot{\theta} \int_{\Omega_f} y dA \right), \quad (7.8)$$

$$F_{c,y} = 2 \int_{\Omega_f} \frac{\partial \hat{v}_f}{\partial z} \Big|_{z=0} dA \approx \int_{\Omega_f} (v_f + x\dot{\theta}) f' dA = f' \left(v_f A_f + \dot{\theta} \int_{\Omega_f} x ds \right), \quad (7.9)$$

in the x and y directions. The value f' approximates the gradient of the velocity profile and allows to formulate the problem using mean velocities. The profile f shall be determined further down and A_f is the area of the object side that faces the ceiling or floor.

Note that, because the center of rotation is in the center of area, the remaining domain integrals are zero, which follows from eq.(7.1). Hence one obtains:

$$\mathbf{F}_c = 2f' A_f \begin{pmatrix} u_f \\ v_f \end{pmatrix}. \quad (7.10)$$

¹ $f(z)$ is the shape of the velocity profile in the z direction and not to be confused with the traction forces f_x or f_y .

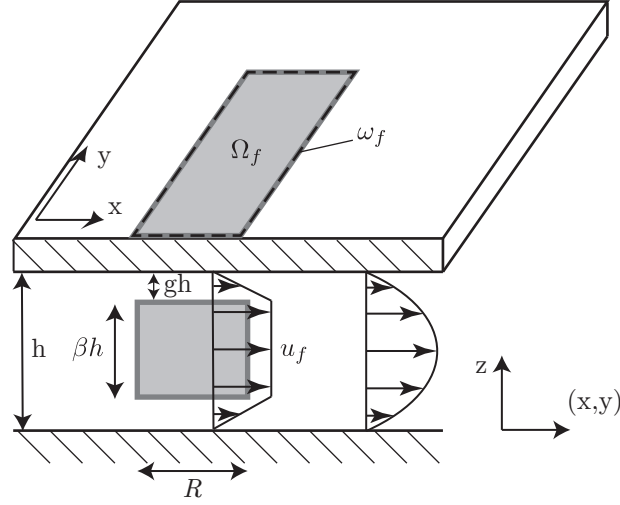


Figure 7.1: Schematic view of a vertical cut of a rigid object in a microfluidic channel. Characteristic lengths are shown and the velocity profile in the z direction is sketched.

The torque is then given by

$$M_c = \int_{\Omega_f} \frac{\partial(\hat{v}_f x - \hat{u}_f y)}{\partial z} \Big|_{z=0} dA = 2 \int_{\Omega_f} \dot{\theta} f'(x^2 + y^2) dA. \quad (7.11)$$

The velocity is expressed by the solid body rotation $\dot{\theta}$. Here, in contrary to the translation, where a constant value was integrated over the area, the square distance from the center of area varies in the domain of integration.

The integration can be performed in terms of surface integrals as shown in appendix A.5.2.

$$M_c = \dot{\theta} f' \oint_{\omega_f} (xy^2 n_x + x^2 y n_y) ds. \quad (7.12)$$

Discretizing the fluid equations and the force and momentum equations composes a linear equation system. The solution of this system is composed of the surface stresses \mathbf{f} and u_f, v_f and $\dot{\theta}$. The final problem boils down to modeling the velocity profile in the film between the object faces and the top/bottom walls and therefore to find an accurate description of the flow in the gap.

7.2 Lubrication gap flow profile

Symmetry in z -direction is assumed and the normalized gap size g is defined as the distance between rigid object and top or bottom confinement divided by the channel height h . Similarly the confinement β expresses the fraction of the channel height that is occupied by the object,

$$\beta = 1 - 2g.$$

Gap with linear velocity profile First let us first assume a Couette-flow, where the velocity profile between object and channel ceiling/floor is linear. The solid objects section and velocity profile is sketched in figure 7.1. The assumption of a linear velocity profile is natural when $g \rightarrow 0$. Continuity of the velocity on the top and bottom faces of the object yields:

$$\begin{aligned} f(0 \leq z \leq gh) &= Cz, \quad f(gh \leq z \leq h/2) = Cgh, \\ \int_0^{h/2} f(z) dz &= \frac{h}{2} \Rightarrow C = \frac{1}{hg(1-g)}, \quad f(z) = \frac{1-2z/h}{2g(1-g)}. \end{aligned} \quad (7.13)$$

The rigid object velocity u_f is calculated from the mean flow velocity by:

$$\bar{u} = u_f(1-2g) + 2g \frac{u_f}{2} \Rightarrow u_f = \frac{\bar{u}}{1-g}, f(g) = \frac{1}{h(g-g^2)} \quad (7.14)$$

The linear velocity profile fails however when the object becomes thin and the gap approaches $g = 1/2$. In fact, in that case, eq.(7.14) gives $u_f = 2\bar{u}$, where one would have expected $u_f = \frac{3}{2}\bar{u}$, the ratio of maximal velocity to mean velocity for the plane Poiseuille profile.

Gap with parabolic velocity profile A better approximate profile has to be found such that when $g = 1/2$, the object velocity goes to $3/2\bar{u}$ with a parabolic profile, and when g approaches zero, the object velocity is approximately the mean velocity.

This suggests to use a Poiseuille profile of undetermined strength but truncated at distance gh from the wall and rescaled, in order to preserve a mean value of 1. From the Poiseuille profile f_p of undetermined strength C we obtain the velocity at the top and bottom of an object at gap size gh :

$$\hat{u}(0 \leq z \leq gh) = \bar{u} f_p = \bar{u} \frac{C}{h^2} (h-z)z \xrightarrow{z=gh} u_f = \bar{u} C(1-g)g. \quad (7.15)$$

C is a scaling coefficient that should verify that the velocity profile ensures $\int_0^{h/2} f = h/2$. For $g = 1/2$, an infinitely thin object, we expect $u_f = 3/2\bar{u}$ and for $g \approx 0$, an object that fills the channel height, $u_f = \bar{u}$. Integrating the mean of the profile between 0 and $h/2$, using symmetry, allows to determine C :

$$\begin{aligned} \frac{h}{2} &= \int_0^{h/2} f(z) dz = \int_0^{gh} f_p(z) dz + C(1-g)g \frac{h(1-2g)}{2} \\ &= \int_0^{gh} \frac{C}{h^2} (h-z)z dz + C(1-g)g \frac{h(1-2g)}{2} \Rightarrow C = \frac{1}{g-2g^2+4/3g^3}. \end{aligned} \quad (7.16)$$

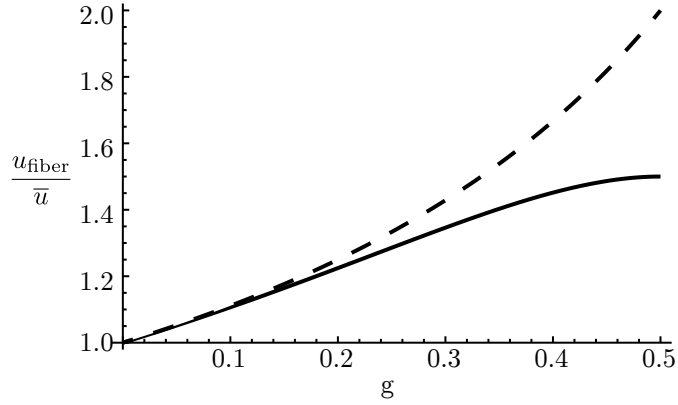


Figure 7.2: Ratio of rigid object velocity to mean velocity against gap width g . Dashed line: Couette profile, only valid for small g , and full line: The truncated Poiseuille profile.

The velocity profile is $f(z \leq gh) = \frac{(1-z)z}{g-2g^2+4/3g^3}$ and the ratio between solid object and mean flow velocity is:

$$u_f = \hat{u}(gh) = \bar{u} \frac{3-3g}{3-6g+4g^2}. \quad (7.17)$$

The relation of rigid object velocity to normalized gap height g is plotted in figure 7.2 and compared to the Couette profile from eq.(7.14). The gradient is obtained then from the profile:

$$f' = \frac{1}{h(g-2g^2+4/3g^3)}. \quad (7.18)$$

Using the gradient in the equations (7.9) to (7.11) closes the film lubrication model. Figure 7.3 shows velocity profiles for different confinements. For an increasing confinement the object velocity to mean velocity u_f/\bar{u} decreases, while the velocity gradient at the wall increases. The profile makes a smooth transition between the strongly confined case with a trapezoidal profile to the parabola in the unconfined case.

7.3 Microfluidic transport of discs

7.3.1 Analytical expression and validation of the numerical implementation

In analogy to the problem of streaming droplets we consider disc or pancake shaped rigid objects in an infinitely wide microchannel and address the question of their streaming velocity. The characteristic length scale is $L = R$, so the disc has a non-dimensional radius $r_d = 1$.

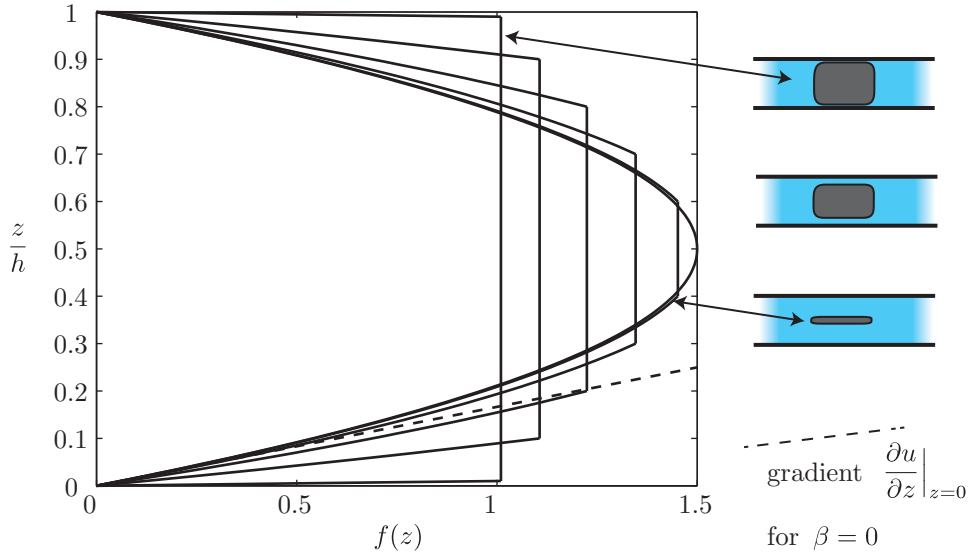


Figure 7.3: Model velocity profiles in the shallow direction in the presence of a rigid object. The flat region is where the object is located and hence the velocity is constant. Profiles are shown for $\beta = 0.98, 0.8, 0.6, 0.4, 0.2$ and 0 . For $\beta = 0$ the object is infinitely flat and the velocity profile becomes a parabola. The velocity gradient for $\beta = 0$ is illustrated by a tangent $- -$ line.

A disc at rest in free stream has a viscous drag (see section 2.3.1 eq.(2.68)) of:

$$F_{\text{disc}} = -\frac{\pi h v_{\infty}}{K_0(k)} (2 + 2A_3(k) - k^2 A_2(k) + k^2 K_0(k)). \quad (7.19)$$

A disc in linear motion in a quiescent fluid has a viscous drag on the lateral boundaries of:

$$F_{\text{mobil}} = \frac{\pi h u_f}{K_0(k)} (2 + 2A_3(k) - k^2 A_2(k)), \quad (7.20)$$

which is the same as F_{disc} except for absence of the linear pressure gradient in the absence of channel flow.

And additionally a drag component from the lubricating gap between disc and floor and ceiling, eq. (7.10):

$$F_{\text{gap}} = \frac{2\pi u_f}{h(g - 2g^2 + 4/3g^3)}. \quad (7.21)$$

Although the disc will not undergo rotation in an infinitely wide channel we will check that the respective force components for a disc with imposed rotation. The angular velocity and stress around a rotating disc is:

$$u_{\theta} = \dot{\theta} \frac{K_1(kr)}{K_1(k)}, \quad \sigma_{\theta} = \left(\frac{1}{r} \frac{\partial u_r}{\partial \theta} + r \frac{\partial}{\partial r} \left(\frac{u_{\theta}}{r} \right) \right). \quad (7.22)$$

Chapter 7. Solution of rigid objects

The viscous torque on the lateral boundaries on a rotating disc is

$$T_{\text{mobil}} = 2\pi r^2 \left. \frac{\partial}{\partial r} \left(\frac{u_\theta}{r} \right) \right|_{r=1} = 2\pi \dot{\theta} h \left(\frac{K_0(k)}{K_1(k)} k + 2 \right). \quad (7.23)$$

And the additional drag from rotation in eq. (7.10) in the lubricating gap:

$$T_{\text{gap}} = \frac{4\pi \dot{\theta}}{h(g - 2g^2 + 4/3g^3)} \int_{\Omega} r^2 dr = \frac{\pi \dot{\theta}}{h(g - 2g^2 + 4/3g^3)} \quad (7.24)$$

A component wise comparison between numerical and analytical results for a disc of aspect ratio $R/H = 8$ and gap size $g = \frac{1}{10}$, discretized with 400 elements reveals relative errors below 10^{-3} for each of the forces or torques.

The droplet velocity is obtained by imposing sum of forces equal to zero:

$$\begin{aligned} \sum F &= \frac{\pi h v_\infty}{K_0(k)} (2 + 2A_3(k) - k^2 A_2(k) + k^2 K_0(k)) \\ &+ \frac{\pi h u_f}{K_0(k)} (2 + 2A_3(k) - k^2 A_2(k)) + \frac{2\pi u_f}{h(g - 2g^2 + 4/3g^3)} = 0, \end{aligned} \quad (7.25)$$

$$\frac{u_f}{v_\infty} = \frac{2 + 2A_3(k) - k^2 A_2(k) + k^2 K_0(k)}{2 + 2A_3(k) - k^2 A_2(k) + \frac{2K_0(k)}{h^2(g - 2g^2 + 4/3g^3)}}. \quad (7.26)$$

The theoretical disc velocity is 0.7433, while numerically 0.7432 is obtained, corresponding to a relative error less than 10^{-4} .

In figure 7.4 disc velocities using eq.(7.26) are shown in comparison to numerical results. A decreasing confinement leads to higher disc velocities, the radius of the droplet has only a small influence and becomes negligible for large aspect ratios. The result has a certain resemblance with the droplet velocity, whose dependence on the aspect ratio was weak. For discs the confinement β finds its homologue in the droplet viscosity λ .

7.3.2 Disc shaped objects in experiments

Experiments on rigid objects were performed on the setup and under guidance of H el ene Berthet at PMMH, Physique et M ecanique des Milieux H et erog ene, in July 2012. In these experiments small discs were created inside the microchannels by photo-reticulation of a polymer solution, which crosslinks upon UV exposure, for method see Berthet et al. (2013).

The method of creation on demand of rigid objects inside the microchannels has the advantage that the alignment, or mathematically speaking the initial condition, can be controlled. Rigid objects fill almost the entire channel height except for a thin diffusion layer close to the PDMS. The gas diffuses from PDMS into the liquid which creates a $\approx 5\mu m$ thick layer that does not

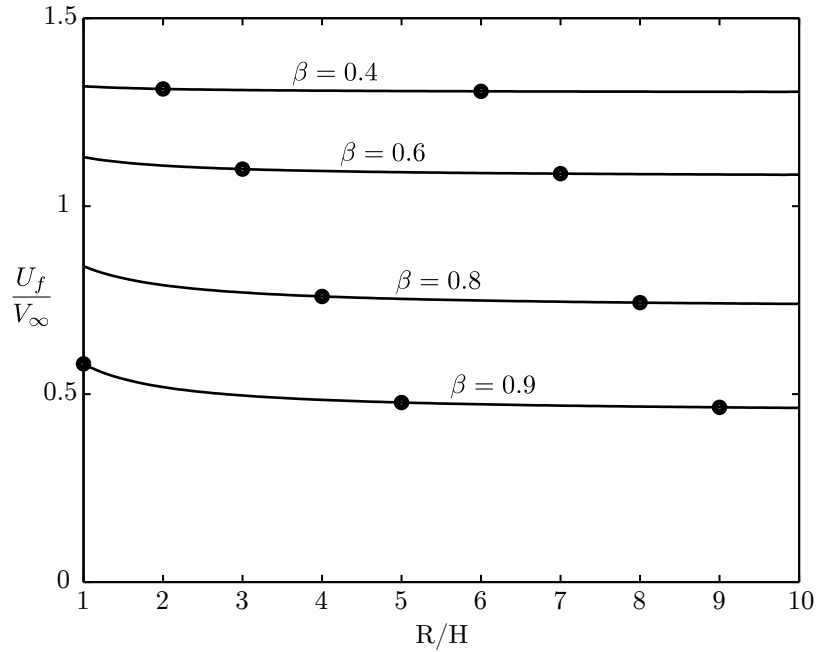


Figure 7.4: Relative velocity of disc shaped objects streamed in microchannels for varying aspect ratio. Four lines are shown, corresponding to different gap sizes or confinement, black $\beta = 0.9$, blue $\beta = 0.8$, red $\beta = 0.6$ and green $\beta = 0.4$. Dots correspond to numerical simulations with an interface discretized by 400 elements.

crosslinks. As a consequence the solid object does not attached to the channel ceiling/floor and remains mobil.

Two kinds of channels and two kinds of disc masks have been used. Channel 1 of high aspect ratio, $800\mu\text{m}$ wide and $22\mu\text{m}$ high, $W/H = 36.36$. And channel 2, $600\mu\text{m}$ wide and $61\mu\text{m}$ high, with aspect ratio $W/H = 9.84$. A small mask was used: disc of radius $55\mu\text{m}$ and a big mask: disc of radius $138\mu\text{m}$.

We measured the height of some fibers to infer the gap distance between disc and top/bottom confinement. Measurements were done creating elongated fibers of width $B_f < H$, these fibers turned sideways after some distance in the flow. Once turned sideways the height could be measured. In channel 1 fibers had a height of $H_{f,1} = 11\mu\text{m}$ thus a gap width of $5.5\mu\text{m}$ and channel 2 fibers were $H_{f,2} = 49\mu\text{m}$ high, meaning a gap width of $6\mu\text{m}$. There is one gap on the top and bottom side of the object, sketched in figure 7.1. The dimensions of the objects in a microchannel is illustrated in figure 7.5 and images from a microscope mounted camera are shown in figure 7.6.

We non-dimensionalize with disc radius R as length scale. Table 7.1 displays the aspect ratios for four cases obtained from channel height H , confinement $\beta = H_f/H$ and channel width W .

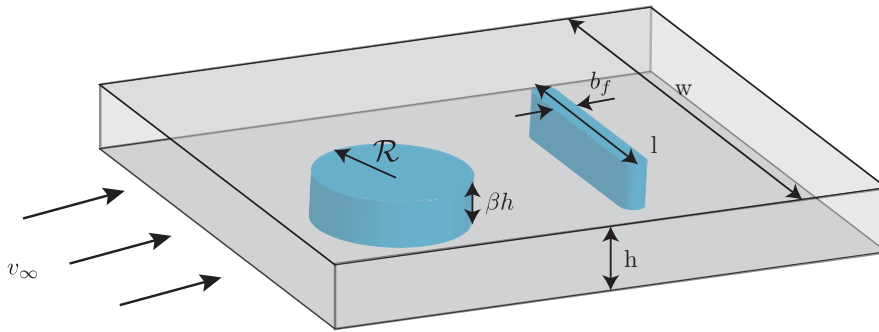


Figure 7.5: Schematic view of a disc and a fiber with their dimensions.

	Aspect ratio $\frac{R}{H}$	conf. β	lateral conf. $\frac{W}{2R}$
Case 1: High channel/big disc:	2.26	0.80	2.17
Case 2: High channel/small disc	0.90	0.80	5.46
Case 3: Flat channel/big disc	6.27	0.50	2.90
Case 4: Flat channel/small disc	2.50	0.50	7.27

Table 7.1: Geometrical parameters for disc transport experiments.

Velocities of the objects are non-dimensionalized with the mean flow velocity of the incoming fluid that was imposed by a syringe pump. The disc shaped objects are recorded with a camera and their displacement evaluated in MATLAB. Their velocity had only little variance for each single disc but varied considerably from disc to disc. In some cases the standard deviation was almost 20%. Deviation might be due to changed disc geometry at different flow rates because the fluid is in motion when under exposure ($t < 1$ s). In total 12 discs were analyzed, which is a small number of samples. A general rule of thumb is that increasing the confinement β lowers the disc velocity. The results are shown in table 7.2, the relative discrepancy $|\text{mean}(u_{exp}) - u_{th}| < 15\%$.

U_{disc}	Exp.	Model for $\frac{W}{2R} \rightarrow \infty$	Simu. with lateral conf.
Case 1:	0.916	0.783	0.898
Case 2:	0.876	0.850	0.915
Case 3:	1.076	1.207	1.232
Case 4:	1.318	1.216	1.237

Table 7.2: Disc velocities obtained in disc transport experiments.

The experiments performed show a lot of variation and more tests should have been tried to get reliable data. An experiment with a sequence of multiple discs, forming a train with

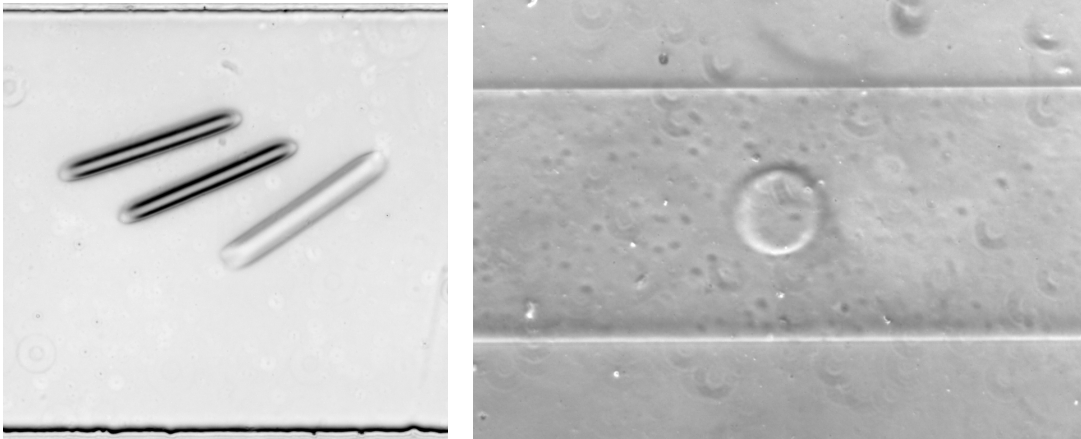


Figure 7.6: Images from the microscope of measurement of fiber height with two fibers in upright position and one fiber turned sideways (left). And image of a disc object in a microchannel (right).

spacing between the droplets bigger than 5 radii was done but the data not evaluated. A problem observed was that the discs got successively slower, most likely because the gap width decreased. This gap only exists because oxygen diffusion from the PDMS inhibits cross linking during UV exposure. Otherwise the exposure would form a column that sticks to the top and bottom walls. During successive disc formation the diffusion time might be too low and the oxygen gets depleted and the layer becomes thinner. An alternative explanation could be that partially reticulated material close to the wall is accumulated.

In a few cases some discs got blocked or stuck, which might be due to attachment to residue polymerized material on the wall. Experiments on trains of discs might only be realized with a mask of multiple discs to avoid creating discs at the same position.

The velocity for a disc almost as large as the channel tends towards $u_f = 1$, whereas the limit of far away boundaries depends on the gap size/confinement. When the disc in free stream travel slower than v_∞ there exists a maximum velocity for laterally confined discs, illustrated in figure 7.7. The maximum exists when the dissipation in the lateral gap becomes comparable to the dissipation in the direction perpendicular to the flow plane, which increases the pressure drop over the disc.

With growing gap size the disc velocity increases, which finally suppresses the local maximum present in figure 7.7. A word of caution: When the lateral gap width becomes equal to the lubricating gap in the perpendicular direction, it is no longer possible to argue that leaking in the lateral gap is present while the gap in the perpendicular direction has no leakage.

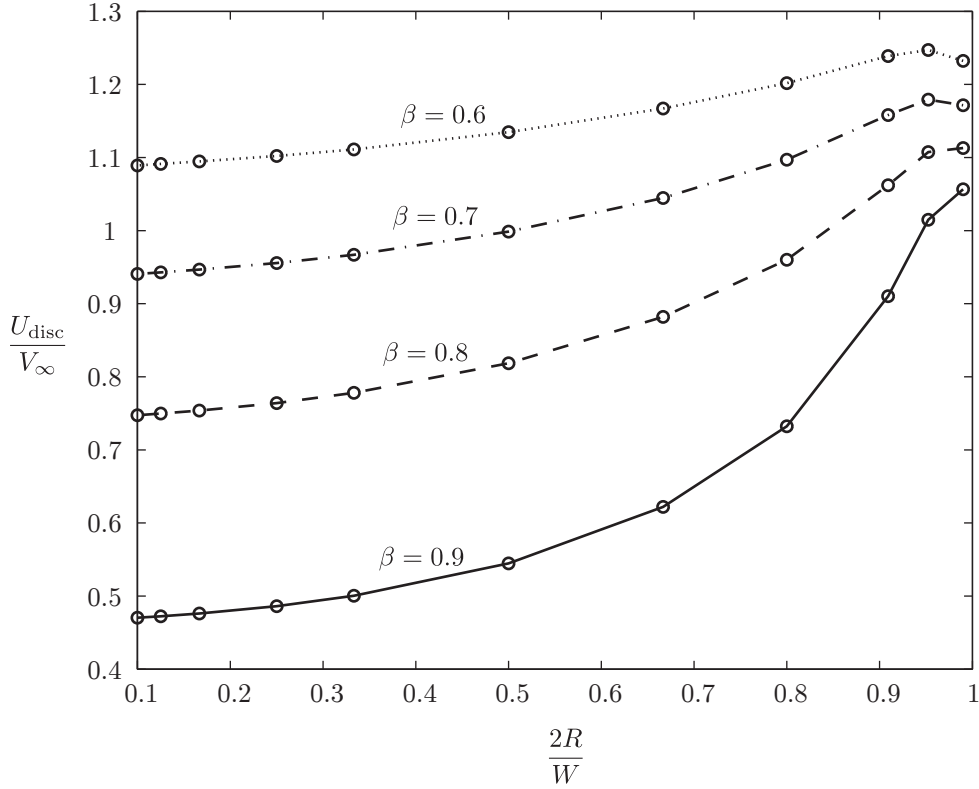


Figure 7.7: Velocity of a disc with confinement $\beta = 0.6\dots 0.9$ at disc aspect ratio $R/H = 8$ for changing lateral confinement $2R/W$.

7.4 Microfluidic transport of fibers

Experiments on elongated fibers that are transported in microchannels have been undertaken by Berthet et al. (2013). As in the previous experiments on the disk shaped objects, the experimental parameters are not known accurately and they have to be estimated. Fibers are elongated rigid objects of approximately square section, geometrically similar to a match stick. The fiber has a height H_f , width B_f and length L_f . Its ends are rounded with a radius $B_f/2$ and it is initiated in a microchannel of width W with an initial angle of attack of α_0 . The total length of the fiber is $L_f + B_f$ because L_f considers only the rectangular section of the fiber, not the half circle caps.

The system we simulate corresponds to:

$$\frac{B_f}{H_f} = 1, \quad \frac{W}{L_f} = 2 \text{ and } \frac{L_f}{B_f} = 10. \quad (7.27)$$

Note that when the confinement $\beta = H_f/H$ varies, so does the channel aspect ratio W/H .

$$\frac{W}{H} = \frac{W}{L_f} \frac{L_f}{B_f} \frac{B_f}{H_f} \frac{H_f}{H} = 20\beta. \quad (7.28)$$

7.4.1 Velocity of a fiber

The dependence of fiber velocity as a function of its orientation has been addressed both experimentally and numerically by Berthet *et al.* (2013). The fiber adopts a different velocity, when it is parallel or perpendicularly aligned with the streamlines in a flow. Furthermore the confinement β influences the velocity.

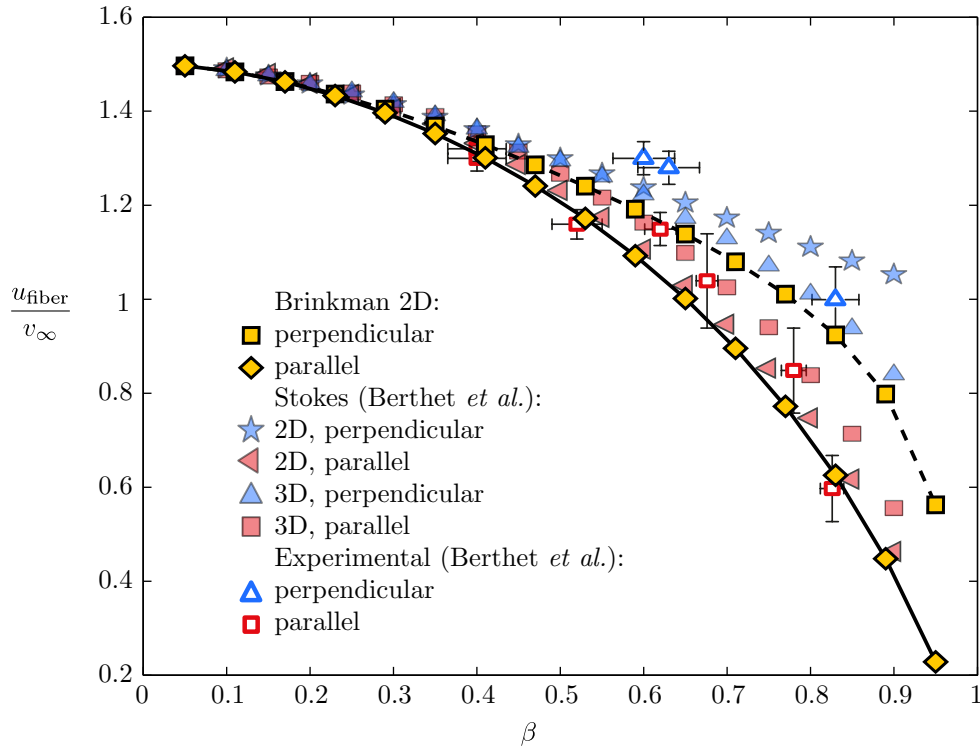


Figure 7.8: Fiber velocities for varying confinement β , computed with Brinkman 2D (yellow symbols) and compared to 3D & 2D Stokes simulations. The fiber has either parallel and perpendicular orientation to the flow.

Solving the problem numerically reveals a good agreement for the full range of confinement $\beta = 0 \dots 1$ shown in figure 7.8. Our 2D simulation agrees much better than the 2D simulations which considered Stokes flow in the x-z plane, unlike the x-y plane in our Brinkman simulations. For dynamical simulations of a fiber in a channel the method described here is likely to out-perform a 3D Stokes simulation since the calculation time for one iteration was about 1s.

Fibers at arbitrary angle α_0 between fiber angle and flow direction experience a drift velocity when the fiber orientation is different from 0° and 90° and the confinement $\beta > 0$. By drift we understand motion of the fiber perpendicular to the flow direction, which follows from different parallel and perpendicular streaming velocities. Berthet *et al.* showed that the incoming velocities on a fiber can be decomposed in parallel and perpendicular components and a resulting streaming vector can be obtained by adding the contributions. Picking parallel

Chapter 7. Solution of rigid objects

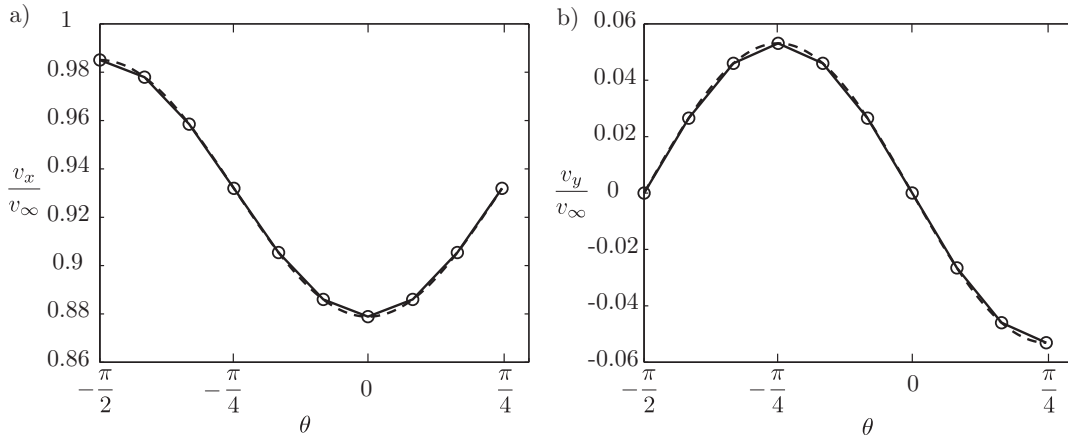


Figure 7.9: Fiber streaming velocities in flow direction a) and drift velocities b) for different angles of orientations, $\beta = 0.75$. Simulation results are shown as black line and model (eq. 7.29 and 7.30) as dashed line.

and perpendicular streaming velocity, v_{\parallel} and v_{\perp} , from figure 7.8 allows to determine the streaming with the flow v_x and drift v_y :

$$\frac{v_x}{v_{\infty}} = \frac{v_{\parallel}}{v_{\infty}} \cos^2(\theta) + \frac{v_{\perp}}{v_{\infty}} \sin^2(\theta), \quad (7.29)$$

$$\frac{v_y}{v_{\infty}} = \left(\frac{v_{\parallel}}{v_{\infty}} - \frac{v_{\perp}}{v_{\infty}} \right) \cos(\theta) \sin(\theta). \quad (7.30)$$

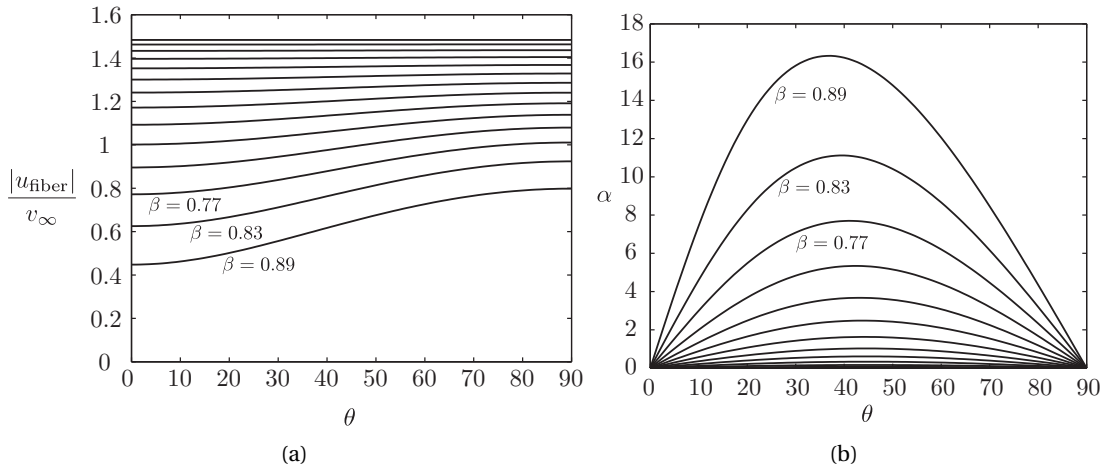


Figure 7.10: (a) Absolute fiber velocity and (b) Fiber drift angle for varying confinement $\beta = 0.89, 0.83, 0.77, \dots$, decreasing incrementally by 0.06.

This behavior is reproduced in simulations for a confinement $\beta = 0.75$ and compared against the theory (eq.(7.29) & eq.(7.30)), plotted in figure 7.9. The velocities v_{\parallel} and v_{\perp} for the model

equation have also been obtained from the simulation. Therefore perfect agreement of the two curves at $\theta = -\frac{\pi}{2}$ and $\theta = 0$ is obvious. Nevertheless there is good agreement for all intermediate angles.

The absolute velocity of a fiber for a given orientation θ and the drift angle α are to be determined.

$$|u_{\text{fiber}}| = \sqrt{v_x^2 + v_y^2} = \sqrt{v_{\parallel}^2 \cos^2(\theta) + v_{\perp}^2 \sin^2(\theta)}, \quad \alpha = \arctan\left(\frac{v_y}{v_x}\right). \quad (7.31)$$

In figure 7.10 the quantities are plotted. It shall be noted that the absolute fiber velocity is maximal for fibers aligned perpendicular to the flow ($\theta = 90^\circ$), while the maximum drift angle is obtained at $\theta = 45^\circ$ for low confinement and tends towards $\theta = 35^\circ$ with $\alpha_{\text{max}} = 16.33^\circ$ for $\beta = 0.89$.

7.4.2 Influence of lateral walls

Microfluidic channels have lateral walls and a fiber that is inclined to the flow by an angle different than 0° or 90° will at some moment approach the wall. When the fiber approaches the wall two distinct behaviors have been observed, the fiber undergoes either a reflection shown in figure 7.11 or a pole vault shown in figure 7.12. These two regimes have been observed by H el ene Berthet and reported in her thesis (Berthet, 2012).

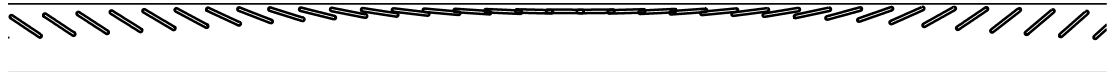


Figure 7.11: Time lapse of a simulated fiber inclined at 45° in a microchannel that is streamed from left to right. As the wall is approached the fiber turns and drifts in the opposite direction.

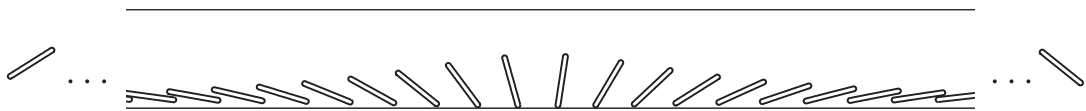


Figure 7.12: Time lapse of a simulated inclined fiber in a micro channel. The fiber has turned and starts moving away from the wall but gets into almost contact with the wall, pole vaults and reapproaches the wall.

The origin of the oscillating motion is understood by an imbalance of traction forces on the fiber. In free flow the symmetric fiber experiences a symmetric distribution of surface forces.

	F_x	F_y	M_θ
red	185.345	29.519	-1.873
blue	177.801	-2.94025	-2.52354
green	185.993	-32.2842	-1.47793

Table 7.3: Force and torque on a fiber during reflection, corresponding to figure 7.13.

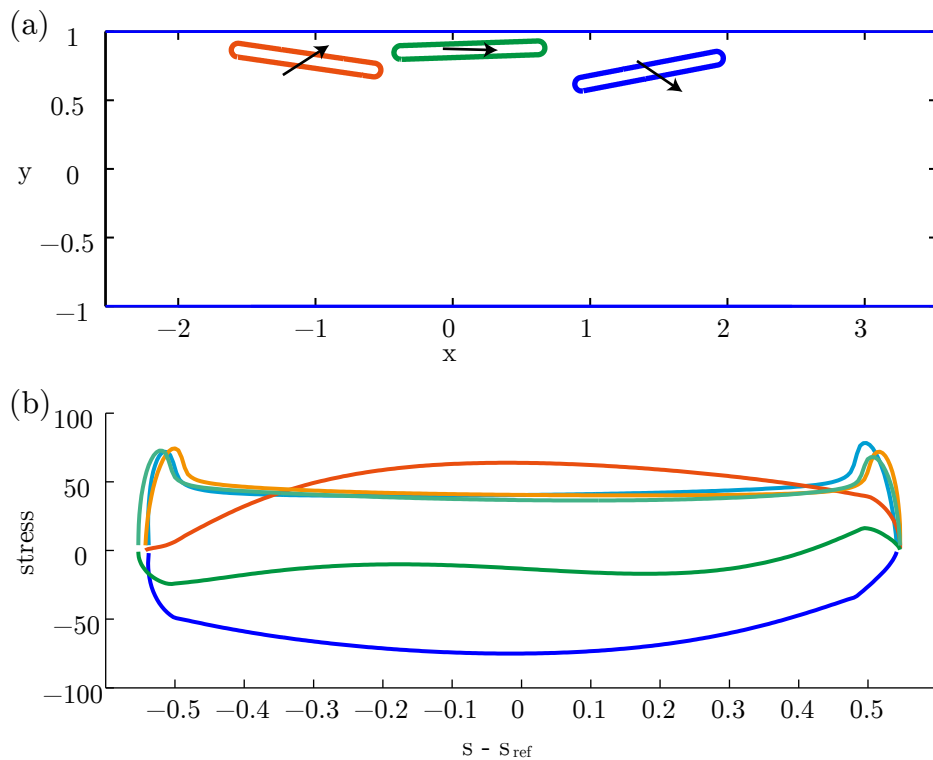


Figure 7.13: (a) A Fiber is reflected from a wall at $y \pm 1$. (b) The force distribution along the fiber is plotted, primary colors state the normal stresses and light colors the tangential forces. The tangential stresses remain almost constant but the normal stress changes its behavior. From upward force (red), to zero mean force, where asymmetry in x induces rotation (green) and downward force away from the wall and almost symmetric along the fiber (blue).

Oscillation When a symmetric fiber approaches a wall the symmetry is broken by interaction of the stress field with the wall and an asymmetric force distribution steers the fiber away from the wall. In figure 7.13 the approach of a fiber is plotted together with normal and tangential traction forces on the fiber. A collapse of all stress distributions during a half period of the oscillation cycle of a fiber is plotted in figure 7.14. One remarks the symmetric upward or downward force, when the fiber is far from the wall, and the asymmetric force distribution of zero drift at the inflection of the drift velocity.

Fiber motions are first simulated with fiber aspect ratio $\beta = 0.9$, that is $W/H = 18$ for the fiber and channel relations established in eq.(7.27). At different initial angles α_0 the fiber exhibits a closed orbit in the (y, α) phase space for small angles. In order to obtain accurate results even when the fiber comes close to the walls, the discretization of the fiber used 800 elements and the walls were discretized with 3400 elements. For larger initial angles very small time steps were necessary, $\Delta t = 10^{-3}$ using either Euler or a Runge-Kutta 2nd order scheme.

It is crucial to notice that the information of the initial fiber angle at the moment when the fiber is parallel to the wall is "stored" in the minimal fiber barycenter distance to the wall. The

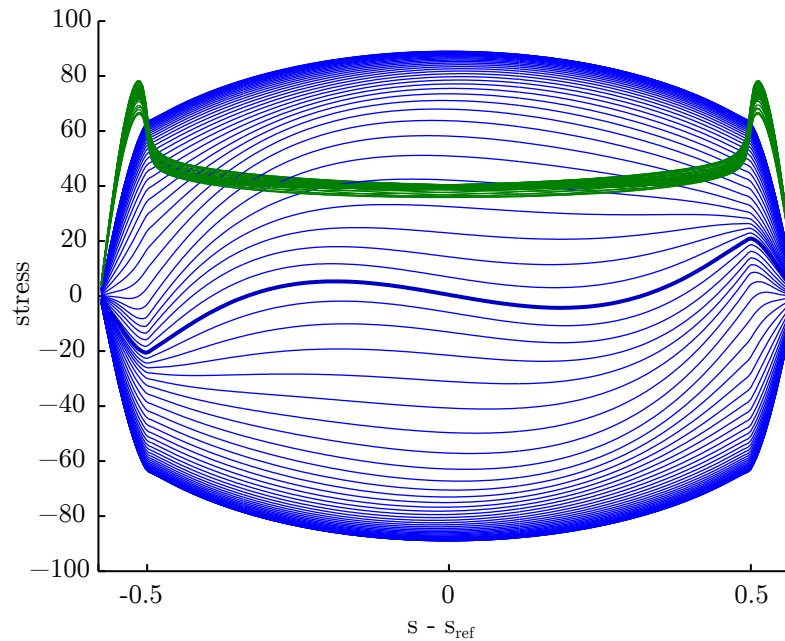


Figure 7.14: Superposition of all stress distributions of a fiber that approaches the wall from the channel center at $y = 0$. It is reflected from the wall and reapproaches the channel center line. Normal stress is given in blue and tangential stress in green.

higher the initial angle, the closer is the fiber approaches the wall. In a quasi stationary system there is indeed no other way to book keep this information. This behavior is demonstrated in figure 7.15, where is shown that ultimately all fibers attain an angle of zero degrees before bouncing back. Observe that the fiber reaches the minimal distance to the wall at incidence angle $\alpha = 0^\circ$.

For initial angles $\theta_i > 17^\circ$ the fiber tips get very close to the wall during the approach and departure phase, making the problem numerically difficult to tackle. This close contact introduces chaotic motion because slight deviations of position y_c change the orbit of the fiber. In figure 7.15 b) the minimum wall distance of the fiber is plotted against the initial angle. As the angle becomes larger than 17° the fiber distance form the wall at $\alpha = 0$ seems to saturate to a finite value.

This induces an extreme sensitivity to numerical errors, which further develops into chaotic trajectories for $\alpha_i > 17^\circ$. As seen in figure 7.15 a), for initial angles 20° and 25° one observes a change the orbit of the fiber. Although this effect is likely to be purely numerical, one can surely observe this behavior in experiments because even the most neat microchannel has a nanometric roughness. In a channel with lower aspect ratio and lower confinement the minimal distance between fiber and channel wall increases, as shown in table 7.4. Fibers in high confinement approach the wall so close that no space is left to accommodate the pole vaulting regime.

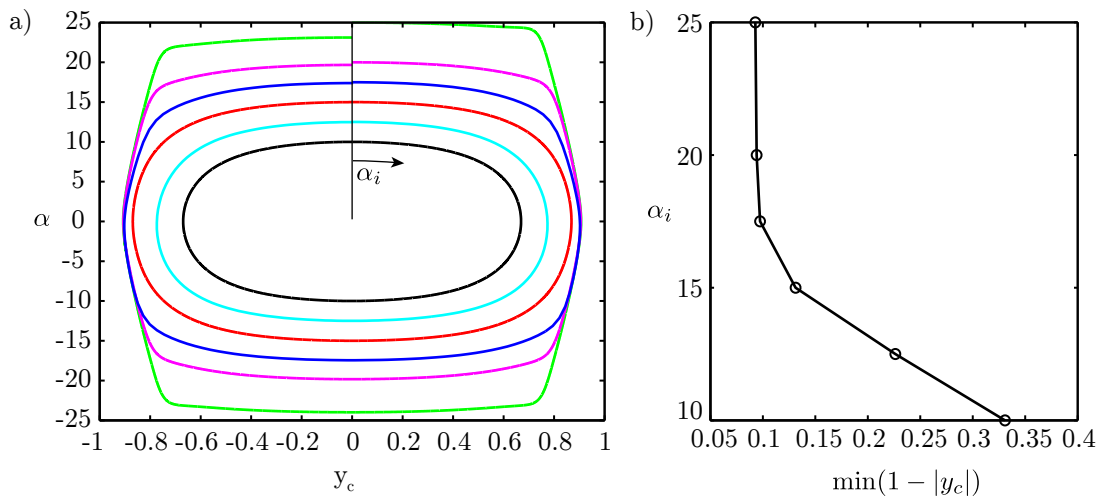


Figure 7.15: a) Orbits of fibers oscillating between channel walls, as the fiber center y_c approaches the channel walls $y \pm 1$ its angle approaches zero. b) Droplet initial angle α_i plotted against the minimum wall distance of the fiber center, when the angle $\alpha = 0^\circ$.

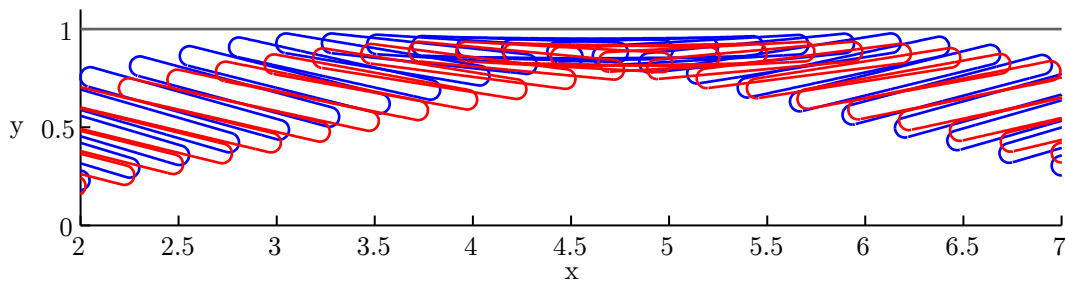


Figure 7.16: Fibers of initial angle $\alpha_i = 15^\circ$ (red) and $\alpha_i = 17.5^\circ$ (blue) approaching the wall. For 17.5° the fiber tip and tail get very close to the channel walls.

W/H	10	12	13	14	15	16	18
β	0.5	0.6	0.65	0.7	0.75	0.8	0.9
$\min(1 - y)$	0.2576	0.1972	0.1743	0.1545	0.1365	0.1210	0.0941

Table 7.4: Minimal wall distance for an initial angle $\alpha_i = 20^\circ$ increases with increasing confinement.

7.4.3 Pole vault motion of fibers

In pole vaulting the departing fibers tip gets trapped in the lateral wall boundary layer and induces a rotation around the tip that brings it back to the wall. Figure 7.12 shows an example of this type of motion.

Pole vaulting was never observed in channels of aspect ratio $W/H = 18$ with confinement $\beta = 0.9$. In a series of numerical simulations with $W/H = 12$ and $\beta = 0.6$ pole vaulting is

obtained for several initial conditions. Above initial angles of $\alpha \geq 30^\circ$ the fibers started pole vaulting but in an unpredictable fashion. One example with $\alpha_i = 30^\circ$ and $\Delta t = 0.1$ is shown figure 7.17. The position of the fiber center relative to the channel center line y_c and the orientation angle α is plotted in figure 7.18. For comparison y and α are plotted two identical fibers, one for time step $\Delta t = 0.1$ and one for a time step $\Delta t = 0.01$. With a lower time step, $\Delta t = 0.01$, the fiber preserves its initial orbit in the y, α phase space, while the fiber at a larger time step, $\Delta t = 0.1$ shows a chaotic motion.

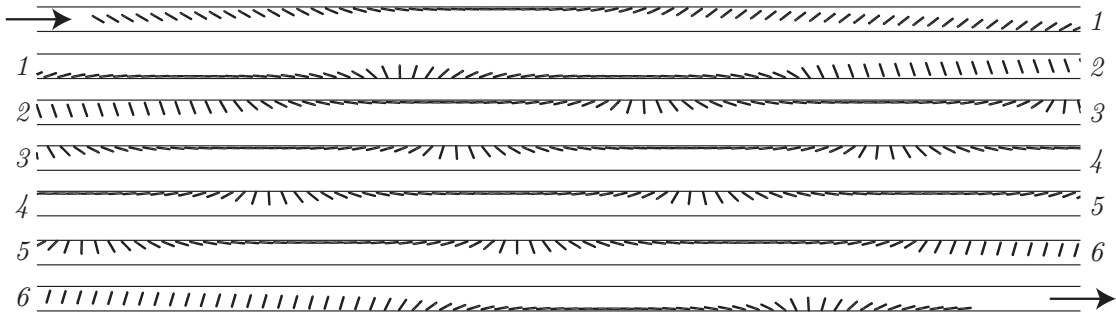


Figure 7.17: A fiber with an initial angle $\alpha = 30^\circ$ moves in a channel of aspect ratio $W/H = 12$. The time step of the simulation is $\Delta t = 0.1$, the sequence shows every 10^{th} time step. The fiber motion changes arbitrarily between oscillation and pole vaulting.

At the moment it can only be postulated that the pole vault state exists also as a closed loop orbit in the $y - \alpha$ phase space. Its minimal position y_c is closer to the wall than for the oscillating fibers. The closest wall distance of the oscillating fiber depends on the initial angle, on the confinement β and the channel aspect ratio W/H . More confined fibers tend to approach the wall closer than less confined fibers and thus might suppress a pole vault regime, which was impossible to observe in the simulations for $W/H = 18$.

The pole vault phenomenon is likely due to the close distance between the wall and the fiber tip. This close distance is very sensitive to errors and thus for larger time steps or insufficient spatial resolution the orbit changes between pole vaulting and oscillations.

Summary

The numerical study showed that small perturbations can lead to changes in the dynamics of the system. Although purely numeric this effect is also present in experiments due to imperfections and perturbations of the system. These imperfections introduce random change of the angle, steepening and flattening.

The numerical study presented shows that agreement of the simulated system with the experimental system can be established. Interaction between multiple rigid objects can be simulated, which opens a perspective to study collective behavior.

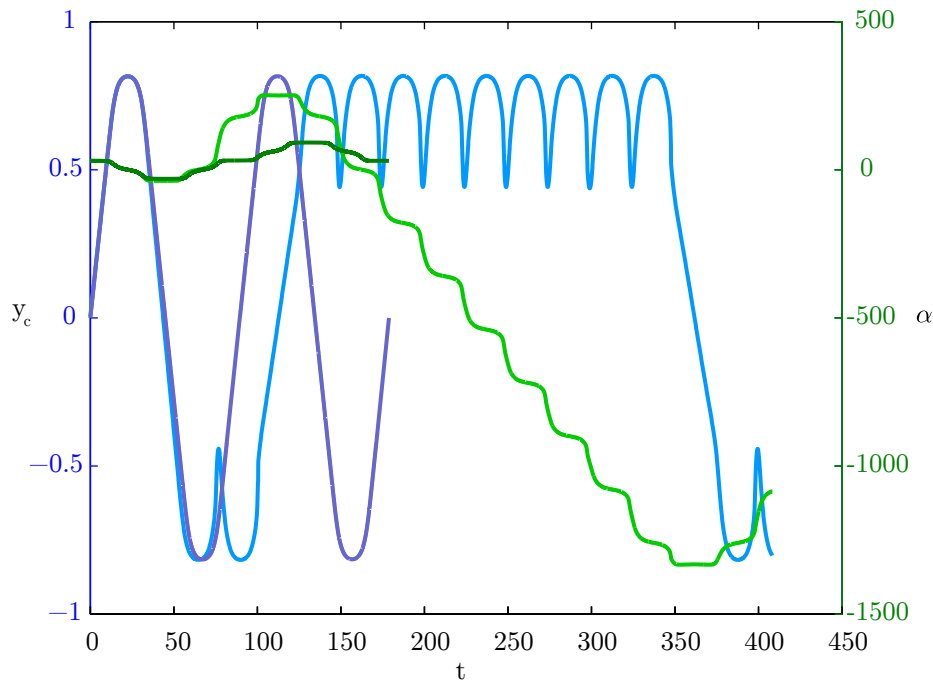


Figure 7.18: Two alternative evolutions of a fiber of $\alpha_i = 30^\circ$ in a microchannel of $W/H = 12$. The fiber center position y_c is shown in blue and the angle α in green, darker colors correspond to a time step $\Delta t = 0.01$ (only two periods shown) and the lighter colors to $\Delta t = 0.1$. While the fiber at a lower time step repeats its movement during two cycles, the fiber at a larger time step switches between pole vault motion and regular oscillation.

A deficiency of the rigid object so far is that they do not allow for a leaking flow in the gap. This could be solved by introducing a "porous" object, where the fiber region is solved by the Darcy equation to allow a flow past a blocked fiber.

Another simplification was to assume undeformable fibers. The boundary element method can also solve for problems in elasticity, which is governed by a different law than the fluid. Alternative one could model rigid objects by droplets with a viscosity that matches friction in the thin direction and a surface elasticity that tries to maintain a given shape. Flow of capsules has been studied and there is literature, which explains how modelling can be achieved (Pozrikidis, 2001).

An interesting link can be made between the motion of a fiber and the collective motion of droplets (Shen et al., 2014). The motion of two droplets shows the same type of oscillatory motion than the fiber. Both systems may be modelled in potential flow by a dipole distribution, where each droplet corresponds to a dipole or where the fiber is modelled by a two-dipole system.

8 Conclusion and perspectives

In this thesis a mathematical model for confined microfluidic flow was presented together with a numerical solution method adapted to two-phase flows. A number of simplifications were necessary to arrive at a description that combines the dominant mechanisms. The approximations were numerous:

1. Discarding inertia in general.
2. Averaging out dominant viscous effects, when assuming the plane Poiseuille profile in the perpendicular direction and when neglecting their variations in depth varying channels.
3. Reducing the interface shape to a line with a lumped model for the meniscus shape in the thin direction.

It is common sense in fluid dynamics to perform simplifications in an asymptotic sense (Bender and Orszag, 1999), which means ruling out small terms but reintroducing them as a perturbation to the simplified system. Reintroducing the perturbation creates a series of higher order approximations, which develops a solution that approaches the original system asymptotically.

In order to follow that strategy we would have needed to march in the foot steps of boundary layer approaches. That would have meant to use the Darcy equation and add the in-plane viscous stress by a singular perturbation approach only in the vicinity of boundaries. Examples in the literature have been pointed out, where singular perturbation was applied. For a versatile numerical approach with deformable interfaces a unified description was favored, which includes in-plane viscous stresses without the necessity to introduce boundary layers. This type of model was found in the Brinkman equation. The price to pay was the loss of a rigorous physical model that could be developed to higher orders till equivalence to the 3D Stokes equation may be obtained.

Chapter 8. Conclusion and perspectives

This decision was not taken arbitrarily: in light of the difficulty of some of the droplet microfluidic problems in which we engaged, we had the conviction that obtaining a leading order solution would already be a challenge. We further chose to exploit the linearity of the governing fluid equations to breed the Brinkman model with the Boundary Element Method, with the only limitation of domain wise constant parameters. The combination of both methods proved efficient for free interface problems, since only boundaries and interfaces were discretized. That meant the 3D flow problem around a deformable object was first turned into 2D by depth-averaging and then into 1D by a boundary integral transform.

For several applications the advancing interface was simulated and showed in most cases good agreement. The fact that the curvature is directly accessible from the numerical data led to the subtle observation that an symmetric shape relaxes to a so-called κ_2 oval before becoming a circle. A fine observation that engaged us, together with Pierre-Thomas Brun, to investigate closer the relaxation dynamics of liquid interfaces.

The numerical implementation left us with a quite general tool to investigate confined two-phase flow. Confinement for this type of model is a necessary condition because depth-averaging is based on the assumption that the height of the channel is small. In that regard the study on deformable droplets, which was compared to experiments by Brosseau et al. (2014), conducted at aspect ratio $W/H = 1$ showed still reasonable, though fragile, agreement with the experimentally observed scaling laws.

However, by virtue of depth-averaging, one of the largest problems of microfluidic simulation was circumvented: Where in 3D the droplet interface is deformed by the top and bottom confinement, the 2D interface feels only the confinement of lateral walls. Friction due to the top and bottom confinement was included in the equation by the permeability parameter k , which is high for high confinement and low for low confinement. A comparison of the droplet velocity to experiments nevertheless showed a disagreement with numerically obtained velocities. At the origin of the disagreement are the dreaded thin films, which do not contribute much themselves but induce a deformation of the meniscus at the lateral droplet interface.

There is something capricious to these thin films, which makes them a singular problem in the film formation theory of Bretherton (1961). The slower a droplet interface moves, the smaller are the films, but the smaller they are the more difficult they are to calculate. In a twist of perspective the thin direction in the microchannel was simulated, perpendicular to the axis of sight of the microscope. Computing the Stokes flow around the free interface one was able to simulate the film formation of films as small as $\sim 10^{-3}$ times the channel height. This being a formidable task in a 2D interface tracking method, gives an idea of the challenge to simulate 3D free interface of a droplet under confinement.

A corrected interface curvature, accounting for the dynamic meniscus, yielded droplets with a free stream velocity that agreed well with the experiments. Although the measurements were made without surfactants, there is confidence in the combined approach of the 2D Stokes film formation investigation and the 2D Brinkman lumped parameter model.

Inspired by the work of Rémi Dangla and Charles Baroud at LadHyX in Paris, further models for three-dimensional modifications of the channel geometries were invented. In a detailed analysis, together with Pierre-Thomas Brun, an investigation of droplet trapping was undertaken, which led to an illustration of numerous microfluidic applications by simulation as droplet parking and release and droplet mixing on a rail. The amalgam of 2D Stokes and Darcy equation of the Brinkman equation conforms well with theoretical considerations that Rémi Dangla developed in order to determine the deformation of anchored droplets.

As a final subject we considered the transport of solid objects like fibers with other microfluidic application is mind. The basic idea that led to the successful simulation of rigid objects was to explore the flow in the thin gap and to develop a lumped parameter model for the dissipation in the gap, as well as for the relation between rigid object and mean fluid velocity. The oscillating movements that have been observed in the channels were reproduced and an explanation proposed to elucidate why the oscillating fiber motion at low Reynolds number in these microchannels behaved in a chaotic way. Sudden changes of fiber drift angle between successive reflections from the walls were interpreted in connection with the minimal distance of the fiber position with respect to the wall and the free space drift angle. Small perturbations of the fiber position close to the wall during the reflection phase were seen to have a big influence on the fiber angle.

With all these approximations it is likely that only in few cases an exact agreement with experimental data can be obtained. Nevertheless in most cases the results agreed surprisingly well. More importantly, although the approximations are numerous there are only very few tuneable parameters introduced, probably the only ones being the blending function for the anchoring potential in chapter 6.1 and the transition function between front and rear meniscus in chapter 5.2, which are merely blending functions and not directly involved in the physics.

In the studies performed I often favored illustrative examples instead of a precise parametric analysis. It is not as much a matter of attitude as it follows the will to express a vision. A vision that microfluidic simulation can be performed at low computational cost and in a generalized framework that treats a wide range of microfluidic problems. In order to achieve that it was necessary to provide at a glance that well established droplet microfluidic phenomena are reproducible.

The numerical tool described in this thesis lies somewhere between a possibly impossible 3D computation of a confined droplet and the imaginative thought of the human mind. It can be considered as an intermediate virtual prototyping tool for microfluidic chip design, allowing quick and rather quantitative estimations.

Perspectives

Beyond that rush of impressions there are some studies that provided a deeper insight into the physics of droplet flow. The most important being to revisit the anchoring of droplets and the relaxation of droplets. Some other studies were left out for a more coherent presentation and because the results were too premature, such as for instance preliminary simulations of droplet shedding in a T-junction, droplet splitting in a T-junction, droplet merging by decompression (Bremond et al., 2008) or a qualitative study of the influence of soluto-capillary effects on the shape of an anchored droplet (Dangla et al., 2011). However these provide possible future fields of research. I shall present as promising perspectives two situations where the depth-averaged paradigm and the associated Brinkman equations reach their limitations and need further refinements: (i) when facing interfaces become too close and should lead to break-up of a droplet into two droplets through a complex pinch-off scenario and (ii) when an interface start to approach and tangent a wall.

Break-up model To this point a numerical tool has been developed that allowed for comparative studies of single droplet motion and deformation but in order to provide a tool that allows to design a microfluidic chip, it is necessary to simulate droplet break-up. Droplet break-up is driven by two competing curvatures, one curvature thinning the neck and the other opposing the deformation. Since the purely 2D model has only the opposing curvature component a geometrical model was devised that would induce break-up on physical grounds, in the spirit of transverse curvature manipulation developed for dynamic film formation and channel topography. This allows to simulate droplet shedding in a flow-focussing geometry, without having validated the approach on experimental data.

The rupture of liquid interfaces is a representation of finite time singularities. As such they have been studied as free interface flows of liquid jets, e.g. Ganan-Calvo and Gordillo (2001). In microfluidics the rupture of liquid threads is a key element of droplet microfluidics since usually continuous fluid threads are injected and need to be segmented into drops. Since the first discussion droplet shedding geometries, see Garstecki et al. (2005), a lot of research has been devoted to the investigate the scaling laws of the break-up process, see Dollet et al. (2008).

The choice of a pure 2D description is again flawed by a paradox that a viscous thread resists break-up because the thinning of the thread does not initiate rupture.

In 1873 Lord Rayleigh explained theoretically the formation of droplets from a liquid thread, which was observed in experiments by Joseph Plateau, the book by Charru (2011) gives a didactic presentation of the problem. Key to the break-up is that the radial curvature of the liquid thread increases when a neck is formed. As a consequence of Laplace's law, the fluid in the neck region gets pushed out the stronger, the smaller the neck radius. A confinement between plates stabilizes the liquid thread since the out-of-plane curvature remains bound to $h/2$, except when the interface approach each other closer than the distance h , so that the

thread turns cylindrical and is unconfined.

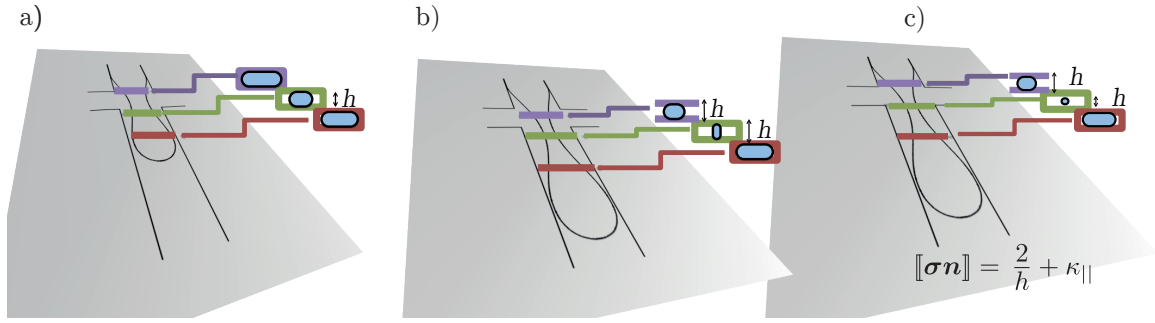


Figure 8.1: Model of Rayleigh-Plateau Instability. a) The liquid thread has a constant height prescribed by the channel. b) Necking occurs and the section of the thread becomes at some point narrower than the height, which is unphysical. c) Model correction assumes that the thread becomes circular and corrects the out-of-plane curvature to the corresponding value.

In order to achieve droplet break-up of a liquid thread, the boundary condition is modified on physical arguments to include the effect of non-constant dispersed liquid height in the z -direction. Modification is due to the fact that the interface in the perpendicular direction minimizes its area. For confined droplets, with diameter $d > h$, the curvature of the meniscus in the perpendicular to the flow plane in the absence of films is $\frac{2}{h}$, stated in chapter 2.2.3.

When the distance d^* between two opposite faces of a liquid interface approach each other at a distance closer than h , the meniscus curvature becomes $\frac{2}{d^*}$. That is because in the unconfined case the interface becomes cylindrical, an illustration is given in figure 8.1. The curvature of the dispersed fluid is calculated as for the axisymmetric case but is limited to a maximum of $2/h$ because of the confinement.

$$\kappa_{\perp}(\mathbf{x}) = \max\left(\frac{2}{d^* \sqrt{1 + (dy_d/dx)^2}}, \frac{2}{h}\right). \quad (8.1)$$

With y_d being the interface distance from the y axis and dy_d/dx being the derivative interface shape in x direction. It should be mentioned that by assuming a correct curvature of the cylindrical thread while keeping the depth-averaged realm of channels of constant thickness, the effective flux in the thread is overestimated.

A flow focusing device is cross shaped intersection with three inlets and one outlet. A liquid thread is cut into a train of droplets by two flows coming from the sides. This cross geometry is simulated with all channels having the same width. The liquid interface is not a closed ring, like in the case of droplets but an open line that joins the two walls at a distance of one channel diameter away from the crossing as presented in chapter 3.2.2.

Once the interfaces distance d^* falls below a certain threshold, here $d^* < h/100$, we artificially change the topology of the interface. The closes points are deleted and the neighboring points

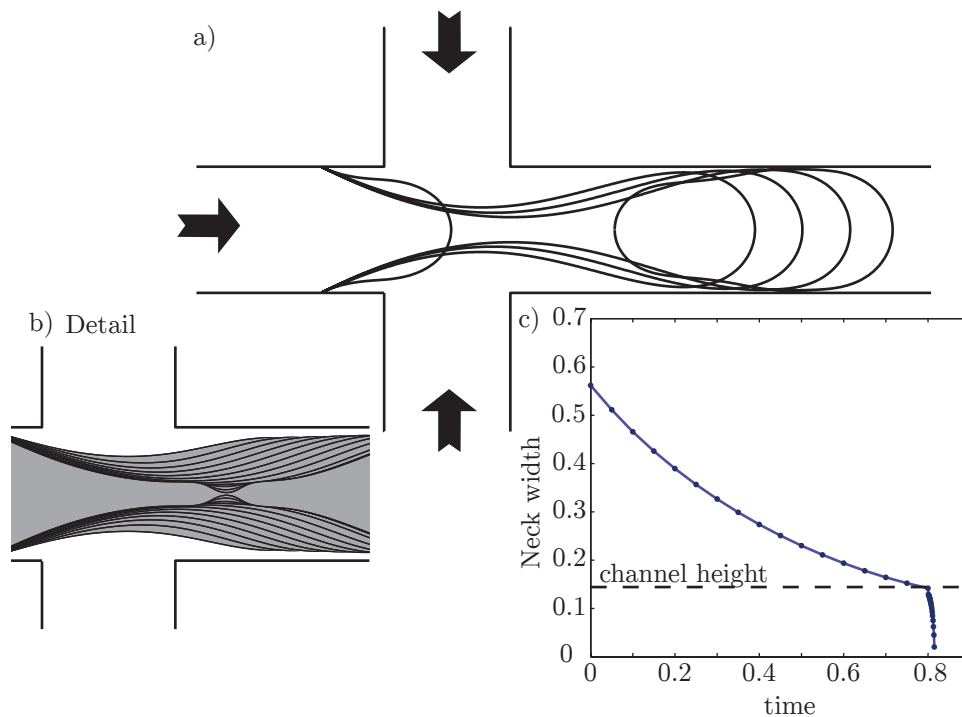


Figure 8.2: a) Liquid interface in a flow focussing geometry, shown are 3 interface positions before and 1 after break up. b) Zoom on the neck region. c) Collapse of the neck distance normalized by channel width d^*/w over time.

reconnected to their neighbors from the opposite interface, forming two distinct interfaces. We have observed that, in absence of interface correction accounting for the cylindrical thread geometry, d^* never reaches values as small as $h/100$.

As was shown by Dollet et al. (2008) by highspeed imaging the break-up in a flow focussing geometry undergoes several regimes with the ultimate collapse being in a highly inertial regime. We can not expect to observe these scaling laws but the initiation of necking is still in the viscous-capillary regime and the error induced by the lack of inertial is expected to be small on the droplet volume, due to the short time nature of the event.

An adhoc comparison between a simulation of droplet shedding and an experiment shows a good correlation for the volume of the droplet that is shed. The capillary number has been constructed on the velocity of the side channels, $Ca = 1.5 \cdot 10^{-4}$ and the center phase has a flow velocity that is 10 times lower. Break-up in the simulation appears earlier than in the experiment. Possibly in the experiment the outer fluid passes the inner fluid in gutters and reduces therefore the viscous entrainment. The numerical droplet has no gutters and is exposed to more shear, which accelerates the break-up.

Interfaces approaching walls-modeling gutters Gutters appear when an interface becomes close to a wall, in particular when a droplet adopts the racing oval shape visible in figure 8.3, a

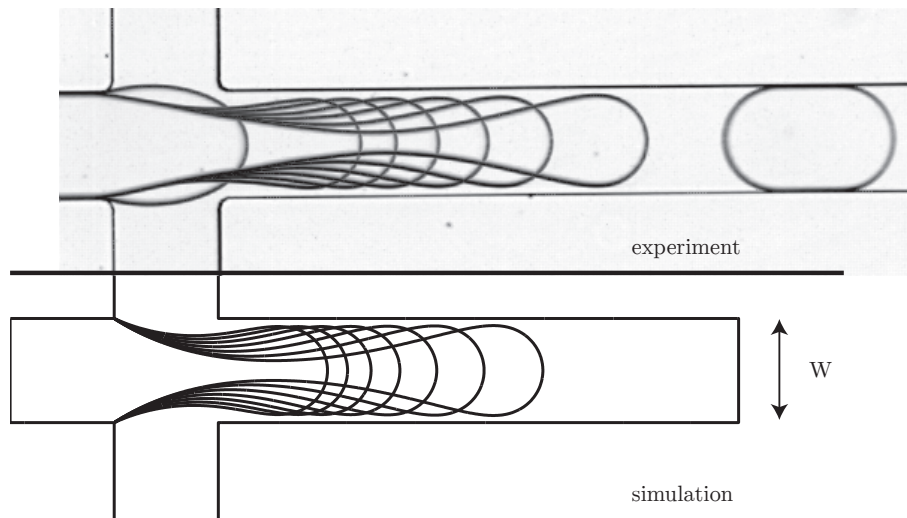


Figure 8.3: Simulation and experiment of droplet shedding in a flow focussing geometry. The channel aspect ratio in both experiments $W/H = 6.4$, viscosity ratio $\lambda = 4.1$ and the capillary number $Ca = 1.5 \cdot 10^{-4}$. The coflow ratio is 1/10.

situation which has been evoked earlier in section 4.3, as the influence of lateral confinement on droplet velocity was studied.

The gutters that were mentioned come from Latin *gutta*, a drop, according to Websters Dictionary originated in late Middle English and designates drops of molten wax that cuts a groove in a candle. From *gutta* and cutter to gutter. Later used for the channels on the side of street that carry away rain water.

When a non-wetting droplet moves through non-cylindrical channels, where it is confined by top/bottom and lateral walls its interface has to comply to the channel walls but leaves some unoccupied space due to finite curvature. This space is called a gutter, it appears on moving and static droplets, as illustrated in figure 8.4.

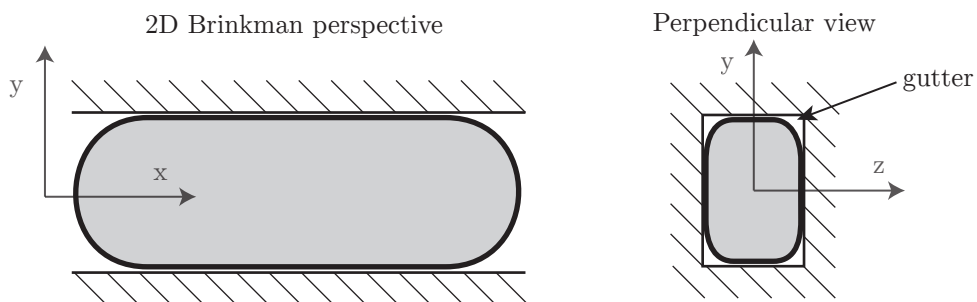


Figure 8.4: Schematic view of an elongated droplet in a narrow channel. The 2D depth-averaged point of view adopted in the realm the Brinkman equation does not account for the appearance of gutters.

By a etymological twist the gutter again turns its meaning to the drop, but curiously now not

Chapter 8. Conclusion and perspectives

being a groove cut by the drop but rather a groove formed by the drop.

This phenomenon is intrinsically three dimensional. Here I present a simple model to estimate them. The result is not new but it is much clearer to understand how to derive it. To illustrate the physical reasoning and because no connection with the rest of the work results we return to dimensional variables to make the topic clearer.

We begin the reasoning for a static droplet in a square channel. In the most approximate case the droplet might have a circular section in the channel with a radius of half the channel width. Its ends would have a spherical shape, depicted in figure 8.5 a) and b).

We assume constant pressure inside the droplet, which is true for a droplet at rest or a bubble ($\lambda = 0$) or approximately true when the capillary number is low. Then the pressure jump on the cylindrical part of the interface should be equal to the pressure jump over the spherical cap. Channel walls can deform the interface of the cylindrical part so we consider the curvature in the diagonal direction.

The pressure jumps associated to the cylindrical part $[[p_c]]$ or to the end caps $[[p_e]]$ written with half channel width a and surface tension γ are:

$$[[p_c]] = \frac{\gamma}{a}, \quad \text{and} \quad [[p_e]] = \frac{2\gamma}{a}. \quad (8.2)$$

Not surprisingly the pressures do not match and hence this approximate shape is not a static solution. The front caps create an higher pressure difference than the cylindrical section, thus the droplet interface gets pushed against the walls, the contact point in the cylindrical section moves and its radius decreases and the pressure jump increases. Secondary the curvature of the front cap decreases as the contact area increases.

One could draw the consequences of the opposite limit to the cylindrical geometry that is a droplet that adapts the square channel geometry and has an infinite pressure jump in the corners and a cap pressure jump of $\sqrt{2}/a$. This configuration, shown in figure 8.5 c) is what the depth-averaged dynamics actually represent but again the pressure jumps are not equal. Therefore the limit is found somewhere in between, this is illustrated in figure 8.5 d).

Imposing equal pressure jumps:

$$\frac{2}{\sqrt{1+b^2}} = \frac{1}{1-b} \Rightarrow b = \frac{8-\sqrt{28}}{6} \approx 0.45142. \quad (8.3)$$

Implementing lumped gutter models in the vicinity of walls could maybe be done by adding lateral porous layers, which would mimic the leaky piston effect.

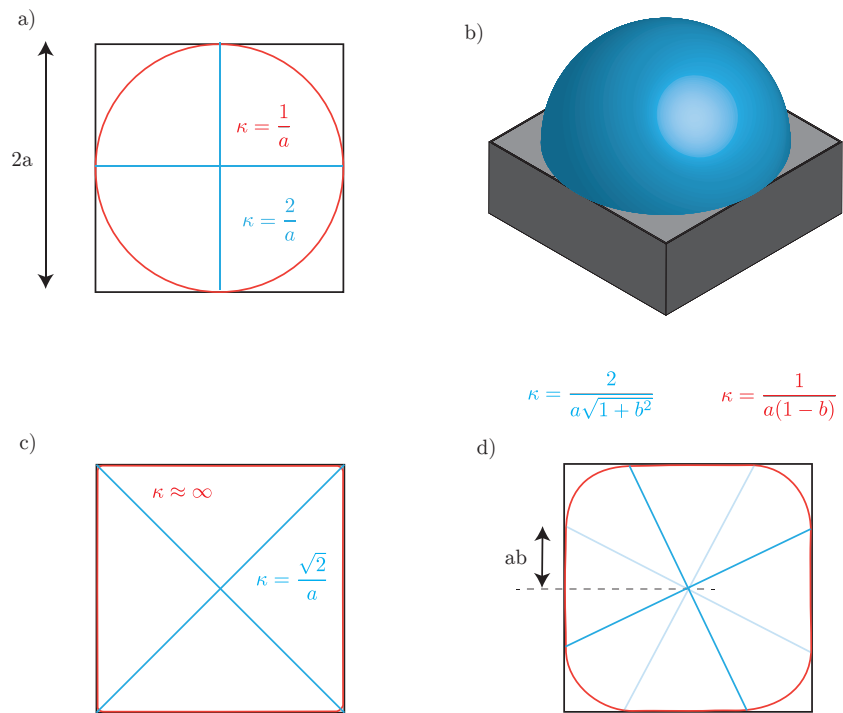


Figure 8.5: The origin of gutter: Curvature on a droplet in a square channel draw by a black line. Red line shows principal radius at the cylindrical region and blue line principal radii in the cap region. Top-left and bottom-left sketches show two limits that do not verify equality of pressure. Top-right sketch of cap region blue in a grey channel and bottom-right shows the static limit with equal pressure.

A Appendix

A.1 Numerical evaluation of Bessel functions

The modified Bessel function of second kind, zero and one, are needed $K_0(x), K_1(x)$.

These functions are solutions to the following equation, with boundary condition $K_n(0) = \infty, K_n(\infty) = 0$. When interchanging the boundary values one obtains the modified Bessel function of first kind $I_n(x)$. We approach for linear differential equations proposed by Bender and Orszag (1999) and write the Bessel equation:

$$x^2 y'' + x y' - (x^2 + n^2) y = 0.$$

The function has a irregular singular point at zero and at infinity. We set up to asymptotic developments around $x = 0$ and $x = \infty$.

A.1.1 Limit $x = \infty$

Because of the regular singular point we make an Ansatz $y = e^{S(x)}$.

$$y' = S' e^S, y'' = (S'' + S'^2) e^S$$

$$x^2(S'' + S'^2) + xS' - (x^2 + n^2) = 0.$$

When x goes to infinity and assuming that $S' < xS''$:

$$S'' = 1 \Rightarrow y = e^{\pm x/2} w(x)$$

We are interested in the solution that tends to zero. We peel of the known solution:

$$w'' x^2 + w'(x - 2x^2) - w(x + n^2) = 0.$$

Appendix A. Appendix

This equation is still regular singular and the dominant terms for a $w(x) = Cx^\alpha$ with unknown power are:

$$2xw' + w = 0 \Rightarrow w = Cx^{-1/2}.$$

One can peel of this term as well to look for a solution $y = C \frac{e^{-x}}{\sqrt{x}} v(x)$.

$$v''x^2 - 2x^2v' + \left(\frac{1}{4} - n^2\right)v = 0.$$

From this point on the problem has no singular points anymore and one is advised to insert an Taylor series in negative powers of x , $v = 1 + \sum_1^i a_n x^{-i}$.

$$2a_1 + \left(\frac{1}{4} - n^2\right) + \sum_1^i x^{-i} ((i(i+1) + 1/4 - n^2)a_i + 2(i+1)a_{i+1}) = 0.$$

Comparing leading order fixes $a_1 = (n^2/2 - 1/8)$.

Higher orders are determined from the summation:

$$a_{i+1} = -\frac{(i(i+1) + 1/4 - n^2)}{2(i+1)} a_i.$$

For K_0 : $a_{1..6} = -1/8, 9/128, -75/1024, 3675/32768, -59535/262144, 2401245/4194304$.

For K_1 : $a_{1..6} = 3/8, -15/128, 105/1024, -4725/32768, 72765/262144, -2837835/4194304$. Above this value the series becomes divergent, which would requires more elaborate summation techniques.

A.1.2 Limit $x = 0$

We proceed as before and insert $y = e^{S(x)}$ into the Bessel equation, again:

$$x^2(S'' + S'^2) + xS' - (x^2 + n^2) = 0.$$

This time $x \approx 0$, what makes the situation more complicated is that the behaviour is entirely different for $n = 0$ or $n = 1$. For $n = 0$ We balance $xy'' = -y'$ and obtain $y = C \ln(x)$ at leading order.

K_0 :

We peel off $\ln(x)$ and obtain:

$$x^2 \ln(x) v'' + (2x + x \ln(x)) v' - x^2 v = 0.$$

Which is asymptotically equivalent to the initial problem, where $y = Ce^{1/4x^2}$ would have been the leading order solution to the I_0 development. However this seemed to have relieved the degeneracy. In fact it indicates that there exists a series that solves the initial problem in the form of $v = \sum_0^j a_j x^{2j} + b_j x^{2j} \ln(x)$.

This way we insert:

$$x^2 v'' = -b_0 + \sum_1^j 2(j(2j-1)a_j x^{2j} + 2j(2j-1)b_j x^{2j} \ln(x) + (4j-1)b_j x^{2j})$$

$$x v' = b_0 + \sum_1^j 2j a_j x^{2j} + 2j b_j x^{2j} \ln x + b x^{2j}$$

$$x^2 v = \sum_1^j a_{j-1} x^{2j} - b_{j-1} x^{2j} \ln x$$

So we need to solve for each power in x

$$\sum_1^j (4j^2 a_j + 4j b_j - a_{j-1}) x^{2j} + (4j^2 b_j - b_{j-1}) x^{2j} \ln(x) = 0.$$

Two coefficients can be set a_0 and b_0 . The others are determined by:

$$b_j = \frac{b_{j-1}}{4j^2}, \quad a_j = \frac{a_{j-1} - 4j b_j}{4j^2}.$$

The variables are to be fixed with the matching conditions. This would give $b_0 = -1$ and $a_0 = \ln(2) - \gamma_E$.

K_1 :

First one tests a Ansatz like $y = x^{-p}$, which determines $p = n$ so in this case the leading order behaviour is $y = C/x$.

We peel this off and get:

$$w'' x - w' + w x = 0.$$

Trying a series shows that again log terms appear and it quickly shows that the series that fits to the problem is analogous to K_0 : $w = C/x + \sum_0^j a_j x^{2j+1} + b_j x^{2j+1} \ln(x)$. We obtain: $b_0 = C/2$,

Appendix A. Appendix

a_0 are undetermined and the recursive formulas are:

$$b_j = \frac{b_{j-1}}{(2j+1)^2 - 1}, \quad a_j = \frac{a_{j-1} - (4j+2)b_j}{(2j+1)^2 - 1}.$$

This allows a development of the Bessel function close to 0. They should be matched in some overlap region and will thus give the global solution.

This gives $C = 1$, $a_0 = 1/4(-1 - 2\ln(2) + 2\gamma_E)$.

A.1.3 Implementation

In this work the Bessel functions are needed for the identities A_1, A_2, A_3 with the option of leaving out the singular contribution, which appears at $x = 0$. Subtracting the singularity is necessary because in computer arithmetics subtraction of big numbers reduces the precision.

With $t = \log(x/2) + \gamma_E$:

$$\begin{aligned} K_0 = & -t + x^2 0.25(1 - t + x^2 0.03125(3 - 2t + x^2 0.009259259(11 - 6t + x^2 0.0078125(25 - 12t \\ & + x^2 0.002(137 - 60t + x^2 0.0208333333333333(49 - 20t + x^2 0.00072886297376(363 - 149t \\ & + x^2 0.001953125(761 - 280t))))))). \end{aligned}$$

$$\begin{aligned} K_1 = & 1/x + x 0.25(-1 + 2t + x^2 0.0625(-5 + 4t + x^2 0.05555555555(-5 + 3t + x^2 0.002604166666(-47 + 24t \\ & + x^2 0.005(-131 + 60t + x^2 0.01666666666(-71 + 30t + x^2 0.0012755102(-353 + 140t \\ & + x^2 0.001116071428(-1487 + 560t))))))). \end{aligned}$$

We will use a modified non-singular form K^M together with a singular term that can be subtracted.

$$K_0(x) = K_0^M x^2 - \log(x/2) - \gamma_E, \quad K_1(x) = \left(K_1^M x^2 + \frac{2\log(x/2) + 2\gamma_E - 1}{4} \right) x + \frac{1}{x}.$$

$$A_1 = 2(K_0^M + K_1^M)x^2 - \log(x/2) - \gamma_E - \frac{1}{2} = A_1^* + 1,$$

$$A_2 = -2(K_0^M + 2K_1^M)x^2 + 1 = A_2^* + 1,$$

A.2. An undeformable droplet based on Darcy's law

$$A_3 = \left(K_1^M x^2 + \frac{2 \log(x/2) + 2\gamma_E - 1}{4} \right) x^2 = A_3^* + 1.$$

Only A_1 is weakly singular, with an explicitly appearing log contribution, which may be subtracted and integrated analytically on a singular boundary element. The strongly singular expression for the test stress can now be written with a non-singular term and a singular contribution:

$$T_{ijk} = \frac{2}{r^2} (A_2 - 1) \delta_{jk} x_i + \frac{2}{r^2} (A_2 - A_3) (\delta_{ij} x_k + \delta_{ik} x_j) - 4 \frac{x_i x_j x_k}{r^4} (2A_2 - A_3).$$

Expressing the equation with non-singular terms A_2^* and A_3^* for a $A_n = A_n^* x^2 + 1$, gives:

$$T_{ijk} = x^2 \left(2A_2^* \delta_{jk} x_i + 2(A_2^* - A_3^*) (\delta_{ij} x_k + \delta_{ik} x_j) - 4 \frac{x_i x_j x_k}{r^2} (2A_2^* - A_3^*) \right) - 4 \frac{x_i x_j x_k}{r^4}.$$

The last term, $4 \frac{x_i x_j x_k}{r^4}$ is strongly singular but since the normals on a straight element can be written as: $n_x = y/r$, $n_y = -x/r$, which leads to:

$$\int_0^1 \tau \mathbf{n} ds \approx \int_0^1 -2 \frac{x_i x_j x y}{r^4} + 2 \frac{x_i x_j x y}{r^4} = 0.$$

Hence the strongly singular contribution cancels out, leaving an expression that can be numerically integrated.

A.2 An undeformable droplet based on Darcy's law

A droplet in a flow of magnitude $u_x = 1$ that moves at velocity u_d gives as a flowfield:

$$u_r = \sin(\theta) + (u_d - 1) \frac{\sin(\theta)}{r^2}, \quad u_\theta = \cos(\theta) - (u_d - 1) \frac{\cos(\theta)}{r^2}.$$

This flowfield is valid outside of the droplet, inside the velocity is simply $u_r = u_d \sin(\theta)$, $u_\theta = u_d \cos(\theta)$.

The flowfield in cartesian coordinates is:

$$u_x = 1 + (u_d - 1) \left(-\frac{1}{r^2} + 2 \frac{x^2}{r^4} \right), \quad u_y = 2(u_d - 1) \frac{xy}{r^4}. \quad (\text{A.1})$$

The external pressure field in cartesian coordinates and polar coordinates for a droplet moving at velocity U in a moving liquid is:

$$p = -k^2 x + (u_d - 1) k^2 \frac{x}{r^2}, \quad p = -k^2 r \sin(\theta) + (u_d - 1) k^2 \frac{\sin(\theta)}{r}, \quad (\text{A.2})$$

Appendix A. Appendix

The pressure field inside without the constant pressure jump is simply:

$$p = -\lambda k^2 r u_d \sin(\theta)$$

The inner fluid is vorticity free and has a different viscosity expressed by the viscosity ratio $\lambda = \mu_d / \mu$.

Forces on the droplet are defined in cartesian coordinates as:

$$F_x = \oint p \sin(\theta) d\theta, F_y = -\oint p \cos(\theta) d\theta.$$

sinus and cosinus represent the normals. We use 2D notation, in 3D the force would need to be multiplied by the height of the channel.

When evaluating the forces we get the inner contribution of:

$$F_{in} = -\lambda \pi k^2 u_d.$$

By the way, one obtains the same when integrating over the top and bottom surface of the droplet, thus adopting a 3 D point of view.

$$F_{in} = u_d \pi \lambda \frac{\partial u}{\partial z}$$

Then integrating the force that acts on the interface by the outer flow, which exerts:

$$F_{out} = \oint p \sin \theta d\theta = \oint \left(-k^2 \sin^2(\theta) + \sin^2(\theta) k^2 \frac{u_d - 1}{r} \right) d\theta = k^2 \pi (u_d - 2).$$

When applying sum of forces equal zero we get the condition:

$$\Sigma F = k^2 \pi (u_d + \lambda u_d - 2) = 0.$$

Without dynamic film formation we obtain $u_d = 2/(1 + \lambda)$. The difference to the Brinkman equation is quite small for small viscosity ratio λ or large aspect ratio.

A.3 Force integration on the top and bottom faces of a confined droplet

Two ways seem to be viable to evaluate F^{top} . One way is by integrating the tangential stresses on the top surface.

$$F^{top} = \mu_i \int_0^R \frac{\partial u}{\partial z} r dA = \frac{\mu_i k^2}{2} \int (E_{11} e + c) dA$$

$$\begin{aligned}
 &= \frac{\mu_i k^2}{2} \int \left(\left(I_0 r \sin^2 \varphi - \frac{I_1}{k} (1 - 2 \cos^2 \varphi) \right) e + U r - \frac{I_1(kR)}{kR} \right) dA \\
 &= \frac{\mu_i k^2 \pi}{2} \left(\int_0^R I_0 r dr - I_1 R \right) + \mu_i \pi k^2 R^2 U / 2 = \mu_i \pi k^2 R^2 U / 2.
 \end{aligned}$$

Using $\hat{u}(x, y, z) = u(x, y) \frac{12}{2h^2} x(h-x)$. Eliminating the Bessel from the integral is possible because of:

$$(x I_1)' = \left(I_0 - \frac{1}{x} I_1 \right) x + I_1.$$

A.4 Green's functions for 2D Stokes flow

Stokes flow Green's functions were taken from Wrobel's book Wrobel and Aliabadi (2002) and normalized with $\frac{-1}{4\pi}$ to yield a Dirac of strength 1. Shown are only the Green's functions with a forcing of the stress equation $a = 1, 2$, because the Green's function for a forced continuity equation, $a = 3$, is identical for 2D Stokes and Brinkman flows.

$$G_{ab} = \frac{1}{4\pi} (-\ln(r) \delta_{ab} + \frac{x_a x_b}{r^2}) \text{ and } T_{abc} = \frac{x_a x_b x_c}{\pi r}. \quad (\text{A.3})$$

A.5 Integral transformations

A.5.1 Integration by parts and Divergence Theorem

These techniques are used to derive the boundary integral equation in chapter 3.1. In fact integration by parts can be used to derive the Divergence Theorem.

One dimensional integration by parts is:

$$(uv)' = u'v + uv', \quad (\text{A.4})$$

$$\int (uv)' dx = uv = \int u'v dx + \int uv' dx. \quad (\text{A.5})$$

The divergence theorem simply turns into the definition of the integral:

$$\int_{x_0}^{x_1} \frac{du(x)}{dx} dx = u(x_1) - u(x_0). \quad (\text{A.6})$$

In two dimensions the integral becomes becomes:

$$\int_{\Omega} \frac{\partial u(x, y)}{\partial x} dx dy = \oint_{\omega} u(x(y), y) dy = \oint_{\omega} u(x(s), y(s)) n_x ds, \quad (\text{A.7})$$

$$\int_{\Omega} \frac{\partial v(x, y)}{\partial y} dx dy = \oint_{\omega} v(x, y(x)) dx = \oint_{\omega} v(x(s), y(s)) n_y ds, \quad (\text{A.8})$$

where ω is the contour of the area Ω . The contour might have x varying with y . In a last step the inetgration is performed along the contour increment ds instead of dy or dx . Since ds is the length of the contour $ds^2 = dx^2 + dy^2$ and one can express $dx = t_x ds$ and $dy = t_y ds$. Recalling the relation between tangent and normal: $n_x = -t_y$ and $n_y = t_x$.

Now writing for:

$$\int \nabla \cdot \begin{pmatrix} u \\ v \end{pmatrix} dA = \oint_{\omega} \begin{pmatrix} u \\ v \end{pmatrix} \cdot \begin{pmatrix} n_x \\ n_y \end{pmatrix} ds. \quad (\text{A.9})$$

A.5.2 Area, center of area and higher order moments

Area is is defined as: $A = \int 1 dA$ or expressing the infinitesimal aread element dA by $dx dy$: $A = \int \int 1 dx dy$. The volume in depth averaged channels is obtained simply by $V = Ah$, with height h . For boundary integral techniques it is advantagous to obtain all information from the boundary. Therefore we use Gauss law to calculate area and higher order moments, for which the equations are given here. The last equation states the discrete form for piece-wise linear geometries. It is accurate in the sense that it gives the result for piece-wise linear boundaries.

$$A = \int_{\Omega} 1 dA = \frac{1}{2} \int_{\Omega} \nabla \cdot \begin{pmatrix} x \\ y \end{pmatrix} dA = \frac{1}{2} \oint_{\omega} \begin{pmatrix} x \\ y \end{pmatrix} \cdot \mathbf{n} ds = \frac{1}{4} \sum_i ((x_{i+1}^2 - x_i^2) n_x + (y_{i+1}^2 - y_i^2) n_y). \quad (\text{A.10})$$

Center of area

$$X_c = \frac{1}{A} \int_{\Omega} x dA = \frac{1}{2A} \int_{\Omega} \nabla \cdot \begin{pmatrix} x^2 \\ 0 \end{pmatrix} da = \frac{1}{2} \oint_{\omega} x^2 n_x ds = \frac{1}{6A} \sum_i (x_{i+1}^3 - x_i^3) n_x \quad (\text{A.11})$$

The routine can be tested for example with the 2nd moment of a circle:

$$\int x^2 + y^2 dA = 2\pi \int_0^r r^3 dr = \frac{\pi}{2} r^4. \quad (\text{A.12})$$

And also on the 2nd moment of a long beam ($x \gg y$ and $L \gg h$):

$$\int x^2 + y^2 dA \approx \int_{L/2}^{L/2} x^2 h dx = \frac{L^3 h}{12}. \quad (\text{A.13})$$

A.6 Resolving issues with singular integrals

Typical boundary integral equations for BEM have singular kernels. These are weakly and strongly singular and methods have been proposed in the literature that tackle this problem. When using higher order singularities that are necessary to evaluate pressure, velocity gradients or stress gradients directly one faces hyper-singular kernels. Treatment of these terms is difficult and shall be discussed here.

A.6.1 The singular boundary integral equation

A strong singular term is encountered when evaluating the pressure on the boundary. The boundary integral equation is given as:

$$\int_{\Omega} ((\Delta \mathbf{v} - k^2 \mathbf{v} - \nabla q) \cdot \mathbf{u} + p \nabla \cdot \mathbf{v}) dA + \oint_{\omega} \boldsymbol{\sigma} \mathbf{n} \cdot \mathbf{v} - \begin{pmatrix} 2 \frac{\partial v_1}{\partial x} - q & \frac{\partial v_1}{\partial y} + \frac{\partial v_2}{\partial x} \\ \frac{\partial v_1}{\partial y} + \frac{\partial v_2}{\partial x} & \frac{\partial v_2}{\partial x} - q \end{pmatrix} \mathbf{n} \cdot \mathbf{u} ds = 0. \quad (\text{A.14})$$

The test functions are \mathbf{v} a velocity and q a pressure:

$$v_i = \frac{1}{2\pi} \frac{x_i}{x^2 + y^2}, \quad q = -\frac{k^2}{4\pi} \ln(r^2). \quad (\text{A.15})$$

Integration is done on the singular element, for domain integrals with Gauss law on the element and a half circle around it. See figure A.1 for an illustration of the coordinate system and an arbitrary boundary turned by an angle θ .

A.6.2 Term 1: Domain integral $p \nabla \cdot \mathbf{v}$

Now the domain integral $p \nabla \cdot \mathbf{v}$ can be integrated, we assume at first that p is constant:

$$\int p \nabla \cdot \mathbf{v} dA = \frac{p}{2\pi} \oint \begin{pmatrix} \frac{x}{x^2 + y^2} \\ \frac{y}{x^2 + y^2} \end{pmatrix} \cdot \begin{pmatrix} n_x \\ n_y \end{pmatrix} ds. \quad (\text{A.16})$$

Here the divergence theorem has been applied in order to avoid the singularity. Splitting the integral into two part. The first on the half circle, transforming to polar coordinates $x = r \cos(\phi)$, $y = r \sin(\phi)$, $n_x = \cos(\phi)$ and $n_y = \sin(\phi)$.

$$\frac{p}{2\pi} \int_{\theta}^{\theta+\pi} \begin{pmatrix} \frac{\cos(\phi)}{r} \\ \frac{\sin(\phi)}{r} \end{pmatrix} \cdot \begin{pmatrix} \cos(\phi) \\ \sin(\phi) \end{pmatrix} r d\phi = \frac{p}{2\pi} \int_{\theta}^{\theta+\pi} \cos^2(\phi) + \sin^2(\phi) d\phi = \frac{p(x_0)}{2}. \quad (\text{A.17})$$

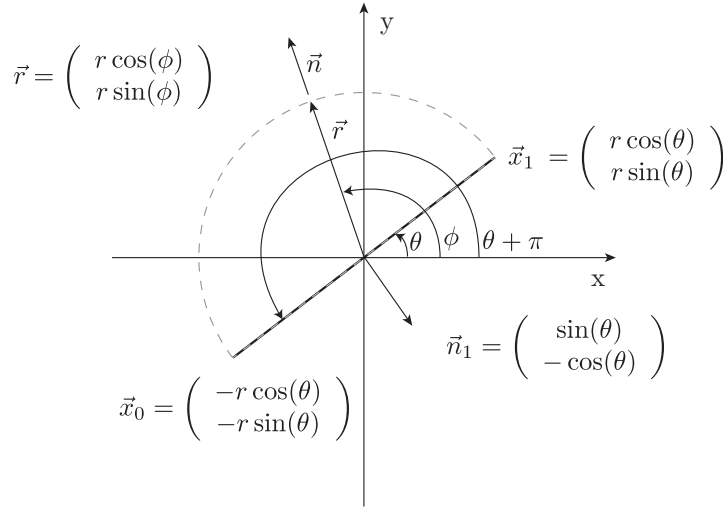


Figure A.1: Coordinate system with an integration path on the singular boundary between \mathbf{x}_0 and \mathbf{x}_1 and a half circle.

The second part between \mathbf{x}_0 and \mathbf{x}_1 :

$$\frac{p}{2\pi} \int_{\theta}^{\theta+\pi} \begin{pmatrix} \frac{\cos(\phi)}{r} \\ \frac{\sin(\phi)}{r} \end{pmatrix} \cdot \begin{pmatrix} \sin(\phi) \\ -\cos(\phi) \end{pmatrix} r d\phi = 0. \quad (\text{A.18})$$

The integral is performed on a Dirac distribution and therefore the assumption that p is constant is verified.

A.6.3 Term 2: Boundary integral $\sigma \mathbf{n} \cdot \mathbf{v}$

For a straight line element we express x, y in terms of s oriented by an arbitrary angle θ . We replace $x = s \cos(\theta)$, $y = s \sin(\theta)$ and $r = s$. For the x -member of the normal stress we write f_1 and for the y -member f_2 .

$$\oint_{-e}^e \sigma \mathbf{n} \cdot \mathbf{v} ds = \oint_{-e}^e f_1 \frac{x}{2\pi r^2} + f_2 \frac{y}{2\pi r^2} ds = \oint_{-e}^e f_1 \frac{\cos(\theta)}{2\pi s} + f_2 \frac{\sin(\theta)}{2\pi s} ds. \quad (\text{A.19})$$

The integrals will result in a $\log(s)$, since \log is only defined in the positive half space of x we therefore separate the integral into two parts, that are now both in positive s but one with $\theta + \pi$, turned by 180° .

$$\int_0^e f_1 \frac{\cos(\theta)}{2\pi s} + f_2 \frac{\sin(\theta)}{2\pi s} ds - \int_0^e f_1 \frac{\cos(\theta)}{2\pi s} + f_2 \frac{\sin(\theta)}{2\pi s} ds = 0. \quad (\text{A.20})$$

A.6.4 Term 3: Boundary integral $\tau \mathbf{n} \cdot \mathbf{u}$

The second term however shows to be strongly singular and does not cancel itself off.

$$\begin{aligned}
 & \oint_{-\epsilon}^{\epsilon} \begin{pmatrix} 2 \frac{\partial v_1}{\partial x} - q & \frac{\partial v_1}{\partial y} + \frac{\partial v_2}{\partial x} \\ \frac{\partial v_1}{\partial y} + \frac{\partial v_2}{\partial x} & \frac{\partial v_2}{\partial x} - q \end{pmatrix} \begin{pmatrix} n_x \\ n_y \end{pmatrix} \cdot \mathbf{u} ds \\
 = & \frac{1}{2\pi} \oint_{-\epsilon}^{\epsilon} \begin{pmatrix} \frac{2}{s^2} - \frac{4 \cos^2(\theta)}{s^2} + k^2 \ln(s) & -\frac{4 \sin(\theta) \cos(\theta)}{s^2} \\ -\frac{4 \sin(\theta) \cos(\theta)}{s^2} & \frac{2}{s^2} - \frac{4 \sin^2(\theta)}{s^2} + k^2 \ln(s) \end{pmatrix} \begin{pmatrix} \sin(\theta) \\ -\cos(\theta) \end{pmatrix} \cdot \mathbf{u} ds \\
 = & \frac{1}{2\pi} \oint_{-\epsilon}^{\epsilon} \frac{-2}{s^2} \begin{pmatrix} \sin(\theta) \\ -\cos(\theta) \end{pmatrix} \begin{pmatrix} u_1 \\ u_2 \end{pmatrix} ds = \frac{-1}{\pi} (\sin(\theta) u_1 - \cos(\theta) u_2) \oint_{-\epsilon}^{\epsilon} \frac{1}{s^2} ds \\
 = & \frac{-1}{\pi} (\sin(\theta) u_1 - \cos(\theta) u_2) \left(\frac{2}{\epsilon} - \frac{2}{0} \right). \quad (\text{A.21})
 \end{aligned}$$

I omitted $k^2 \ln(s)$ not because it is zero but because it is finite and can be obtained easily. We are left with a term that is infinite. This is curious because the pressure should remain bound.

The only possible explanation I have so far is that the domain integral has an infinite contribution as well. This suspicion come from the fact that the classical test function, which has a Greens function with its Dirac in the divergence of the stress tensor, does not contribute to the divergence of the velocity field. One could say this is because the order of the singularity is lower (one derivative and not two).

When forcing the divergence of the velocity field one could expect that at the same time arises a singularity in the divergence of the stress tensor that is infinite. Moreover since practical cases so far did not show a malfunction of the pressure integration in the domain, one could believe that this infinite contribution cancels out when integrating over the whole singularity and not only on half of it, when on the boundary.

A.6.5 Term 4: The unexpected strong singular domain integral

When integrating over the domain, without taking care of the singularity the integral is zero. Just as for the domain integral over the divergence of the velocity field.

In fact in equation A.14 the domain integral that is multiplied by u has two parts that cancel each other out because they are constructed to compensate each other $\nabla q = -k^2 \mathbf{v}$. The other term $\Delta \mathbf{u}$ however opens a possibility to be non-zero.

The divergence for the first component, assuming u is constant:

$$\int \mathbf{u} \Delta \mathbf{v} dA = \frac{1}{2\pi} \oint u_1 \begin{pmatrix} \frac{1}{r^2} - \frac{2x^2}{r^4} \\ -\frac{2xy}{r^4} \end{pmatrix} \cdot \begin{pmatrix} n_x \\ n_y \end{pmatrix} + u_2 \begin{pmatrix} -\frac{2xy}{r^4} \\ \frac{1}{r^2} - \frac{2y^2}{r^4} \end{pmatrix} \cdot \begin{pmatrix} n_x \\ n_y \end{pmatrix} ds \quad (\text{A.22})$$

Appendix A. Appendix

An equivalent gradient form ∇v would have been the stress tensor, however the chosen form is shorter. Integrating around a half circle, whose planar side is oriented by the angle θ and delimited between ϵ and ϵ , just as the boundary above. Beginning integration with the half circle from $(\epsilon \cos(\theta), \epsilon \sin(\theta))$ counter clockwise to $(-\epsilon \cos(\theta), -\epsilon \sin(\theta))$.

$$\begin{aligned} & \frac{1}{2\pi} \oint \left(u_1 \left(\frac{\frac{1}{r^2} - \frac{2\cos^2(\phi)}{r^2}}{-\frac{2\sin(\phi)\cos(\phi)}{r^2}} \right) \cdot \begin{pmatrix} \cos(\phi) \\ \sin(\phi) \end{pmatrix} + u_2 \left(\frac{-\frac{2\sin(\phi)\cos(\phi)}{r^2}}{\frac{1}{r^2} - \frac{2\sin^2(\phi)}{r^2}} \right) \cdot \begin{pmatrix} \cos(\phi) \\ \sin(\phi) \end{pmatrix} \right) r d\phi \Big|_{r=\epsilon} \\ = & -\frac{1}{2\pi} \int_{\theta}^{\theta+\pi} \frac{u_1 \cos}{r} + \frac{u_2 \sin}{r} d\phi = -\frac{1}{2\pi} \frac{u_1 \sin(\phi)}{\epsilon} - \frac{u_2 \cos(\phi)}{\epsilon} \Big|_{\theta}^{\theta+\pi} = \frac{1}{\pi} \left(\frac{u_1 \sin(\theta)}{\epsilon} - \frac{u_2 \cos(\theta)}{\epsilon} \right) \end{aligned} \quad (\text{A.23})$$

Now integrating equation A.22 along the center line from $(-\epsilon \cos(\theta), -\epsilon \sin(\theta))$ to $(\epsilon \cos(\theta), \epsilon \sin(\theta))$.

$$\begin{aligned} & \int_{-\epsilon}^{\epsilon} \frac{u_1 \sin(\theta)}{2\pi s^2} (1 - 2\cos(\theta) - 2\sin(\theta)) - \frac{u_2 \cos(\theta)}{2\pi s^2} (1 - 2\cos(\theta) - 2\sin(\theta)) ds \\ & = \frac{2u_1 \sin(\theta)}{\pi s} - \frac{2u_2 \cos(\theta)}{\pi s} \Big|_0^{\epsilon} = \left(\frac{2u_1 \sin(\theta)}{\pi} - \frac{2u_2 \cos(\theta)}{\pi} \right) \left(\frac{1}{\epsilon} - \frac{1}{0} \right). \end{aligned} \quad (\text{A.24})$$

A.6.6 Combination of singular integrals

So in fact the singular integrals, coming from domain integral and boundary integral, eq.(A.21), (A.23) and (A.24) on an element that coincides with the singularity, is:

$$\left(\frac{2u_1 \sin(\theta)}{\pi} - \frac{2u_2 \cos(\theta)}{\pi} \right) \left(\frac{1}{\epsilon} - \frac{1}{0} \right) + \frac{1}{\pi} \left(\frac{u_1 \sin(\theta)}{\epsilon} - \frac{u_2 \cos(\theta)}{\epsilon} \right) \quad (\text{A.25})$$

$$+ \frac{-1}{\pi} (\sin(\theta)u_1 - \cos(\theta)u_2) \left(\frac{2}{\epsilon} - \frac{2}{0} \right) = \frac{1}{\pi} \left(\frac{u_1 \sin(\theta)}{\epsilon} - \frac{u_2 \cos(\theta)}{\epsilon} \right). \quad (\text{A.26})$$

A.6.7 Conclusion

The result shows that the singular terms indeed cancel out. The problem was a hyper singularity that was plus and minus infinite at the same time. When evaluated on the boundary this singular behaviour became evident. It seems that in physical problem any strong or hyper singular terms will cancel off and always leave a finite contribution. The approach sketched here should provide the means to tackle those.

The reason is that the singular boundary integral that comes from the evaluation of the singularity is identical to the boundary integral. It differs only in the fact that u is localized to a point for the domain integral and not for the boundary integral. The proposed procedure is

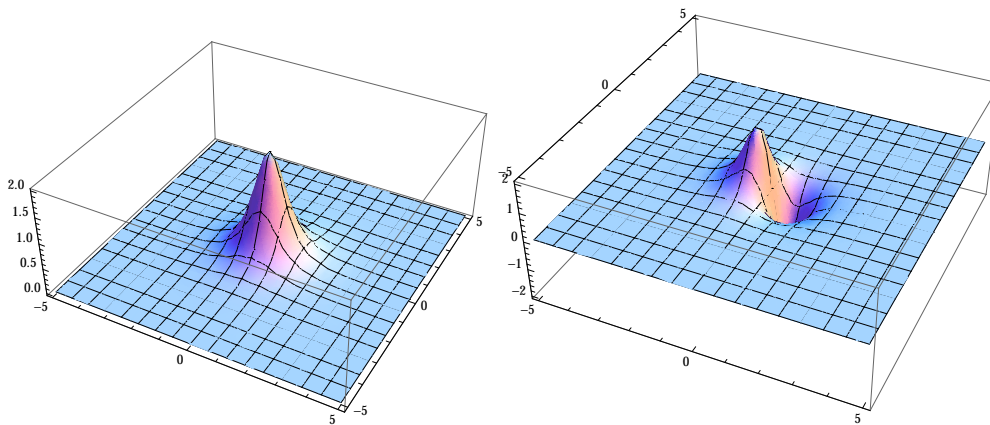


Figure A.2: In order to visualize the singularities I plot the regularized source points where $v_i = \frac{x_i}{x^2+y^2+1}$. The graph above shows $\nabla \cdot \mathbf{v}$ for (x, y) and the figure below $\Delta \mathbf{v}_1$. One can see that latter, although strongly singular, disappears when one integrates inside the domain because it has plus minus infinite parts that cancel out. Only on the boundary this integral is infinite but cancels with the corresponding boundary integral.

to replace the singular integral by a half circle path around the singularity.

A.7 Fabrication of microfluidic chips

Mask preparation A mask is a plate of glass with a chrome layer and a photo resist on top. Alternatively cheaper plastic masks exist. In this work we used a Laser writer DWL200 from Heidelberg, which is accurate to about a 0.8 or 2.5 micrometers on a 100mm wafer, depending on the writing head and writing velocity. The laser exposes the desired structure, areas that are not channels on a photo resist, which covers the chrome layer. Configuration and writing takes about one hour.

After this process the mask is developed, which means the resist on the chrome mask hardened, except where it was exposed by the laser. Then the mask is put in an acid bath (Cr etch) for a minute, which etches the unhardened resist together with the chrome underneath. In a liquid bath during 5 minutes a solvent (TechniStrip) peels of the remaining resist. The result is a glass plate with a chrome layer that has openings of the shape of the channel layout.

Wafer preparation This mask is used to mask a resin that is exposed to UV light. Before that, the wafer coated with a resist and is put in an oven with HMDS, a gas that provides a surface activation needed further processes. After 30 minutes in the oven a wafer is spin coated with a resist called AZ1512 on a EVG150 spin coating machine and then exposed using the mask on a Süss MA6/BA6. Then the wafer is then developed on the EVG150, which hardens the unexposed resin. The wafer is etched anisotropically in a plasma etcher, ALCATEL AMS200. Based on empirical data the etching depth is estimated on the residence time in the chamber.

Appendix A. Appendix

The size of the areas to be etched influences the etching velocity and it is necessary to check on a microscope or a profilometer the actual depth. Final etching by microwaves in Tepla GIGAbatch takes off the resist. One obtains a micro structured wafer that serves as a mold, that means the channel structures stick out.

Creating PDMS replica The wafer should be exposed to a TCMS solvent to clean the surface and make it unsticky for the PDMS. Without this step the PDMS adheres to the wafer making it impossible to separate the channels from the wafer. It is advised to activate the wafer in a Plasma oven for a short time. The TCMS receptacle is placed with the wafer carrier under a desiccator. With 5-6 drops of TCMS the vacuum line should be closed after 5 minutes with some TCMS remaining leaving it at low pressure without risking to be sucked out immediately.

One prepares a container of PDMS with curing agent at ratio 10:1, well mixed and degassed. Pours the mixture on the wafer, degasses again and pours the mold in an oven for 30 min. In the meantime one spin coats glass slides with PDMS which are put in the oven for about 3 minutes. The PDMS on the wafer is now solid. One cuts out the chips and punches hole, where the inlets and outlets are. Then glass slide and chip are pressed firmly together and are cured for 2 more hours in the oven.

Optionally the wafer can be put in the oven for 2 hours right away and bound to an uncoated glass slide.

The following complements the explanations in the introduction on the operation of a microfluidic experiment.

Syringe preparation Take out plunger of the syringe and screw on tubing. Flush with some liquid from the backside of the syringe using a plastic syringe with plastic nipple. Take care no bubbles are in the circuit, one might want to degas the water. Then put in the plunger but making certain that a droplet is formed around the hole so no air can get in. Put in plunger a little bit and mount on pump. If the syringe is not full push 5µl out so a drop forms at the connector and insert into container, then fill by pulling up the plunger

Chip preparation Keep chips in clean room box put tape on the outlets. Bond them with plasma, press together zipping from one direction to another so that air doesn't get trapped. When pressing firmly do not press on top of channels as flat channels might collapse. Then take a syringe with pure water and a plastic connector and put a drop of water on the outlet. Insert the tip and exert moderate pressure and observe water dwells forming on the inlet holes. Add some water on top of the inlets, now there is no air in the circuit.

Nomenclature

Non-dimensional variables

\mathcal{A}	area	
β	confinement of a fiber	$1 - 2g$
b_f	film thickness, normalized by channel height	
Ca	capillary number	$\frac{\mu U}{\gamma}$
χ	distinct contribution of the Brinkman equation to force balance of a droplet, eq.(2.89)	
D	deformation, difference in major and minor half axis over sum of half axes	$\frac{a-b}{a+b}$
d	anchor diameter	
D_f	deformation, difference of major and minor half axis over minor half axis	$\frac{L-W}{W}$
Eo	Eötvös number	$\frac{\Delta\rho g L^2}{\gamma}$
η	fluid interfacial boundary between two domains or viscosity ratio	$\frac{\mu_1}{\mu_1 + \mu_2}$
\mathbf{f}	traction force on an interface	$\sigma \mathbf{n}$
g	gap size between fiber and top/bottom wall normalized by channel height	
γ	interfacial tension	$\frac{\tilde{\gamma} t}{\gamma_{\text{ref}}}$
h	channel height	$\frac{H}{L}$
i	index for spatial coordinates	
k	permeability	$\sqrt{12} \frac{L}{H}$
κ	curvature	
λ	viscosity ratio of droplet against carrier fluid viscosity	$\frac{\mu_d}{\mu_c}$
M	number of discrete unknowns on the fixed walls; except chapter 7, where it is the torque	

Appendix A. Appendix

\mathbf{n}	outward normal vector of a boundary curve	
N	number of discrete unknowns on the droplet interface	
n	index for temporal coordinates. Except for chapter 4.1 where it is the wavenumber.	
$\dot{\Omega}$	angular velocity of the reference frame	$\frac{\dot{\rho}L^3\omega^2}{\gamma_{\text{ref}}}$
Ω	fluid domain in 2D coordinate space	
ω	outer Boundary of the fluid domain	
\mathcal{P}	perimeter	
p	pressure	$\frac{\tilde{p}}{\bar{p}}$
ϕ	velocity potential	
ψ	stream function	
q	pressure field; used for boundary integral transform	
\mathcal{R}	radius	$\frac{R}{L}$
Re	Reynolds number	$\frac{\rho UL}{\mu}$
ρ	radius; Not to be confused with the density in chapter 1 and 2.	
S	prefactor due to domain integral of the singularity in chapter 3 or distance from the center of rotation	
s	position coordinate on a boundary curve	
σ	stress tensor; Except for section 4.1, where it is the growth rate	$\frac{\tilde{\sigma}}{\gamma_{\text{ref}}L}$
\mathbf{t}	tangent vector of a boundary curve	
t	time	$\frac{\tilde{t}}{T}$
τ	stress field; used for boundary integral transform	
\mathbf{u}	velocity (vector), components are u_x, u_y and till section 2.3 also u_z	$\frac{\tilde{\mathbf{u}}}{U}$
\mathbf{v}	velocity field; used for boundary integral transform	
v	second component of the velocity vector, where u_y is inconvenient.	
\mathbf{w}_a	weight vector, $a = 1$ or 2 ; contains zeros and a one at component a	
w	channel width	$\frac{\tilde{W}}{L}$
\mathbf{x}	position (vector), components are x, y and till section 2.3 also z	$\frac{\tilde{\mathbf{x}}}{L}$

Dimensional variables

$\tilde{\gamma}$	surface tension, in chapter 1 simply γ	$[Pa\ m]$
μ	viscosity	$[Pa\ s]$
ρ	density	$[kg/m^3]$
A	area	$[m^2]$
g	gravitational acceleration	$[m/s^2]$
γ_{ref}	reference surface tension	$[Pa\ m]$
H	channel height	$[m]$
L	length scale	$[m]$
$\dot{\omega}$	angular velocity of rotating reference frame	$[s^{-1}]$
\tilde{p}	pressure	$[Pa]$
P	pressure scale	$[Pa]$
Q	flow rate	$[m^3/s]$
R	radius	$[m]$
$\tilde{\sigma}$	stress tensor	$[Pa]$
\tilde{t}	time	$[s]$
T	time scale	$[s]$
$\tilde{\mathbf{u}}$	position (vector), in chapter 1 simply \mathbf{u}	$[m/s]$
U	velocity scale	$[m/s]$
V	volume	$[m^3]$
W	channel width	$[m]$
$\tilde{\mathbf{x}}$	position (vector), in chapter 1 simply \mathbf{x}	$[m]$

Bibliography

- Abbyad, P., R. Dangla, A. Alexandrou, and C. N. Baroud (2011). Rails and anchors: guiding and trapping droplet microreactors in two dimensions. *Lab Chip* 11, 813–821.
- Agresti, J. J., E. Antipov, A. R. Abate, K. Ahn, A. C. Rowat, J.-C. Baret, M. Marquez, A. M. Klibanov, A. D. Griffiths, and D. A. Weitz (2010). Ultrahigh-throughput screening in drop-based microfluidics for directed evolution. *Proceedings of the National Academy of Sciences* 107(9), 4004–4009.
- Anderson, E., Z. Bai, C. Bischof, S. Blackford, J. Demmel, J. Dongarra, J. Du Croz, A. Greenbaum, S. Hammarling, A. McKenney, and D. Sorensen (1999). *LAPACK Users' Guide*. Society for Industrial and Applied Mathematics.
- Aussillous, P. and D. Quere (2000). Quick deposition of a fluid on the wall of a tube. *Physics of Fluids (1994-present)* 12(10), 2367–2371.
- Barenblatt, G. I., V. M. Entov, and V. M. Ryzhik (1989). *Theory of Fluid Flow Through Natural Rocks*, Volume 3 of *Theory and Applications or Transport in Porous Media*. Kluwer AP.
- Baroud, C. N., F. Gallaire, and R. Dangla (2010). Dynamics of microfluidic droplets. *Lab Chip* 10, 2032–2045.
- Baroud, C. N., M. Robert de Saint Vincent, and J.-P. Delville (2007). An optical toolbox for total control of droplet microfluidics. *Lab Chip* 7, 1029–1033.
- Bartolo, D. and D. G. A. L. Aarts (2012). Microfluidics and soft matter: small is useful. *Soft Matter* 8, 10530–10535.
- Bataille, J. (1968). Stabilité d'un déplacement radial non miscible. *Revue Inst. Petrole* 23, 1349–1364.
- Batchelor, G. K. (1967). *An Introduction to Fluid Mechanics*. Cambridge University Press.
- Bender, C. M. and S. A. Orszag (1999). *Asymptotic Methods and Perturbation Theory*. Springer.
- Berthet, H. (2012). *Single and collective fiber dynamics in confined microflows*. Ph. D. thesis, PMMH, ESPCI Paris, France.

Bibliography

- Berthet, H., M. Fermigier, and A. Lindner (2013). Single fiber transport in a confined channel: Microfluidic experiments and numerical study. *Physics of Fluids (1994-present)* 25(10), 103601.
- Bocquet, L. and E. Charlaix (2010). Nanofluidics, from bulk to interfaces. *Chem. Soc. Rev.* 39, 1073–1095.
- Boos, W. and A. Thess (1997). Thermocapillary flow in a Hele-Shaw cell. *Journal of Fluid Mechanics* 352, 305–330.
- Bremond, N., A. R. Thiam, and J. Bibette (2008, Jan). Decompressing emulsion droplets favors coalescence. *Phys. Rev. Lett.* 100, 024501.
- Bretherton, F. P. (1961). The motion of long bubbles in tubes. *Journal of Fluid Mechanics* 10, 166–188.
- Brinkman, H. C. (1949). A calculation of the viscous force exerted by a flowing fluid on a dense swarm of particles. *Applied Scientific Research* 1(1), 27–34.
- Brosseau, Q., J. Vignon, and J.-C. Baret (2014). Microfluidic dynamic interfacial tensiometry ([small mu]dit). *Soft Matter* 10, 3066–3076.
- Brun, P.-T., M. Nagel, and F. Gallaire (2013, Oct). Generic path for droplet relaxation in microfluidic channels. *Phys. Rev. E* 88, 043009.
- Bruus, H. (2008). *Theoretical Microfluidics*. Oxford University Press.
- Burgess, D. and M. R. Foster (1990). Analysis of the boundary conditions for a hele–shaw bubble. *Physics of Fluids A: Fluid Dynamics (1989-1993)* 2(7), 1105–1117.
- Bush, J. W. M. (1997, 12). The anomalous wake accompanying bubbles rising in a thin gap: a mechanically forced marangoni flow. *Journal of Fluid Mechanics* 352, 283–303.
- Cabral, J. T. and S. D. Hudson (2006). Microfluidic approach for rapid multicomponent interfacial tensiometry. *Lab Chip* 6, 427–436.
- Cahill, B. P. (2014). *Micro-Segmented Flow, Applications in Chemistry and Biology*, Volume 17 of *Biological and Medical Physics, Biomedical Engineering*. Springer.
- Cantat, I. (2013). Liquid meniscus friction on a wet plate: Bubbles, lamellae and foams). *Physics of Fluids (1994-present)* 25(3), 031303.
- Carlson, A., M. Do-Quang, and G. Amberg (2010). Droplet dynamics in a bifurcating channel. *International Journal of Multiphase Flow* 36(5), 397 – 405.
- Charru, F. (2011). *Hydrodynamic Instabilities*. Cambridge University Press.
- Chen, C., D. Hirdes, and A. Folch (2003). Gray-scale photolithography using microfluidic photomasks. *Proceedings of the National Academy of Sciences* 100(4), 1499–1504.

- Choi, K., A. H. Ng, R. Fobel, and A. R. Wheeler (2012). Digital microfluidics. *Annual Review of Analytical Chemistry* 5(1), 413–440. PMID: 22524226.
- Couder, Y. (2000). *Perspectives in fluid dynamics, A Collective Introduction to Current Research*. Cambridge University Press.
- Cristini, V. and Y.-C. Tan (2004). Theory and numerical simulation of droplet dynamics in complex flows-a review. *Lab Chip* 4, 257–264.
- Dai, W.-S. and M. J. Shelley (1993). A numerical study of the effect of surface tension and noise on an expanding hele–shaw bubble. *Physics of Fluids A: Fluid Dynamics (1989-1993)* 5(9), 2131–2146.
- Dangla, R., F. Gallaire, and C. N. Baroud (2010). Microchannel deformations due to solvent-induced pdms swelling. *Lab on a Chip* 21(10), 2972–2978.
- Dangla, R., S. C. Kayi, and C. N. Baroud (2013). Droplet microfluidics driven by gradients of confinement. In *Proceedings of the National Academy of Sciences*.
- Dangla, R., S. Lee, and C. N. Baroud (2011, sep). Trapping Microfluidic Drops in Wells of Surface Energy. *Physical Review Letters* 107(12), 124501.
- Dawson, G., S. Lee, and A. Juel (2013, 5). The trapping and release of bubbles from a linear pore. *Journal of Fluid Mechanics* 722, 437–460.
- de Gennes, P.-G. (1992). Soft matter. *Science* 256(5056), 495–497.
- de Gennes, P.-G., F. Brochard-Wyart, and D. Quere (2004). *Capillarity and Wetting Phenomena, Drops, Bubbles, Pearls, Waves*. Springer.
- Delaunay, C. (1841). Sur la surface de révolution dont la courbure moyenne est constante. *Journal de Mathématiques Pures et Appliquées* 6, 309–314.
- Dollet, B., W. van Hoeve, J.-P. Raven, P. Marmottant, and M. Versluis (2008, Jan). Role of the channel geometry on the bubble pinch-off in flow-focusing devices. *Phys. Rev. Lett.* 100, 034504.
- Eggers, J., J. R. Lister, and H. A. Stone (1999, 12). Coalescence of liquid drops. *Journal of Fluid Mechanics* 401, 293–310.
- Gallaire, F., P. Meliga, P. Laure, and C. N. Baroud (2014). Marangoni induced force on a drop in a hele shaw cell. *Physics of Fluids (1994-present)* 26(6), 062105.
- Ganan-Calvo, A. M. and J. M. Gordillo (2001). Perfectly monodisperse microbubbling by capillary flow focusing. *Phys. Rev. Lett.* 87(27), 274501.
- Garstecki, P., H. A. Stone, and G. M. Whitesides (2005, Apr). Mechanism for flow-rate controlled breakup in confined geometries: A route to monodisperse emulsions. *Phys. Rev. Lett.* 94, 164501.

Bibliography

- Geertz, M., D. Shore, and S. J. Maerkl (2012). Massively parallel measurements of molecular interaction kinetics on a microfluidic platform. *Proceedings of the National Academy of Sciences* 109(41), 16540–16545.
- Gorkin, R., J. Park, J. Siegrist, M. Amasia, B. S. Lee, J.-M. Park, J. Kim, H. Kim, M. Madou, and Y.-K. Cho (2010). Centrifugal microfluidics for biomedical applications. *Lab Chip* 10, 1758–1773.
- Gupta, N. R., A. Nadim, H. Haj-Hariri, and A. Borhan (2002). A numerical study of the effect of insoluble surfactants on the stability of a viscous drop translating in a Hele-Shaw cell. *Journal of Colloid and Interface Science* 252(1), 236–248.
- Helsing, J. and R. Ojala (2008). On the evaluation of layer potentials close to their sources. *Journal of Computational Physics* 227(5), 2899 – 2921.
- Hodges, S. R., O. E. Jensen, and J. M. Rallison (2004, 2). The motion of a viscous drop through a cylindrical tube. *Journal of Fluid Mechanics* 501, 279–301.
- Janssen, P. J. A. and P. D. Anderson (2007). Boundary-integral method for drop deformation between parallel plates. *Physics of Fluids* 19(4), 043602.
- Kim, H., T. Funada, D. D. Joseph, and G. M. Homsy (2009). Viscous potential flow analysis of radial fingering in a Hele-Shaw cell. *Physics of Fluids* 21, 074106.
- Kim, S. and S. J. Karrila (1991). *Microhydrodynamics, Principles and Selected Applications*. Butterworth-Heinemann.
- Kohr, M., G. P. R. Sekhar, and J. R. Blake (2008). Green's function of the brinkman equation in a 2d anisotropic case. *IMA Journal of Applied Mathematics* 73(2), 374–392.
- Kopf-Sill, A. R. and G. M. Homsy (1988). Bubble motion in a hele-shaw cell. *Physics of Fluids (1958-1988)* 31(1), 18–26.
- Langlois, U. E. and M. O. Deville (2014). *Slow Viscous Flow, 2nd edition*. Springer.
- Lindstrom, S. and H. Andersson-Svahn (2010). Overview of single-cell analyses: microdevices and applications. *Lab Chip* 10, 3363–3372.
- Liu, H. and Y. Zhang (2011). Droplet formation in microfluidic cross-junctions. *Physics of Fluids (1994-present)* 23(8), 082101.
- Logvinov, O. A., O. A. Ivashnyov, and N. N. Smirnov (2010). Evaluation of viscous fingering width in Hele-Shaw flows. *Acta Astronautica* 67, 53–59.
- Maruvada, S. R. K. and C.-W. Park (1996). Retarded motion of bubbles in Hele-Shaw cells. *Physics of Fluids* 8(12), 3229–3233.
- Maxworthy, T. (1989). Experimental study of interface instability in a Hele-Shaw cell. *Physical Review A* 39(11), 5863–5866.

- McWhirter, J. L., H. Noguchi, and G. Gompper (2011). Deformation and clustering of red blood cells in microcapillary flows. *Soft Matter* 7, 10967–10977.
- Meiburg, E. (1989). Bubbles in a Hele–Shaw cell: Numerical simulation of three-dimensional effects. *Physics of Fluids A* 1(6), 938–946.
- Nagel, M., P.-T. Brun, and F. Gallaire (2014). A numerical study of droplet trapping in microfluidic devices. *Physics of Fluids (1994-present)* 26(3), 032002.
- Nagel, M. and F. Gallaire (2013). A new prediction of wavelength selection in radial viscous fingering involving normal and tangential stresses. *Physics of Fluids (1994-present)* 25(12), 124107.
- OpenMP Architecture Review Board (2008). OpenMP application program interface version 3.0.
- Park, C.-W. and G. Homsy (1984). Two-phase displacement in hele shaw cells: theory. *Journal of Fluid Mechanics* 139, 291–308.
- Paterson, L. (1981). Radial fingering in a hele shaw cell. *Journal of Fluid Mechanics* 113, 513–529.
- Paterson, L. (1985). Fingering with miscible fluids in a Hele-Shaw cell. *Physics of Fluids* 28(1), 26–30.
- Pozrikidis, C. (1992). *Boundary Integral and Singularity Methods for Linearized Viscous Flow*. Cambridge University Press.
- Pozrikidis, C. (2001). Interfacial dynamics for stokes flow. *Journal of Computational Physics* 169(2), 250 – 301.
- Probstein, R. F. (1989). *Physicochemical Hydrodynamics, An Introduction*. Butterworths.
- Py, C., P. Reverdy, L. Doppler, J. Bico, B. Roman, and C. N. Baroud (2007, Apr). Capillary origami: Spontaneous wrapping of a droplet with an elastic sheet. *Phys. Rev. Lett.* 98, 156103.
- Rabello Dos Anjos, G. (2012). *A 3D ALE Finite Element Method for Two-Phase Flows with Phase Change*. Ph. D. thesis, STI, Lausanne.
- Reinelt, D. A. (1987). Interface conditions for two-phase displacement in Hele-Shaw cells. *Journal of Fluid Mechanics* 183, 219–234.
- Russel, W. B., E. J. Hinch, L. G. Leal, and G. Tieffenbruck (1977, 11). Rods falling near a vertical wall. *Journal of Fluid Mechanics* 83, 273–287.
- Saffman, P. and G. Taylor, Sir (1958). The penetration of a fluid into a porous medium or Hele-Shaw cell containing a more viscous liquid. *Proceedings of the Royal Society of London. Series A, Mathematical and Physical Sciences* 245(1242), 312–329.

Bibliography

- Saffman, P. F. and S. Tanveer (1989). Prediction of bubble velocity in a hele–shaw cell: Thin film and contact angle effects. *Physics of Fluids A: Fluid Dynamics (1989-1993)* 1(2), 219–223.
- Schwartz, L. W. (1989). Instability and fingering in a rotating Hele-Shaw cell or porous medium. *Physics of Fluids A* 1(2), 167–169.
- Seemann, R., M. Brinkmann, T. Pfohl, and S. Herminghaus (2012). Droplet based microfluidics. *Reports on Progress in Physics* 75(1), 016601.
- Shen, B., M. Leman, M. Reyssat, and P. Tabeling (2014). Dynamics of a small number of droplets in microfluidic hele–shaw cells. *Experiments in Fluids* 55(5), 1–10.
- Squires, T. and S. Quake (2005, oct). Microfluidics: Fluid physics at the nanoliter scale. *Reviews of Modern Physics* 77(3), 977–1026.
- Taylor, G. I. (1961, 3). Deposition of a viscous fluid on the wall of a tube. *Journal of Fluid Mechanics* 10, 161–165.
- Taylor, G. I. and P. G. Saffman (1959). A note on the motion of bubbles in a Hele-Shaw cell and porous medium. *The Quarterly Journal of Mechanics and Applied Mathematics* 12(3), 265–279.
- Tryggvason, G., R. Scardovelli, and S. Zaleski (2011). *Direct Numerical Simulations of Gas-Liquid Multiphase Flows*. Cambridge University Press.
- Ulloa, C., A. Ahumada, and M. L. Cordero (2014, Mar). Effect of confinement on the deformation of microfluidic drops. *Phys. Rev. E* 89, 033004.
- Wandersman, E., N. Quennouz, M. Fermigier, A. Lindner, and O. du Roure (2010). Buckled in translation. *Soft Matter* 6, 5715–5719.
- Wexler, J. S., P. H. Trinh, H. Berthet, N. Quennouz, O. du Roure, H. E. Huppert, A. Lindner, and H. A. Stone (2013). Bending of elastic fibres in viscous flows: the influence of confinement. *Journal of Fluid Mechanics* 720, 517–544.
- Whitesides, G. M. (2006). The origins and the future of microfluidics. *Nature* 442(7101), 368–373.
- Wrobel, L. C. and M. H. Aliabadi (2002). *The boundary element method*. Wiley.
- Wrobel, L. C., D. Soares Jr., and C. L. D. Bhaumik (2009). Drop deformation in stokes flow through converging channels. *Engineering Analysis with Boundary Elements* 33(7), 993–1000.
- Yokota, M. and K. Okumura (2011). Dimensional crossover in the coalescence dynamics of viscous drops confined in between two plates. *Proceedings of the National Academy of Sciences* 108(16), 6395–6398.

Young, N. O., J. S. Goldstein, and M. J. Block (1959, 10). The motion of bubbles in a vertical temperature gradient. *Journal of Fluid Mechanics* 6, 350–356.

Zhu, G., A. A. Mammoli, and H. Power (2006). A 3-d indirect boundary element method for bounded creeping flow of drops. *Engineering Analysis with Boundary Elements* 30, 856–868.



Mathias Nagel
Chemin des Grands Pins 7
2000 Neuchtel
Switzerland
mathias.nagel@epfl.ch
(+ +41) 76 469 0981

Website:
lfmi.epfl.ch/
simcomics

Date of birth:
26. Sep. 1981

Nationality: German

Mathias Nagel

Laboratory of Fluid Mechanics and Instabilities (LFMI)

About me I have been working for the SimCoMiCs project, an acronym of Simulations of Complex Microfluidic Circuits. A project funded by the European Research Council that is focused on simulations and experiments around the microhydrodynamics encountered in Lab-On-A-Chip applications. This work consists of mathematical aspects of simulation of two-phase flows and of practical work with clean room facilities and operation of microscope, syringe pumps and a highspeed camera.

Education

2009 - 2014, PhD student at EPFL Switzerland

Research in the Laboratory of Fluid Mechanics and Instabilities in the domain of microfluidics with participation at several international conferences and publication in renown journals. Elected as student representative in the Doctoral program in Mechanics.

2003 - 2009, Studies at RWTH-Aachen, Germany

Diploma (MSc.) in Mechanical Engineering, domain of aeronautical engineering. Including and exchange to study for 6 month at Keio University in Tokyo, Japan.

1998 - 2001, Abitur at Gymnasium Wandlitz, Germany

Principle subjects: Mathematics, Politics, Physics and English

Work Experience

2003 - 2008, Internships and student jobs

- 6 month, intern at EADS Space Transportation, R & D for propulsion systems, Germany.
- 6 month, student job (12h/week) at the Fraunhofer Institute for precision manufacturing IPT, Germany.
- 2 weeks, intern at a manufacturer for pumps, Sanjo-Seiki, Japan. Finow, Germany.

Dec 2001 - Dec 2002, Volunteer for an NGO in Thailand

Humanitarian aid for refugee camps located at the Thai/Burmese border and in an immigration detention center in Bangkok.

Additional Information

Language skills

- German
- English
- French
- Japanese (JLPT level 4)

Other skills and Interests

- Beneficiary of Japanese Jasso scholarship
- Assistant for hydrodynamics course
- Projectionist for an art and essay cinema
- Accompanied an excursion to Brazil

References

Publications and conference participation can be found at people.epfl.ch/mathias.nagel.